Copyright © 2001, by the author(s).
All rights reserved.

Permission to make digital or hard copies of all or part of this work for personal or classroom use is granted without fee provided that copies are not made or distributed for profit or commercial advantage and that copies bear this notice and the full citation on the first page. To copy otherwise, to republish, to post on servers or to redistribute to lists, requires prior specific permission.

DOMAIN DECOMPOSITION METHODS FOR THE ELECTROMAGNETIC SIMULATION OF SCATTERING FROM THREE-DIMENSIONAL STRUCTURES WITH APPLICATIONS IN LITHOGRAPHY

by

Konstantinos Adam

Memorandum No. UCB/ERL M01/42

20 December 2001

DOMAIN DECOMPOSITION METHODS FOR THE ELECTROMAGNETIC SIMULATION OF SCATTERING FROM THREE-DIMENSIONAL STRUCTURES WITH APPLICATIONS IN LITHOGRAPHY

by

Konstantinos Adam

Memorandum No. UCB/ERL M01/42

20 December 2001

ELECTRONICS RESEARCH LABORATORY

College of Engineering
University of California, Berkeley
94720

Domain Decomposition Methods for the Electromagnetic Simulation of Scattering from Three-Dimensional Structures with Applications in Lithography

Copyright © 2001
by
Konstantinos Adam
All rights reserved

Domain Decomposition Methods for the Electromagnetic Simulation of Scattering from Three-Dimensional Structures with Applications in Lithography

by

Konstantinos Adam

Diploma (National Technical University of Athens, Greece) 1996
M.S. (University of California, Berkeley) 1999

A dissertation submitted in partial satisfaction of the requirements for the degree of
Doctor of Philosophy
in

Electrical Engineering
and Computer Sciences

in the

GRADUATE DIVISION

of the

UNIVERSITY of CALIFORNIA, BERKELEY

Committee in charge:

Professor Andrew R. Neureuther, Chair
Professor William G. Oldham
Professor Panayiotis Papadopoulos

Fall 2001

Abstract

Domain Decomposition Methods for the Electromagnetic Simulation of Scattering from Three-Dimensional Structures with Applications in Lithography

by

Konstantinos Adam

Doctor of Philosophy in Electrical Engineering

University of California, Berkeley

Professor Andrew R. Neureuther, Chair

An integrated methodology has been developed for the computer simulation and modeling of the electromagnetic scattering from large, non-periodic, two-dimensional layouts of advanced photomasks (masks with optical proximity correction and phase shifting masks). The name *domain decomposition method* (DDM) was used, since it describes the central mechanism of the method.

Domain decomposition consists of three important steps: First, by virtue of the linearity of the Kirchhoff-Fresnel diffraction integral, the mask layout is decomposed into a set of constituent single-opening masks. Secondly, the rigorous electromagnetic simulation of each three-dimensional structure from the set of these single-opening masks is circumvented, and instead, the result for the scattered field is synthesized based on two two-dimensional rigorous electromagnetic simulations that model the mask geometry in two cross-sectional planes. Subsequently, based on the results of the electromagnetic scattering from these two-dimensional geometries, compact equivalent source models are used to describe the scattered fields on a reference plane. These models are constructed in such a way as to minimize the error in the part of the diffraction spectrum that is passing through the projection system allowing accurate and efficient image simulation.

Excellent accuracy in the calculation of the near scattered fields of better than 99% (in a normalized mean square error sense) compared with the fully rigorous mask model has been achieved, accompanied by speed-up factors for the total simulation time in excess of 200. A further revision of the method consisting of the decomposition of the layout into

edges (edge-DDM) allows for easier algorithmic implementation. The algorithm of the edge-DDM was programed in the MATLAB environment and together with TEMPEST cross-sectional simulations resulted in speed-up factors for the total simulation time of 172,800 (1sec. *vs.* 2days) using a library of pre-calculated edge-diffraction simulations. The normalized mean square error of the near field results between the edge-DDM and full three-dimensional simulation is less than 1%. A 12μm by 16μm layout of a three level alternating PSM, that is out of reach for fully rigorous methods, was simulated in under 1min.

The domain decomposition method was extended in two ways: Energy cross-coupling between neighboring apertures in alternating phase shift masks was modeled through simulation, enabling the accurate modeling of masks with large vertical topography. Another revision of the domain decomposition method suitable for handling the case of scattering from masks when phase defects are present was also realized, enabling rapid defect printability assessment.

Finally, useful engineering design data relevant to the design of optical proximity correction were produced and the electromagnetic behavior of isolated phase defects was examined to understand their interaction with layout features.

Professor A.R. Neureuther

Committee Chairman

ACKNOWLEDGMENTS

The completion of this work would have been much harder without the help and encouragement of many people. I would like to acknowledge their support. First, I would like to thank my advisor, Professor Neureuther, for his guidance, support and for giving me the opportunity to be part of his research group and continue my studies at Berkeley. His knowledge and free-spirited ideas have been a great inspiration for my research. I would also like to thank Professor Oldham who was a member in my qualifying exam committee and helped me with many details in my dissertation. Professors Papadopoulos, Spanos, Bokor and Attwood were also a very positive influence for me during my studies and I feel grateful for having interacted with them.

This research was supported by industry and the State of California under the SMART program SM97-01.

During my graduate years I also had the opportunity to work as a summer intern for two summer periods at National Semiconductor and at Intel Corp. There, I met and collaborated with people who positively influenced my research and in many cases helped expand my research horizons. I would like to thank Dr. Mircea Dusa and Dr. Robert Socha, at the time from National Semiconductor, and Dr. Kenny Toh, Dr. Francisco Leon and Dr. Edita Tejnil from Intel Corp.

Many thanks are also directed to friends and colleagues who, in one way or another, assisted me, supported me, listened to me, or laughed with me. Hoping that I will not forget any of them and that none will be disappointed by the (alphabetic) order that I list them, here they are: Nick Biziouras, Mosong Chen, Ebo Croffie, Yunfei Deng, Mike Lam, Yiannis Lygeros, George Pappas, Tom Pistor, Dimitris Psilos, Garth Robins, Yashesh Schroff, Mike Shumway, Bob Socha, Regina Soufli, Manolis Terrovitis, Jason Vassilliou, Mike Williamson, Lei Yuan, and my other friends in Berkeley and back in Greece. I would also like to thank my good friend George Papadopoulos for his support.

I owe so much to my family back in Greece. Even from such a great distance their love, support and (im)patience can be felt. Stelina, mom and dad you can maybe stop worrying just a little bit now!

Last, and definitely not least, I would like to thank the other inspiration and love in my life who has vastly helped, encouraged and supported me. Thank you Lisa.

TABLE OF CONTENTS

CHAPTER 1. Introduction 1

1.1. Organization of text 2
1.2. Thesis contributions 5

CHAPTER 2. The photolithography process and its simulation 6

2.1. Operation principle of optical photolithography 6
2.1.1. Illumination system 7
2.1.2. Projection system 10
2.1.3. Photomask 12
2.2. Resolution in optical lithography 15
2.3. Photolithography simulation and modeling 16
2.3.1. Simulation of image formation 18
2.3.2. The simulation program SPLAT 24
2.3.3. Rigorous simulation of the object and the simulation program TEMPEST 26
2.3.4. Diffraction orders and integration of rigorous mask simulations in the simulation of image formation 30
2.3.5. Polarization effects in imaging 35
2.4. Approximate vs. rigorous, scalar vs. vector, k-mask vs. r-mask and Abbe's vs. Hopkins' methods 40

CHAPTER 3. Analysis of OPC Features in Binary Masks 43

3.1. Scatter Bars 45
3.1.1. Designing the Placement and Size of the Scatter Bars at Best Focus 47
3.1.2. Out-of-focus Performance of Scatter Bars 50
3.1.3. Polarization Effects of Scatter Bars 51
3.2. Serifs 54
3.2.1. Modeling OPC serifs through simulation 55
3.2.2. Corner Rounding 59
3.2.3. Shape fidelity requirements for good performance of OPC serifs 60
3.3. Conclusions 62

CHAPTER 4. Domain decomposition methods for the rapid simulation of photomask scattering 63

4.1. Background 64
4.1.1. Superposition and domain decomposition 64
4.1.2. Simulation approaches and the imbalance problem in alt. PSM 68
4.2. Development of a new domain-decomposition and spectral-matching methodology for alt. PSM with 1D layouts 72

4.2.1. 0th-order domain decomposition method (DDM) of an alt. PSM into single-opening masks 72
4.2.2. Identifying the discrepancy between k-mask and r-mask models - The new mk-mask model 74
4.2.3. Systematic manipulation of the Fourier spectrum for the adjustment of the k-mask model 76
4.2.4. Other possible functions for the mk-mask model 80
4.3. Towards a comprehensive quasi-rigorous method and the mk-mask for alt. PSM with arbitrary 2D layouts 80
4.3.1. Example 1: Dense line/space pattern 82
4.3.2. Example 2: Semi-dense contact hole mask 84
4.3.3. Speed-up factor of the qr-DDM and mk-mask methodology 85
4.3.4. Accuracy issues 86
4.3.5. The qr-DDM for arbitrary 2D layouts 88
4.3.6. Off-axis illumination 92
4.4. Conclusions 93

CHAPTER 5. Deep Phase-Well and Cross-Talk Effects in Alternating Phase-Shifting Masks 95

5.1. Towards a comprehensive model for cross-talk 96
5.2. Scattering off of a 90° air/glass discontinuity 96
5.3. Modeling the cross-talk between phase-wells 98
5.4. 1st-order domain decomposition method of alt. PSM 100
5.5. Cross-talk dependence on the geometrical characteristics of the alt. PSM 104
5.6. Ideas for cross-talk elimination 110
5.7. 3D simulations where cross-talk is significant 115
5.8. Off-axis illumination 120
5.9. Conclusions 121

CHAPTER 6. The Edge Domain Decomposition Method 123

6.1. The edge-DDM applied in 1D layouts 124
6.1.1. Decomposition of a space into two edges 125
6.1.2. Decomposition of a line into two edges 126
6.1.3. Limits of the edge-DDM 128
6.2. The edge-DDM applied in 2D layouts 129
6.2.1. Algorithmic implementation of the edge-DDM 130
6.2.2. Dependence of edge-scattering on profile and polarization 132
6.2.3. Application of edge-DDM in simple 2D layouts 136
6.2.4. Example of edge-DDM on a large, arbitrary layout of a $0^{o}/90^{o}/270^{o}$ alt. PSM 140
6.3. Further speeding-up the edge-DDM 142
6.4. Conclusions 144

CHAPTER 7. Characterization of Phase Defects in Phase Shift Masks 146

7.1. Phase and brightness of isolated phase defects 147
7.2. Simulation results for defective alt. PSMs 152
7.3. Efficient phase defect modeling via DDM 155
7.4. Conclusions 164

CHAPTER 8. Conclusions 166

8.1. Summary of important results 166
8.2. Future research 169

APPENDIX A. Angular spectrum decomposition of electromagnetic waves .. 171

A.1. The angular spectrum and its physical interpretation 171
A.2. Propagation of the spectrum 173
A.3. Choosing the location of the observation plane 174

BIBLIOGRAPHY 177

1 Introduction

ONE of the most extraordinary achievements of engineering ingenuity has been the ability of the semiconductor industry to make a law out of a prediction in 1965 by Gordon Moore, meant to be valid for no more than 10 years, and according to which "the complexity of an integrated circuit, measured by the number of components (transistors, capacitors, diodes, resistors) per chip, would double approximately every two years" [58]. More than thirty five years later and after an increase in complexity approaching a factor of one hundred million (the one billion transistor integrated circuit is expected to appear before the end of the decade), the end of this spectacular exponential growth has yet to happen. Arguably, by far the biggest contributor to this progress has been what is known as *optical projection lithography*. This term loosely implies the physical process by which the integrated circuit is printed on a semiconductor wafer while all the circuitry information travels through a complex optical system in the form of ultraviolet light rays.

The end of optical lithography has been unsuccessfully predicted many times over the past ten years. However, everybody now agrees that certain physical and excessive cost barriers will eventually, probably in this decade, necessitate the replacement of this technology. *Extreme ultraviolet lithography* (EUVL) has emerged as the most prominent replacement candidate[1]. Although EUV lithography is a profoundly different technology, the main physical principles are nevertheless the same, since it will again be through information carried by higher frequency photons that the printing of integrated circuits will be realized.

1. See for example: "Extreme Ultraviolet Lithography: Will it be Ready in Time?" in November 2001 issue of IEEE Spectrum.

Optical photolithography will not go out without a fight. This fight is currently taking place in various fronts, most of which are grouped under what is known as *resolution enhancement techniques* (RET). RET is nothing more than an elaborate way to convey the "tricks" that engineers are using to make further increases in integrated circuit complexity possible. Two important such tricks are *optical proximity correction* (OPC) and *phase shift masks* (PSM), that are central to this work.

The widely accepted practice of using physical modeling through computer simulation in order to predict, design and model the outcomes of the lithography process was used in this research. Such a practice is justified for various reasons having to do with the reduced cost of conducting "virtual experiments" through computer simulations as opposed to costly real experiments in state-of-the-art integrated circuit fabrication facilities, and also with the fact that the various physical phenomena can be easily decoupled and better understood. However, the value of modeling through computer simulation goes far beyond that. Certain resolution enhancement techniques, such as the optical proximity correction, the optimization of phase-well topography in alternating phase shift masks and the concurrent illumination/mask optimization rely heavily on modeling through computer simulation [24]-[27], [63]-[64], [76].

This research focuses on the modeling of optical phenomena (scattering and propagation) that relate to photomasks. In particular, the techniques developed aim to bridge the gap between fully rigorous modeling methods that are not applicable in larger scale problems because of enormous computational requirements (speed and memory) and faster but less accurate methods that derive from light diffraction theory.

1.1. Organization of text

The operation of an optical projection system is introduced in Chapter 2 with special focus on the details that are relevant to this work. Elements of the scalar diffraction theory for partially coherent light are reviewed and the application of rigorous models for the mask diffraction problem are more extensively examined. In particular, issues that relate to the modeling of an extended illumination source and the origin of polarization

effects and their simulation are discussed in detail. Various simulation approaches for the mask diffraction problem are briefly reviewed and categorized.

Chapter 3 deals with optical proximity correction from a design point-of-view. The purpose is to uncover the type and magnitude of the corrections that are influenced by the geometrical parameters of assist features, such as scatter bars and corner serifs. The need for rigorous mask diffraction simulation owing to the small (wavelength-sized) size of assist features is critically examined and a simple perturbation approach is used to adapt the scalar diffraction model to the correct solution in the case of binary Chromium-on-glass (COG) masks.

The body of the more significant work begins with Chapter 4. A methodology is systematically developed that permits accurate electromagnetic simulation of the problem of mask diffraction for masks with large and arbitrary two-dimensional layouts. The starting point is the linearity of the Kirchhoff-Fresnel diffraction integral and what it implies for complex two-dimensional diffracting screens. Based on this linearity, a decomposition of the domain into a set of constituent parts is performed that is in principle the same as the field stitching method of Layet *et al.* [49] and Prather *et al.* [72] for solving the problem of large, one-dimensional diffraction gratings. Following this first decomposition, a second division of the elemental two-dimensional problems into a set of one-dimensional diffraction problems takes place. The accuracy of this step is explored and the physical reasons behind this accuracy are pointed out. Specifically, corner effects and polarizations perpendicular to the excited one are shown to be insignificant. Next, the act of the optical system as a low pass filter on the diffraction spectrum is pointed out and the idea of spectrally matched simpler models is developed. The algorithmic implementation of the method is also outlined.

In Chapter 5 the problem of energy cross-coupling between neighboring apertures of an alternating phase shift mask is treated. This is a critical step for the practical implementation of the domain decomposition framework, since the cross-communication, if not modeled, can severely confound the accuracy. From a single scattering simulation the physical mechanism of cross-talk becomes clear and a model is built to quantitatively take

cross-talk into account. Details that pertain to the dependence of cross-talk on the geometrical characteristics of the mask, the insertion point when the model is necessary and ideas for cross-talk elimination are also given.

The decomposition methods of Chapters 4 and 5 are further expanded in Chapter 6. Here, one extra division of the elemental one-dimensional diffraction problems into a set of edges takes place. The idea is similar to the technique of using edge-diffraction information for the field reconstruction of one-dimensional dielectric gratings by Kettunen *et al.* [48], but important differences are pointed out. The critical step of edge decomposition brings tremendous versatility and the algorithmic implementation is now less complicated. The accuracy of the method is, again, systematically examined. The implementation of the proposed algorithm into the MATLAB environment and examples of large, arbitrary layouts that are out of reach for rigorous methods are presented. The idea of spectrally matched elements that are compact is also used for the edge diffraction problem.

Phase defects in alternating phase shifting masks are the topic of Chapter 7. In the first part, the electromagnetic fingerprint of phase defects based on their type (glass protrusions or cavities) and size is quantified. Fundamental differences between the electromagnetic scattering of the two types of defects are revealed and used to explain the differences of linewidth variations when identically sized defects are present. Recent publications have provided experimental support of the results that were first obtained through computer simulation [93], [23]. In the second part of the Chapter, the domain decomposition method is adapted for simulation of defective alternating phase shifting masks in a way that should be suitable either for rapid defect printability assessment or die-to-database comparisons in mask inspection systems.

Finally, a summary of the most important results and ideas for future research on the methods developed can be found in Chapter 8.

The organization of each Chapter (other than Chapter 2, which can be considered introductory material in its entirety) is such that a short introduction relevant to the subsequent topics is given first, followed by the body of main ideas and concluded with impor-

tant results and observations. References to each topic can be found in the beginning of each Chapter, but are also scattered throughout, whenever it is appropriate.

1.2. Thesis contributions

Chapters 3 and 7 contain a rich amount of engineering data relevant to the design of optical proximity correction and phase defects respectively. The successful application of a perturbation model to adapt the accuracy of the scalar method is probably the most significant contribution of Chapter 3, whereas the quantitative characterization of phase defects and, in particular, the observation that the actual phase shift that they induce locally, depends strongly on the lateral dimension of the defect is the highlight of the first part of Chapter 7.

By far though, the most important contribution of this thesis has to be the development of the simulation methodology in Chapters 4 - 7 based on decomposition of the original mask geometry, that enables rapid diffraction analysis of large masks with arbitrary layouts, without sacrificing accuracy. This methodology should have a direct impact in model-based optical proximity correction and in the inspection and printability assessment of phase defects, where speed is critical.

2 The photolithography process and its simulation

THE purpose of this Chapter is to provide the theoretical and other background on the subsequent thesis material. An effort is made to keep the discussion short, yet concise, but some important topics are presented with greater detail.

2.1. Operation principle of optical photolithography

The general components of an optical lithography tool, shown schematically in the diagram of Figure 2-1, are the *illumination system*, the *projection system*, the *photomask* (also called *reticle*), and the *photoresist* spun on top of a semiconductor wafer. The operation principle of the system is based on the ability of the resist to record an image of the pattern to be printed. The mask, already carrying this pattern, is flooded with light and the projector forms an image of all mask patterns simultaneously onto (and into) the resist. The inherent parallelism of this process is the main reason why optical photolithography is favored over any other lithography, since it facilitates a very high throughput of 30-120 wafers per hour. The light intensity distribution on top of the resist surface is commonly referred to as *aerial image*. The resist itself is a photosensitive material whose chemical composition changes during light exposure. The pattern is thereby stored in form of a *latent (bulk) image* within the resist. After exposure has occurred, the resist is developed by means of a chemical process that resembles the process of developing photographic film. After development, the exposed parts of the resist remain or dissolve depending on its polarity (negative or positive respectively). The end-result of the lithography process is a more or less exact (scaled or not) replica of the mask pattern on the wafer surface that will play the role of a local protective layer (mask) for subsequent processing steps (etching, deposition, implantation).

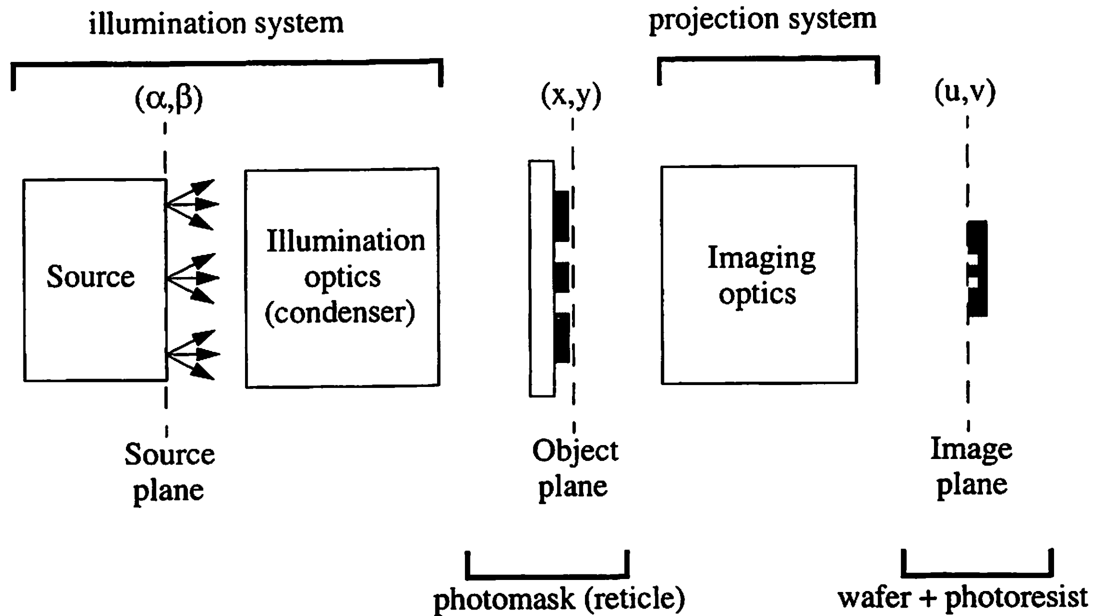

Figure 2-1. General diagram of an optical photolithography tool

Brief descriptions of the illumination system, the projection system and the photomask are given next. The complex role of the photoresist in the photolithography process is beyond the scope of this thesis, and the details of the resist chemistry will not be discussed in the following.

2.1.1. Illumination system

The role of the illumination system is to deliver a light beam that uniformly trans-illuminates the entire reticle. It typically consists of various optical elements, such as lenses, apertures, filters and mirrors. The light source is responsible for generating very powerful and monochromatic radiation. Power is necessary because it is directly related to throughput. Monochromaticity is important because high quality refractive (or reflective in the case of EUV lithography) optics can only be fabricated for a very narrow illumina-

tion bandwidth. State-of-the-art optical lithography tools employ *excimer*[1] lasers as their light source. Deep Ultra Violet (DUV) lithography is the term used for lithography systems with illumination wavelengths λ=248nm (excimer laser with KrF), λ=193nm (excimer laser with ArF) and λ=157nm (excimer laser with F_2). The successful development of current and future optical photolithography technologies is hinged upon research advances in both excimer laser technology and novel materials that possess the required properties (high optical transmission at DUV wavelengths, thermal properties, stability after heavy DUV radiation exposure) by which the optical elements of the system will be made.

All illumination systems in optical projection printing tools are designed to provide what is known as Köhler illumination [12]. By placing the source or an image of the source in the front focal plane of the condenser column, the rays originating from each source point illuminate the mask as a parallel beam, as seen in Figure 2-2. Each parallel beam is a plane wave whose direction of propagation depends on the relative position of the source point with respect to the optical axis. Nonuniformity in the brightness of the source points is averaged out so that every location on the reticle receives the same amount of illumination energy. As we will see in subsequent Sections Köhler illumination can be modeled in a concise mathematical way.

In addition to dose uniformity, the lithography process should also maintain directional uniformity such that the same features are replicated identically regardless of their orientations. The shape of the light source is therefore circular (or rotationally symmetric) in traditional optical lithography, although this is not true for certain advanced illumination schemes such as quadrupole illumination, where directional uniformity is sacrificed in order to maximize the resolution of features with certain orientations.

1. The term "excimer" originates from the expression *excited dimer*, meaning a molecule consisting of an excited atom and its unexcited (ground) state. Lasing of excimer lasers is highly multimode and this offers a crucial advantage for lithography applications, because it relaxes the problem of "speckle" [39], [80].

The coherence of the light source is another important attribute. Temporal coherence[1] is usually not a big concern, since the narrow bandwidth of excimer lasers implies high temporal coherence. Spatial coherence (or just plain coherence) on the other hand is always carefully engineered and in most cases adjustable. Using special scrambling techniques, the light emitted from any point of the source is made completely uncorrelated (incoherent) to the light emitted from every other point. However, light gathers coherence as it propagates away from its source [14], [82]. The frequently quoted partial coherence factor σ is a characteristic of the illumination system and is a measure of the physical extent and shape of the light source. The larger the light source, the larger the partial coherence factor, and the light source has a lower degree of coherence[2]. In the limit of an infinite

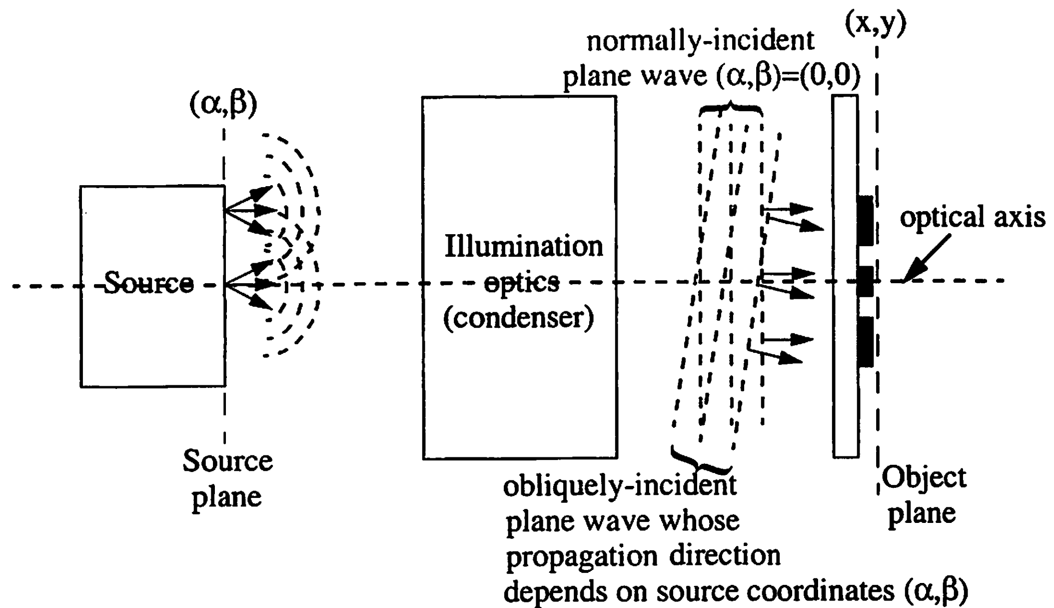

Figure 2-2. Illumination with Köhler's method

Each source point emits a spherical wave that is converted by the illumination system into a plane wave incident on the object (photomask). The angle of incidence of the plane wave depends on the location of the source point (α,β) with respect to the optical axis (0,0).

1. Temporal coherence has to do with the ability of light emitted from the same point to interfere with a delayed wavefront of itself, whereas spatial coherence has to do with the interference properties of light along the same wavefront.

2. Conceptually, a larger light source contains a greater number of mutually incoherent source points. The degree of coherence is therefore less.

source, imaging is incoherent and $\sigma = \infty$. On the other hand, the smaller the light source, the smaller the partial coherence factor, and the higher the degree of coherence. Imaging with a point source is fully coherent and $\sigma=0$. Note that a point source in a Köhler illumination will result in a single plane wave illuminating the mask and the angle of incidence of this wave depends on the relative position of the point source with respect to the optical axis. For partial coherence factors between zero and infinity, imaging is partially coherent. Typical partial coherence factors in optical lithography range from 0.3 to 0.9.

2.1.2. Projection system

The projection system typically consists of a multi-element lens column (up to 30-40 lenses) that may also have apertures, filters or other optical elements and it is a marvel of engineering precision in order to be able to reliably project images with minimum dimensions on the order of 100nm for state-of-the-art systems. One of the main reasons for the required high precision is control of the aberrations, or deviations of the wavefront from its ideal shape, but since aberrations are not an immediate topic of this thesis no further details on aberrations will be needed. Two relevant parameters of the projection system are the *numerical aperture*, NA, and the *reduction factor*, R. The numerical aperture is by definition the sine of the half-angle of the acceptance cone of light-rays as seen from the image side of the system. The ratio of image height to object height is by definition the *magnification factor* M of the system. The inverse of the magnification factor is the reduction factor R. Since a typical system in photolithography projects at the image plane a scaled down version of the object (mask)[1], M is less than 1 and R is greater than 1. State-of-the-art systems currently have reduction factors of R=4 or 5 and it is exactly because of these (relatively) large reduction factors that the powerful methods described in the subsequent Chapters have a wide range of applicability. Note that two numerical apertures exist in the projection system, namely NA_i (or simply NA) and NA_o, which refer to the half-angle of the acceptance cone as seen from the image side and from the object (mask) side respectively. They are related through the reduction factor as follows:

1. For reasons having to do primarily with relaxation of the process requirements in the fabrication of the photomasks.

Equation 2-1. $$R = \frac{NA_i}{NA_o}$$

For a circularly shaped light source the partial coherence factor σ mentioned above is related to the numerical apertures of both the projection system and the illumination system. Specifically σ is given by:

Equation 2-2. $$\sigma = \frac{NA_c}{NA_p}$$

where NA_c is the numerical aperture of the condenser lens (illumination system) and NA_p is the numerical aperture of the projector lens. Some confusion arises from the fact that in the above equation the reduction factor of the imaging system is implicitly taken into account. Figure 2-3 clarifies the situation by showing simplified diagrams of two optical systems with parameters NA=0.5, σ=0.5 and R=5 or R=1.

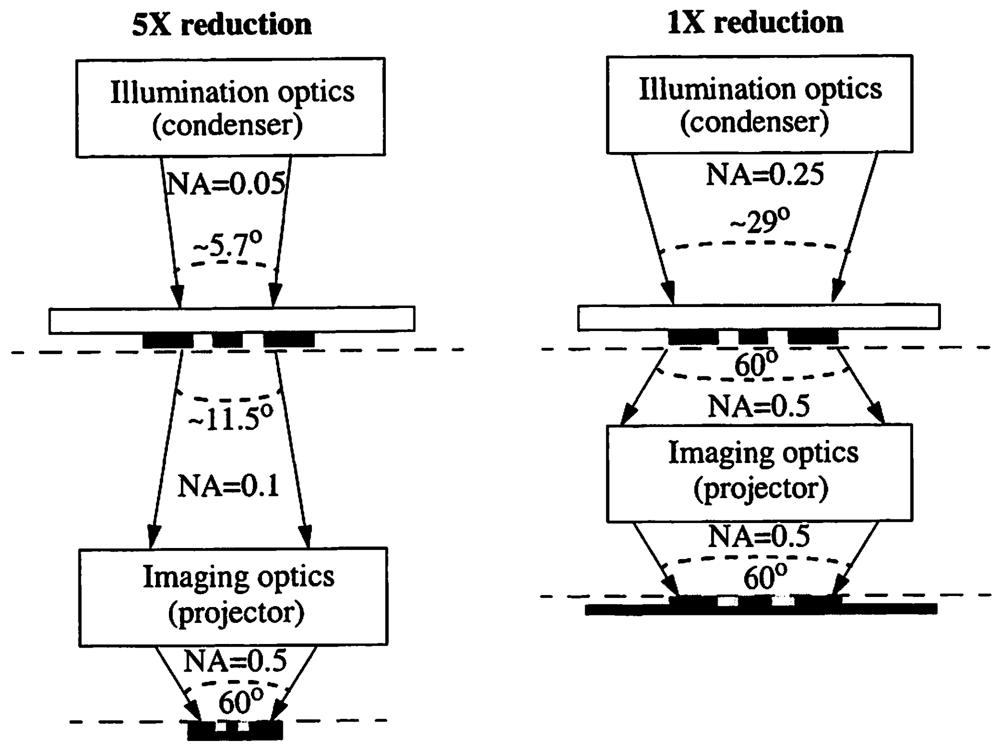

Figure 2-3. Numerical apertures and corresponding light acceptance cones of illumination and projection lenses for NA=0.5, σ=0.5 at 5X and 1X reduction

2.1.3. Photomask

The photomask, also called reticle, carries the pattern to be printed at a given lithography processing step. The masks of integrated circuits having large die-sizes or footprints, (that is, occupying large areas on the semiconductor wafer), typically carry just one copy of the chip pattern. A matrix of several chip patterns is contained in one mask whenever the chip size permits. Note that the mask is drawn R times the actual size on the semiconductor wafer, since the dimensions of the circuit will be scaled down by the reduction factor R. For this reason it is not sufficient to just provide feature sizes, since it may not be immediately obvious from the context whether these are photomask (object) or resist (image) sizes. A typical convention for distinguishing photomask feature sizes from resist feature sizes is to include in parenthesis the reduction factor R. For example, a 600nm (4X) line has a size of 600nm on the mask, and would produce a 600nm/4=150nm line if used in a 4X imaging system. Similarly, a 130nm (1X) line refers to the size of a line at the image (wafer) plane and would result from the printing of a 130nm line on the mask for a system with R=1, or a 520nm (4x130nm) line on the mask for a system with R=4, or a 1.3μm (10x130nm) line on the mask for a system with R=10.

Depending on their operation principle photomasks can be divided into two broad categories: conventional *binary or chrome-on-glass (COG) masks* and advanced *phase-shifting masks (PSM).*

A binary or COG mask consists of a transparent substrate (mask blank), covered with a thin opaque film that bears the desired pattern. Light can either pass unobstructed through an area not covered by the opaque film or be completely blocked if it is incident on an area that is protected by the film. This binary behavior of the transmission characteristic of the mask is responsible for its name. The mask blank for DUV lithography typically consists of fused silica glass that has excellent transmission at λ=248nm and somewhat poorer but acceptable transmission at λ=193nm and λ=157nm. The opaque film is typically on the order of 100nm thick and has a chromium (Cr) composition.

Adding phase modulation to the photomask can profoundly increase the attainable resolution. This is the principle followed by phase-shifting masks, which employ discrete

transmission and discrete phase modulation[1]. There are many different flavors of PSMs depending on the way that the phase modulation is achieved. One of the most promising PSM technologies is what is known as alternating phase-shifting mask (alt. PSM, or APSM) and since it will be a center part in this thesis it is introduced in some more detail. The principle of an alt. PSM is compared with that of a binary mask in Figure 2-4. The center line is bordered by transmitting regions with 180° phase difference on an alt. PSM and by clear areas of the same phase on a binary mask. The phase difference on the alt. PSM leads to destructive interference, resulting in a sharp dark image. The binary mask image in not as sharp because of the lack of phase interaction. The 180° phase difference is created by etching trenches, also called *phase-wells*, into the fused silica substrate during the alt. PSM fabrication process, which is now more complex than the COG fabrication process. The difference in the amount of material removed d_{etch} is such that the path length difference between light passing through the different phase regions is half of the wavelength in air[2]. The theoretical etch depth difference is determined by the following expression:

$$n_{substrate}(\lambda)d_{etch} - n_{air}(\lambda)d_{etch} = \frac{1}{2}\lambda$$

Equation 2-3.
$$d_{etch} = \frac{\lambda}{2[n_{substrate}(\lambda) - n_{air}(\lambda)]}$$

where $n_{substrate}(\lambda)$ is the refractive index of the fused silica substrate at the exposure wavelength and $n_{air}(\lambda)$ is the refractive index of air. For commonly used DUV wavelengths (248, 193 and 157nm), $n_{substrate}(\lambda) \cong 1.5$ and $n_{air}(\lambda) \cong 1$, and Equation 2-3 simplifies to $d_{etch} \cong \lambda$. The performance of alt. PSM depends strongly on the geometrical details of the etched phase-wells and accurate characterization and understanding is of great importance for the successful utilization of alt. PSMs in the lithographic process.

1. There are usually two levels of transmission and two, three or four phase levels. Other combinations have also been reported.

2. In principle, any path length difference that is an odd multiple of $\lambda/2$ would be appropriate, but because of fabrication considerations it is almost always $\lambda/2$.

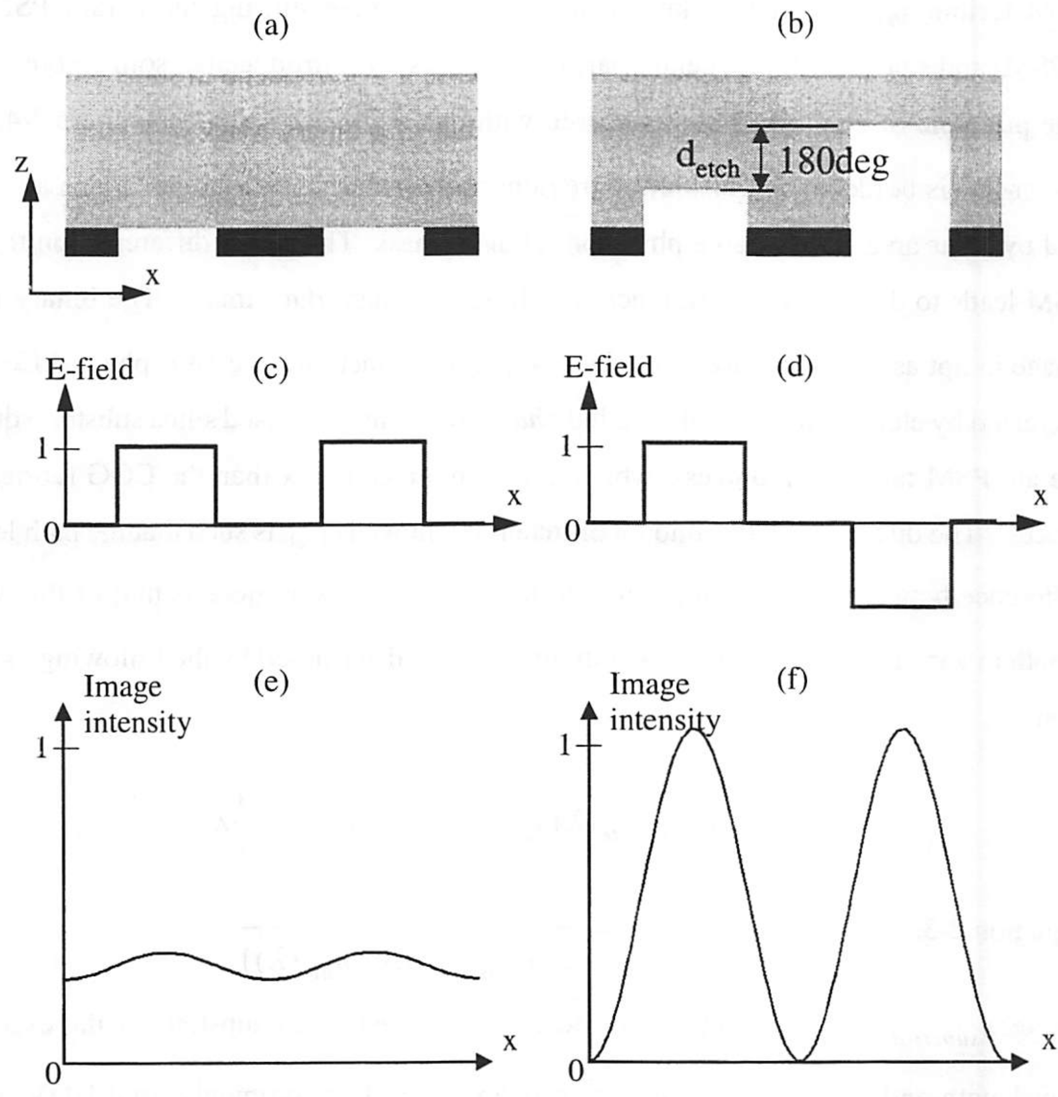

Figure 2-4. Comparison of operation principles of an alternating phase shift mask (alt. PSM) and a binary (COG) mask

Cut-planes of geometry of a binary (COG) mask (a) and an alternating phase-shift mask (b). The ideal electric field distribution for the binary mask (c) leads to a poor image intensity distribution (e) at the image plane, whereas the ideal electric field distribution for the alt. PSM (d), because of destructive interference, leads to a robust image.

2.2. Resolution in optical lithography

The smallest resolvable feature or *critical dimension* (CD) of a lithographic imaging system is given by:

Equation 2-4. $$CD = k_1 \cdot \frac{\lambda}{NA}$$

where λ is the wavelength of the exposure light, NA is the numerical aperture of the projector and k_1 is a process-related factor. In order to increase the resolution (decrease the critical dimension) any combination of reducing k_1, decreasing λ and increasing NA is required. Decreasing λ arbitrarily is not possible for many practical reasons[1], increasing the numerical aperture beyond 0.8-0.85 (the physical limit of NA is one) is difficult and costly and reducing k_1 to arbitrarily low values is not possible [103]. Equation 2-4 is somewhat confusing, in the sense that the ultimate resolution of a system is determined by its ability to resolve (small) features that are densely packed and not isolated features. Actually, arbitrarily small isolated features can be resolved since in this case there is no theoretical resolution limit [104]! Nevertheless, by Equation 2-4 it is usually implied that the distance between the minimum resolvable CD and its neighbors is on the order of one CD, that is, the period p of a dense array of (small) features is on the order of two times the critical dimension. With that important consideration in mind, theoretically the smallest resolvable period p_{min} is given by the following expressions for coherent ($\sigma=0$), partially coherent ($0 < \sigma < 1$) and incoherent ($\sigma = \infty$) imaging respectively:

Equation 2-5. $$p_{min} = \frac{\lambda}{NA}, (\sigma = 0)$$

Equation 2-6. $$p_{min} = \begin{cases} \frac{1}{1+\sigma} \cdot \frac{\lambda}{NA}, (\sigma \le 1) \\ \frac{1}{2}\frac{\lambda}{NA}, (\sigma > 1) \end{cases}$$

1. At the exposure wavelength, a powerful light source needs to exist to satisfy the throughput requirements. Suitable optical materials for lenses and mask substrates and also resist materials are not easy to develop at arbitrary wavelengths.

Equation 2-7. $$p_{min} = \frac{1}{2}\frac{\lambda}{NA}, (\sigma = \infty)$$

Hence, the critical dimension for 1:1 packed features (feature size of 1CD followed by a space of 1CD before the next feature) is half of p_{min} and theoretically the minimum k_1 factor is 0.25 (for σ>1). However, photolithography imaging and processing below k_1=0.5 becomes extremely difficult and it is generally accepted that k_1=0.3 is a more attainable limit.

2.3. Photolithography simulation and modeling

The key role of simulation and modeling of the photolithography process is widely recognized. In many aspects, simulation in not just another tool that augments the process development, testing and understanding of the complex relationships of the large number of lithographic parameters, but it is a true enabling technology that allows innovative solutions to be applied. Particularly relevant to the work in this thesis is the role of simulation in the application of optical proximity correction (Chapters 3-6).

One of the distinct modeling phases in photolithography simulation is the simulation of the *photomask imaging*. Under specified illumination conditions (size, shape, wavelength, bandwidth of source and details of the illuminator), a photomask (binary, alt. PSM or other) bearing the pattern to be printed, a given illumination system (NA, filters, apertures, aberrations) and a certain photoresist "thin film stack" with possible underlying topographical features, one is interested in calculating through computer simulation the image projected onto (or into) the photoresist. Subsequently, important attributes of the quality of this image, such as the critical dimension or the edge slope, can be extracted, or the aerial image can be used directly as input to the next module of photolithography simulation that models the *exposure* and *development* of the photoresist. The same considerations apply in the photomask imaging simulation whether it is performed merely to extract the aerial image under a certain system setting, or in more complex optimization problems that involve, for example, finding the optimum illumination setting that will result in the most robust lithographic performance[1] [76], [42], or adjusting the mask pattern such that it will result in an image that is a more exact replica of the IC designer's intention[2].

The most rigorous way to simulate the imaging of the photomask would be to model the whole photolithography system of Figure 2-1 using Maxwell's equations. The continuous form of the two independent Maxwell's equations for linear, isotropic, non-magnetic, non-dispersive materials are:

Equation 2-8. $$\nabla \times \vec{E} = -\frac{\partial \vec{B}}{\partial t}$$

Equation 2-9. $$\nabla \times \vec{H} = \vec{J} + \frac{\partial \vec{D}}{\partial t}$$

where $\vec{J}$ is the electric current density, $\vec{E}$, $\vec{H}$ are the electric and magnetic field strengths and $\vec{D}$, $\vec{B}$ are the electric and magnetic flux densities respectively. The following constitutive relations also apply:

Equation 2-10. $$\vec{D} = \varepsilon(\vec{r})\vec{E}$$

Equation 2-11. $$\vec{B} = \mu(\vec{r})\vec{H}$$

Equation 2-12. $$\vec{J} = \sigma(\vec{r})\vec{E}$$

Every distinct material in the system enters the above equations through its dielectric permittivity ε (or index of refraction $n = \sqrt{\varepsilon}$) and magnetic permeability μ, while appropriate boundary conditions are enforced at all material interfaces present. Under given parameters for the illumination source, the electromagnetic field $(\vec{E}, \vec{H})$ being established everywhere within the system can be determined by the numerical solution of the boundary value problem, including the aerial image into or onto the photoresist. However, the size of such a problem is monstrous! With a system volume on the order of one cubic meter and illumination wavelengths less than 1μm the size of the problem expressed in

1. For example, maximizing the process window or maximizing the overlapping areas of process windows for a range of feature sizes.

2. This process is known as optical proximity compensation (or correction) - OPC.

cubic wavelengths exceeds 10^{18}! Clearly, some simplified models need to be considered for certain parts of the problem.

Luckily, both the illumination and the imaging optics parts of the system, as their name suggests, can be accurately modeled using the *science of optics* [11], [36]. Light propagation through the illumination and imaging optics is modeled with either scalar or vector diffraction theory. Elements of the scalar diffraction theory of partially coherent light are summarized in the next Section. A treatment of vector diffraction theory can be found in [89], [114]. The light propagation effects in the vicinity of the photomask or the resist-coated semiconductor wafer may require knowledge of the exact solution of Maxwell's equations. Rigorous methods for the calculation of electromagnetic wave scattering that occurs during the passage of light through the object and subject to substrate topography during the formation of the image are outlined in Section 2.3.3.

2.3.1. Simulation of image formation

The material in this Section follows closely reference [40], but the same ideas and concepts can be found in most advanced textbooks on optics. The following theory of image formation with partially coherent light will allow numerical calculation of the intensity distribution expected at the image plane under a specified set of system parameters.

Integration over the source (Abbe's method)

When the illumination of the object originates from a quasi-monochromatic, spatially incoherent source, as is the case in photolithography systems, there exists a method for calculating the image intensity that has the special appeal of conceptual simplicity. First, each point on the source is considered individually and the image intensity produced by the light from that single point is calculated. Then, the image intensity contributions from all points that comprise the source are added, with a weighting factor proportional to the source intensity distribution. Simple addition (integration) of the image intensity distributions is justified, since the original source is assumed to be spatially incoherent.

Referring back to Figure 2-1, under the quasi-monochromatic conditions, each optical system can be represented by an amplitude spread function (impulse response). Let

$F(x,y;\alpha,\beta)$ and $K(u,v;x,y)$ be the amplitude spread functions of the illuminating and imaging systems, respectively. A single source point at coordinates (α,β) emits light that can be represented by the time-varying phasor amplitude $U_s(\alpha,\beta;t)$. For Köhler illumination each source point corresponds to a plane wave impinging on the object with the angle of incidence depending on (α,β), as shown in Figure 2-2. The illumination reaches the object and passes through it, resulting in a time-varying phasor amplitude $U_0(x,y;\alpha,\beta;t)$ to the right of the object given by:

Equation 2-13. $$U_o(x,y;\alpha,\beta;t) = F(x,y;\alpha,\beta)T_o(x,y)U_s(\alpha,\beta;t-\delta_1)$$

where δ_1 is a time delay that depends on (x,y) and (α,β), and $T_0(x,y)$ is the amplitude transmittance of the object, which, for now, is assumed to be independent of the particular source point providing the illumination. Finally, the time-varying phasor amplitude of the light reaching coordinates (u,v) on the image plane from source point (α,β) is given by:

Equation 2-14.

$$U_i(u,v;\alpha,\beta;t) = \int\int_{-\infty}^{\infty} K(u,v;x,y)T_o(x,y)F(x,y;\alpha,\beta)U_s(\alpha,\beta;(t-\delta_1-\delta_2))dxdy$$

where δ_2 is a time delay that depends on (u,v) and (x,y).

The partial aerial image $I_i(u,v;\alpha,\beta)$, or the intensity of the light reaching image coordinates (u,v) from the source point at (α,β) is the expected value (time average) of the squared amplitude of $U_i(u,v;\alpha,\beta;t)$. Under the quasi-monochromatic assumption, $I_i(u,v;\alpha,\beta)$ can be calculated to be:

Equation 2-15.

$$I_i(u,v;\alpha,\beta) = I_s(\alpha,\beta)\int\int\int\int_{-\infty}^{\infty} K(u,v;x_1,y_1)K^*(u,v;x_2,y_2)$$

$$\times F(x_1,y_1;\alpha,\beta)F^*(x_2,y_2;\alpha,\beta)T_o(x_1,y_1)T_o^*(x_2,y_2)dx_1dy_1dx_2dy_2$$

where the asterisk represents complex conjugation and $I_s(\alpha,\beta)$ is the source intensity at (α,β). Finally, the partial intensity $I_i(u,v;\alpha,\beta)$ can be integrated over the source coordinates (α,β) giving the result:

Equation 2-16.
$$I_i(u, v) = \int\int_{-\infty}^{\infty} I_s(\alpha, \beta)\int\int\int\int_{-\infty}^{\infty} K(u, v;x_1, y_1)K^*(u, v;x_2, y_2)$$
$$\times F(x_1, y_1;\alpha, \beta)F^*(x_2, y_2;\alpha, \beta)T_o(x_1, y_1)T_o^*(x_2, y_2)dx_1dy_1dx_2dy_2d\alpha d\beta$$

With knowledge of I_s, F, K and T_0 the numerical calculation of the image intensity distribution is possible. This model of image formation is attributed to Abbe [1] and although it is conceptually simple, it is not always the best method to use in practice.

Representation of the source by an incident mutual intensity function (Hopkins' method)

Another approach for the calculation of image intensity distributions is possible if the explicit integration over the source is suppressed and the effects of the source are represented by the mutual intensity function, describing the illumination incident on the object. Under the quasi-monochromatic assumption, the time-varying phasor amplitude $U_i(u,v;t)$ of the light arriving at image coordinates (u,v) can be represented by the time-varying phasor amplitude $U_c(x,y;t)$ of the light incident on the object at coordinates (x,y) by:

Equation 2-17.
$$U_i(u, v;t) = \int\int_{-\infty}^{\infty} K(u, v;x, y)T_o(x, y)U_c(x, y;t - \delta)dxdy$$

where, again, K is the amplitude spread function of the imaging system, T_0 is the amplitude transmittance of the object, and δ is a time delay that depends on (x,y) and (u,v). Note that $U_0(x,y;t)$ and $U_c(x,y;t)$ are related through:

Equation 2-18.
$$U_o(x, y;t) = U_c(x, y;t)T_o(x, y)$$

The intensity at (u,v) is given by:

Equation 2-19.
$$I_i(u, v) = \langle|U_i(u, v;t)|^2\rangle \Rightarrow$$

$$I_i(u,v) = \int\int\int\int_{-\infty}^{\infty} K(u,v;x_1,y_1)K^*(u,v;x_2,y_2)T_o(x_1,y_1)T_o^*(x_2,y_2)$$

$$\times \langle U_c(x_1,y_1;t-\delta_1)U_c^*(x_2,y_2;t-\delta_2)\rangle dx_1dy_1dx_2dy_2$$

Under the quasi-monochromatic assumption the difference $|\delta_1 - \delta_2|$ is much smaller compared to the coherence time[1] and hence:

Equation 2-20. $$\langle U_c(x_1,y_1;t-\delta_1)U_c^*(x_2,y_2;t-\delta_2)\rangle = J_o(x_1,y_1;x_2,y_2)$$

where J_o is the mutual intensity distribution incident on the object. Finally, the image intensity is derived upon substitution of Equation 2-20 into Equation 2-19:

Equation 2-21.

$$I_i(u,v) = \int\int\int\int_{-\infty}^{\infty} K(u,v;x_1,y_1)K^*(u,v;x_2,y_2)T_o(x_1,y_1)T_o^*(x_2,y_2)$$

$$\times J_o(x_1,y_1;x_2,y_2)dx_1dy_1dx_2dy_2$$

With knowledge of K, T_o and J_o the image I_i can be calculated. The above nonlinear integral equation is often referred to as the Hopkins model and there are situations that this model is superior for the numerical simulation of imaging, as will be seen shortly. Note that although Equation 2-16 requires six integrations whereas Equation 2-21 only four, the latter is not really simpler than the former, for four integrations are in general required to determine J_o. However, when an incoherent source is assumed, as was done for deriving Equation 2-16, calculation of J_o requires only two integrations, for a total of six for the complete image calculation.

1. There exist slightly different definitions of the coherence time τ_c of a disturbance U(t), involving the complex degree of coherence of U(t). Here, it suffices to note that the coherence time is always on the order of $1/\Delta\nu$, where $\Delta\nu$ is the finite bandwidth of U(t). Since U(t) is nearly monochromatic in photolithography applications, $\Delta\nu$ is very small and consequently τ_c is large.

Remarks

• A key assumption made in the derivation of both Equation 2-16 and Equation 2-21 was the independence of the transmission characteristics of the object on the source points (α,β). This assumption is not always valid in photolithography systems. While it can be easily lifted in Abbe's (Equation 2-16) method it is not trivial to do that in Hopkins' method (Equation 2-21), since in the former case the integration over the source is performed last and a dependence of T_0 on (α,β) is straightforward to include by $T_0(x,y;\alpha,\beta)$, whereas in the latter this is not possible because the integration over the source takes place first, during the calculation of the incident mutual intensity J_0. Ways to overcome this significant obstacle are discussed in Section 2.3.5.

• Under the assumption of a space-invariant or isoplanatic system, which is in general valid for photolithography systems, the following simplifications are true:

$$K(u, v;x, y) = K(u - x, v - y), \text{ and}$$

$$J_o(x_1, y_1;x_2, y_2) = J_o(x_1 - x_2, y_1 - y_2)$$

Then, the special cases of completely coherent and completely incoherent illumination follow from Equation 2-21. For completely coherent illumination it is $J_o(x_1 - x_2, y_1 - y_2) = 1$ and Equation 2-21 simplifies to:

Equation 2-22. $$I_i(u, v) = |K \otimes T_o|^2$$

where $\otimes$ denotes the two-dimensional convolution operator. The imaging system in this case is said to be linear in the complex electromagnetic field amplitude.

For incoherent illumination it is $J_o(x_1 - x_2, y_1 - y_2) = \delta(x_1 - x_2, y_1 - y_2)$ and Equation 2-21 reduces to:

Equation 2-23. $$I_i(u, v) = |K|^2 \otimes |T_o|^2$$

and in this case the imaging system is said to be linear in intensity.

The Transmission Cross-Coefficient Approach

With the assumption of space-invariance Equation 2-21 can be restructured in the following significant form:

Equation 2-24.

$$\bar{I}_i(f,g) = \int\int_{-\infty}^{\infty} TCC(f'+f, g'+g; f', g')\overline{T_o}(f'+f, g'+g)\overline{T_o}^*(f', g')df'dg'$$

The overbars on I_i and T_0 denote Fourier transforms of the image intensity and the object transmission respectively. The quantity TCC is often referred to as the *transmission cross-coefficient*. It is totally independent of the object and is a complete description of the optical system from source to image plane. It is given by:

Equation 2-25.

$$TCC(f,g;f',g') = \int\int_{-\infty}^{\infty} \overline{J_o}(f'',g'')\bar{F}(f+f'',g+g'')\bar{F}^*(f'+f'',g'+g'')df''dg''$$

where, again, the overbars denote Fourier transforms of the respective quantities.

Finally, the image $I_i(u,v)$ as a function of image-space coordinates can be retrieved by the inverse Fourier transform of Equation 2-24. The elegance and power of this approach lie exactly in the fact that all illumination and imaging parameters are completely modeled in the TCCs, so that they can be pre-calculated and stored via Equation 2-25, and the image of a number of different objects can be quickly simulated through Equation 2-24. Moreover, the existence of efficient algorithms, like the FFT, for the forward and backward Fourier transforms involved in this method coupled with methods for the decomposition of the incident mutual intensity J_0 ([25], [97]) render the Hopkins' method superior over Abbe's in a large number of situations.

2.3.2. The simulation program SPLAT[1]

A notable implementation of Hopkins' method for the simulation of optical images of one-dimensional objects was implemented by O'Toole *et al.* [61], [60] as part of the photolithography process simulator SAMPLE[2]. Subsequently, Flanner extended the optical imaging simulation program to handle two-dimensional objects [32]. At that time the simulator's name was "2D". Toh made significant additions in the simulator's capabilities, which included the ability to simulate lens aberrations [94] and also upgraded the name of the simulator to SPLAT. Yeung's key theoretical work in extending Hopkins' theory of partially coherent imaging to include thin-film interference effects [113] and more accurate high-NA models [114], [28] resulted in the current version of the simulation program SPLAT, which was used extensively in this work.

The calculation of images with SPLAT is straightforward. The illumination and the projection system are specified through a number of parameters that include λ, σ, NA, aberrations, reduction factor R, defocus, pupil filters, *etc.* Next, the photomask pattern is specified and this provides the object complex transmission characteristics T_0. Since there is no inherent restriction in the complex transmission values, any (periodic) object that adheres to a rectilinear grid can be specified, having arbitrary values of transmission and phase. The Fourier spectrum $\bar{T}_o$ (Fourier series actually, since the object is assumed periodic) of the object complex transmission is then numerically evaluated. The TCCs are obtained through the numerical evaluation of Equation 2-25 and the intensity at all points in the image field is found by taking the inverse Fourier transform of Equation 2-24.

Other commercial simulation programs with imaging capabilities similar to those in SPLAT that are heavily utilized by the lithography research community include PROLITH [117], SOLID-C [116] and I-Photo[3].

---

1. SPLAT stands for simulation of projection lens aberrations via TCCs.
2. SAMPLE stands for simulation and modeling of profiles for lithography and etching.
3. I-Photo is the internally developed photolithography simulator of Intel Corp. It was initially developed by Michael Yeung in the late 1980's, but the simulator has been through many revisions since then.

The major limitations of SPLAT (and most other imaging simulators based on either scalar or vector diffraction theory) arise from the fact that modeling of the transmission of light through the object (photomask) and scattering from substrate topography (wafer) at the image plane are circumvented sparing the large computational cost involved in properly accounting for these phenomena. The problem of scattering and notching from substrate topography has been extensively investigated by other researchers in the past [101], [102], [90], [91]. Since it is beyond the scope of this work it will not be considered further. However, accurate modeling of the electromagnetic effects that occur during passage of light through the object (photomask) is central in this work. Modeling of the object in SPLAT is done through what is known as the *thin mask approximation*, in which the photomask complex transmission characteristics are assumed to have ideal transitions at all edges of the pattern. In the following, instead of the term *thin mask approximation*, the term *Kirchhoff mask model*, or *k-mask* will be adopted, since this approximation stems from Kirchhoff's assumed boundary conditions for the problem of diffraction behind a screen and is the basis of *Kirchhoff's (scalar) diffraction theory*. Based on the k-mask approximation, when a plane wave is incident on the object, the emerging field is approximated by a nonphysical piecewise constant modulation. It turns out that when the feature sizes on the mask are large compared to the wavelength and when the thickness of the mask topography is small compared to the wavelength this approximation is sufficient. However, for a large set of objects of interest (phase-shifting masks, masks with OPC) this approximation fails and rigorous simulation of the edge effects at the object becomes necessary. In these cases the tapered on-off transitions of the actual fields at the edges, polarization dependent effects due to different boundary conditions for the electric and magnetic field as well as lateral cross-mixing of the field components in passing through the mask cannot be neglected. Simulation has been used to investigate the extent to which such edge effects are present and produce significant image effects [105], [33], [2]-[4].

2.3.3. Rigorous simulation of the object and the simulation program TEMPEST[1]

The literature for numerical solution of Maxwell's equations for problems of interest in photolithography is quite extensive and rich. Research efforts is this area were intensified after the mid 1980's, as the necessary computing power to handle some problems of practical interest was becoming available. The origins of virtually all proposed solutions can be traced back to methods that had existed for years, even as early as 1900's, and had been applied to the investigation of other electromagnetic phenomena. Such methods include Rayleigh's method [73], Green's functions [8], modal expansion methods, the method of moments [9] and the finite-difference time-domain (FDTD) method proposed by Yee [111], [92].

One of the most frequent classification of rigorous simulations methods in photolithography is between frequency-domain and time-domain methods. For frequency-domain methods the electromagnetic field is expanded into some set of predefined basis functions and the unknown coefficients are determined via a matrix inversion problem. The matrix inversion part of the problem is computationally intensive and plagues frequency-domain techniques, albeit their inherent simplicity. For time-domain methods, a time parameter is introduced and the electromagnetic field is found by time-marching, that is, electromagnetic interaction with matter is solved in time until the field converges to a harmonic steady-state. A comparison of techniques for the simulation of topography scattering can be found in [112].

The rigorous electromagnetic field solver TEMPEST is used throughout this thesis, but it will be obvious from the following Chapters that this work is independent on which rigorous simulation method is used for the light transmission through the object. TEMPEST is based on Yee's FDTD method. It was formulated by Guerrieri *et al.* [44] and implemented by Gamelin [34], [35] on a massively parallel computer architecture and it was initially used to study the electromagnetic scattering from non-planar topography on the wafer (image plane). Reflective notching [91], metrology of polysilicon gate structures [90] and alignment mark signal integrity [110] were some of the first problems that were

1. TEMPEST stands for time-domain electromagnetic massively parallel evaluation of scattering from topography.

tackled with TEMPEST. Subsequently, Wong extended the program to handle three-dimensional structures and dispersive materials [105]. He also ported the code to single processor architectures and used TEMPEST to investigate issues in photomask edge effects, such as the image imbalance in phase-shifting masks [109]. Then, Socha used TEMPEST to study imaging and inspection problems and included partial coherence effects in scattering from topography [82]. Finally, Pistor optimized and re-parallelized the code, added versatile boundary conditions (perfectly matched layer - PML - absorbing boundary condition and Fourier boundary condition - FBC) and used TEMPEST to examine imaging in extreme-ultra-violet (EUV) lithography and defect printing and inspection [68].

Using TEMPEST for the simulation of light propagation through the object

TEMPEST can be used to calculate the time-evolution of the electromagnetic field throughout a two or three dimensional structure under the excitation of a monochromatic harmonic field. An example 2D simulation is shown in Figure 2-5. A plane wave with specified amplitude, phase, polarization and angle of incidence originates at the excitation plane and propagates downward into the simulation domain interacting with the mask structures that comprise of materials with different (complex, in general) refractive indices. The whole transient behavior of the electromagnetic field is readily available as seen for example in Figure 2-5(b) that depicts a plot of the real E-field 5 cycles[1] after the excitation started. Typically one is more interested in the steady-state electromagnetic behavior, hence the simulator is allowed to run for enough cycles until the fields remain constant (to within some defined error bound) at the same fraction of each cycle of duration T, in which case convergence has occurred. This is seen in Figure 2-5(c) and (d), where the E-field is shown after convergence at two time instants that are a quarter-cycle apart. The transmission characteristics of the photomask are extracted at the observation plane located below the mask. Since the fields are harmonic the phasor notation can be used:

1. One cycle or period T of the harmonic excitation of frequency f (radial frequency $\omega=2\pi f$) is related with the free-space wavelength λ_0 through: $c = \lambda_0 f = \lambda_0/T$, where c is the speed of light in vacuum.

Equation 2-26. $\underset{\sim}{\vec{E}}(\vec{r}, t) = Re\left[\vec{E}(\vec{r})e^{j\omega t}\right] = \left|\vec{E}(\vec{r})\right|\cos(\omega t + \phi)$

where $\vec{E}(\vec{r}) = \left|\vec{E}(\vec{r})\right|e^{j\phi} = \left|\vec{E}(\vec{r})\right|\cos\phi + j\left|\vec{E}(\vec{r})\right|\sin\phi$ is the complex (phasor) E-field. If the instantaneous field $\underset{\sim}{\vec{E}}(\vec{r}, t)$ is available at t_1=nT $(n \in N)$ after convergence and t_2=nT+T/4 (a quarter-cycle apart), then, from Equation 2-26:

$$\underset{\sim}{\vec{E}}(\vec{r}, t_1) = \left|\vec{E}(\vec{r})\right|\cos(n\omega T + \phi) = \left|\vec{E}(\vec{r})\right|\cos\phi = Re\left[\vec{E}(\vec{r})\right]$$

$$\underset{\sim}{\vec{E}}(\vec{r}, t_2) = \left|\vec{E}(\vec{r})\right|\cos\left(n\omega T + \frac{T}{4} + \phi\right) = -\left|\vec{E}(\vec{r})\right|\sin\phi = -Im\left[\vec{E}(\vec{r})\right]$$

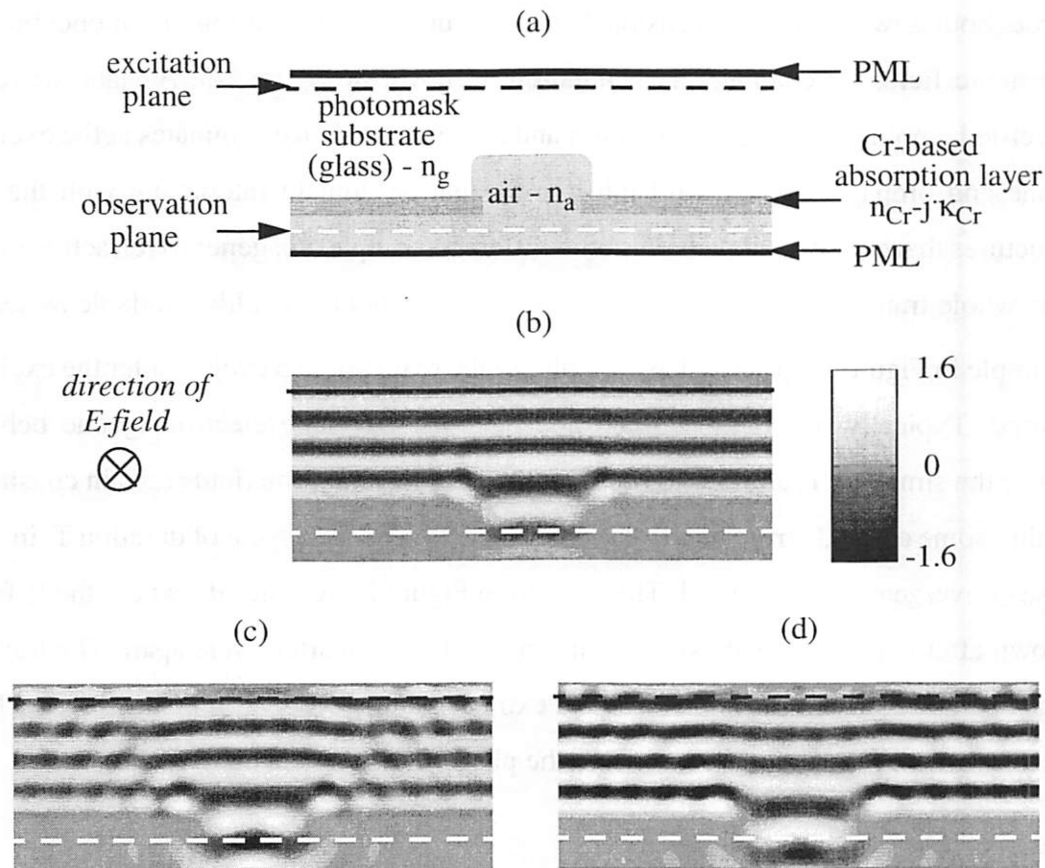

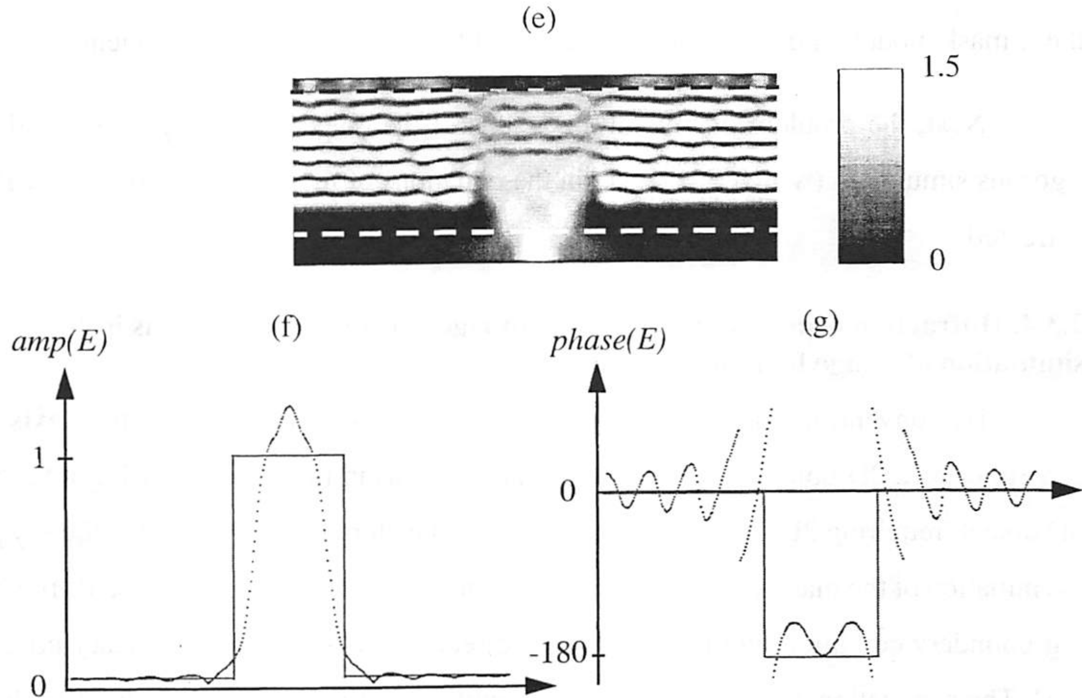

Figure 2-5. Example 2D simulation of the object (photomask) with TEMPEST

(a) Geometry of a 2D object (mask). A normally incident plane wave originates at the excitation plane and propagates downward, interacting with the structure and materials that are present. The properties of each material are described through the complex refractive index. The simulation domain is isolated in the vertical direction with the PML and is periodic in the lateral direction. (b) Instantaneous (real) electric field 5 cycles after the birth of the excitation. (c)-(d) Instantaneous (real) electric fields after convergence has occurred (15 cycles in this case) that are a quarter-cycle apart. (e) Amplitude of the complex electric field. The complex field is constructed using the two instant real fields of (c) and (d). (f) Amplitude and (g) phase of the complex electric field at the observation plane overlaid with the k-mask model.

Thus, the complex E-field, $\vec{E}(\vec{r})$, can be assembled using the following expression:

Equation 2-27.
$$\vec{E}(\vec{r}) = \underset{\sim}{E}(\vec{r}, nT) - j\underset{\sim}{E}\left(\vec{r}, nT + \frac{T}{4}\right)$$

The amplitude of the complex E-field throughout the mask of Figure 2-5(a) is shown in (e) and the amplitude and phase across the observation plane are shown in (f) and (g) respectively. Compare the true transmission characteristics with the ideal k-mask model (Kirchhoff approximation for the mask scattering) for this mask, which are overlaid

on the plots of (f) and (g). The large error incurred in the subsequent image calculation with the k-mask model renders the approximation of the k-mask model insufficient.

Next, the problem of linking the results of the object scattering acquired through rigorous simulation (with TEMPEST) in the equations of the imaging simulator (SPLAT) is treated.

2.3.4. Diffraction orders and integration of rigorous mask simulations in the simulation of image formation

By convention, the object (photomask) is positioned normally to the z-axis and it can either be a 2D object (requiring 2D simulation), as in the example of Figure 2-5, or a 3D object (requiring 3D simulation) that bears a 2D pattern layout existing in the x-y plane. Termination of the mask simulation domain in the z-direction is done with the PML absorbing boundary condition and in the x- and y-directions with periodic boundary conditions [71]. The application of periodic boundary conditions to the x- and y- directions of the simulation domain has certain implications on the allowed plane wave excitations and the resulting angular spectrum representation of the fields across the observation plane. The electric field (similarly for the magnetic field) of a propagating plane wave is given by (a $e^{j\omega t}$ time-dependence of the steady-state harmonic fields is suppressed):

Equation 2-28. $$\vec{E}(x, y, z) = \vec{E}o e^{-j(k_x x + k_y y + k_z z)}$$

where $\vec{k} = (k_x, k_y, k_z)$ is the wave vector (units of radians/meter) that indicates the wavelength, $k = |\vec{k}| = 2\pi/\lambda$, and $\vec{E}o$ is a complex vector indicating the polarization of the electric field and also its magnitude and phase. Assuming that the x- and y-dimensions of the object are P_x and P_y respectively, because of the periodic boundary conditions in x and y, it is:

Equation 2-29. $$\vec{E}(x + P_x, y, z) = \vec{E}(x, y, z) \Rightarrow k_x P_x = m2\pi \Rightarrow k_x = m\frac{2\pi}{P_x}$$

and

Equation 2-30. $\vec{E}(x, y+P_y, z) = \vec{E}(x, y, z) \Rightarrow k_y P_y = n2\pi \Rightarrow k_y = n\frac{2\pi}{P_y}$

where m,n are integers. Therefore, periodic boundary conditions restrict the possible values of the k-vector of a propagating plane wave inside the simulation domain to a discrete set, determined by the condition of periodicity of the fields, with periods P_x and P_y, equal to the dimensions of the object in the x- and y-directions. As a result, only a discrete set of angles of incidence can exist inside the TEMPEST simulation domain.

Since only two components of the triad (k_x, k_y, k_z) can be independent, one convenient mapping of plane waves is a k-space diagram (Figure 2-6). With the object periodicity present in the x- and y- directions, it is convenient to express k_z with respect to k_x and k_y, which can be arbitrary but adhering to Equation 2-29 and Equation 2-30:

Equation 2-31. $k_z = \sqrt{k^2 - k_x^2 - k_y^2}$

Then, the angle of plane wave propagation is given by:

Equation 2-32. $\theta = \mathrm{asin}\left(\frac{k_z}{k}\right)$

and

Equation 2-33. $\phi = \mathrm{atan}\left(\frac{k_y}{k_x}\right)$

where $\theta = \angle(\vec{k}, \hat{z})$ and $\phi = \angle(\vec{k} - \vec{k} \cdot \hat{z}, \hat{x})$. The k-space (k_x,k_y) diagram of Figure 2-6 shows all (discrete number of) plane waves that can exist inside the TEMPEST simulation domain. The location of each "x" indicates the direction of propagation through Equation 2-31-Equation 2-33. It is implied that the amplitude of the k-vector (*i.e.* the wavelength) is constant for all points on a k-space diagram. Therefore, points that are further away from the origin correspond to larger angles of propagation with respect to the z-axis. Note that the separations of allowable plane waves in k_x and k_y are in general different, corresponding to different P_x and P_y. Three important circular limits are indicated on the k-space diagram of Figure 2-6: Points within the outermost circle with radius $2\pi/\lambda$

represent all propagating plane waves. Points within the center circle with radius $2\pi NA/\lambda R$ represent plane waves which get collected by the numerical aperture of the imaging optics. Finally, points within the innermost circle with radius $2\pi\sigma NA/\lambda R$ represent plane waves that are incident on the object.

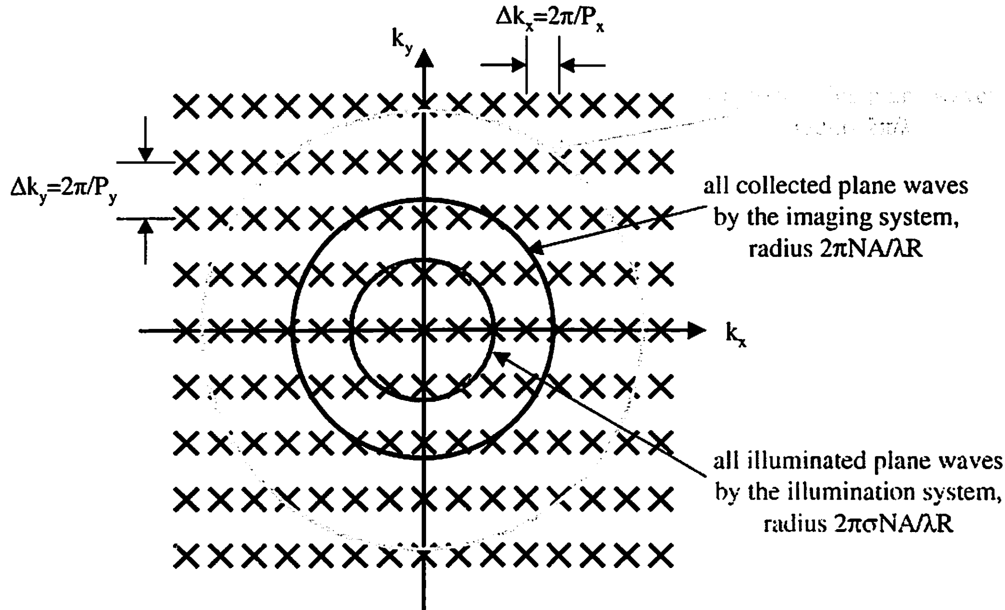

Figure 2-6. k-space diagram for plane waves

The k-space diagram shows plane waves in their spatial frequency representation. The origin of the axis represents normal incidence, while points further away from the origin represent plane waves with higher angles of incidence (as measured from the optical axis). Note that the separation of the discrete number of plane waves allowed by the size of the TEMPEST simulation domain can, in general, be different in k_x and k_y. Also, note that in a typical lithographic system NA/R is < 0.25 so that the radius of the circle containing all collected plane waves will be less than 1/4 of the radius of the circle of all propagating waves. In this diagram, the relative sizes of these circles are drawn different than the typical lithographic imaging situation for illustration purposes.

Based on the analysis so far, the following steps can be followed in order to incorporate results obtained from rigorous (TEMPEST) simulations of the object scattering into the simulation of image formation: Since the object is illuminated using Köhler's method, the radiation from each source point reaches the object as a plane wave, whose angle of incidence depends on the location of the source point relative to the optical axis. Although the source is continuous, and this implies that an infinite number of plane waves are incident on the mask, it can be represented with sufficient accuracy using a discrete rectilinear

grid of points. The problem of determining the necessary number of source integration points has been worked out by Socha [83]. For each discrete source point a separate TEMPEST simulation can be executed that will determine the true scattering of the object. The scattered electromagnetic field across the observation plane is then decomposed into its angular spectrum, that is, into a discrete sum of plane waves propagating below the mask at angles that accommodate the requirements imposed by the periodicity of the object in the x- and y-directions (Equation 2-29-Equation 2-33). This discrete set of complex numbers that fully describe the amplitude and phase of each plane wave component of the electromagnetic field scattered by the mask will be hereafter referred to as the *diffraction orders*[1] of the scattered field. A more detailed discussion about plane waves and the angular spectrum representation of waves propagating in source-free media can be found in Appendix A.

The next key observation is that the illumination from each individual source point is fully coherent. The mutual intensity function is then given by:

Equation 2-34.

$$J_o(x_1 - x_2, y_1 - y_2) = e^{-j[k_{x,sp}(x_1 - x_2) + k_{y,sp}(y_1 - y_2)]} \Rightarrow \bar{J}_o(f, g) = \delta(f - k_{x,sp}, g - k_{y,sp})$$

where $k_{x,sp}$ and $k_{y,sp}$ are the x- and y- components of the k-vector of the plane wave incident on the mask and they represent the exact location of the source point with respect to the optical axis. Therefore the partial image $\delta I_i(u,v)$ of the respective source point can be calculated through Equation 2-24 and Equation 2-25, by taking the inverse Fourier transform of Equation 2-24. The rigorously calculated diffraction orders are substituted in place of the diffraction orders (Fourier transform $\bar{T}_o$) of the k-mask model in Equation 2-24. Finally, the total image $I_i(u,v)$ can be found by repeating the above process for each source point and summing up all partial images:

Equation 2-35.

$$I_i(u, v) = \sum_{source-points} \delta I_i(u, v)$$

1. Other common names include *diffraction harmonics* or *scattering coefficients*.

Note that all source points are mutually incoherent, hence all partial images can be summed up. This method follows Abbe's formulation of image formation (Equation 2-16).

Although the aforementioned procedure is simple to implement, it is a total waste of computer resources, since it requires a time-consuming (especially for 3D objects) TEMPEST simulation of the mask for each source point of the discretized source and it does not take advantage of the fact that the scattering characteristics of the object do not change abruptly with the angle of incidence of the incoming plane wave. This problem has been successfully addressed in various ways. Wong used a single rigorous (TEMPEST) simulation to solve the imaging problem of 2D phase shift masks and 3D contact masks [107]. His assumption was that the scattering characteristics of the object remain constant for all source points for typical imaging situations and can therefore be adequately captured by a single rigorous simulation with the plane wave illumination being normally incident at the object. This approach was independently verified by Wojcik *et al.* [100], who concluded that for typical lithographic imaging with reduction factors of 4X or 5X there is no need for more than one rigorous simulation, even for objects such as phase shift masks that exhibit large vertical steps, where the approximation is more suspect. Later, Pistor re-verified these results for binary masks with optical proximity correction and for phase shift masks, and showed that this approximation breaks down at a reduction factor of 1X that is encountered in inspection imaging systems [70]. Alternatively, Socha implemented the Karhunen-Loeve [41] expansion as a means of decomposing the illumination of the source into a more compact representation [85], rather than the aforementioned plane wave decomposition, and Pistor formulated an Abbe-type method [69] that can incorporate as many rigorous simulations of different incident plane waves as are necessary to achieve the required accuracy, while avoiding the exhaustive rigorous simulation for all discrete source points.

For the work in this thesis all imaging simulations that incorporate rigorous mask simulations were performed using Wong's approach [108], which is summarized here for completeness:

Using a normally incident plane wave with linearly polarized electric field in either x- or y-direction that originates at the excitation plane, the electromagnetic scattering of the

photomask geometry is calculated with TEMPEST. The steady-state (after convergence) complex electromagnetic field across the observation plane contains all the mask scattering information that is necessary. As mentioned before and further explained in Appendix A, the Fourier spectrum of each scattered field component (E_x, E_y, E_z, H_x, H_y, H_z) across the observation plane represents a decomposition of that component into a spectrum of plane waves propagating at different (discrete) angles below the object. Because of the periodic boundary conditions in the x- and y- directions in TEMPEST, the Fourier spectrum is discrete. The quantity $\overline{T_0}\overline{T_0}^*$ of Equation 2-24 for the k-mask model can be thought of as the energy transmitted through the ideal mask. Thus, it is analogous to the Poynting vector $\vec{S} = \vec{E} \times \vec{H}^*$ for the rigorously calculated scattered fields. This rigorous mask model will be hereafter referred to as the *r-mask model.* Since by convention the mask lies in the xy-plane, the quantity of interest is then the energy travelling in the z-direction. Therefore, only the z-component of the Poynting vector $S_z = (E_x H_y^* - E_y H_x^*)$ is of interest. The Fourier transform of the image intensity can thus be expressed by modifying Equation 2-24 as:

Equation 2-36.

$$\bar{I}_i(f, g) = \iint_{-\infty}^{\infty} TCC(f' + f, g' + g; f', g')[E_x(f, g)H_y^*(f', g') - E_y(f, g)H_x^*(f', g')]df'dg'$$

where the TCC's are given again by Equation 2-25.

2.3.5. Polarization effects in imaging

Yet another complication that was suppressed so far arises from the light polarization properties. The light being emitted from a laser source in a photolithography imaging system can potentially be linearly polarized in a certain orientation, circularly or elliptically polarized. As mentioned before, the light from the source goes through a scrambling process and as a result each source point emits light that has random polarization with a uniform distribution and is also, as seen so far, completely incoherent with all other points. Light with random polarization is also called unpolarized or natural light[1]. Viewing the

source as an emitter of plane waves that travel in the illumination system, impinge on the mask at various angles of incidence, scatter into a spectrum of diffracted orders and subsequently propagate in the projection system, until they reach the image location to form the image, is an effective way of modeling and conceptually understanding the whole phenomenon. Since the polarization of each plane wave in the system is random, one needs two mutually incoherent, perpendicular directions on the plane normal to $\vec{k}$ (direction of propagation) to capture fully the polarization properties of the electric and magnetic fields [13]. Traditionally, these directions are the TE ($\vec{E} \perp (\vec{k} \times \hat{z})$) and the TM ($\vec{H} \perp (\vec{k} \times \hat{z})$) defined by the following direction (unit) vectors:

Equation 2-37. $$\hat{a}_{TE} = -\sin\phi\hat{x} + \cos\phi\hat{y}$$

Equation 2-38. $$\hat{a}_{TM} = \sin\theta\cos\phi\hat{x} + \sin\theta\sin\phi\hat{y} - \cos\theta\hat{z}$$

for a propagating plane wave with $k_z<0$ (which is the convention used in this work) and $\theta \neq 0$. When $\theta = 0$ (normal incidence on the object) $\hat{a}_{TE}$ and $\hat{a}_{TM}$ are by convention:

Equation 2-39. $$\hat{a}_{TE} = \hat{y}$$

Equation 2-40. $$\hat{a}_{TM} = \hat{x}$$

The propagation of the waves into the illumination and projection systems typically preserves the polarization properties of the waves, although dependencies on wave polarization could be modeled if needed. The object (photomask) however, more often than not, scatters light of different polarizations differently. Moreover, a 3D object illuminated for example with a TE wave will scatter energy into diffraction orders of not only the TE polarization type but also the TM (cross-mixing)! Finally, TE and TM waves recombine in different ways at the image space to form the image. This phenomenon is more pronounced for waves that are travelling at larger angles θ. This is exactly the reason why scalar imaging theory becomes invalid when modeling the imaging of systems with higher numerical apertures, where highly oblique waves are present.

1. Oftentimes residual polarization exists in the source and it may be necessary to be properly modeled.

In summary, the polarization properties are initially set by the light source itself. Although the source generally emits unpolarized light, the preferential treatment of the illumination/imaging system and/or the object on one type of polarization over the other gives rise to polarization effects. The usually unpolarized light emitted by each source point can be modeled as two mutually incoherent, linearly polarized plane waves [13] with $\vec{E} \parallel \hat{a}_{TE}$ (TE-polarization) and $\vec{E} \parallel \hat{a}_{TM}$ (TM-polarization). Each of these polarizations can be treated separately and propagated through the illumination optics that generally preserve the polarization properties and be incident on the object. A rigorous simulation is then executed to determine the scattering properties (diffraction orders) of the object for that particular source point and field polarization. Mask polarization effects arise from the different scattering response of the object under different incident polarizations. Then, all diffraction orders (that generally contain mixed polarization although only TE or TM was incident on the object) are propagated through the projection optics, that typically do not alter the polarization properties, to the image space where they recombine to form the image. Simulation of this recombination process can follow either the simpler scalar diffraction theory or the more involved vector diffraction theory that properly accounts for different field polarizations in the image formation. The two mutually incoherent images arising from the two mutually incoherent source polarizations are then averaged to result in the final image for an unpolarized light source. This technique is basically followed by Pistor [68] in his Abbe's formulation of imaging. Wong [105], [109], Wojcik [100], Socha [82] and Adam [2]-[4], [6] used the Hopkins' formulation, calculating the diffraction orders for two mutually incoherent, with perpendicular polarizations and normally incident plane waves illuminating the object and averaged the two resulting images to calculate the total images for unpolarized sources.

One gray point still remains. Upon close investigation it becomes clear that only Abbe's method can properly take into account the source polarization properties. The directions of $\hat{a}_{TE}$ and $\hat{a}_{TM}$ change quite abruptly at different source points. This is shown in Figure 2-7(a), where the unit direction vectors $\hat{a}_{TE}$ and $\hat{a}_{TM}$ are shown on a k-space dia-

gram of the (discrete) source points. Note that $\hat{a}_{TE}$ always lies on the k_x-k_y plane, while $\hat{a}_{TM}$ has a z-component out of the k_x-k_y plane and only its projection on the k_x-k_y plane is shown. Abbe's method can properly account for the rapidly changing directions of the illuminating fields at the various source integration points. On the other hand, in Hopkin's method the assumption of constant diffraction orders with respect to the angle of incidence of the illuminating wave contradicts the fact that the TE and TM polarizations scatter differently at the object! The TE polarization of a source point lying on the k_y=k_x line, for example, is seen to have almost equal power in the x- and y-directions. Therefore, even within the range of accuracy of Hopkins' approximation, the scattering response of the object will be different from source points with k_x=k_y with TE polarization than the normal incidence response for a TE plane wave, where by convention $\hat{a}_{TE} = \hat{y}$! Here is how this

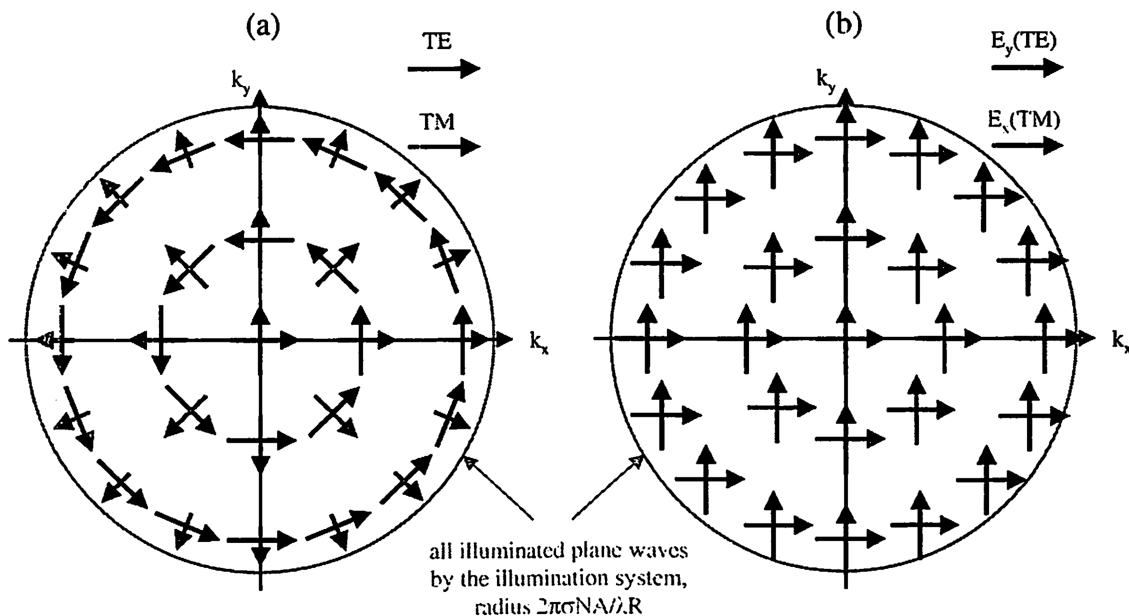

Figure 2-7. Simulation of the source polarization

(a) The unpolarized light emitted by each source point can be modeled by two mutually incoherent polarizations, $\hat{a}_{TE}$ and $\hat{a}_{TM}$, or any other combination of mutually perpendicular directions that are normal to $\hat{k}$. The direction of $\hat{a}_{TE}$ and $\hat{a}_{TM}$ changes abruptly for the various source points and only $\hat{a}_{TE}$ lies completely in the x-y plane. Modeling of the source polarization in Abbe's method is straightforward, but in Hopkin's method the diagram in (a) cannot be applied. Instead, $\hat{x}$ and $\hat{y}$ are taken as the two mutually incoherent polarizations of each point, as shown in (b). Although nonphysical, it is a good approximation for typical imaging situations (R=4X or 5X) because of the negligible projection of $\hat{a}_{TM}$ on $\hat{z}$.

contradiction can be reconciled: In Hopkins' method, TE illumination is modeled by forcing all source points to emit a polarization that results in a non-physical[1] plane wave incident on the object with E_y polarization only, same as the polarization for the normally incident TE plane wave for which the diffraction orders of the mask have been rigorously calculated, as seen in Figure 2-7(b). Similarly, TM illumination is modeled by forcing all source points to emit a polarization that results again in a non-physical plane wave incident on the object with Ex polarization only, which is the same as the polarization for the normally incident TM plane wave for which the diffraction orders of the mask have been rigorously calculated through a second simulation. This is also shown in Figure 2-7(b). The validity of this scheme depends on the same conditions that Hopkins' method relies on, *i.e.* constant diffraction orders with respect to angle on incidence. In the same way that Hopkins' approximation holds for a relatively small illumination cone, the above decomposition between E_y and E_x polarizations instead of between TE and TM, for all source points, is accurate only for source points that are not "too far away" from the origin. The TM illumination from such source points has negligible E_z component and to a good accuracy results in a plane wave with E-field completely on the x-y plane of the object space. Then, instead of modeling the source polarization by treating each source point as an emitter of mutually incoherent TE and TM plane waves, equivalently the mutually incoherent E_y and E_x polarizations can be used everywhere. Hence, the calculated diffraction orders from two separate simulations with the excitation field being a normally incident plane wave with E_y (TE) or E_x (TM) polarization suffice for the application of Hopkins' technique. Again, the two aerial images are added for the final image under unpolarized illumination.

In this work, Hopkins' method with two separate normally incident TE and TM rigorous object simulations is used when calculating aerial images for completely unpolarized sources. All approximations are valid for typical imaging situations with R=4X or 5X even for NA and σ close to unity. The scalar approximations however are not accurate for NA exceeding 0.6-0.7, but this is not a limiting factor for this work, since the core of the devel-

1. Non-physical because a plane wave propagating in source-free media can never have a field component parallel to the direction of propagation $\hat{k}$.

oped methodology is concerned with speeding up the rigorous simulations of the object and can fit equally well in a vector imaging simulator. Extensions of Hopkins' method to cases with R=1X or 2X are not obvious. An outline for a possible such extension can be found in [113]. The most promising direction for achieving such an extension is believed by the author to be a break-up of the source into a number of judiciously chosen, mutually incoherent sectors and the application of Hopkins' method within each sector, where the diffraction orders of the object should remain relatively constant. Such an extension is beyond the scope of this thesis.

2.4. Approximate *vs.* rigorous, scalar *vs.* vector, k-mask *vs.* r-mask and Abbe's *vs.* Hopkins' methods

In summary, it is worth stressing the following distinctions about the classifications of the various methods that exist in the literature for the modeling of an imaging system with applications in projection printing: As mentioned previously, a truly "rigorous" method would involve solving the system of Maxwell's equations throughout the imaging system. Because of the immensity of such a problem this is not possible. Therefore, strictly speaking, all methods that are used in practice for the calculation of optical images are "approximate". However, the degrees of approximations used in different methods vary and as a result so does the achieved accuracy. Methods that employ a relatively small number of approximations are usually advertised as "rigorous" and are typically more accurate, whereas the ones that involve more approximations are quoted as "approximate" and are less accurate.

The classification of methods between "scalar" and "vector" is a different one. Although a "vector" method is in general more accurate than a "scalar" method they are both "approximate". In a "vector" method the electromagnetic field $(\vec{E}, \vec{H})$ maintains its vector nature throughout the calculations whereas in a "scalar" method at least in one module of the calculations the six components of the electromagnetic field (E_x, E_y, E_z, H_x, H_y, H_z, for a cartesian coordinate system) are treated as scalar quantities and therefore any cross-mixing that occurs between those components or any preferential treatment by the system on one versus the others is lost. The terms "scalar" and "vector" should be reserved

to distinguish whether the illumination and/or the projection system are modeled using scalar or vector diffraction theory.

The terminology of k-mask (short for Kirchhoff mask) and r-mask (short for rigorously simulated mask) introduced earlier, refers to the way that one models the object (mask) scattering. In a k-mask model (also called the thin mask model) no simulation of any kind is executed. The mask is assumed to be infinitely thin and the electromagnetic field leaving the mask and entering the projection system is approximated by the product of the incident field and the ideal complex mask transmission function. In an r-mask model (sometimes called the thick mask model) at least one rigorous simulation is needed in order to determine the mask scattering. For most imaging situations in practice two rigorous simulations are needed to account for an unpolarized source.

Finally, the classification of methods in "Abbe-type" or "Hopkins-type" has to do with the order by which the various integrals in the imaging formulas are evaluated. In an "Abbe-type" method, the partial image from each source point is calculated first and then all partial images are integrated owing to the assumed source incoherence. This method is conceptually attractive and is much easier to incorporate r-mask models, even on imaging systems with small reduction factors. In a "Hopkins-type" method a quantity called the transmission cross coefficient is calculated first. This quantity characterizes fully all propagation and image formation phenomena from source to image, except for the mask scattering effect, that is taken into account separately with either k-mask or r-mask models. The key assumption for the application of a "Hopkins-type" method is that the mask scattering characteristics do not materially change for the various source points. Owing to this assumption the application of the r-mask model in a "Hopkins-type" method for imaging situations with small reduction factors, where the assumption of constant scattering characteristics breaks down, is cumbersome and has not been demonstrated yet.

The simulation programs utilized (SPLAT, TEMPEST) and properly linked for this work result in approximate, scalar, Hopkins' image modeling methods. Both k-mask and r-mask models are employed depending on the circumstances of the problem. One of the goals of this thesis is to always identify the most efficient simulation strategy for each type

of problem and devise methods that can maintain excellent accuracy while allowing for large reductions in required simulation time.

3 Analysis of OPC Features in Binary Masks

SUB-WAVELENGTH lithography, where the size of printed features is smaller than the exposure wavelength, places a tremendous burden on the lithographic process. Distortions of the intended images inevitably arise, primarily because of the nonlinearities of the imaging process and the nonlinear response of the photoresist. Two of the most prominent types of distortions are the wide variation in the linewidths of identically drawn features in dense and isolated environments (dense-iso bias) and the line-end pullback or *line-end shortening* (LES) from drawn positions. The former type of distortion can cause variations in circuit timing and yield, whereas the latter can lead to poor current tolerances and higher probabilities of electrical failure.

Optical proximity correction or *optical proximity compensation* (OPC) is the technology used to compensate for these types of distortions. OPC is loosely defined as the procedure of compensating (pre-distorting) the mask layout of the critical IC layers for the lithographic process distortions to follow. This is done with specialized OPC software. In the heart of the OPC software lies a mathematical description of the process distortions. This description can either be in the form of simple shape manipulation rules, in which case the OPC is referred to as "rule-based OPC" [62], [17]-[22], or a more detailed and intricate process model, for a "model-based OPC" [54]-[57], [24]-[27], [10], [52], [63]-[64], [74]-[75], [87]-[88]. The OPC software automatically changes the mask layout by moving segments of line edges and adding extra features that (pre-)compensate the layout for the distortions to come. Although after OPC has been performed the mask layout may be quite different than the original (before OPC) mask, the net result of this procedure is a printed pattern on the wafer that is closest to the IC designer's original intent.

The idea of pre-compensation in printing can be traced back to techniques used by Eastman Kodak Company [29], who were the first to introduce serifs around corners and other "decorative", non-printable, assist features to remove the rounding effects. Sharp local reductions of the thickness of the absorbing layer were used in intersecting lines to prevent the formation of fillers. These corrections were based on experience gained by a process of trial and error. The first attempt for a systematic method for determining such corrections appeared in 1981 by Saleh [77], who discussed the general aspect and also showed some specific implementations including serifs (corner shape alterations) and sub-resolution assist features for better pattern fidelity. Global linewidth biasing for process compensation and the use of serifs crafted onto line-ends in memory cells have been employed in photolithography for over a decade to enhance the ability to make these structures [86]. These techniques were not widely adopted for ICs in general, however, because their reliance on (semi-empirical) hand crafted design manipulations made them possible only for addressing specific problems in repeating layouts, such as memory cells.

In the early 1990's the problem of OPC for large mask layouts was addressed formally as an optimization problem. The size of such a problem is formidable, but through introduction of appropriate constraints - induced primarily from mask fabrication constraints, local optimal mask "points" were successfully demonstrated. This research was performed independently by Liu, Cobb and Zakhor [54]-[57], [24]-[27], Pati, Wang and Kailath [63]-[64] and Stirniman [87]-[88] and has lead to commercially available software tools that perform OPC on a full-chip scale. All three approaches rely heavily on speedy calculations of the image intensity at selected points of the image field. Although the methods by which they achieve this appear seemingly different, they are nevertheless the same, in the sense that they all rely on a decomposition of the kernel of the imaging equation for partially coherent light. A methodology for improving the insufficient accuracy for OPC on alternating phase shifting masks (alt. PSM) is developed in Chapter 4 - Chapter 6.

The material of this Chapter was originally presented at the SPIE 2000 Microlithography conference. The aim of this Chapter is to develop through simulation a better physical understanding of how optical proximity correction works for binary photomasks, and how the available geometrical and imaging parameters influence the performance of spe-

cific OPC configurations. This is done for "scatter bars" in Section 3.1 and for "corner serifs" in Section 3.2. The design approach followed resembles a "rule-based OPC" approach, but the developed OPC guidelines could also be helpful for introducing constraints or generating good initial guesses in automated "model-based OPC". Then, polarization effects of assist features are investigated. OPC shape fidelity and photomask corner rounding are also addressed. Finally, the need for rigorous simulations of the photomask scattering (r-mask model) as opposed to the simpler k-mask model (in which no mask scattering simulation is performed) in the presence of wavelength-sized assist features is critically examined.

The analysis methodology used in this Chapter consists of using both k-mask models (SPLAT simulation only) and r-mask models (TEMPEST simulation linked to SPLAT simulation for the imaging) with two perpendicular polarizations at normal incidence, as defined in Chapter 2. The k-mask model is quite adequate for binary COG masks. However, the level of accuracy is quantified through comparison with the r-mask model.

3.1. Scatter Bars

Scatter bars are typically placed near isolated lines as a means of controlling both the critical dimension (CD) of the image at best focus, but also improving the through-focus robustness of the image [19], [21], [22]. The way they work is shown in Figure 3-1, where the resist pattern of the "finger-type" test mask of (a) is depicted in (b) and the aerial image calculated with SPLAT in (c). Notice how the isolated part of the middle line and also to a lesser extent the outermost lines print fatter in resist. This is not just an artifact of the resist, since it is evidenced also in the aerial image in (c). This unacceptable CD variation of the middle isolated line can be addressed by using a pair of symmetrically positioned lines that are sub-resolution (meaning that the are not wide enough for the imaging system to be able to resolve them) and are commonly referred to as *scatter bars.* The mask with OPC scatter bars is shown in Figure 3-1(d). It is obvious from the resist pattern of Figure 3-1(e) and the aerial image of (f) that the scatter bars significantly improve the image of the isolated line, balancing its CD with that of the dense lines.

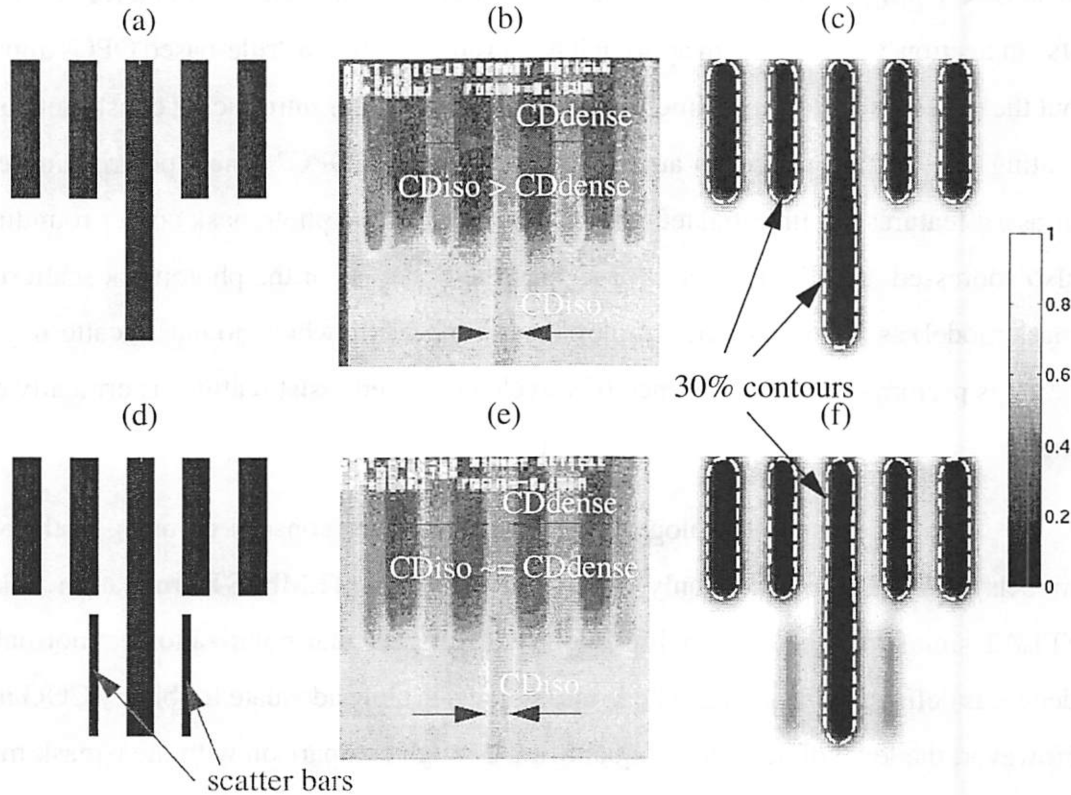

Figure 3-1. Operation principle of scatter bars

The CD of the center isolated line of mask (a) prints larger than the CD of the dense lines as shown in the resist image in (b) and in the aerial image intensity in (c) although it is drawn the same on the mask. The addition of a pair of symmetrically positioned scatter bars in (d) is shown to significantly improve the resist image in (e) and the aerial image in (f).

The mask designer has essentially three parameters at hand by which she can optimize the aerial image of an isolated line, namely the size of the scatter bar, the exact location of the scatter bar and the linewidth of the main feature. In this particular study, the targeted feature size is 130nm (1X) and the illumination parameters of the optical system are: λ=193nm, reduction factor R=4, NA=0.7 and partial coherence factor σ=0.6, unless stated otherwise. All simulations of this Section were performed with SPLAT using the k-mask model (no rigorous solution of mask scattering). Figure 3-2 depicts the simulated geometry of the isolated line assisted with two symmetrically placed scatter bars. The distance from the center of the line to the center of each scatter bar, denoted as d, is expressed as the sum of one CD_{target}(=130nm) plus pCD_{target}. This implies that if the scatter bars were

replaced by lines of width equal to CD_{target}, then p=1 corresponds to a 1:1 dense line/space pattern ($d=2CD_{target}$).

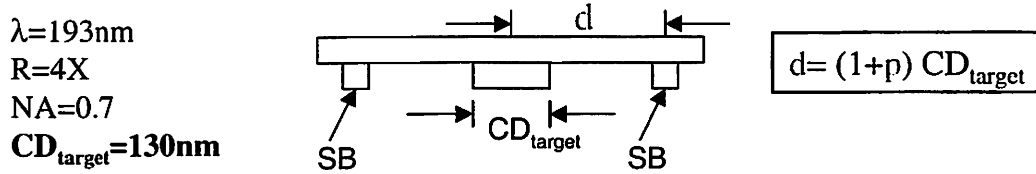

Figure 3-2. Illumination parameters and simulated geometry

3.1.1. Designing the Placement and Size of the Scatter Bars at Best Focus

The placement of the scatter bar has a profound effect on the main feature. This is shown here by aerial image simulations, in which the only thing that varies is the parameter p. The results of these simulations are summarized in Figure 3-3. Observe that when the scatter bar approaches the main feature beyond p=1 the CD_{aerial}[1] increases rapidly, until the point that the image of the scatter bar completely merges with that of the main feature. In the opposite direction, when p>>1 the line behaves as isolated, as one would expect. For intermediate values of p ($1<p<3$) the placement of the scatter bar controls the CD_{aerial} of the line in a fashion captured in Figure 3-3(b), where it is obvious that the CD_{aerial} is more sensitive to p for smaller values of σ. This behavior appears to be independent of scatter bar size, as is also shown in Figure 3-3(b) for SB=55nm and 65nm (1X).

The second design parameter is the size of the scatter bar. The general rule of thumb here is that a larger scatter bar causes a smaller CD_{aerial} of the line for every σ (at best focus), but for larger values of σ the CD_{aerial} becomes progressively insensitive to the scatter bar sizing. This is depicted in Figure 3-4(a), where the CD_{aerial} *vs.* SB size is plotted for various σ. Note that in all these cases the SB is placed at p=1. The slope is steeper for small σ and flattens out for $\sigma \geq 0.8$. The designer needs to take provision not to oversize the SB, otherwise the SB becomes resolvable by the stepper. This fact is depicted in Figure 3-4(b),

1. CD_{aerial} refers to the critical dimension of the aerial image as measured at the 30% level of intensity. This corresponds to a simple resist threshold model.

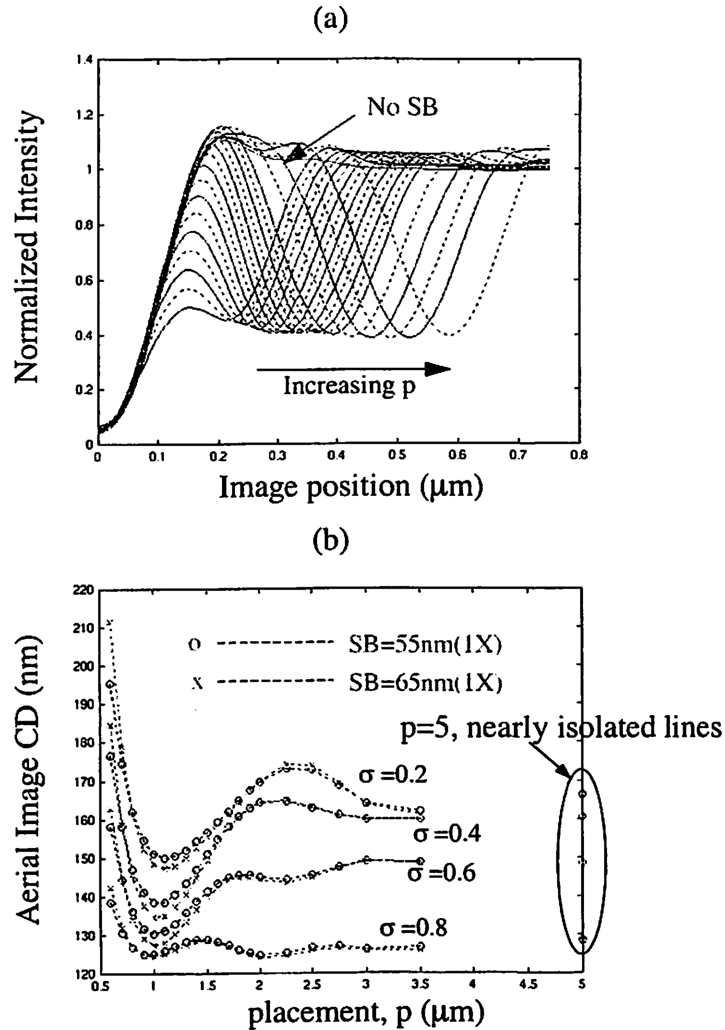

Figure 3-3. The effect of the scatter bar placement

(a) Aerial images at best focus with σ=0.6, SB=55nm(1X) at various placements of the SB. (b) Aerial image CD at best focus at the 30% intensity level for various σ and SB sizes of 55nm(1X) and 65nm(1X).

where it is shown that the intensity underneath the scatter bar drops linearly when increasing the size of the SB. Increasing values of σ shift the line upward. Figure 3-4(c) depicts the aerial images at best focus for σ=0.6, p=1 and various sizes of the SB.

It is also important to understand the role of the partial coherence factor σ on the effectiveness of the scatter bar. To this extent, a specific design of SB is assumed (placement at p=1, size of SB=55nm at 1X) and σ is varied in the simulations. Figure 3-5(a) shows aerial images for various σ and Figure 3-5(b) shows the changes of CD_{aerial} *vs.* σ.

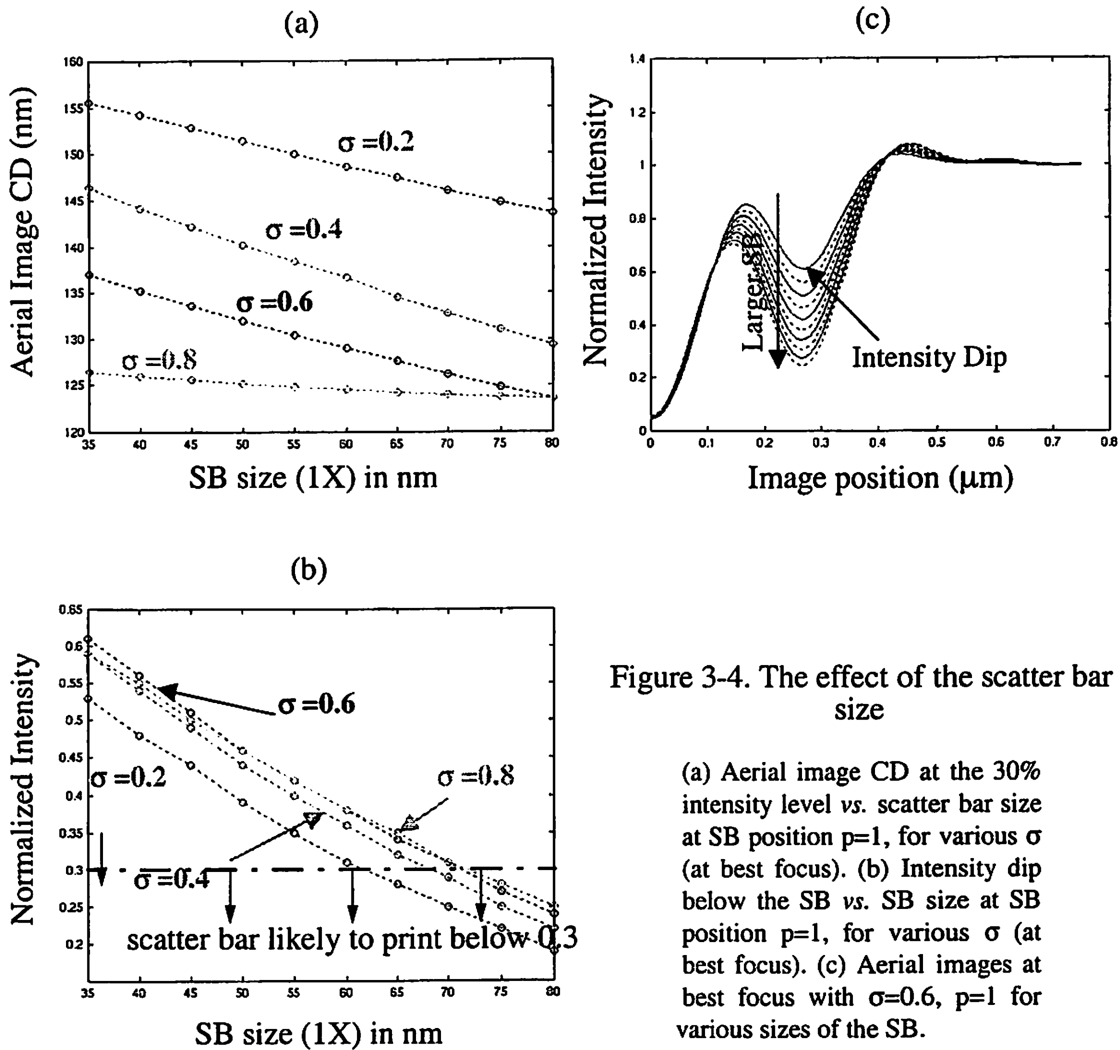

Figure 3-4. The effect of the scatter bar size

(a) Aerial image CD at the 30% intensity level *vs.* scatter bar size at SB position p=1, for various σ (at best focus). (b) Intensity dip below the SB *vs.* SB size at SB position p=1, for various σ (at best focus). (c) Aerial images at best focus with σ=0.6, p=1 for various sizes of the SB.

An important observation here is the fact that the location of the "shadow" of the SB shifts with σ. For large σ it approaches the location of its geometrical shadow. This lateral shift implies that in the case that the two scatter bars are misaligned (not symmetrically positioned around the feature) the main feature will be displaced! Observe in Figure 3-5(a) that the minimum intensity underneath the main feature is increased when σ is increased and in Figure 3-5(b) that the CD_{aerial} changes significantly with σ. For larger σ there is a trade-off between smaller CD_{aerial} and reduced contrast.

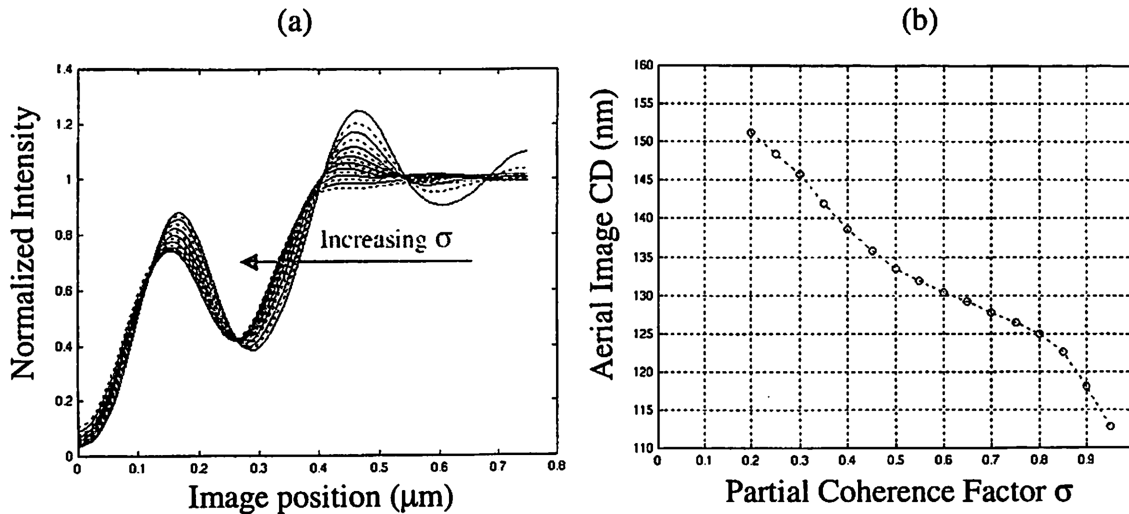

Figure 3-5. The effect of partial coherence

(a) Aerial images at best focus for p=1, SB=55nm(1X) for various σ. (b) Aerial image CD at the 30% intensity level *vs.* σ for SB=55nm(1X) at position p=1 (at best focus).

3.1.2. Out-of-focus Performance of Scatter Bars

The out-of-focus characterization of scatter bars was also performed with SPLAT, k-mask simulations. The results are shown in Figure 3-6. The CD_{aerial} at the 30% intensity level with σ=0.6 is plotted in Figure 3-6(a) versus defocus for various placements (different p values) for SB=55nm(1X). From these plots it is clear that the defocused aerial image is poor when no scatter bars are used, but also that the placements at p=1.5 and p=2 do not improve the situation. Once the scatter bars are brought nearer to the feature the CD_{aerial} *vs.* defocus curves flatten out and this is indicative of improved through-focus aerial images, that resemble the through-focus behavior of dense lines. The best placement in this situation occurs at p=0.8. Sizing the scatter bar when p is kept constant does not alter the aerial image through focus significantly, as is shown in the CD_{aerial} *vs.* defocus plots of Figure 3-6(b), where p is held constant at 1 and the scatter bar size is increased from 45nm to 75nm in steps of 10nm.

In summary, the design process and verification of performance of scatter bars next to isolated features could proceed as follows: First, according to the illumination conditions (λ, NA, σ) the scatter bar size is chosen from a design graph similar to that of Figure 3-4(a) that is consistent with the discretization of the mask making tool and results in the required

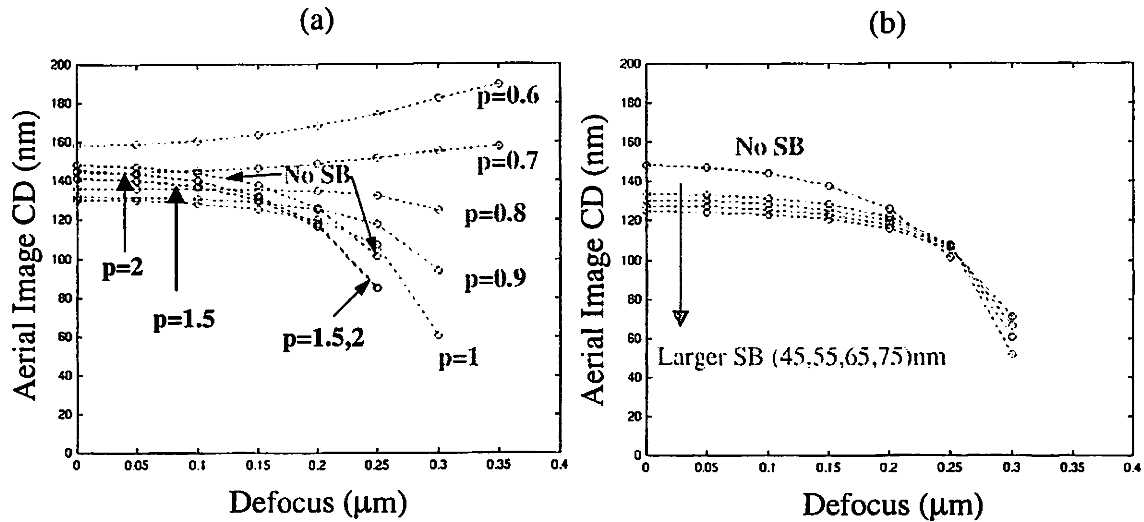

Figure 3-6. Through-focus characterization of scatter bars

Aerial image CD at the 30% intensity level *vs.* defocus at σ=0.6 for (a) SB=55nm(1X) at various positions p and (b) position p=1 for various sizes of the SB.

correction of the CD_{aerial}. Care must be exercised, so that the scatter bar is below the camera resolution and will not print (using Figure 3-4(b)). Second, from Figure 3-3(b) the acceptable range of p is determined so that the CD_{aerial} remains close to its minimum for $p \approx 1$, say 0.75<p<1.2. Third, through aerial image simulation the position p (0.75<p<1.2) is found that shows the best performance through focus. Figure 3-6(b) gives convincing evidence that the size of the scatter bar does not affect the out-of-focus performance. Any residual difference from the target CD_{aerial} will have to be corrected by biasing the main feature. (This makes things a bit more complicated, because biasing the feature changes p and iteration will be needed). Finally, the ability to adjust the partial coherence factor σ provides one extra knob to control the CD_{aerial}, as is apparent from Figure 3-5(b).

3.1.3. Polarization Effects of Scatter Bars

The simulations in the above discussion were performed with SPLAT, using the k-mask (Kirchhoff mask) model, which is based on "vertical propagation", where the mask is assumed to vertically transmit the incident field. It is of interest to know, how well the above assumptions agree with the rigorous, r-mask model, where the mask scattering is rigorously simulated with TEMPEST, and also how scatter bars near isolated features behave

at different polarizations of the incident light. Figure 3-7 depicts a sample TEMPEST simulation where p=1 and SB=50nm(1X). The near field amplitude at a zx cut-plane is shown in (a) for TE polarized incident light (electric field parallel to the line) and in (b) for TM polarized light (electric field perpendicular to the line). Observe that in the TM case the electromagnetic field underneath the mask corresponds to a travelling scattered wave, whereas in the TE case the field also exhibits a standing wave pattern along the x-axis. This can be explained as follows: In the TE case there exist induced currents onto the chromium layers, that are aligned with the incident radiation. These currents at the edges of the feature

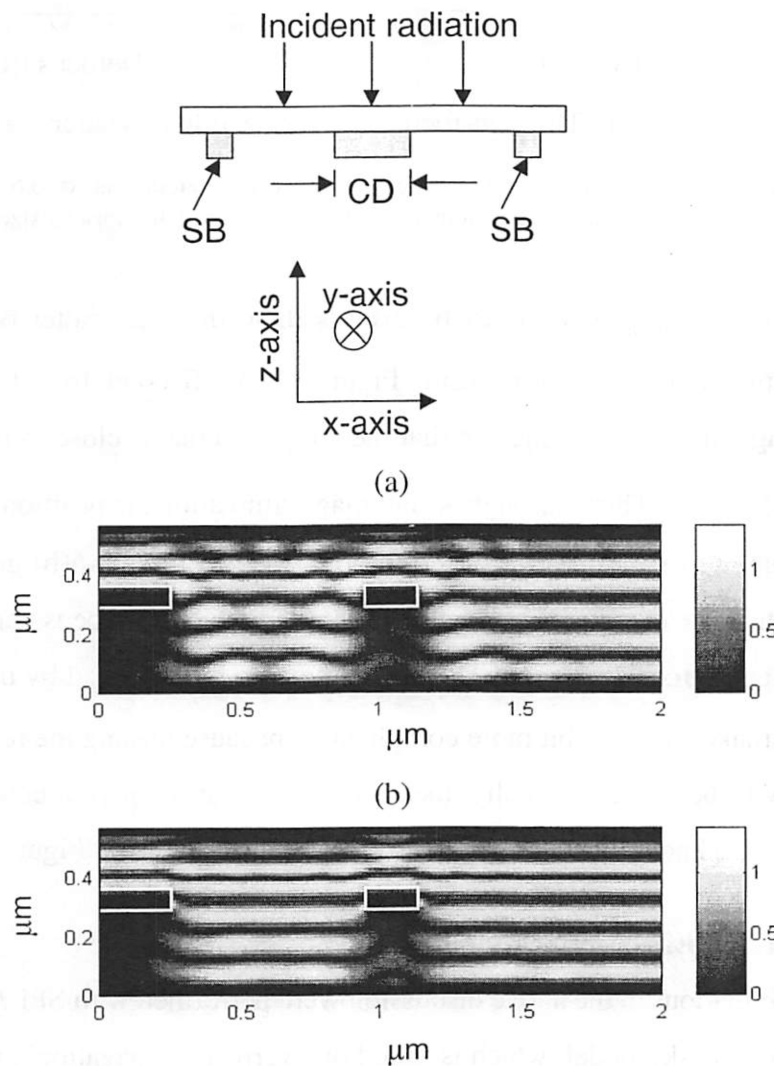

Figure 3-7. Amplitude of the complex near field

(a) TE polarization - E_y only and (b) TM polarization - E_x only. In this example p=1 and SB=50nm(1X). Note that because of the symmetry the TEMPEST simulation is performed only on the right half of the mask geometry

and the scatter bars re-radiate cylindrical waves, which interfere constructively or destructively, and result in the peaks and valleys along x that are spaced by ~100nm (*i.e.* ~λ/2). In the TM case the induced currents are weaker, because the field is now perpendicular to the line and they cannot redirect energy in the region underneath the mask. This results in the transmitted field being basically just the incident field in the open areas.

The aerial images for the TE and TM cases are compared for this example simulation in Figure 3-8, together with the SPLAT simulation. The aerial images when no scatter bars are used are also shown for comparison. Observe that the scatter bars and the main feature appear wider in TM excitation than in TE and narrower with SPLAT simulation. Figure 3-8(b) depicts the intensity dip underneath the scatter bar for various sizes of scatter bars for the TE, TM and SPLAT cases. This dip is always larger (smaller intensity) for the TM case and smaller (higher intensity) for the SPLAT case and the TE case falls in between. Observe also that for larger sizes of scatter bars the three cases give even more similar results. For smaller sizes of scatter bars a simple perturbational model can be used, in which the intensity dip is approximated by the square root of the intensity dip of an opaque pin spot. Although there is a difference of up to 10% between the TEMPEST and

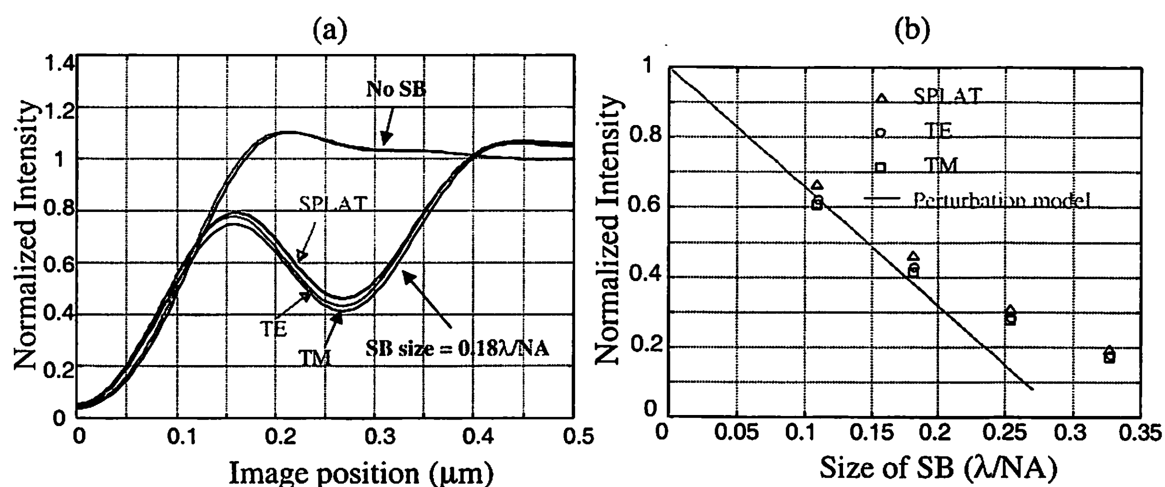

Figure 3-8. The effect of polarization on the performance of scatter bars

(a) Aerial images at best focus without OPC and with a SB=50nm(1X) at p=1 for TE and TM polarizations. The SPLAT simulation result is also shown. (λ=193nm, NA=0.7, σ=0.6, Mag.=4X, CD_{target}=130nm(1X)) (b) Intensity dip of the scatter bar for various scatter bar sizes as predicted by SPLAT, TEMPEST (TE and TM polarizations) and a simple perturbational argument, when SB is placed at p=1.

SPLAT simulations, the general guidelines for the proper design of the scatter bars discussed in Sections 3.1.1 and 3.1.2 still hold, but a final fine-tuning using the rigorous TEMPEST simulation may be necessary, especially when there is need to account for polarization effects.

3.2. Serifs

Square serifs are typically introduced at the corners of lines in order to locally correct the aerial image and in an effort to reduce the line-end shortening (LES). An example of a mask pattern before and after the application of OPC serifs at interior and exterior corners is shown in Figure 3-9(a) and (b). The aerial image is seen to significantly improve in Figure 3-9(d) compared with Figure 3-9(c) near the corners and near the end of the line, reducing the LES.

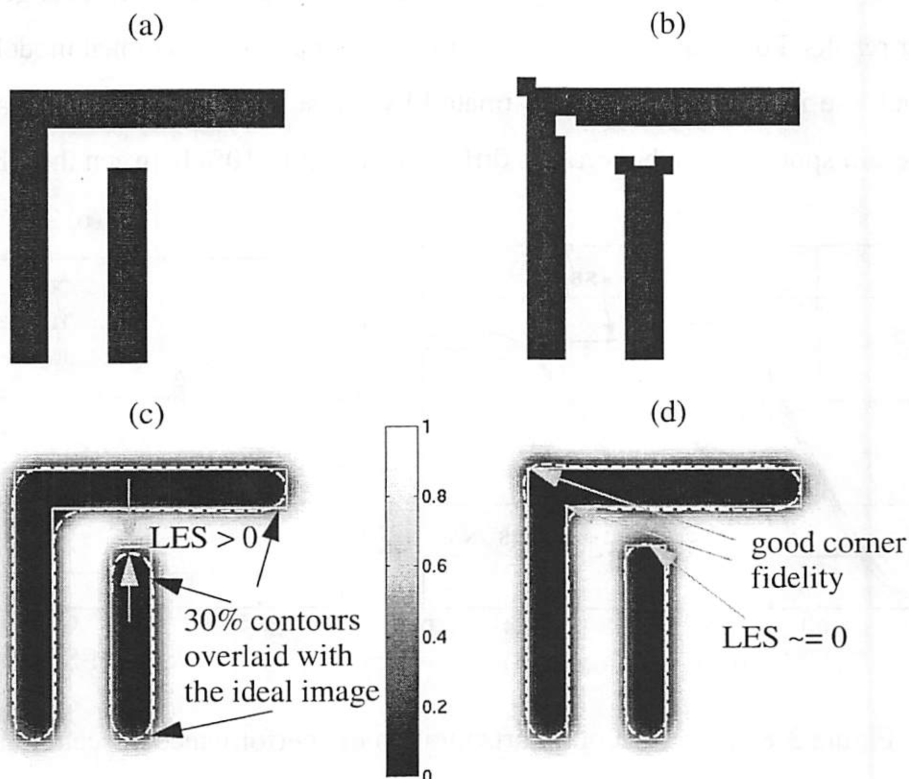

Figure 3-9. Operation principle of corner serifs

Mask before (a) and after (b) corner serif OPC. The aerial images are shown in (c) and (d) respectively and the 30% intensity contours are overlaid with the ideal (geometrical) image. The shape fidelity near the corners is much better after the OPC and the line-end shortening (LES) is significantly reduced.

3.2.1. Modeling OPC serifs through simulation

In this Section the effect of the size and placement of the OPC serif on the LES_{aerial} correction of the aerial image is modeled. Then, the additional accuracy from rigorous 3D electromagnetic simulation (TEMPEST) in predicting the correction in the LES_{aerial} introduced by a specific OPC design is determined. To do this, a number of cases that are simulated with both TEMPEST and SPLAT are compared. In the following, the targeted feature size is 130nm (1X) and the illumination parameters of the optical system are: λ=193nm, reduction factor R=4, NA=0.7 and partial coherence factor σ=0.6. Since only the aerial image improvements near the end of the isolated line are of interest, no scatter bar OPC is used for linewidth correction and out-of-focus improvement of the aerial image.

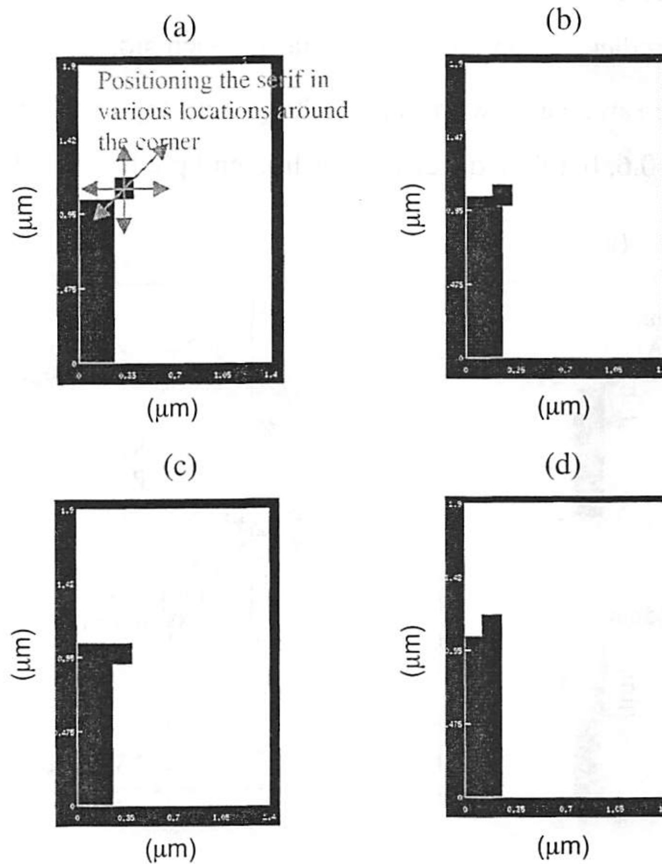

Figure 3-10. Different OPC placements for a clear field (CF) mask

(a) diagonal non-overlapping, (b) 3/4 diagonal overlapping, (c) side and (d) top. Note that because of the 2-fold symmetry with respect to the x, y axes only the top right quadrant of the simulation domain is shown.

Figure 3-10 depicts four different OPC placements for a clear field (CF) mask: (a) diagonal non-overlapping, (b) 3/4 diagonal overlapping, (c) side and (d) top. Intermediate cases where the OPC is shifted along the diagonal to render different than 3/4 diagonal overlapping or up-down for different side and left-right for different top placements were also simulated. In Figure 3-11 an example 3/4 diagonal overlapping design is compared with the reference case (no OPC used). The side of the square serif is 65nm(1X) and it is positioned so that the center of the serif is located at the corner of the line. This geometry is simulated with TEMPEST (r-mask) and SPLAT (k-mask) and the contours of the 30% clear field intensity of the aerial images are shown in Figure 3-11(b). In the same plot the 30% contours for the reference case are also drawn, which again is simulated with TEMPEST and SPLAT. The ideal rectangular image is also shown for comparison. Note that both simulators predict a ~10nm linewidth bias on each side of the CD_{aerial}, which is the approximately the same value with that resulting from Figure 3-3(b) for p=5 (nearly isolated line) and σ=0.6, but they differ in their line-end predictions. The LES_{aerial} resulting

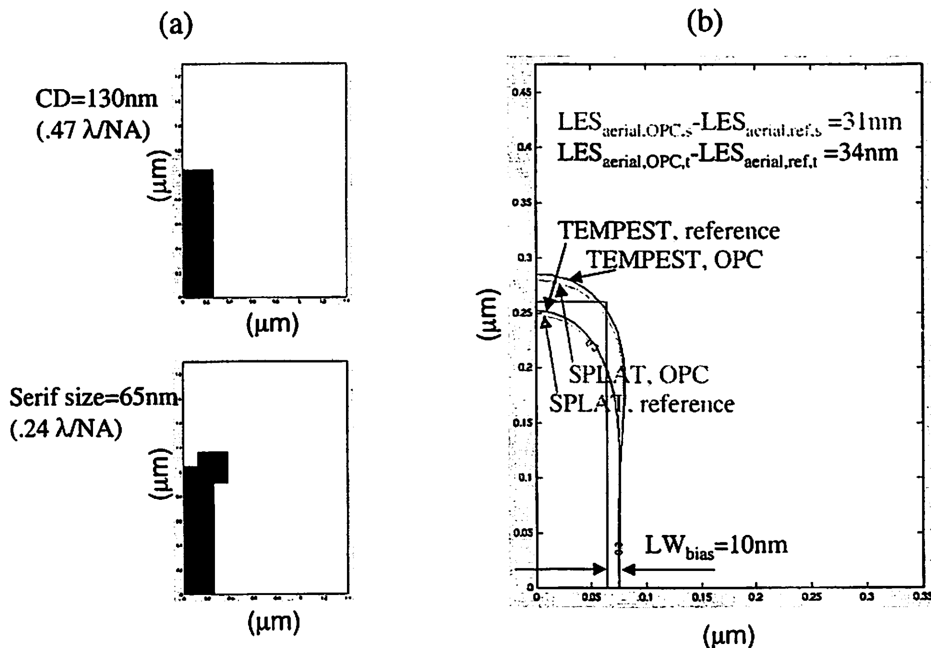

Figure 3-11. An example of 3/4 diagonal overlapping OPC design is compared with the reference case (no OPC used)

(a) The side of the square serif is 65nm(1X) and it is positioned so that the center of the serif is located at the corner of the line. (b) Contours of the 30% clear field intensity of the aerial images from TEMPEST and SPLAT simulations. The ideal rectangular image is also shown for comparison.

from a TEMPEST (r-mask) simulation is always smaller (i.e. longer line) than that resulting from a SPLAT (k-mask) simulation of the same CF (clear field) geometry. But what is a more meaningful comparison, is rather one between the correction in the LES_{aerial} from the reference to each OPC case resulting from the TEMPEST and SPLAT simulations of the same CF masks. In the example shown in Figure 3-11 this correction comes out to be 31nm or 34nm from the SPLAT or TEMPEST simulations respectively.

In Figure 3-12 the square root of the correction of the LES_{aerial} is plotted *vs.* the equivalent size of OPC, where the equivalent size is the square root of the non-overlapping area, for all the different OPC serif sizes and placements that were simulated with TEMPEST and SPLAT, and for both mask polarities (dark field, clear field). For a CF mask the correction in the LES_{aerial} predicted by TEMPEST is larger by ~9% than that predicted by SPLAT, for all OPC designs, whereas for a DF mask TEMPEST predicts a smaller LES_{aerial} correction by ~6% compared to SPLAT, for all OPC designs. Why this is happening can be explained by invoking the boundary conditions of the electromagnetic field in the vicinity of the serif: The electric field that is parallel to the square serif sides (as is true for good conductors) has to vanish within the chromium, which requires the tangential

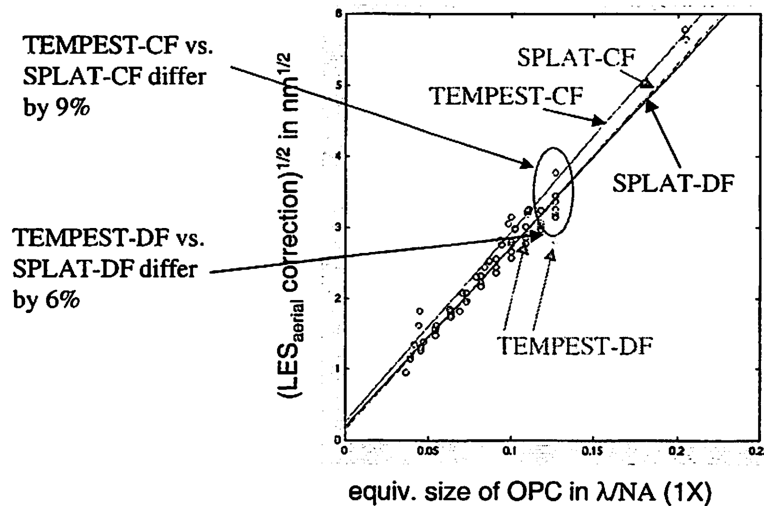

Figure 3-12. Square root of the correction of the LES_{aerial} *vs.* equivalent size of OPC

The equivalent size is the square root of the non-overlapping area for all the different OPC serif designs considered. Both mask polarities (dark field, clear field) are examined. The points that do not fall on the respective straight line correspond to OPC designs where the serif was placed in highly off-diagonal locations.

fields in the neighboring open areas to rapidly vanish in close proximity to the chromium. This effectively implies that the electromagnetic size of a dark serif (CF mask) is somewhat larger than its geometrical size and that the electromagnetic size of an open serif (DF mask) is somewhat smaller than its geometrical size. Hence a dark serif will actually be responsible for a bigger correction in the LES_{aerial} ($\Delta LES_{aerial,TEMPEST} > \Delta LES_{aerial,SPLAT}$), whereas a clear serif for a smaller correction ($\Delta LES_{aerial,TEMPEST} < \Delta LES_{aerial,SPLAT}$). The above trend with serif area can be further pursued by using perturbational arguments to relate the size of a small pin-hole with the peak intensity of light that goes through, and also the size of a small opaque pin-spot with the minimum intensity that appears at its shadow. In that respect, from a previously proposed model [59]:

Equation 3-1. $$I_{peak-PH} = 8.5\left(\frac{CD}{\lambda/(NA)}\right)^4$$

and using perturbational arguments:

Equation 3-2. $$I_{dip-PS} = 1 - 2\sqrt{I_{peak-PH}}$$

For example the 65nm x 65nm (1X) square opaque pin-spot used in the simulations shown in Figure 3-11, when simulated in an isolated configuration with TEMPEST (r-mask), results in an intensity dip of 0.64, whereas the intensity dip resulting from the SPLAT simulation is only 0.69. This renders an equivalent electromagnetic size of 69nm x 69nm from the r-mask model or 63.5nm x 63.5nm from the k-mask model, *i.e.* a difference in their side of ~8%, which correlates with the ~9% difference in the effectiveness of this serif when placed near the corners of the isolated line. An open square pin-hole of the same dimensions appears smaller by ~5.5% in TEMPEST than in SPLAT. Therefore, its effectiveness is reduced when it is placed near the corners of an isolated open line (DF mask), and the reduction in the correction of the LES_{aerial} is ~6%, as shown in Figure 3-12.

Note that in Figure 3-12 the points that do not fall on the respective straight line correspond to OPC designs where the serif was placed in highly off-diagonal locations, but even in those situations the r-mask to k-mask (TEMPEST-SPLAT) correction bias is close to the 9% (CF) and 6% (DF) values that were found above. The important result that the graph of Figure 3-12 conveys is exactly the fact that a rigorous electromagnetic simulation

is not necessary in order to predict the correction in the LES_{aerial} that a certain OPC serif design will cause. This can be done with the k-mask model (just SPLAT) just as well, but one needs to account for the 9% (CF), or the 6% (DF) r-mask to k-mask difference. Viewed a little differently, in order to correct for a certain amount of LES_{aerial}, just SPLAT simulations can be used for the design process, but in the case of a CF mask a correction for 9% smaller LES_{aerial} needs to be done and for the case of a DF mask a correction for 6% larger LES_{aerial}.

3.2.2. Corner Rounding

Here, isolated lines are considered on both clear field and dark field masks with rounded corners. The reason why corner rounding of the mask feature is examined, is because its aerial image behavior with respect to the degree of roundness resembles the OPC serif design, where now the roundness of the corner can be thought of as an anti-serif,

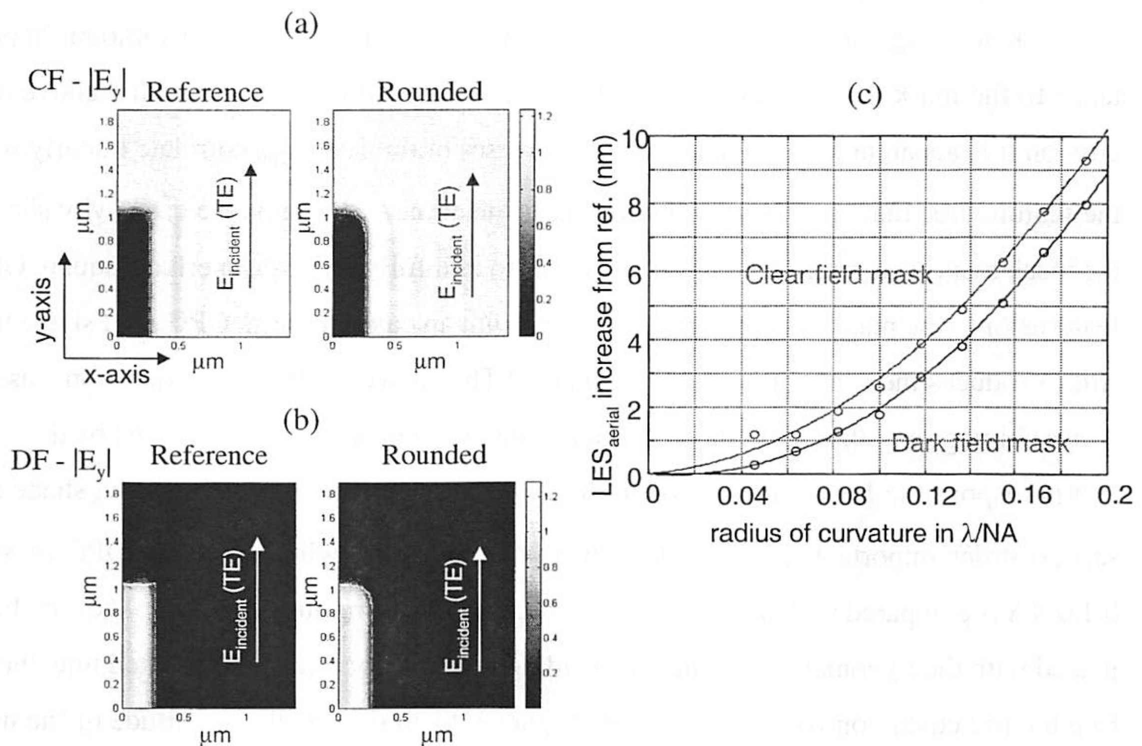

Figure 3-13. The effect of corner rounding

Amplitude of the near field of a reference (not rounded) and a rounded case (a) for a CF mask and (b) for a DF mask. (c) Increase of the LES_{aerial} *vs.* radius of curvature for CF and DF masks.

as it will be obvious shortly. Figure 3-13(a) depicts the amplitude of the near field of a reference (not rounded) and a rounded case for a clear field mask and Figure 3-13(b) for a dark field mask. In both (a) and (b) the incident light is parallel to the line (TE). Varying the radius of curvature of the rounded mask feature the resulting aerial image is examined and the amount by which the contour of 30% intensity retreats from the respective contour of the ideal (right angled) mask is deduced, that is the increase of the LES_{aerial}. The increase of the LES_{aerial} with respect to the reference is plotted versus the radius of curvature for both clear and dark field masks in Figure 3-13(c). From these plots it is apparent that the LES_{aerial} increases quadratically versus the radius of curvature, which implies that it is proportional to the area missing from the corner because of the roundness, hence it is valid to think of corner rounding as anti-serif OPC in a CF mask or serif OPC in a DF mask, which lead to the opposite than the desired direction of LES_{aerial} reduction.

3.2.3. Shape fidelity requirements for good performance of OPC serifs

Knowledge of the required shape fidelity for the OPC serif is of paramount importance to the mask designer and especially to the mask manufacturer. From the above discussion it is apparent that the increases or decreases of the LES_{aerial} correlate linearly with the feature area that is missing or is extra near the corners. If that is the case, why should the mask manufacturer invest in time and effort to faithfully replicate "perfect" square OPC features onto the mask? Is it possible to get by with an easier to print OPC serif shape that still introduces the same non-overlapping area? The answer to the above questions, as far as aerial image simulation predicts, is that indeed, it is the extra area introduced by the serif that is responsible for the correction in the LES_{aerial}, whereas the details of the shape are second order important. Figure 3-14 depicts one example, where a square OPC of side $0.1\lambda/NA$ is compared with a "mouse ear" (circular) OPC of radius $0.06\lambda/NA$. They are both placed with their geometrical centers coinciding with the corners of the isolated line, therefore having equal non-overlapping areas. Figure 3-14(a) depicts the amplitude of the near field for the reference case, the square OPC and the "mouse ear" OPC, (b) depicts the aerial image intensity contours for the two OPC shapes and in (c) a cut-line along y at x=0 is shown, from which it is obvious that the two aerial images are nearly identical. In Figure 3-

15 the LES_{aerial} correction the non-overlapping area of the serif is shown for DF masks and various sizes of square and "mouse ear" serifs, when their center is aligned with the corner of the main feature.

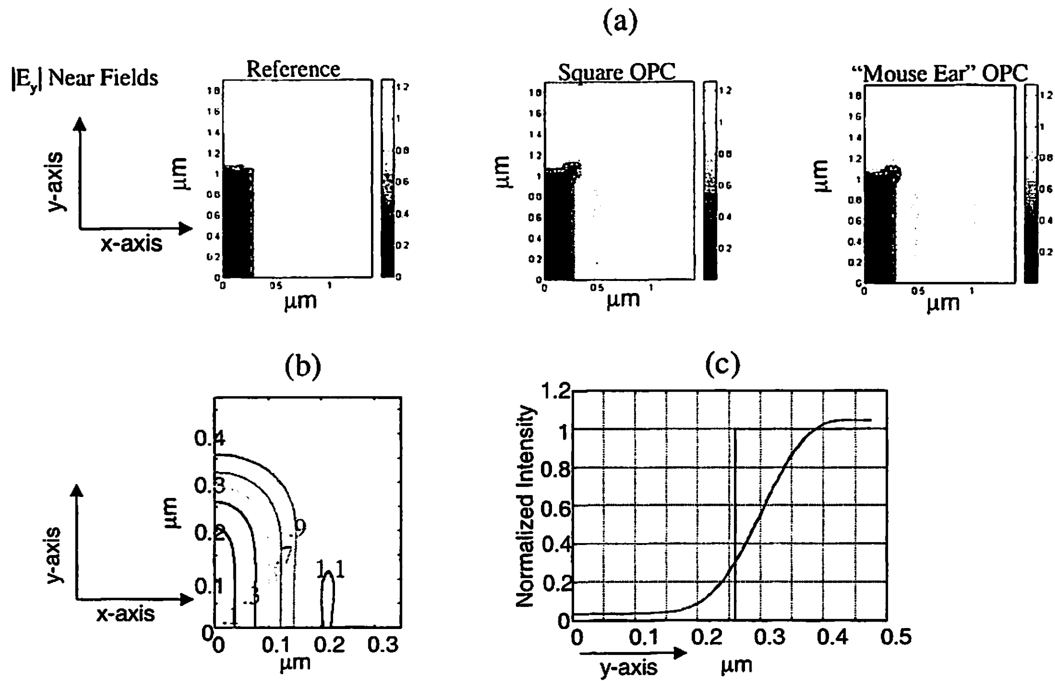

Figure 3-14. Effectiveness of different OPC shapes

(a) Amplitude of the near field of the reference (no OPC), a square OPC with side 0.1λ/NA and a "mouse ear" OPC with radius 0.06λ/NA, so that they have the same non-overlapping area. (b) Aerial image intensity contours of the square and "mouse ear" OPC. (c) Cut-line of the aerial images along the y-axis at x=0.

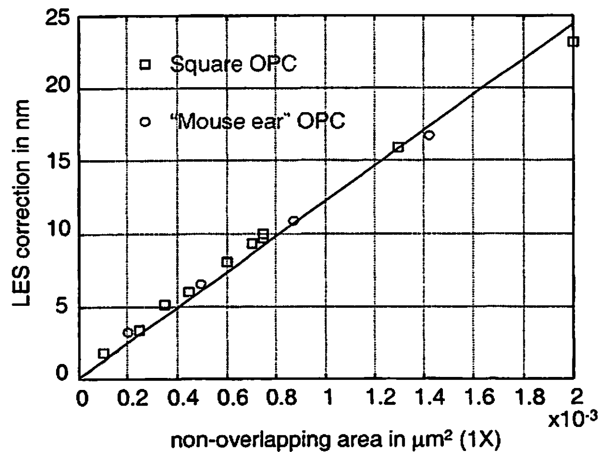

Figure 3-15. Requirements for OPC shape fidelity

LES_{aerial} correction *vs.* the non-overlapping area of the serif for DF masks and various sizes of square and "mouse ear" serifs, when their center is aligned with the corner of the main feature.

3.3. Conclusions

Scalar imaging and rigorous electromagnetic simulation have been used to generate quantitative design data on the placement and sizing of OPC features. Studies of scatter bars showed that both the best-focus and out-of-focus aerial image CD are more sensitive to the scatter bar placement rather than size. For very high σ the CD_{aerial} is a weaker function of both placement and size of the scatter bars. The r-mask to k-mask (TEMPEST-SPLAT) difference for scatter bar simulations is typically only ~10%, but the same trends for scatter bar placement and size still apply.

Using a perturbation approach, it is shown that OPC serifs can be adequately characterized by SPLAT (k-mask) simulations only. The r-mask to k-mask results' bias corresponds well with the bias of the two models in the case of small isolated holes and posts. This behavior is accurately characterized for diagonal placements of the serifs, but for off-diagonal placement it is not as accurate. The actual shape of the serif is shown by rigorous 3D electromagnetic simulation to be less important than previously expected. It is shown that the correction of the LES_{aerial} is proportional to the non-overlapping area of the serif. Corner rounding can be regarded as an anti-serif case in clear field masks and serif in dark field masks. The amount of LES is proportional to the area missing because of the rounding of the mask feature.

4 Domain decomposition methods for the rapid simulation of photomask scattering

SIMULATION has been very successful in the design and optimization of phase-shifting masks. The infamous intensity imbalance problem of an alt. PSM was first discovered by Wong using simulation [105], [109] and later verified experimentally [66]. The optimization of the trench design of alt. PSMs through simulation was demonstrated by Friedrich *et al.* [33]. Hotta *et al.* included the spatial frequency spectrum view in the analysis of an alt. PSM [46]. Hotta also revealed the role of the Chromium-based absorption layer that was first noted by Yuan [115]. One of the remaining major challenges, that is addressed in this Chapter and further developed in Chapters 5 and 6, is the 3D simulation of large non-periodic mask layouts and the considerable computational effort that is involved. The challenge is to not only get the near fields, but to obtain an equivalent and compact representation of the mask that fully captures its diffraction properties. If such a task can be completed rapidly, then it can play a major role as a part of a model-based OPC method that can accurately handle alt. PSM (or any other advanced photomask). The use of an OPC software tool with this important capability can modify the mask in such a way that the resulting spectrum meets the design goals. Issues such as pitch dependent focus behavior, forbidden pitches and small MEEF[1] in alt. PSMs [81] could thus be addressed

1. MEEF stands for mask error enhancement factor. It is typically defined as:
$MEEF = \Delta CD_{wafer} / \Delta CD_{mask}$, where ΔCD_{wafer} is the variation of the critical dimension of the (pre- or post-etch) printed image on the wafer from a nominal CD_{wafer} and ΔCD_{mask} is the variation of the critical dimension on the mask from a nominal CD_{mask}. The nonlinearities of the process lead to a widely varying MEEF at various nominal CDs and this is a serious problem. An intriguing look at the MEEF as a matrix that allows two-dimensional proximity effects to be quantified can be found in [43].

effectively at the mask simulation level, without rigorous techniques that can only be used sparingly.

This Chapter progresses as follows: First, building upon an example that illustrates the discrepancy between the two imaging simulation approaches, namely the k-mask model and the r-mask model for alt. PSMs, the new *quasi-rigorous* mask model (qr-mask) that relies on a domain decomposition method (DDM) is introduced. The linearity rooted into the Kirchhoff-Fresnel diffraction integral is used as a starting point for the domain decomposition method. The qr-mask model is further developed into the more compact *matched-Kirchhoff* mask model (henceforth mk-mask), that allows for the rapid and accurate simulation of the imaging problem. The extension of the qr-mask and mk-mask models in three dimensions is demonstrated and benchmarking results that demonstrate the validity of the method for 3D simulations are presented.

Two other important issues are also discussed at some length, namely the applicability of this method for arbitrary polygonal shapes of the Manhattan-type that are generally encountered in mask layouts and the extension of the method in imaging situations where the mask diffraction orders are not constant for all angles of incidence within the illumination cone. The important topic of cross-talk between adjacent features in alt. PSMs is an integral part for the general applicability of the models developed in this Chapter and is covered in the next Chapter.

4.1. Background

4.1.1. Superposition and domain decomposition

Inherent in the linearity of Maxwell's equations for the electromagnetic field is the principle of superposition. One needs to be careful though, in the fact that the superposition principle applies to the sources of the electromagnetic field and not to the geometry or the materials present in the problem. For example, if the tangential $\vec{E}_{t1}$ and $\vec{H}_{t1}$ fields are given everywhere along a closed surface that surrounds a volume of materials ε_a, μ_a, σ_a (where the material properties are a function of position), then a unique solution exists

everywhere within the volume, say $\vec{E}_{a1}$ and $\vec{H}_{a1}$. Now, if a different set of tangential fields, $\vec{E}_{t2}$ and $\vec{H}_{t2}$, are enforced (owing to different external sources) along the same surface enclosing the same geometry of materials $\varepsilon_a, \mu_a, \sigma_a$, a new unique solution is being established everywhere within the volume, say $\vec{E}_{a2}$ and $\vec{H}_{a2}$. By the linearity of Maxwell's equations the superposition principle follows, according to which, if $\vec{E}_{t1} + \vec{E}_{t2}$ and $\vec{H}_{t1} + \vec{H}_{t2}$ are the tangential fields enforced along the surface, the solution within the volume will now be the sum of the two solutions, namely $\vec{E}_{a1} + \vec{E}_{a2}$ and $\vec{H}_{a1} + \vec{H}_{a2}$. How-

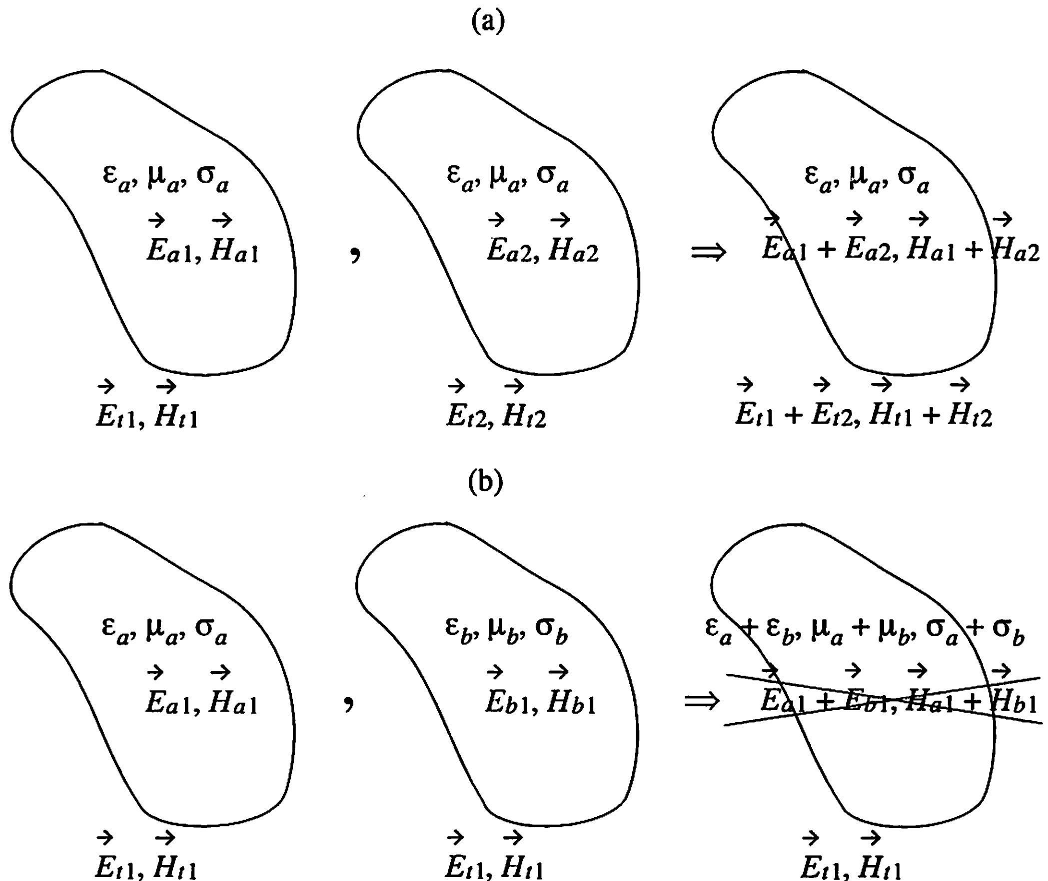

Figure 4-1. Superposition principle

The superposition principle follows from the linearity of Maxwell's equations with respect to the sources of the EM field, as shown in (a). However, a superposition of materials (geometries) such as the one shown in (b) is false.

ever, if the tangential $\vec{E}_{t1}$ and $\vec{H}_{t1}$ fields are given everywhere along the same closed surface that surrounds a volume of new materials ε_b, μ_b, σ_b (different geometry), then a new unique solution exists everywhere within the volume, say $\vec{E}_{b1}$ and $\vec{H}_{b1}$. Note that the superposition principle does not apply in this case, that is, if $\vec{E}_{t1}$ and $\vec{H}_{t1}$ are the tangential fields enforced along the same surface that surrounds a volume of materials $\varepsilon_a + \varepsilon_b$, $\mu_a + \mu_b$, $\sigma_a + \sigma_b$ (composite geometry), it is easy to prove that the solution within the volume is not $\vec{E}_{a1} + \vec{E}_{b1}$ and $\vec{H}_{a1} + \vec{H}_{b1}$, as one might be tempted to suggest.

A different kind of superposition will be invoked in the following, namely the superposition stemming from the linearity of the Kirchhoff-Fresnel diffraction integral [15], that gives the (scalar) disturbance U (any field component) at a point P behind an infinite screen bearing an opening W, when illuminated from a distant point source at P_0 located on the other side of the screen:

Equation 4-1.
$$U(P) = -\frac{jAe^{jkr_0}}{2\lambda r_0}\iint_W \frac{e^{jks}}{s}(1+\cos\chi)dS$$

where λ is the wavelength, A is a constant (complex amplitude from the source), k is the wavenumber and all other parameters are depicted in Figure 4-2. The diffraction integral of Equation 4-1 extends over W, the screen's opening. If the screen consists of multiple openings W_i, according to Equation 4-1, one could calculate the disturbance $U_i(P)$ due to each opening separately and then sum the partial disturbances for the total U(P):

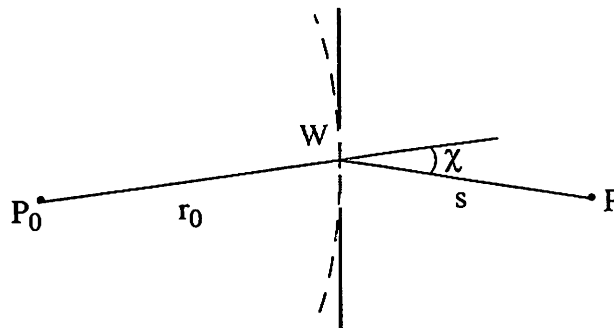

Figure 4-2. Illustrating the Kirchhoff-Fresnel diffraction formula

Equation 4-2. $$U(P) = \sum_i U_i(P)$$

The above equation is the essence of the domain decomposition that will be applied in the following in alt. PSMs. Every single opening of an alt. PSM will be considered (simulated) separately and the scattered field below the mask will be found *via* the DDM as the sum of the scattered fields below each opening. This is shown in Figure 4-3, where an arbitrary alt. PSM layout (2D or 1D) is decomposed *via* the DDM into its constituent single opening masks. For now, each 2D opening is restricted to be rectangular. Arbitrary polygonal shapes are addressed in Section 4.3.5. Note that according to the simulation strategy developed in Chapter 2, only the scattered field from a single, normally incident plane wave needs to be calculated.

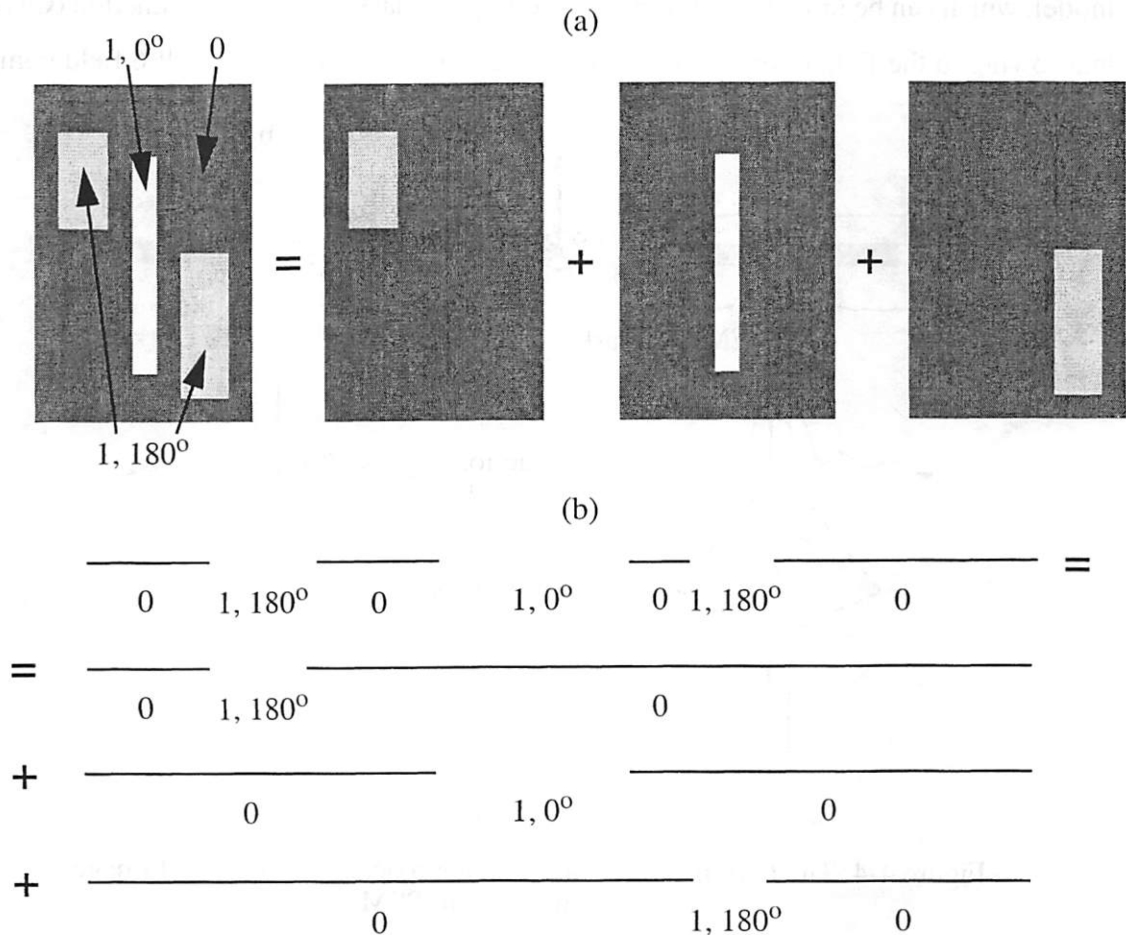

Figure 4-3. The domain decomposition method (DDM) applied in 2D layouts (3D masks) and 1D layouts (2D masks)

4.1.2. Simulation approaches and the imbalance problem in alt. PSM

The simulation of an image intensity distribution (aerial image) that is projected by an optical system through a photomask onto (and into) the resist-coated semiconductor wafer can be performed following one of the two distinct paths shown in Figure 4-4, as discussed in Chapter 2. In the more computationally laborious path of Figure 4-4(a) the exact three-dimensional geometry of the photomask is used for a rigorous calculation of the electromagnetic field (EMF) that is being established as a result of a certain illumination. Such a rigorous solution demands large computational resources, since even for a minute 10λ x 10λ layout more than 100Mb of memory and 10hrs of simulation time may be required. Obviously, large, arbitrary mask layouts cannot be handled. The complex (amplitude and phase) steady-state near EMF that is scattered below the mask constitutes the r-mask model, which can be thought of as a rigorous complex mask transmission function (CMTF) that, owing to the field component cross-mixing, consists in general of all 6 field compo-

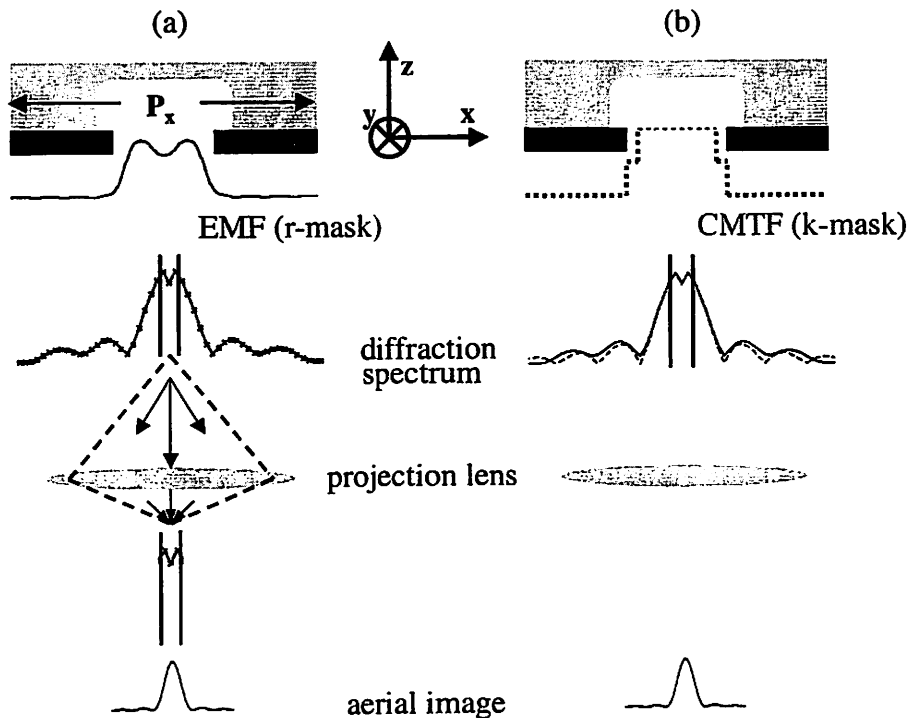

Figure 4-4. The two distinct simulation approaches for the aerial image calculation of an alt. PSM

In (a) the near electro-magnetic field (EMF) is found through rigorous simulation of the exact mask structure (with TEMPEST) and used as the r-mask model for the aerial image calculation (with SPLAT), while in (b) a complex mask transmission function (CMTF) is assumed and used as the k-mask model for the aerial image calculation (with SPLAT).

nents (E_x, E_y, E_z, H_x, H_y, H_z), that is, one CMTF per field component. As seen in Chapter 2, each complex field component across the observation plane can be decomposed into its complex angular spectrum (Fourier spectrum of the near EMF). Note that this diffraction spectrum is continuous for a completely isolated mask structure and discrete for periodic mask structures. Typically, most simulators use periodic boundary conditions in the lateral mask directions and subsequently this makes the spectrum discrete. The frequency separation of the complex discrete diffraction orders depends solely upon the mask period in x- and y-directions, as seen in Chapter 2.

In photolithographic imaging for IC, the objective lens acts as a low-pass filter and only the center part of the diffraction spectrum is collected and contributes in the aerial image formation. In the case of a discrete spectrum, the diffraction orders that are collected by the imaging system's acceptance cone (NA) are referred to as *through-the-lens (TTL) diffraction orders*. Specifically, the collected plane waves have wavenumbers such that:

Equation 4-3.
$$\sqrt{k_x^2 + k_y^2} \leq \frac{2\pi}{\lambda} \cdot \frac{NA(1+\sigma)}{R}$$

where λ is the illumination wavelength, NA is the numerical aperture of the projection optic, σ is the partial coherence factor of the illumination and R is the reduction factor of the optical system.

In the faster simulation approach of Figure 4-4(b) the rigorous but time-consuming calculation of the photomask EMF is omitted and, instead, a scalar CMTF is assumed, *i.e.* a k-mask model is used that typically consists of a piecewise constant function coinciding with the photomask transmission properties in x, y. The limits of validity of this approach have been investigated extensively by many authors and it has been established that it breaks down when either the minimum feature on the photomask layout or the vertical structure of the photomask is comparable to the illumination wavelength. Unfortunately, this is true for advanced photomasks with OPC or alternating PSM and the simulation path of Figure 4-4(b) leads to inaccurate results. It suffices to say that the accuracy of this approach is contingent upon how closely the spectrum resulting from the k-mask model

matches the spectrum from the rigorously calculated r-mask model within the bandwidth of the projection system, as depicted pictorially in Figure 4-4(b).

An example of a CD=400nm (4X), 1:1 line/space, $0^o/180^o$ alt. PSM is shown in Figure 4-5(a) and the resulting EMF solution calculated with TEMPEST for λ=193nm TE-excitation[1] is shown in Figure 4-5(b). The amplitude and phase of the near EMF at the observation plane located 50nm below the end of the 80nm-thick Chromium absorbing layer is shown in Figure 4-5(c) and (d) respectively. The amplitude and phase of the k-mask model is also shown for comparison. Finally, the two distinct aerial images resulting from the r-mask and k-mask models for imaging through a system with NA=0.7, R=4 and σ=0.3 are shown in Figure 4-5(e). The imbalance effect of the alt. PSM, evident only through the r-mask model, is the pronounced difference of the two image lobes, with the lobe resulting from the 180° phase-shifted region having lower intensity than the lobe resulting from the unshifted 0° region. This kind of discrepancy between the two aerial images is usually attributed to "vertical" or "deep-trench" EM effects, that, as their cryptic names suggest, are impossible to model using a k-mask model. In the remaining of this Chapter, properly *matched k-mask* models, hereafter referred to as *mk-mask* models, capable of accurately including these effects in imaging are sought.

1. Unless stated otherwise, the illumination is a plane wave that is normally incident on the photomask and consequently TE and TM excitations are indistinguishable. The convention used here is the one noted in Chapter 2, where the TE has the E-field parallel to the y-axis and the TM parallel to the x-axis.

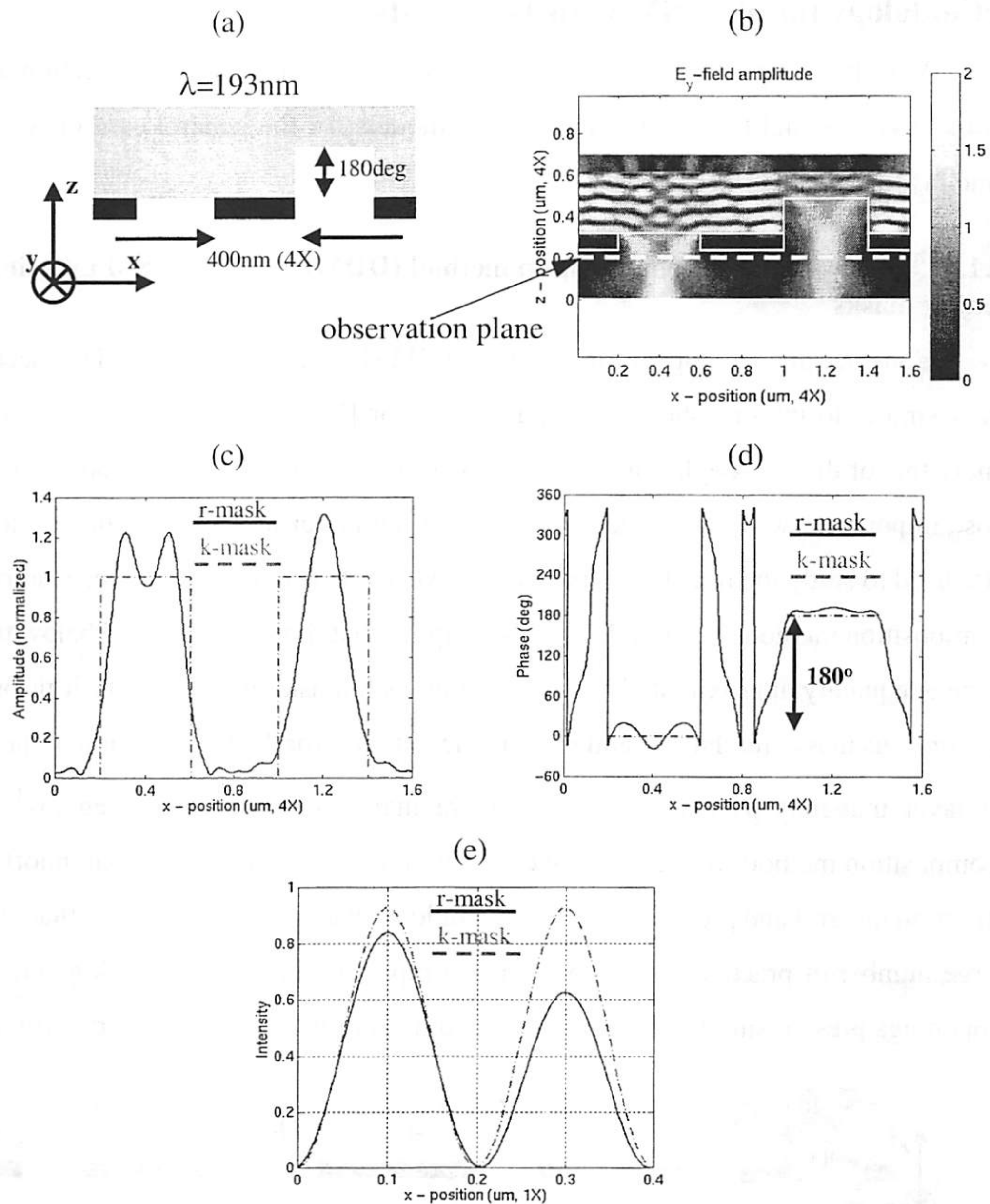

Figure 4-5. The intensity imbalance problem of a 0°/180° alt. PSM

(a) Mask geometry, (b) amplitude of the near EM field solution from TEMPEST (λ=193nm), (c) amplitude and (d) phase of the near EMF solution at the observation plane, located 50nm below the absorption layer, compared with the assumed k-mask model, (e) the resulting aerial images of the r-mask and k-mask models for an imaging system with NA=0.7, R=4, σ=0.3.

4.2. Development of a new domain-decomposition and spectral-matching methodology for alt. PSM with 1D layouts

Models for one-dimensional mask layouts are the subject of this Section and their treatment is essential for the development of models for the general case of two-dimensional layouts.

4.2.1. 0th-order domain decomposition method (DDM) of an alt. PSM into single-opening masks

Consider the decomposition of an alt. PSM shown in Figure 4-6. This decomposition is similar to the one shown in Figure 4-3(b) or [79], but it contains one extra term, namely that of the non-negligible transmission of the "opaque" Cr-based absorption layer, whose importance was first noted by Yuan [115] and later incorporated in the model that Hotta used to study the trench design of alt. PSMs [46]. The pictorial representation of the decomposition method shown in Figure 4-6 implies that the scattered field below the mask can be adequately approximated by considering each mask opening by itself through distinct rigorous mask simulations and properly accounting for the transmission of the absorption layer that may have been counted more than once in the dark regions[1]. Such a decomposition method was seen to have its origin in the linearity of the Kirchhoff-Fresnel diffraction integral and predicts the scattered field with an accuracy of better than 0.5%, for a large number of practical situations, when compared with the true mask geometry with all openings present simultaneously. This decomposition was found accurate for shallow-

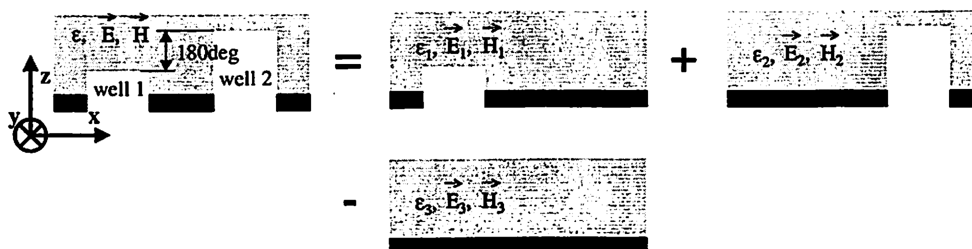

Figure 4-6. 0th-order domain decomposition method (DDM) of an alt. PSM into single opening masks

1. In the case of two openings (i.e. two single opening masks) the light below each dark region of the original mask is double-counted before subtracting the uniform transmission from the absorption layer. It is straightforward to verify that in the case of an N-opening mask decomposed into N single-opening masks the uniform transmission of the absorption layer should be subtracted (N-1) times.

trench alt. PSM technologies, but it breaks down for deep-trench technologies because of cross-talk between adjacent features [46]. These limits will be explored in more detail in the following. The question of why one should bother decomposing a 1D mask layout problem, that requires a fairly quick 2D rigorous simulation to determine the mask scattering properties, into a set of 1D masks, each requiring a 2D simulation, will be settled after considering the decomposition of masks bearing 2D layouts.

For the 400nm (4X), 1:1 line/space pattern considered in Figure 4-5 the decomposition of the $0^o/180^o$ alt. PSM according to Figure 4-6 is shown in Figure 4-7. In Figure 4-7(a) the EM field of the original mask domain is decomposed into the first two single-opening domains shown in Figure 4-6. In Figure 4-7(b) the EM field across the observation plane is shown for both the original alt. PSM (both openings are present simultaneously) as well as the superposition of the two openings. The agreement between the two is almost

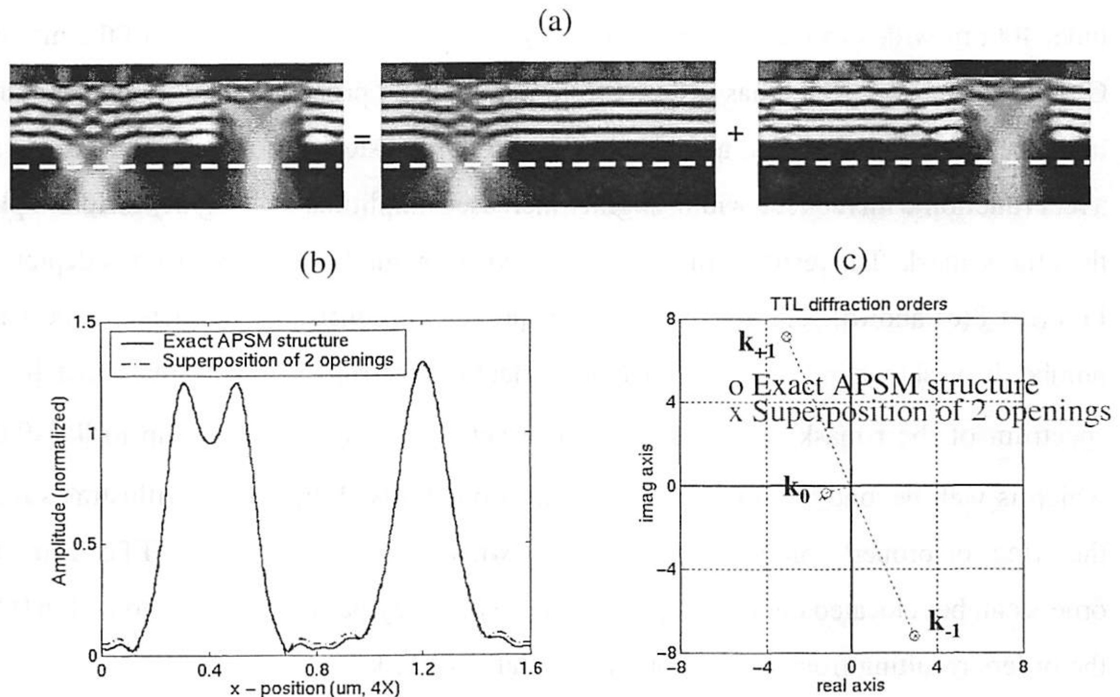

Figure 4-7. Example of the 0th-order DDM

(a) Decomposition of the EM field of Figure 4-5(b) into the first two terms of Figure 4-6, (b) comparison of the near field after the decomposition shown in (a) with the near field of the exact alt. PSM geometry of Figure 4-5(a) at the observation plane, (c) comparison of the "through-the-lens" (TTL) complex diffraction orders of the EM fields shown in (b).

perfect, but upon close inspection it is clear that the near fields differ slightly at the dark regions. This is because the third term of Figure 4-6 is also needed. Adding it gives an accuracy better than 0.5% everywhere. Finally, Figure 4-7(c) depicts on the complex plane the three TTL (through-the-lens) diffraction orders (k_{-1}, k_0, k_{+1}), for both the original alt. PSM and the decomposition shown in Figure 4-7(a). Note that the non-zero k_0 is responsible for the imbalance effect and that the small difference of the two methods in k_0 is fully attributed to the residual background transmission, which was not accounted for.

4.2.2. Identifying the discrepancy between k-mask and r-mask models - The new mk-mask model

Figure 4-8(a) shows the EM field solution of a single 180^0 opening under TE plane wave excitation. The amplitude of the rigorously calculated diffracted field at the observation plane located 50nm below the absorbing layer is shown in Figure 4-8(b). Also shown in Figure 4-8(b) are the amplitude of the original k-mask model, which is just a unit-amplitude, 400nm-wide (4X) rect function properly centered, and the amplitude of the modified CMTF (mk-mask), which has resulted from a systematic procedure that will be explained in the next Section. For now, note that the modified (adjusted) mk-mask in this case is also a rect function with reduced width, slightly increased amplitude and slightly different phase than the k-mask. The result of this modified CMTF on the Fourier spectrum is depicted in Figure 4-8(c) and (d). The magnitude of all propagating diffraction orders *vs.* the wavenumber k_x is shown in Figure 4-8(c). Notice that the spectrum of the mk-mask matches the spectrum of the r-mask (rigorous CMTF) to better than 1% accuracy up to $|k_x|$~0.012, which is well beyond the objective lens collection ability. Figure 4-8(d) illustrates nicely the effect of properly modifying the k-mask, where it is shown that the TTL diffraction orders can be relocated on the complex plane, so that they perfectly match (to within 0.5%) the orders resulting from the rigorously calculated r-mask.

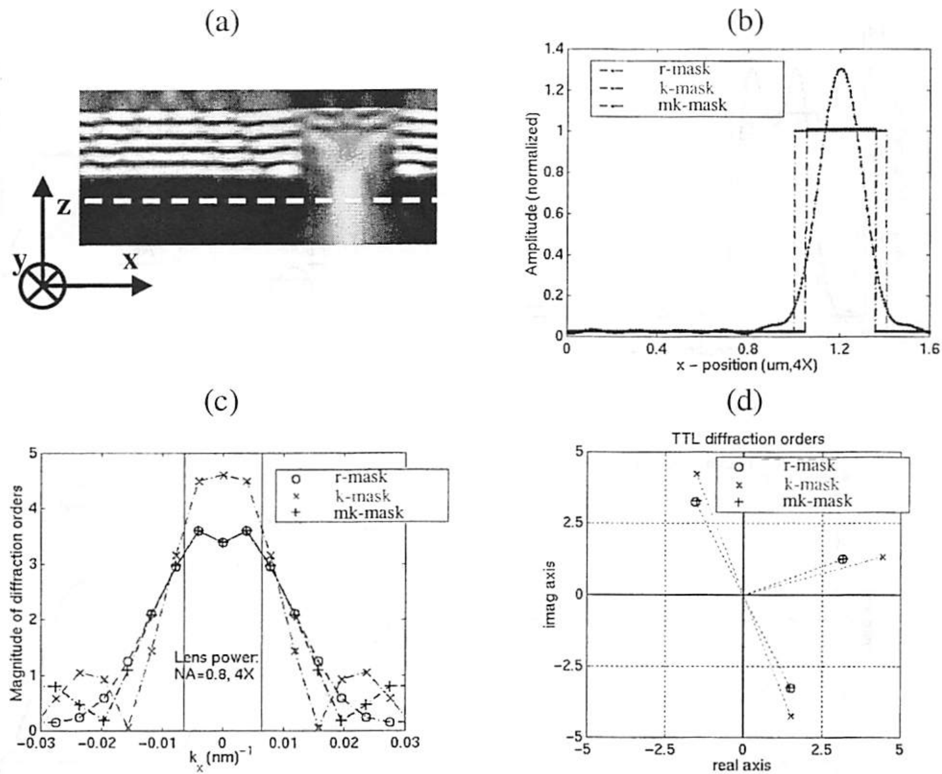

Figure 4-8. Matching the k-mask of each individual opening to the r-mask

(a) Electromagnetic field amplitude of a single 180° phase-shifted opening, (b) amplitude of the EM field at the observation plane shown in (a) (r-mask) compared with the original CMTF (k-mask) and the matched CMTF (mk-mask), (c) magnitude of diffraction orders vs. k_x and (d) the TTL complex diffraction orders on the complex plane for the three mask models shown in (b).

A similar adjustment can be independently performed for a single 0° opening, which will result in a modified CMTF for that opening. Putting together the two mk-masks for the 0° and the 180° openings, as described in Figure 4-6, to form the mk-mask of the complete 1D alt. PSM layout, results in a simulation of the aerial image that perfectly matches (to within <0.5%) the aerial image using the rigorous CMTF (r-mask). This is shown in Figure 4-9.

The normalization used in spectra plots is such that a constant (DC) value of 1 (clear field) would produce a Dirac δ-function at zero frequency with amplitude of 19.4 ($\sqrt{\eta} = \sqrt{\sqrt{\mu_0/\varepsilon_0}} \approx 19.4\Omega$)

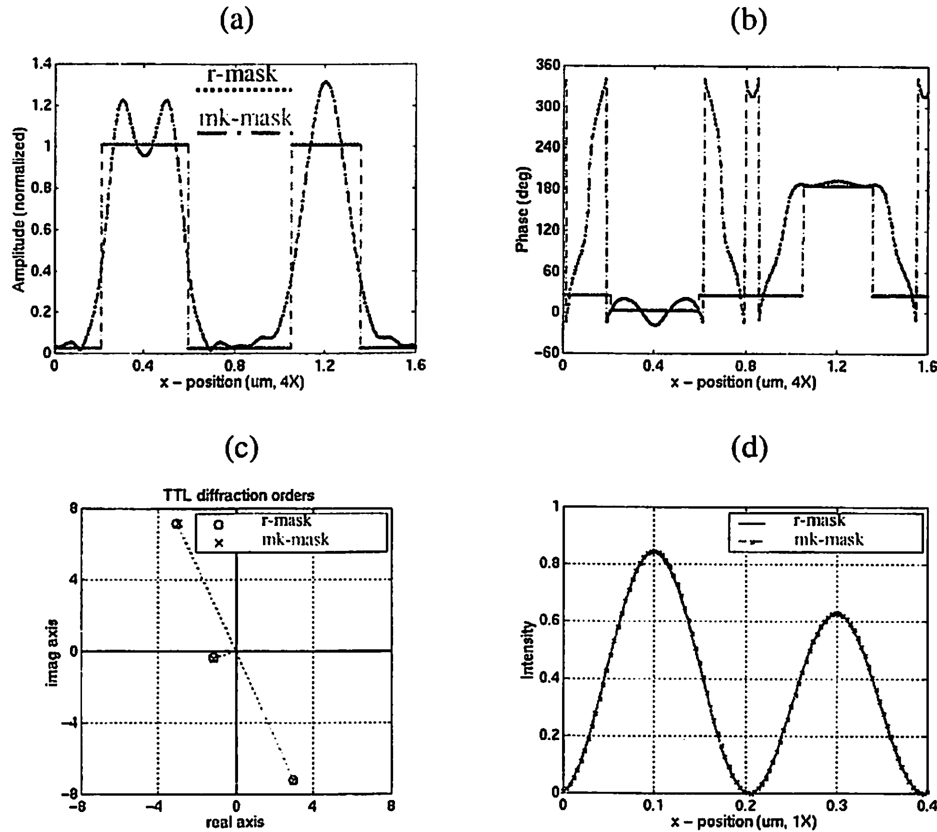

Figure 4-9. The mk-mask model for the example of Figure 4-5

(a) Amplitude and (b) phase of the rigorous CMTF (r-mask) of the complete alt. PSM shown in Figure 4-5(a) and the matched CMTF (mk-mask). Note that the smaller opening corresponds to the 180° phase-well. (c) The TTL complex diffraction orders of the two CMTFs in (a), (b) are aligned and consequently the aerial images in (d) are identical.

4.2.3. Systematic manipulation of the Fourier spectrum for the adjustment of the k-mask model

In this Section we examine in depth how the attributes of the k-mask model can be adjusted to lead to a Fourier spectrum that closely matches the spectrum resulting from the r-mask. This is done through the example shown in Figure 4-10(a), where a single 180° phase-well of CD=600nm (4X) with 50nm of isotropic glass underetch is considered. The mk-mask model (shown in Figure 4-10(b)) is a properly centered rect function, but its width L_{x0}, amplitude T_0 and phase ϕ_0 are now varied until the best spectral match with the r-mask is achieved. The residual transmission of the background with amplitude T_b and

phase ϕ_b are treated as constants, whose values are related to the thickness and the optical properties of the Chromium-based absorption layer.

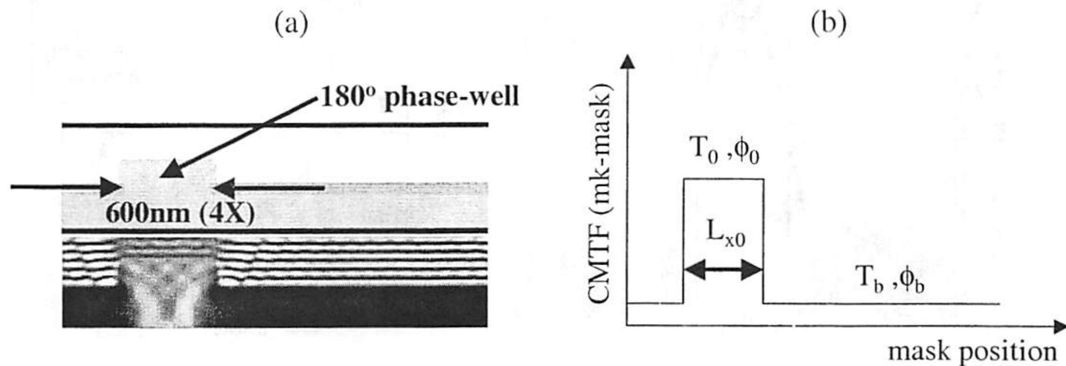

Figure 4-10. The rect-function mk-mask model

(a) Single 180° phase-well of CD=600nm (4X) with 50nm of isotropic underetch. The mask period is 4xCD=2.4μm. (b) The rect-CMTF model, where its width L_{x0}, amplitude T_0 and phase ϕ_0 are varied until the best spectral match with the rigorous CMTF (r-mask) is achieved. T_b and ϕ_b are the amplitude and phase of the residual background light.

Figure 4-11(a) and Figure 4-10(b) show the effect of reducing L_{x0}, while keeping T_0 and ϕ_0 constant. The spectrum of the r-mask is also shown for comparison. As expected from simple Fourier theory, reducing L_{x0} results in a broader amplitude spectrum (Figure 4-11(a)). The behavior of the seven TTL diffraction orders (up to +/- 3 for NA~0.8) on the complex plane as L_{x0} is varied is shown in Figure 4-11(b).

Figure 4-11(c) and Figure 4-11(d) depict the effect of reducing T_0, while keeping L_{x0} and ϕ_0 constant. Note that varying T_0 does not change the overall shape of the spectrum (the nulls in the amplitude spectrum of Figure 4-11(c) remain unchanged), but simply scales the amplitude level of the spectrum.

Figure 4-11(e) and Figure 4-11(f) illustrate the effect of varying ϕ_0, while keeping L_{x0} and T_0 constant. The amplitude spectrum of Figure 4-11(e) is completely unaffected by the changes in ϕ_0, but the phase of the diffraction orders is changing in liaison with ϕ_0, in such a way that increasing ϕ_0 results in a counter-clockwise rotation of the spectrum, as shown in Figure 4-11(f) for the TTL diffraction orders.

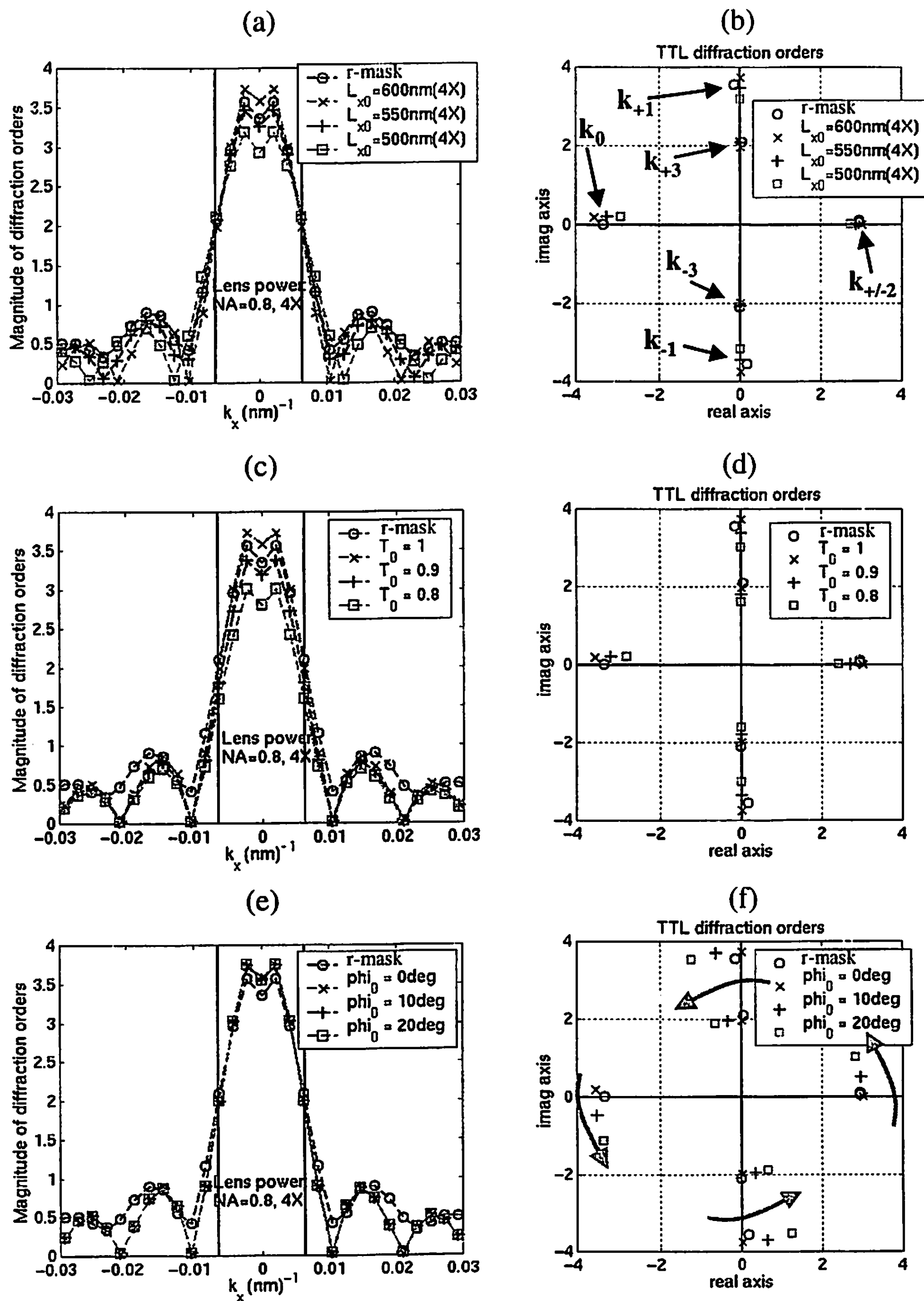

Figure 4-11. Adjusting the mk-mask for good spectral matching

(a), (c), (e) Magnitude of diffraction orders vs. k_x of the rigorous CMTF (r-mask) and three rect-CMTFs (mk-masks), (b), (d), (f) the seven "through-the-lens" (TTL) diffraction orders (for NA~0.8). In (a), (b) T_0=1, ϕ_0=0° are kept constant and L_{x0}=600, 550, 500nm. In (c), (d) L_{x0}=600nm, ϕ_0=0° are kept constant and T_0=1, 0.9, 0.8 and in (e), (f) L_{x0}=600nm, T_0=1 are kept constant and ϕ_0=0°, 10°, 20°.

In summary, the adjustment of the three parameters of the matched Kirchhoff (mk-mask) model (L_{x0}, T_0, ϕ_0) proceeds as follows: First, L_{x0} is adjusted (usually reduced) from its originally designed mask value, CD=600nm (4X) in this case, until the overall shape of the k-mask amplitude spectrum matches that of the r-mask spectrum. A good measure of the "degree of spectral matching" is to look at the location of the first nulls for the two spectra. Next, T_0 (originally is 1) is raised or reduced accordingly, until the same TTL amplitude spectra are achieved. In practice, this model matched the amplitude spectra of all mask geometries that were considered well beyond $|k_x|=0.01$, *i.e.* it is more than adequate even for ideal lenses of NA up to 1. Finally, ϕ_0 (originally set to the true phase of the EM field emerging from the phase-well with respect to an unetched clear background) is adjusted accordingly, so that the spectrum of the k-mask is rotated by the proper amount that will overlap it with the r-mask spectrum.

The above steps have been automated through the use of custom routines written in the MATLAB environment. Although the aforementioned procedure for obtaining the mk-mask model is seemingly simple, there are nevertheless some points that require caution. Adjustment of L_{x0}, T_0, ϕ_0 should start from a judiciously chosen starting point. A "sharp" global optimum solution is usually not available, and, if the spectral matching is restricted only in the lens collection band, with L_{x0}, T_0, ϕ_0 allowed to take values in a large interval, the resulting solution for L_{x0}, T_0, ϕ_0 may be a set of values vastly different than the k-mask model. Although there is nothing fundamentally wrong with that, a solution that is "elegant" is preferred, in the sense that such a solution should have a "good degree of resemblance" with the original k-mask. If such is the case, then the new mk-mask model makes more physical sense, since, in a way, it conveys information about the edge-diffraction effects that take place in an alt. PSM and that the k-mask model fails to capture. For example, as seen in Figure 4-8, the mk-mask for the 180° opening looks similar to the unadjusted k-mask, but it has a smaller L_{x0}, since owing to edge diffraction less light goes through the opening and the opening appears smaller than L_{x0}. Its amplitude and phase are also adjusted so that they compensate for the average amplitude and phase distortions of the true r-mask for that opening.

4.2.4. Other possible functions for the mk-mask model

Functions for the mk-mask other than the rect were also tried and evaluated. These included the Gaussian, the raised-cosine and one with local rect-functions near each edge to model the edge diffraction phenomena. They all yielded relatively successful spectral matching for bandwidths ranging from half to slightly more than that achieved using the above rect function mk-mask. Note that both the Gaussian and the raised-cosine can be constructed to have good resemblance with the true scattered fields and subsequently offer performance equivalent to the rect-function. The model that attempted to replicate the edge-diffraction effects present to the mask geometry by adding local rect functions close to the edges was by 50% inferior (it only matched up to half of the bandwidth of the rect mk-mask). Although such a model might be intuitively satisfactory, and potentially versatile, since it suggests that regardless of the opening size the edge diffraction can be modeled in the same way, it was found to suffer from narrower bandwidth performance compared to the rect-CMTF, reminding us that edge-diffraction in the photomask is not localized near the edges, but rather extents over most of the feature opening.

4.3. Towards a comprehensive quasi-rigorous method and the mk-mask for alt. PSM with arbitrary 2D layouts

So far, an alternative methodology for the imaging simulation of alt. PSMs with arbitrary 1D layouts has been developed. It consists of two basic steps: First, a decomposition of the 1D layout into multiple single-opening masks is performed, depicted in Figure 4-6, by virtue of the superposition principle of the Kirchhoff-Fresnel diffraction integral. This 0th-order DDM was found accurate for all cases where cross-talk is negligible. Next, through exhaustive rigorous simulation of each of these single-opening masks a matched-Kirchhoff-mask is found for each constituent and subsequently for the original layout. This compact mk-mask model, if used in the imaging simulation program, renders an image that is an excellent approximation to the r-mask model. The above methodology has no value, other than pedagogical, since it requires multiple rigorous simulations instead of just one with the complete 1D layout in place. The same remarks are true in the extension of the 0th-order DDM in 2D layouts (Figure 4-3(a)).

However, the following conjecture can be used to revive the interest in the above methodology applied in 2D layouts: After the 0th-order DDM has been performed in the 2D layout, similar to Figure 4-3(a), but including the transmission of the absorbing layer as in Figure 4-6, *no 3D rigorous simulation of the constituent masks is required!* Instead, each constituent single-opening mask of the 2D layout is further decomposed as shown in Figure 4-12. According to this proposition, a quasi-rigorous result (qr-mask) of the scattered field can be obtained by executing two much faster 2D simulations and recombining the results as shown in Figure 4-12, where the last term is just a k-mask model that requires no rigorous simulation. There is no easy way to prove (or disprove) this conjecture. The large variety of cases that it works successfully, by giving accurate results is the closest thing to a proof. Remember also that our concern is an accurate calculation of the aerial images, and not near fields! Errors in near field calculations can be tolerated, provided that the aerial images are accurate. This is exactly what the k-mask model is, an inaccurate near field estimate that works well in aerial image calculations for certain situations. Note that the qr-mask model is expected to work well when the lateral dimensions of each feature are larger than λ and cross-talk is negligible.

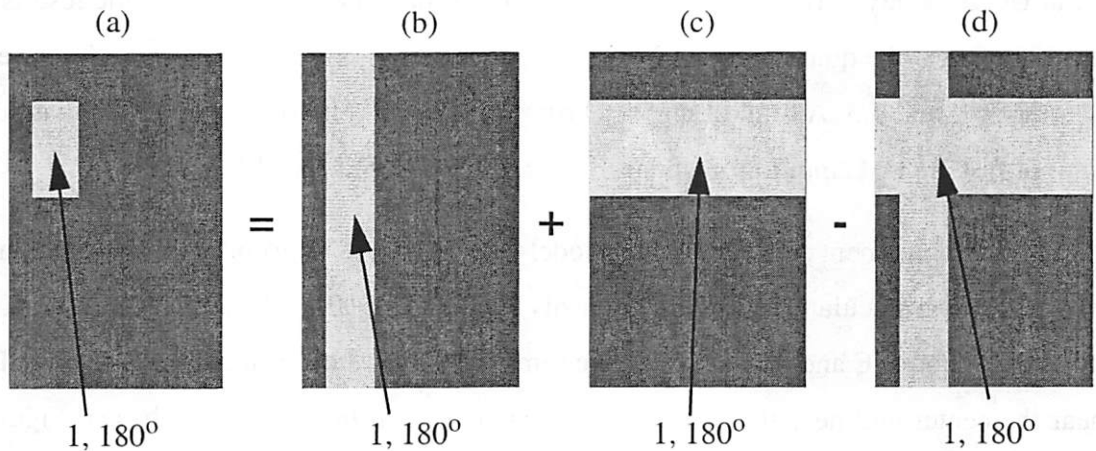

Figure 4-12. Illustration of the quasi-rigorous decomposition method

Instead of the slow but completely rigorous 3D simulation of the original mask in (a), that would lead to the r-mask model, the scattered field below the mask is found by adding the r-masks shown in (b) and (c) and the k-mask shown in (d). Note that the r-masks in (b) and (c) require only 2D rigorous simulations that are much faster and the k-mask in (d) requires no simulation. The resulting approximate mask model is dubbed the qr-mask (quasi-rigorous mask).

Next, two examples that demonstrate the validity and value of this method are presented. The qr-mask model can either be used as shown in Figure 4-12, or each r-mask from the respective 2D rigorous simulation can be reduced to a compact mk-mask model, that matches the TTL-spectrum, as discussed in Section 4.2.

4.3.1. Example 1: Dense line/space pattern

Figure 4-13 depicts a $0^o/180^o$, CD=100nm (1X), 1:1 dense line/space, simple layout of an alt. PSM with 50nm of isotropic underetch. The fully rigorous calculation of the aerial image of this mask under completely unpolarized illumination, with λ=193nm, NA=0.7, σ=0.3 and R=4 requires, according to the discussion in Chapter 2, the rigorous EM field solutions under both TE and TM plane wave excitations. Although a discretization of ~25 cells per λ is sufficient for most practical cases [105], in this example the 3D mask domain was discretized with 40 cells per λ, in order to achieve indisputable accuracy of the near EM fields of better than 0.5% and make the benchmarking comparisons with the quasi-rigorous and mk-mask methods. Consequently the processing time and memory requirements for the 3D simulations rose dramatically. Each 3D TEMPEST simulation (TE and TM) ran for approximately 43hrs on a single 550MHz processor of the ~100 CPU Millennium cluster at UC Berkeley [118] and used up to 1.57Gb of memory. Alternatively, the results can be obtained *via* the quasi-rigorous DDM and subsequent mk-mask models, as described in Sections 4.2 and 4.3. A total of eight 2D rigorous EM simulations are required that take a total of just under 12min to run and utilize negligible memory (~2.5Mb).

The agreement of the mk-mask model with the full 3D rigorous EM field simulation (r-mask) is spectacular. The image intensity contours at 30% of the clear field virtually overlap for both TE and TM light and the same is true for the aerial images at the cut-lines near the center and near the edge of the lines, as shown in Figure 4-13(b) and Figure 4-13(c). For comparison, the aerial image contours and at the same cut-lines of the original k-mask (unmatched CMTF) without adjustment is also shown on these plots.

Note that in this example there is virtually no cross-talk. The reasons for that will be obvious after the end of the next Chapter.

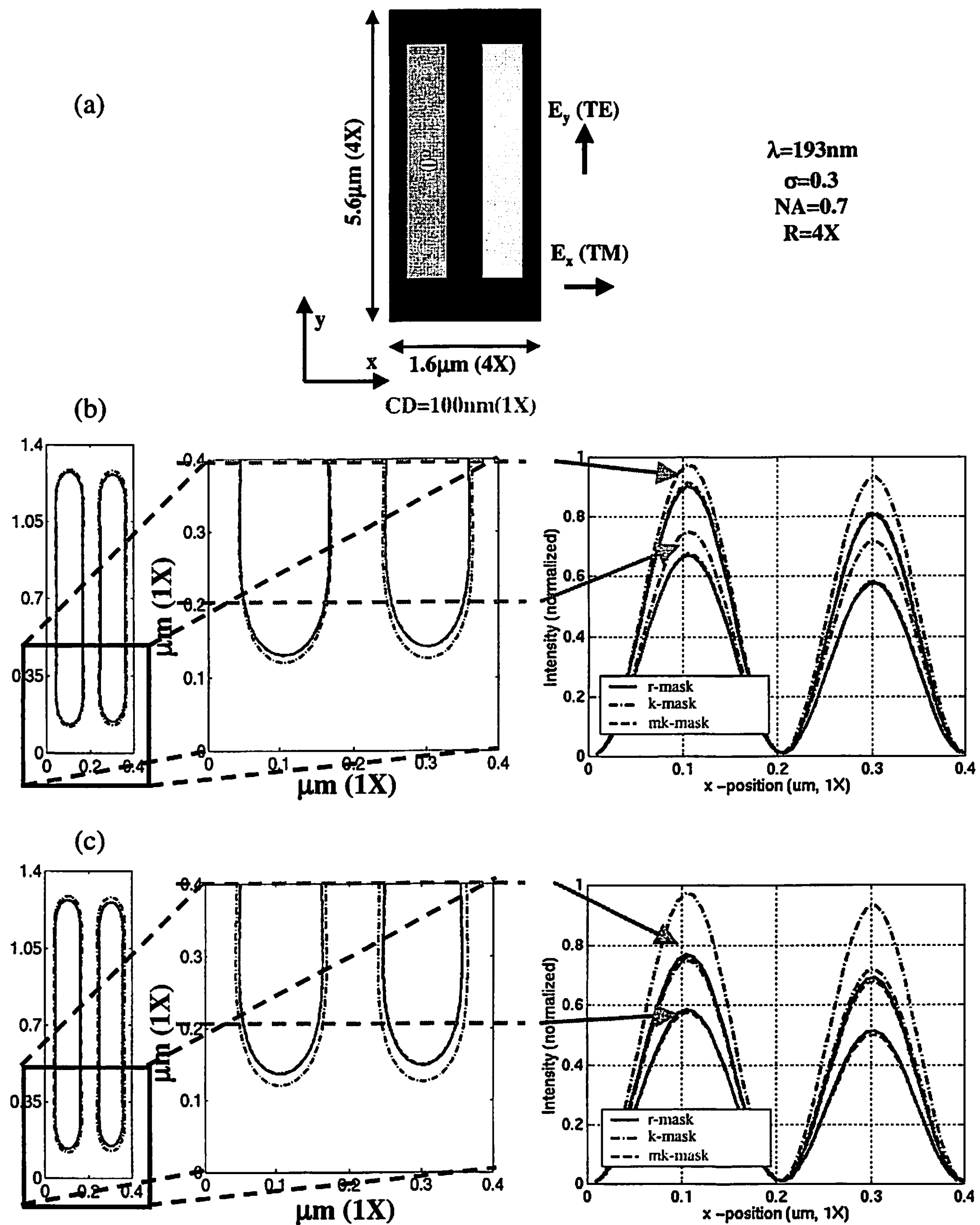

Figure 4-13. Example1: Simple dense line/space layout

(a) Mask layout, (b) aerial images under TE excitation and (c) aerial images under TM excitation. The 30% intensity contours are shown and the intensity profiles at the specified cut-lines.

4.3.2. Example 2: Semi-dense contact hole mask

Figure 4-14 depicts a 90°/270°, CD=150nm (1X), 1:1.5 semi-dense contact hole alt. PSM with 50nm of isotropic underetch. The calculation of the aerial image of this mask under completely unpolarized illumination, with λ=193nm, NA=0.7, σ=0.3 and R=4 requires again the rigorous EM field solutions under both TE and TM plane wave excitations. However, owing to the 90° rotational symmetry of this mask it suffices to run only one 3D simulation. Again, a discretization of the mask domain with 40 cells per λ was used and TEMPEST ran for approximately 55hrs on a single 550MHz processor in the Millennium cluster and used 1.82Gb of memory. A total of four 2D rigorous EM simulations are required by the qr-mask and mk-mask methods, that require a total of less than 8min to run and utilize approximately 3Mb of memory. The aerial images are compared with the one obtained using the conventional (unadjusted for edge-diffraction) k-mask model. Once more, the mk-mask model is able to capture accurately the edge-diffraction effects, since the image overlaps with the one obtained using the r-mask. The image with the k-mask model is seen to be vastly different. Cross-talk in this example is negligible.

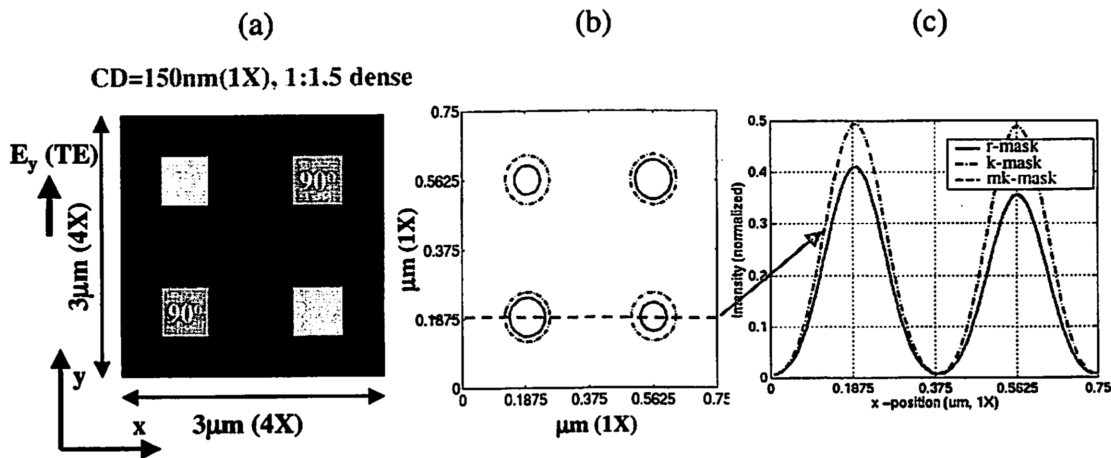

Figure 4-14. Example 2: Simple semi-dense contact hole layout

(a) Mask geometry of a 90°/270°, CD=150nm (1X), 1:1.5 semi-dense contact hole alt. PSM with 50nm of isotropic underetch. (b) Contours at 30% intensity of the aerial image under unpolarized light at λ=193nm, imaged with NA=0.7, σ=0.3 and R=4. Three images are compared, namely the one resulting from full 3D rigorous simulation (r-mask), the one from a conventional scalar simulation with the k-mask model and the one from with the mk-mask model of the qr-DDM. (c) The same three images as in (b) at the cut-line that runs through the center of the contact holes.

4.3.3. Speed-up factor of the qr-DDM and mk-mask methodology

In the examples presented, the speed-up factors of the qr-DDM and mk-mask methods were seen to be ~400. These speed-up factors would have been almost halved for a discretization of ~25 cells per λ at the expense of reduced accuracy. The speed-up factor S resulting from the quasi-rigorous domain decomposition method (qr-DDM) combined with the mk-mask model is proportional to the size of the 2D mask layout, the discretization chosen for the rigorous EM field simulations and inversely proportional to the number of rectangles that constitute the layout of the dark-field alt. PSM (mask density):

Equation 4-4.
$$S \propto \frac{a}{\lambda} \cdot \frac{d}{2N}$$

where α is the length of the 2D layout (let length=width), d is the number of cells per λ in the discretization of the mask domain and N is the number of rectangles that constitute the layout. The factor 2 enters because every rectangle requires two 2D simulations, according to the qr-DDM of Figure 4-12.

Although speed-up factors of ~400, while maintaining excellent accuracy, are quite impressive they are probably not sufficient for rapid aerial image simulations in an OPC environment, where the full-chip mask layout is broken up in *coherence windows*[1] and multiple small perturbations of the original mask layout within each coherence window should be evaluated in fractions of a second. To do this, another idea that is being used extensively in OPC software can be exploited, namely the idea of using *look-up tables* to further speed-up some calculations. To this end, a large variety of 1D features that spans the whole interval of mask feature sizes that need to be addressed can be pre-calculated, converted to the compact mk-mask model and stored. Every time that a certain feature size is encountered in the layout, instead of using the k-mask model, the mk-mask model is retrieved from the look-up table for an accurate aerial image evaluation, since the edge-diffraction effects are properly modeled with the mk-mask. If the task of creating the look-up table is completed, then the notion of a speed-up factor is irrelevant, since the whole

---

1. The notion of a coherence window can be found in [27]. It can be loosely defined as a mask fracturing, such that the image intensity at the center point of each fractured piece depends only on the layout within this piece. Proximity effects outside the coherence window can be safely neglected.

procedure is executed off-line and the speed is fixed - how fast the look-up table can be addressed. With mask feature sizes for every technology generation usually restricted within a relatively small set of values, the look-up tables are expected to be fairly easy to generate, compact and consequently the look-up time short.

A powerful alternative to the look-up table approach based on edge decomposition is presented in Chapter 6.

4.3.4. Accuracy issues

Two main concerns about the accuracy of the qr-DDM, and as a result the mk-mask model, can be identified: First, the corner effects are not modeled. Using the decomposition proposed in Figure 4-12, the solution for the scattered field below the mask is synthesized by two 2D simulations and as a result the electromagnetic interaction of light near the corners is not accurately modeled. Specifically, the more strict boundary conditions that the field components need to satisfy near the corners are effectively substituted by a pair of more relaxed boundary conditions that hold near the edges of the absorbing layer in the 2D simulations. Second, the qr-DDM effectively does not allow for any cross-mixing of energy between the components of the scattered field to happen. If the illuminating light is polarized in the x-direction, then, according to the proposed method in Figure 4-12, all scattered energy will be polarized in the x-direction also. The same is true for the y-polarization. However, cross-mixing of energy between field components is known to happen in real 3D masks and this cannot be modeled *via* the qr-DDM.

It may seem puzzling by the two examples presented earlier how an aerial image was achieved that was hardly distinguishable by the one obtained with the fully rigorous r-mask model, albeit the accuracy concerns raised above. The reason for this can be understood if one considers the spatial extent of any corner effects and the spatial frequencies in the energy that is coupled into polarizations other than the excited one. The spatial extent of corner effects is typically much less than the wavelength. Therefore, it only affects the highest diffraction orders, that in a typical imaging system do not contribute at all to the image formation. A similar argument holds for the energy cross-coupled into polarizations other than the excited one, as seen in Figure 4-15. The mask from the example presented

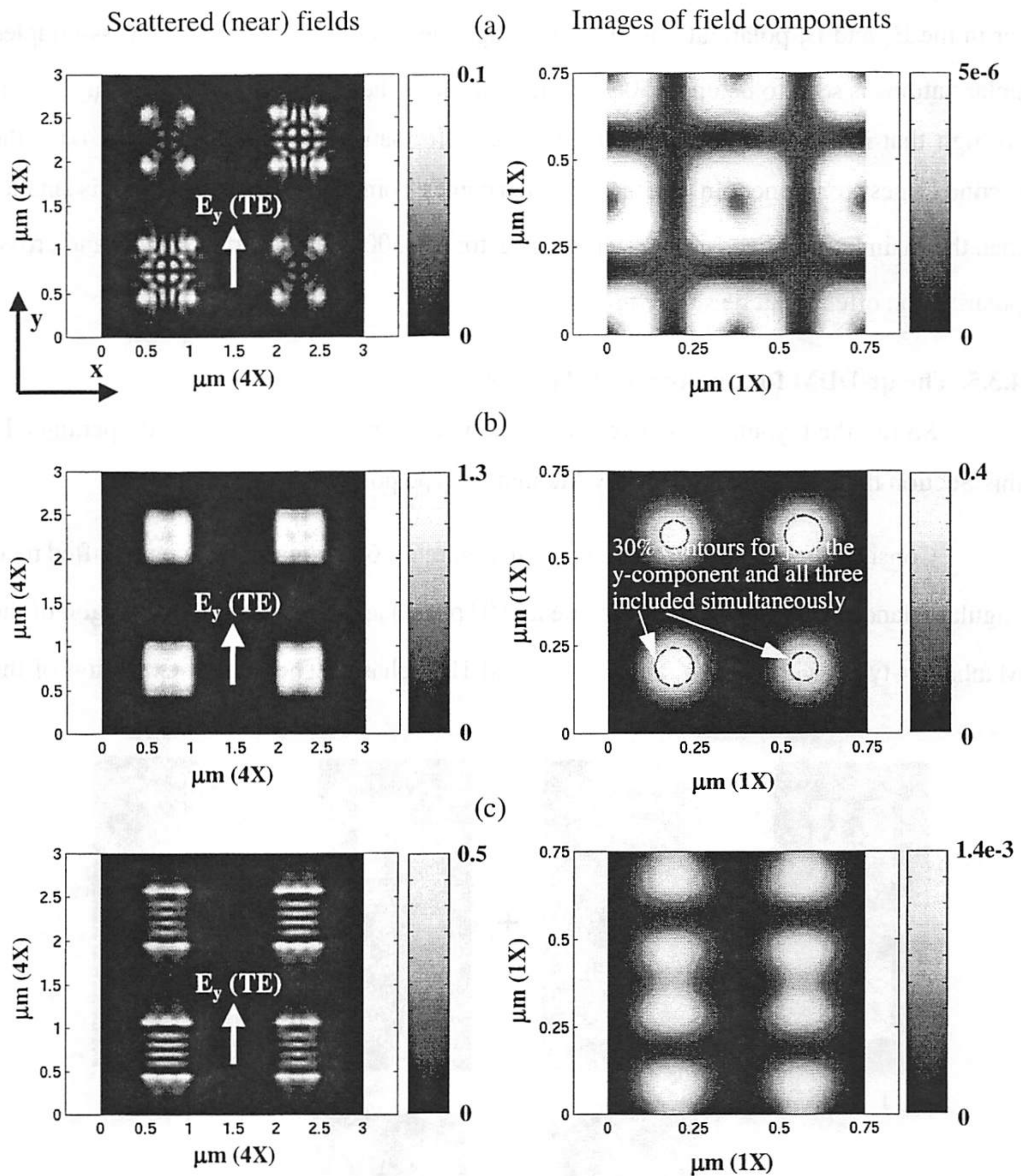

Figure 4-15. Ignoring the perpendicular polarizations

The example of Figure 4-14 is examined in more detail. The mask is illuminated with light polarized in the y-direction. Therefore most of the energy of the scattered near field is in the y-polarization, as seen from the graphs on the left. The non-negligible light in the x- and z- polarizations, due to cross-mixing, is seen to have a very high spatial frequency texture. This is exactly why, as seen at the plots on the right, the contribution of the x- and z- polarizations to the aerial image is negligible, at least by a factor of ~300 smaller. (a) Amplitude of E_x scattered field and contribution to the image, (b) and (c) the same for the E_y and E_z components respectively.

in Figure 4-14 is illuminated with an E_y polarization.However, some energy is seen to scatter in the E_x and E_z polarizations also. Although the local amplitude of the cross-coupled polarizations is seen to be up to 50% of the clear field, the spatial frequency of this light is so high that it does not contribute to the image formation. As seen in Figure 4-14, the second largest component in the image, which comes from the E_z-polarized light, is smaller than the main E_y-polarized component by a factor of ~300. Hence corner effects and cross-polarization effects can be safely neglected.

4.3.5. The qr-DDM for arbitrary 2D layouts

So far, the layouts considered were restricted to rectangularly shaped openings. In this Section the extension to arbitrary Manhattan-type polygons is developed.

Consider the example layout shown in Figure 4-16. It consists of two unshifted rectangular islands (with transmission of one and 0° phase) and a phase-shifted polygon of the Manhattan-type (with transmission of one and 180° phase). The natural extension of the

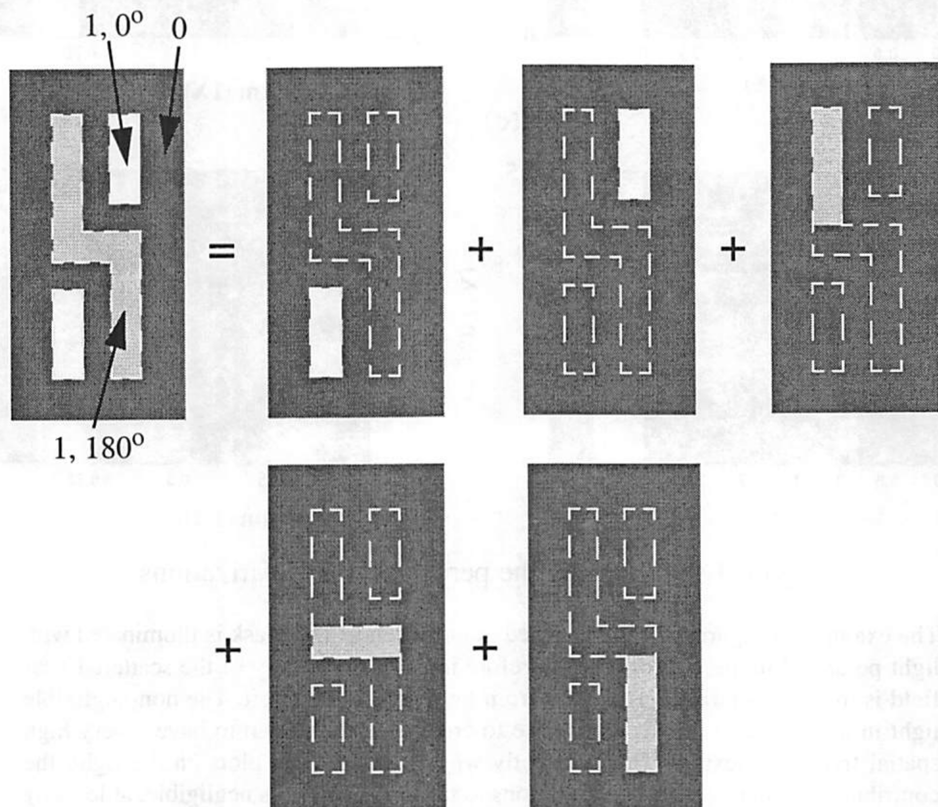

Figure 4-16. qr-DDM of a layout into mutually disjoint rectangles (MDR)

domain decomposition method shown in Figure 4-3 is the one depicted in Figure 4-16, where the layout is decomposed into a set of mutually disjoint rectangles. Note that such a decomposition is not unique. Next, the quasi-rigorous conjecture of Figure 4-12 is applied on each rectangular layout component. This DDM is referred to as the qr-DDM with MDR (mutually disjoint rectangles). Alternatively, instead of a decomposition of the phase-shifted polygon into mutually disjoint rectangles, a decomposition into the set of maximally overlapping rectangles (MOR) is performed as shown in Figure 4-17. The rectangular intersections of the maximally overlapping rectangles are subtracted accordingly, so that no region of the original polygon is counted more than once. Note that this decomposition algorithm is particularly attractive not only because of the uniqueness of the set of rectangles that compose the polygon and have maximum overlapping area, but primarily because no artificial discontinuities are introduced. Observe in Figure 4-16 that, because of the "stitching" that occurs where the MDRs meet, the scattered field solution in those locations will be considerably different than the true solution of the complete polygon. This

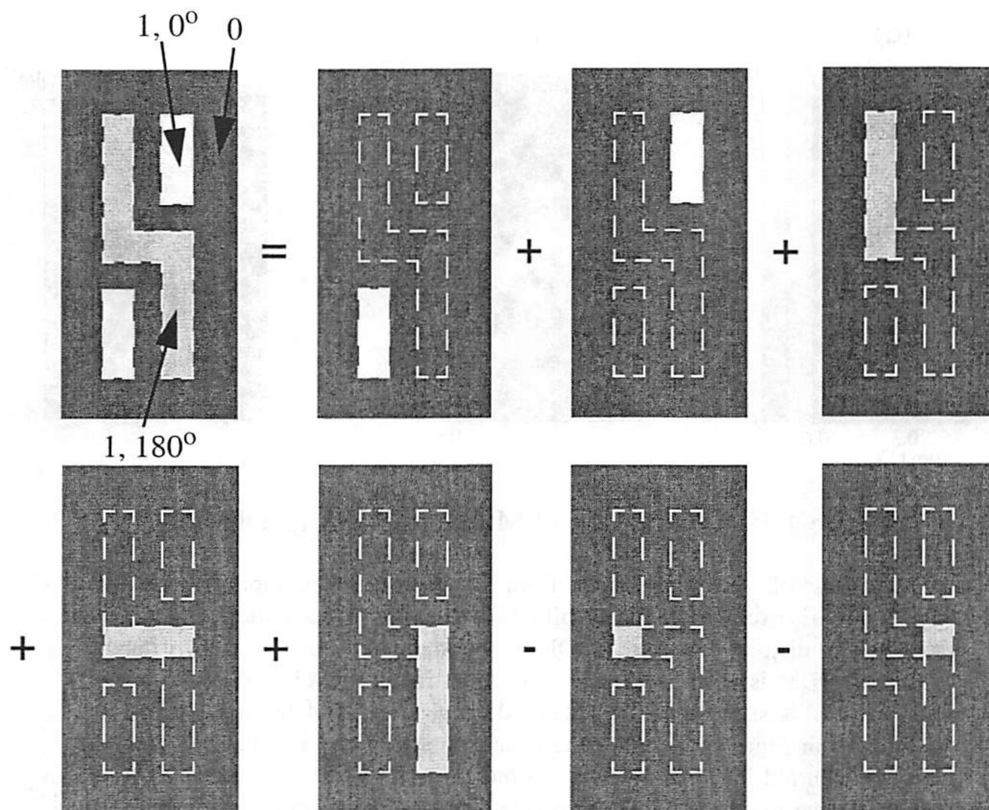

Figure 4-17. qr-DDM of a layout into maximally overlapping rectangles (MOR)

is not the case in Figure 4-17, where the addition of the MORs and the subsequent subtraction of their cross-sections is seen to remove all artificially introduced edges. Evidence of the validity of these arguments is given in Figure 4-18. The amplitude of the scattered E_y field as determined from a 3D rigorous solution of the complete layout under TE (E_y) excitation is shown in Figure 4-18(a). In (b) and (c) the amplitude of the errors of the scattered

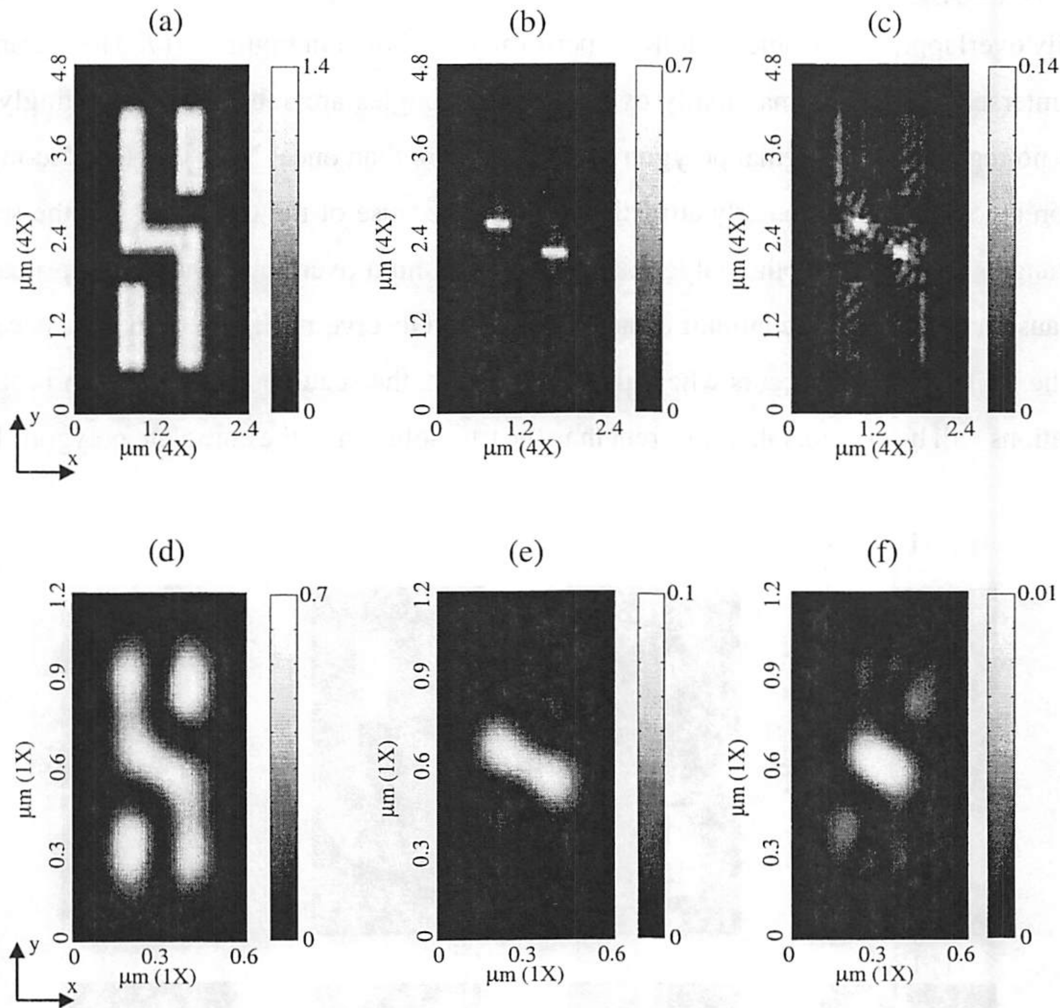

Figure 4-18. Comparison of MDR and MOR qr-DDM (1)

(a) Amplitude of scattered E_y field from 3D rigorous calculation of the whole mask (under E_y excitation). The amplitude of the error of the scattered E_y field, if the mutually disjoint rectangle (MDR) or the maximally overlapping rectangle (MOR) qr-DDM is used, is shown in (b) and (c) respectively. Observe that the MOR method is superior to the MDR. (d) Aerial image of the mask shown in Figure 4-16 or Figure 4-17 using the r-mask model from (a). The amplitude of the error incurred in the aerial image simulation, if MDR or MOR qr-DDM is used, is shown in (e) and (f) respectively. Note that error in (e) approaches an unacceptable 10% of the clear field whereas in (f) it peaks at 1%. Imaging system parameters used: λ=193nm, NA=0.7, σ=0.3 and R=4.

E_y field, if the MDR or MOR method of decomposition is used, is shown respectively. Observe the large error incurred near the "stitching" locations of the MDR method, which will lead to errors in the image simulation. On the other hand, the error of the MOR decomposition method is much smaller and concentrated locally near the "exterior" corners of the layout. Such corners are artificially constructed by the MOR method, as seen in Figure 4-17, and cannot therefore fully capture the true electromagnetic behavior of light. In spite of that, the spatially concentrated nature of the error implies that most of its energy is in the higher spatial frequencies that are discarded by the imaging system. Hence, they should not further contribute to errors in the imaging simulation. This is amply demonstrated in Figure 4-18 and Figure 4-19. The image of this layout if the r-mask model is used is shown in Figure 4-18(d) and the error of the MDR and MOR methods are shown in (e) and (f) respectively. The error level in the image is at an acceptable level of ~1% for the MOR method but it locally approaches ~10% for the MDR method. The images are further compared in Figure 4-19, where the 30% intensity contours are shown to virtually overlap for the r-mask and MOR method, but the contour of the MDR method differs.

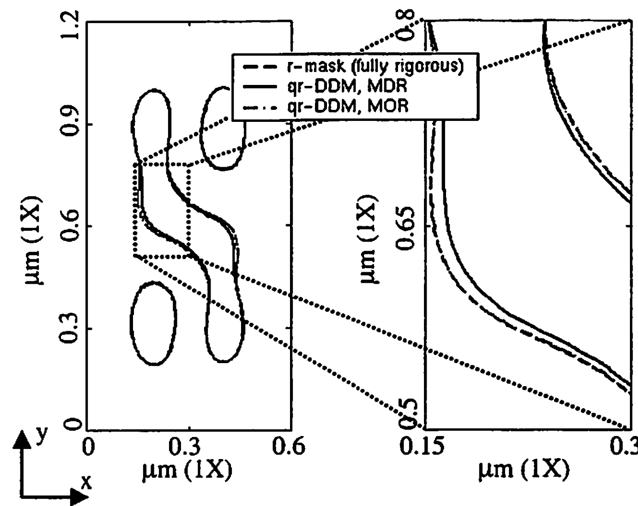

Figure 4-19. Comparison of MDR and MOR qr-DDM (2)

The 30% contours of the aerial images resulting from the fully rigorous r-mask and the qr-DDM methods shown in Figure 4-16 (MDR) and Figure 4-17 (MOR) are compared. Note the excellent agreement between the r-mask and the qr-mask with MOR within the enlarged snapshot. The image resulting from the mutually disjoint rectangle qr-DDM is seen to differ substantially.

4.3.6. Off-axis illumination

All simulation examples presented so far during the development of the domain decomposition methods involved normally incident light on the masks. This was because of the use of Hopkins' method for imaging, as described in Chapter 2. There is however nothing exceptional behind the use of normally incident light and the powerful decomposition techniques should be equally accurate for off-axis angles of incidence. In such an event, other imaging formulations, such as Abbe's, or a modified Hopkins' method that allows for the diffraction orders to depend on the angle of incidence, can incorporate similar decomposition methods that speed-up the imaging simulations without compromising the accuracy.

In the example of Figure 4-20 a $0^o/180^o$, 1:1 dense line/space alt. PSM with CD=400nm (4X) is illuminated by a plane wave that is traveling in air at ~49° off-normal and owing to refraction is entering the glass of the mask ($n_{glass}(\lambda=193nm)=1.563$) at ~$29^o$. Note that in a typical imaging system the incident waves on the mask rarely exceed 10°-15°. The r-mask simulation across the observation plane is compared with the qr-DDM of the mask into the two openings. The two curves are identical! Observe that the scattered fields are highly asymmetrical and mk-mask models should be adjusted accordingly. The

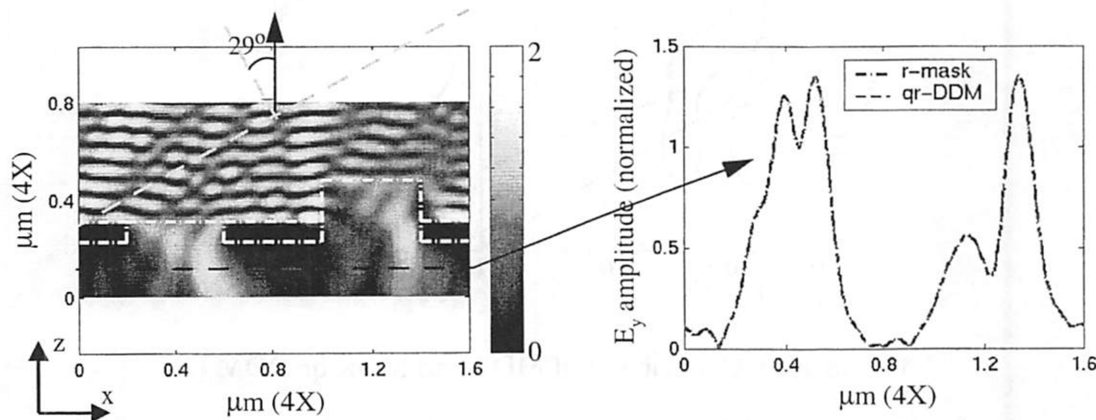

Figure 4-20. The qr-DDM under highly oblique illumination

The qr-DDM is seen to be accurate even for off-axis plane wave illumination at very large angles of incidence. A $0^o/180^o$, 1:1 dense line/space alt. PSM with CD=400nm (4X) is illuminated by a plane wave incident on the mask at θ_{air}~49° (θ_{glass}~29°). The amplitude of the scattered field along the observation plane is compared for the r-mask and the qr-DDM.

simple rect function mk-mask model will not perform adequately for such high angles of incidence.

4.4. Conclusions

Rigorous electromagnetic simulation of the role of the mask in the imaging process has so far been limited to 2D problems and relatively small periodic 3D problems. Although this capability is enough to tackle a variety of advanced photomask design issues, it is unquestionably restrictive. For example, rigorous simulation of a 10μm by 10μm area on an alt. PSM that contains random (non-periodic) structures, at λ=193nm, would require on the order of ~3.6Gb of memory (discretization of the ~14,000λ^3 domain with 20 cells per λ) and would run for many hours on a powerful CPU. Although the scalar theory can handle large mask domains, it has been discarded for advanced photomask technology simulations as being inaccurate.

In this Chapter, domain decomposition methods were developed that allow the division of a larger mask diffraction problem into a set of constituent parts, followed by the application of simple models for each constituent part that match the diffraction spectrum and subsequent synthesis of the original problem using these simplified models of the constituent parts. These methods originate from the linearity of the Kirchhoff-Fresnel diffraction integral. A 1D layout is decomposed into a set of single-opening masks and subsequently each single-opening mask is treated separately. Furthermore, a compact rect-function model for the diffracted near field of each opening is extracted, such that it matches the through-the-lens (TTL) spectrum of the rigorously calculated near field (r-mask). Application of the method in 2D layouts is based on Figure 4-12 and the conjecture that only 2D rigorous electromagnetic simulations will be used to synthesize diffraction from 3D structures. The spectral matching method is again used to simplify the r-mask models of each constituent 2D rigorous electromagnetic simulation. The excellent accuracy of the method applied in 2D layouts (3D diffracting structures) was attributed to the fact that errors arising from neglecting corner effects and cross-coupling of energy into light polarizations other that the excited one, are mapped at the extremities of the spectrum of propagating plane waves and do not contribute to the image formation. The decomposi-

tion of arbitrary 2D (Manhattan-type) layouts was shown to be accurate if it follows the rule of "maximally overlapping rectangles", whereas the decomposition into "mutually disjoint rectangles" is less accurate. Finally, it was shown that the decomposition method is valid even when off-axis illumination is used.

The excellent accuracy (better than 99% compared to the r-mask models) in the examples presented in this Chapter was accompanied by speed-up factors exceeding 200. It was stressed though that an off-line pre-calculation of the diffraction from various 2D geometries and creation of a look-up table of mk-mask models can further speed-up the calculations. The benefits of such accuracy-speed combinations can be reaped for example by model-based OPC software tools, that so far rely on the inaccurate scalar theory for aerial image calculations. Conceivably, accuracy on par with a rigorous 3D simulation becomes feasible for large - even full mask - areas.

The expansion of the domain decomposition methods of this Chapter to include the complex effects of energy cross-coupling between neighboring mask apertures is treated in the next Chapter and a different (more powerful) approach of domain decomposition based on edges is developed in Chapter 6.

5 Deep Phase-Well and Cross-Talk Effects in Alternating Phase-Shifting Masks

SIMULATION can give insight into the complex electromagnetic effects of edges and cross-talk between edges. In this Chapter the domain decomposition technique is expanded in order to isolate and quantify these phenomena.

In order to avoid confusion in the subsequent treatment the following nomenclature is adopted: Referring to the schematic diagram of an alt PSM in Figure 5-1, the glass-etched regions are the two *phase-wells*, namely the *"deep"* and the *"shallow"* phase-well, which always have an etched-depth difference that results in 180° phase-shifting of the EM field emanating from each opening. Each phase-well for a rectangularly shaped mask opening typically resembles a parallelepiped in three dimensions and as such it comprises of 6 *faces*. At the bottom face of each phase-well 4 *edges* and 4 *corners* form. Depending on the details of the actual mask fabrication process the edges and corners may be rounded, whereas the side-faces may be sloped (non-vertical). The two dimensional schematic of an

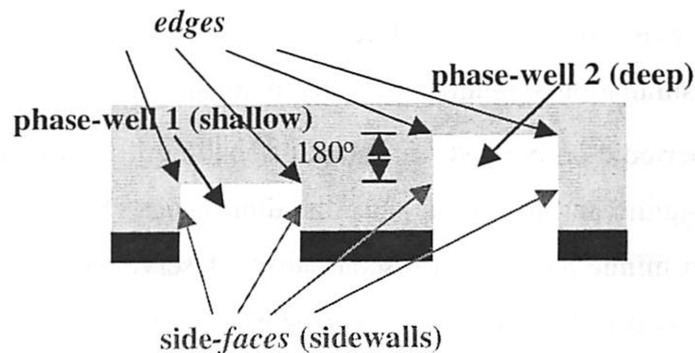

Figure 5-1. Schematic diagram of an alt. PSM

alt. PSM in Figure 5-1 shows only a cut-plane, hence the corners are not shown, the edges are depicted as corners and the faces are depicted as edges.

5.1. Towards a comprehensive model for cross-talk

Qualitative arguments that explain the cross-coupling of energy between neighboring openings in alternating phase-shifting masks have been proposed by other researchers in the past. Socha [84] suggested that the presence of induced currents on the absorbing layers of a mask (with non-zero imaginary part of the refractive index) results in a "shorting out" of the transmitted fields near the boundaries of each opening and consequently decreases the amount of light passing through the openings. Wong [106] observed the tendency of the electromagnetic field to concentrate in the higher refractive index glass, as opposed to the air regions, in the vicinity of an air/glass interface, such as the faces of phase-wells and attributed the differences in the transmission of light between the two adjacent openings (imbalance effect) in this behavior. Levenson *et al.* [50] recently proposed a novel design for alternating PSM. Among other things, it successfully addresses the issue of cross-coupling of energy between adjacent phase-wells. In the following Section, a new model for the representation and calculation of cross-talk is introduced.

5.2. Scattering off of a 90° air/glass discontinuity

Figure 5-2 depicts the rigorous EM field solution for the instantaneous field being established, when a 90° air/glass discontinuity is illuminated from the top by a linearly polarized, monochromatic and normally incident plane wave. The bottom-left part of the plot is the air region with refractive index n=1 and the remaining part, indicated by the dotted line, is the glass-filled region with refractive index n=1.563, at λ=193nm. Note the inherent with the simulation program periodicity along the x-axis, which unavoidably leads to simulating a periodic array of 90° air/glass discontinuities. However, this periodicity does not pose a significant limitation, since the dimensions chosen are sufficiently large compared to λ to mimic an isolated discontinuity. Observe from Figure 5-2(a) that the reduced phase velocity of light in glass causes the wave in the glass region to lag compared

to the wave in the air region, and also the fact that there exists a finite "dark" region to the left and to the right of the air/glass interface, in agreement with Wong's findings [106].

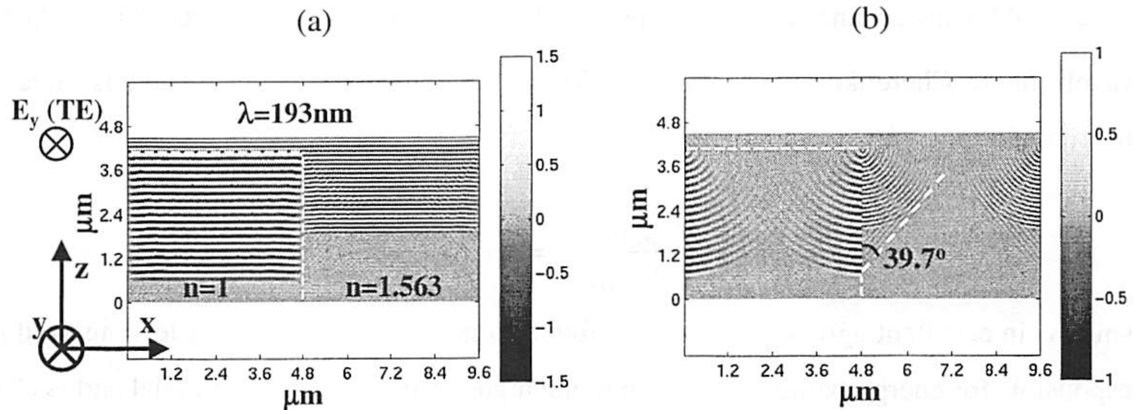

Figure 5-2. Scattering off of a 90° air/glass discontinuity

(a) Instantaneous EM field being established when a 90° air/glass discontinuity is illuminated from the top by a normally incident TE plane wave at λ=193nm, (b) the instantaneous scattered field (at the same instant as (a)) because of the 90° corner.

In order to gain more insight on the effect of the corner itself, the instantaneous field (at the same instant!) of a glass/air interface with no discontinuity along the x-axis was subtracted from the left-half of the original solution and the instantaneous field of a uniform plane wave travelling in glass was subtracted from the right-half of the original solution. The result of this process is the strange looking plot of the scattered field from the corner, depicted in Figure 5-2(b). There are two interesting observations to be made on this plot: First, a 90° corner at an air/glass interface results in a scattered wave that is cylindrical in nature with a non-uniform radiation pattern, where most of the energy is directed in the forward direction (direction of the incident field). Second, inside the glass at the right side of the air/glass interface, but below the location that the instantaneous incident field has had time to propagate there exists a region of non-zero scattered field. Clearly, the source of this field cannot be the corner discontinuity itself, since the scattered field from the corner has not had time to directly propagate in glass to that point. In order to satisfy the boundary conditions of Maxwell's equations everywhere along the vertical interface, a non-zero field should exist in the glass side, although there is no time for either the incident or the scattered field to reach that location. In a way, the "speedier" field on the air side is

depositing elementary Huygens' spherical sources [37] that radiate into the glass side. Since the velocity by which these Huygens' sources are deposited is faster than the phase velocity of the disturbance that they cause inside the glass region, the end result is a "shock wavefront" of Cherenkov radiation[1] [47]. The angle by which this plane wave is tilted is theoretically given by:

$$\phi = arc\sin\left(\frac{v_{p,\,glass}}{v_{p,\,air}}\right) = arc\sin\left(\frac{n_{air}}{n_{glass}}\right) = 39.78^o$$

which is in excellent agreement with that found from our simulation. This leaking field is responsible for energy being "sucked" into the higher refractive index material and is also interfering with the cylindrical scattered field from the corner at the glass side to produce the ripples present in the plot of Figure 5-2(b). Yet another way to explain this field behavior has its origin in the phenomenon of total internal reflection [7]. Total internal reflection results when an EM field that is traveling inside a higher refractive index material (in this case glass with n=1.563) impinges at an oblique enough angle on the interface with a lower refractive index material (in this case air with n=1). The boundary conditions along the interface impose this bizarre behavior, where no energy is reflected backwards in the optically denser (higher refractive index) medium and all the energy is "trapped" in the form of surface waves travelling along the material interface [7]. In the case of the scattering off of the 90° air/glass discontinuity this phenomenon is observed in reverse, whereby the normally incident plane wave along the air/glass interface oriented in the z-axis plays the role of the surface wave, which causes the field on the glass side to take off at an angle equal to the critical angle. Sure enough the critical angle in this case is 39.78^o.

Next, the model for cross-talk between phase-wells is developed.

5.3. Modeling the cross-talk between phase-wells

The wave behavior at the air/glass discontinuities (faces, edges and corners) of the etched phase-wells of alt. PSMs suggests the model for cross-talk that is depicted in

---

1. Strictly speaking, Cherenkov radiation involves relativistic motion of elementary particles. Nevertheless, the physical phenomenon that is observed here follows the same principle.

Figure 5-3. Figure 5-3(a) shows the geometry of a deep-trench alt. PSM with a dense line/space pattern. The incident illumination causes all edges (corners in the 2D schematic diagram) present to scatter a non-uniform in angle, cylindrical radiation pattern, in a way similar to the result of the previous paragraph. Using a geometric ray tracing approach[1] and considering the reflection and transmission coefficients at all interfaces present (glass/air, air/glass, glass/absorption layer) one can identify "favorable angles" in the radiation pattern of the edges that do not contribute to cross-talk, shown in Figure 5-3(b) and also "unfavorable angles" that contribute to cross-talk, such as those shown in Figure 5-3(c) and (d). Note that, according to this model and the development that follows, *the edges at the*

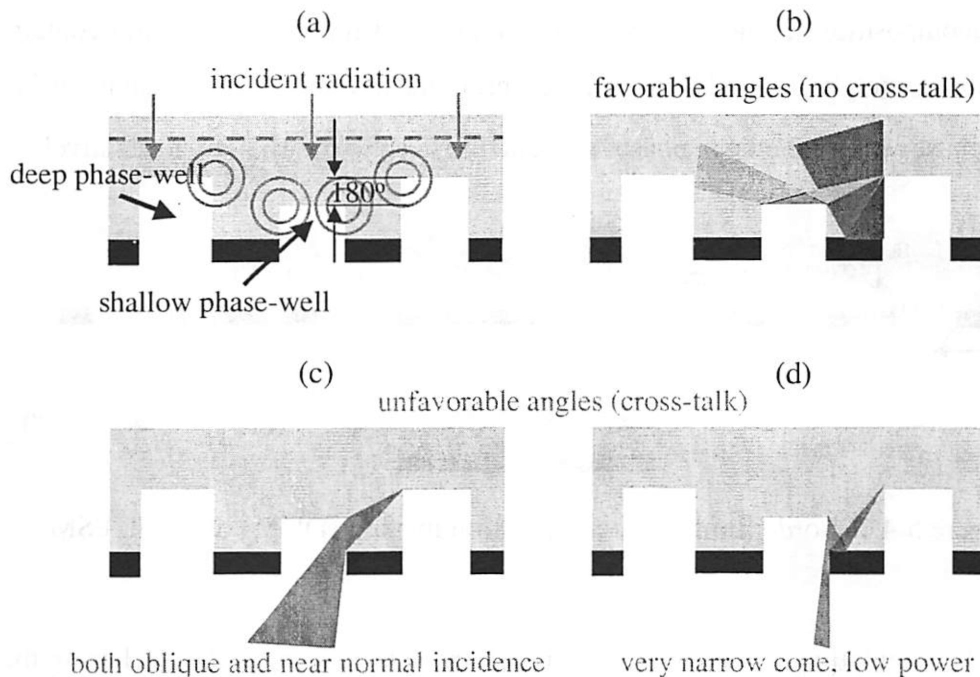

Figure 5-3. A comprehensive model for cross-talk

(a) Geometry of a deep-trench alt. PSM with a dense line/space pattern. All edges at the bottom of the phase-wells scatter radiation non-uniformly in all angles. (b) Cones of scattered radiation that do not contribute to cross-talk, because scattered light is reflected backwards or at highly oblique angles. (c) "Direct" cone of scattered light - cross-coupled light exits at a wide range of spatial frequencies. (d) "Reflected" cone of scattered light - cross-coupled light exits mostly at near-normal incidence.

1. The dimensions of the problem are on the order of a wavelength. The geometric optics approach is not accurate in this regime, but it is nevertheless invoked to offer a qualitative explanation of the argument.

bottom of the phase wells are identified as the primary contributors to cross-talk and neither the faces, nor the corners play a significant role in this effect. This proposition is quite different from the prevailing ideas that the faces of the phase-wells play the most significant role in cross-talk and that the corners and the edges are also equally important. This model will be validated from its successful application in predicting and calculating cross-talk in a wide range of situations.

5.4. 1st order domain decomposition method of alt. PSM

The zero-order domain decomposition of alt. PSMs presented in the previous Chapter is revised in order to include the cross-talk between adjacent phase-wells. This (first order) decomposition method is depicted in Figure 5-4 for 1D layouts and contains two extra terms, namely CT_{12} and CT_{21}, that represent the amount of energy coupled from the shallow phase-well to the deep phase-well and the deep to the shallow respectively.

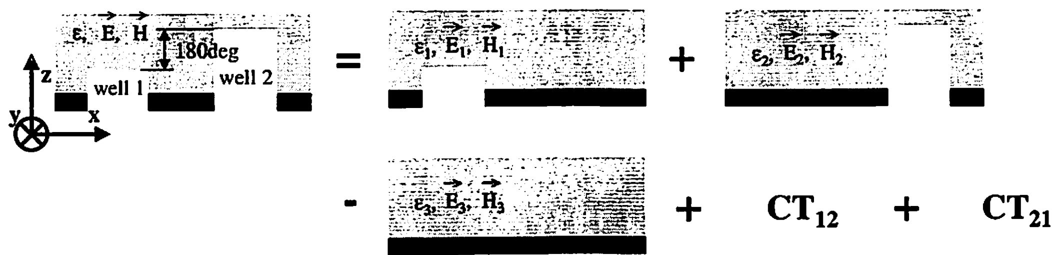

Figure 5-4. 1st-order domain decomposition method (DDM) of an alt. PSM

The calculation of the cross-terms CT_{12} and CT_{21} can be performed using the simulation experiment that is pictorially depicted in Figure 5-5. In order to determine the portion of scattered light from the edges of the shallow phase-well that goes through the opening of the deep phase-well, one proceeds as depicted in Figure 5-5(a): First, a simulation is run, in which the opening of the shallow phase-well is shut with the absorption layer but the phase-well itself is left intact. Then, from the resulting transmitted EM field across the observation plane of this geometry, the EM field solution coming from a simulation in which only the single opening of the deep phase-well is present is subtracted. Finally, the two remaining simulations shown in Figure 5-5(a) have to be run and the transmitted EM fields need to be subtracted/added, owing to the finite residual transmission of the absorp-

tion layer. Similar simulation steps are followed in order to calculate CT_{21}. The cross-terms CT_{12} and CT_{21} can be viewed as perturbation terms necessary to restore the accuracy of the zero-order DDM, since for openings that are spaced far apart these terms are seen to converge to zero. The total number of two dimensional simulations needed in the first-order decomposition is four instead of two for the zero-order decomposition (because of cancellation of terms), so the expected increased accuracy of this decomposition costs a doubling of required simulation time.

Two specifically chosen examples of the first order decomposition are presented in a parallel fashion next and they demonstrate both the accuracy of the method and also resolve the misconception that cross-talk in alt. PSMs always leads to poorer aerial images with larger imbalance between the adjacent phase-shifted openings.

A 1:1 dense line/space geometry with a mask CD of 400nm is patterned on a deep-trench $180^o/360^o$ alternating PSM in two ways: The first mask has no undercut and perfectly vertical sidewalls (faces) and the second mask has 50nm undercut and sloped faces

(a)

CT_{12} =

(b)

CT_{21} =

Figure 5-5. Calculation of the cross-terms:

(a) CT_{12} represents the portion of scattered light from the corners of the shallow phase-well that goes through the opening of the deep phase-well and **(b)** CT_{21} represents the portion of scattered light from the corners of the deep phase-well that goes through the opening of the shallow phase-well

as shown in Figure 5-6. Both masks are illuminated by a normally incident (travelling along the z-axis) plane wave that is TE linearly polarized (E field // y-axis) with λ=193nm. The cross-talk terms CT_{12} and CT_{21} for each mask are calculated according to Figure 5-5 and their amplitudes are plotted in Figure 5-6(a) and (b). Next, the near diffracted fields from each mask along the observation plane are calculated in three ways: First, by simulating the complete mask structure with both openings present (r-mask), then by decomposing the mask using the zero-order domain decomposition method (Figure 4-6) and finally using the first-order domain decomposition that models cross-talk. The amplitude of these near diffracted fields is plotted in Figure 5-6(c) and (d) and the error of both decomposition methods is plotted in Figure 5-7. Clearly, in this situation, ignoring the cross-coupled energy in the domain decomposition would be erroneous. The agreement of the first-order decomposition with the solution from the exact geometry is spectacular. The amplitude of the error is everywhere less than 2% of the clear-field value (which is 1), instead of as much as ~30%! The normalized mean square error[1] (NMSE) for vertical sidewalls drops to 3.9E-4 from 1.5E-2 when cross-talk is included. For the sloped sidewalls alt. PSM it also drops from 3.2E-3 to 2.4E-4. A key observation at the plots of Figure 5-6(c) and (d) is the fact that cross-talk in the case of the vertical sidewalls PSM is pushing the peak of the electric field emanating from the shallow phase-well to a lower value than had cross-talk been negligible, whereas the opposite happens in the case of the PSM with sloped sidewalls, where the peak value of the shallow phase-well increases. The result of this is that in the first case cross-talk is helping balance the aerial image, whereas in the second case it negatively affects the balance, as shown in Figure 5-8 for an imaging system with NA=0.7, σ=0.3 and R=4 at best focus. From these graphs it is also apparent that neglecting cross-talk leads to inaccurate calculation of the aerial images. The peak intensity % error of each lobe and the edge position error for a simple threshold resist model at 30% intensity are indicated on the plots. Note the excellent agreement in the aerial images after the inclusion of the cross-talk terms, where the images virtually overlap.

---

1. The normalized mean square error is defined by: $NMSE = \int |E_r - E_s|^2 dS / \int |E_r|^2 dS$, where E_r is the "true" field resulting from a rigorous simulation of the complete mask geometry and E_s is the synthesized field *via* the 1st-order-DDM.

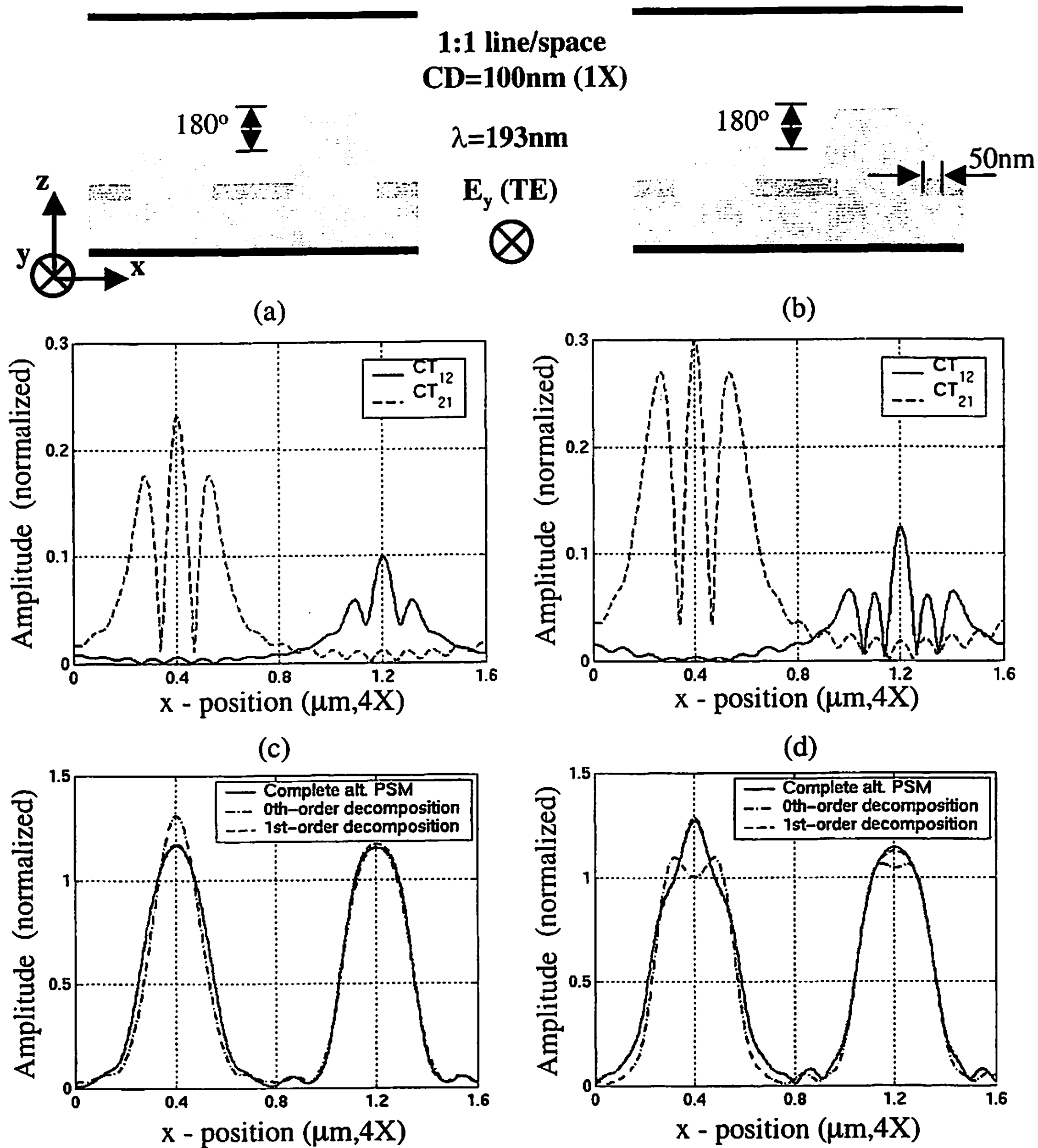

Figure 5-6. Examples of 1st-order domain decomposition method: 1:1 dense line/ space pattern, CD=400nm (4X), 180°/360°, λ=193nm, two different sidewall profiles are considered

Normalized amplitude of CT_{12} and CT_{21} for vertical (a) and sloped (b) sidewall profile. Comparison of the three simulation approaches: Complete alt. PSM simulation (no decomposition, r-mask), 0th-order and 1st-order decomposition for vertical (c) and sloped (d) sidewall profile.

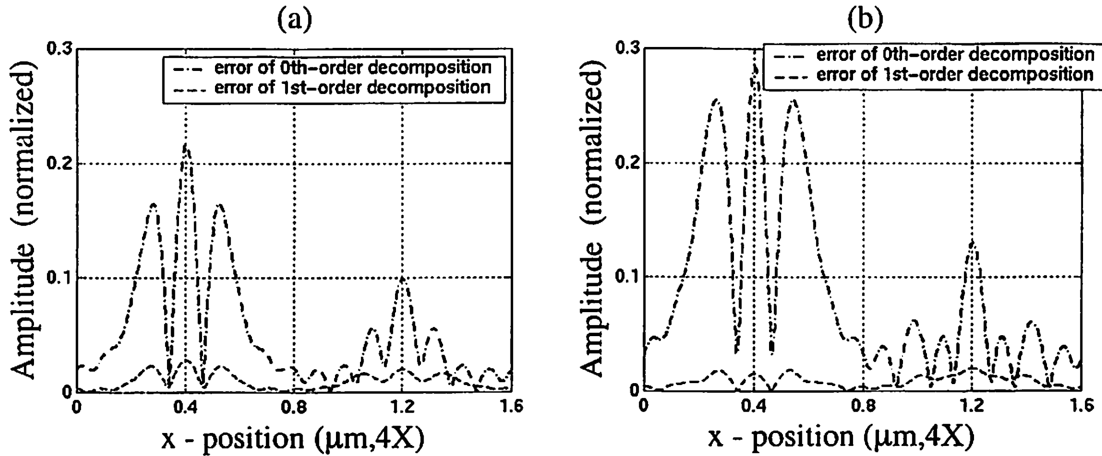

Figure 5-7. Errors of the 0th- and 1st-order decompositions for the examples of Figure 5-6

Normalized amplitude of errors for vertical (a) and sloped (b) sidewall profiles.

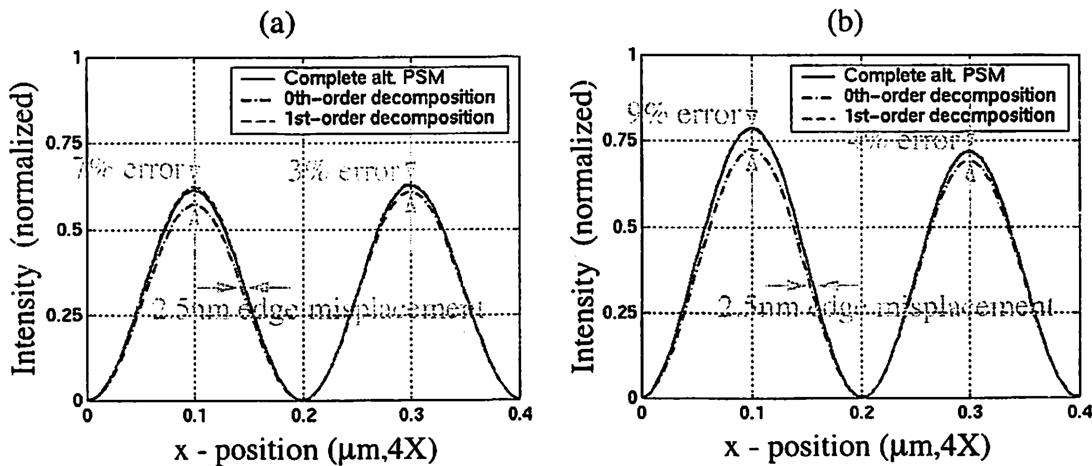

Figure 5-8. Aerial images for the alt. PSMs of Figure 5-6

System parameters: NA=0.7, σ=0.3, R=4, best focus. Normalized image intensity for vertical (a) and sloped (b) sidewall profiles. Again, the three simulation approaches are compared: Complete alt. PSM simulation (no decomposition, r-mask), 0th-order and 1st-order decomposition.

5.5. Cross-talk dependence on the geometrical characteristics of the alt. PSM

Using the above model, a systematic evaluation of the dependence of cross-talk on the geometrical details of the alt. PSM is performed. Although only the results for the terms CT_{12} and CT_{21} are presented, in each case the complete alt. PSM geometry was simulated

separately and the true transmitted field (r-mask) was compared with the field obtained through the first-order decomposition. The local error incurred was never larger than 2% of the clear field value.

Figure 5-9 shows the cross-talk of four possible alt. PSM technologies, namely 0°/180°, 90°/270°, 180°/360° and 270°/450°, with vertical sidewalls under TE illumination[1].

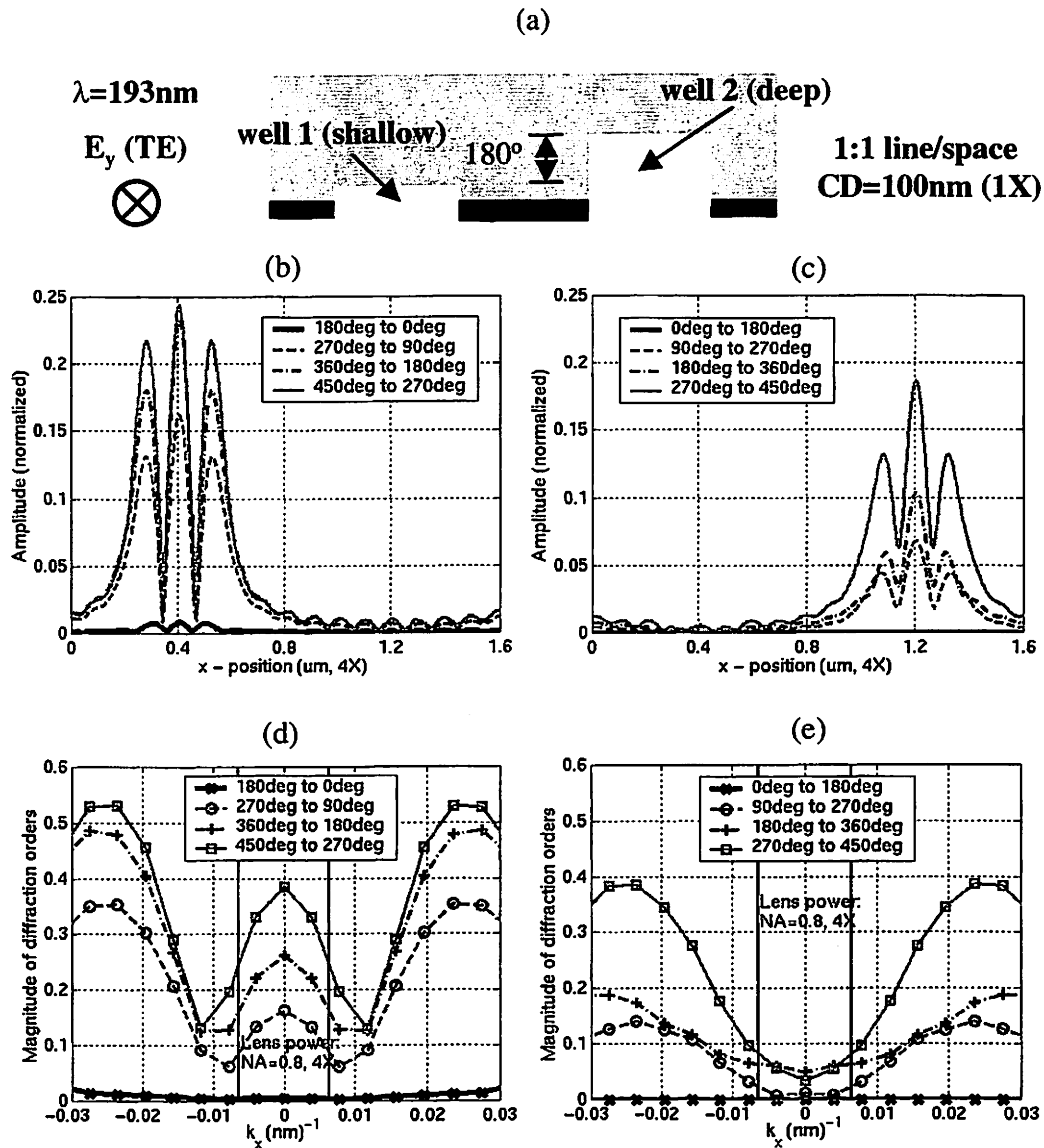

Figure 5-9. Dependence of cross-coupling on phase-well depth

(a) Geometry, (b), (c) normalized amplitude of cross-talk terms CT_{21} and CT_{12} for 0°/180°, 90°/270°, 180/°360° and 270°/450° alt. PSMs, (d), (e) normalized magnitude of CT_{21} and CT_{12}.

Both the near field correction (cross-talk) terms CT_{12} and CT_{21} are shown along with their respective spectra in each case. It is worth to note that the deeper phase-well is contributing more cross-talk to the shallower (*i.e.* $CT_{21}>CT_{12}$) in every technology and that the cross-talk increases for deeper phase-well technologies. Both these results are intuitively satisfactory, since according to the physical understanding of cross-talk based on Figure 5-3 the edges at the bottom of deeper phase-wells are located at more advantageous positions to throw their scattered light into the adjacent shallower phase-wells. Observe also from the spectra plots that most of the cross-talk energy is in specular directions and does not go through the optical system. This can be further quantified by considering the normalized total cross-talk energy and normalized *through-the-lens* (TTL) cross-talk energy, defined by Equation 5-1 and Equation 5-2:

Equation 5-1.
$$S_{CT-total} = \frac{\int_{|\vec{k}| \le k_0} CT^2(k_x, k_y)dk_x dk_y}{\int_{|\vec{k}| \le k_0} E^2(k_x, k_y)dk_x dk_y}$$

Equation 5-2.
$$S_{CT-TTL} = \frac{\int_{|\vec{k}| \le k_{BW}} CT^2(k_x, k_y)dk_x dk_y}{\int_{|\vec{k}| \le k_{BW}} E^2(k_x, k_y)dk_x dk_y}$$

The bar charts of Figure 5-10 show the percentage of total and through-the-lens (TTL) cross-talk energy for the 0°/180°, 90°/270°, 180°/360° and 270°/450° technologies. The lower portion of each bar (blue color) corresponds to the cross-talk energy from the shallow to the deep phase-well and the upper portion (red-brown color) to the cross-talk energy from the deep to the shallow phase-well. Observe that indeed the through-the-lens portion of cross-talk energy in approximately one order of magnitude smaller than the total cross-talk energy, which indicates that most of the cross-talk energy is directed in highly oblique angles and is lost in the sidewalls of the projector column.

1. TM excitation causes similar cross-talk profiles with slightly reduced peak values.

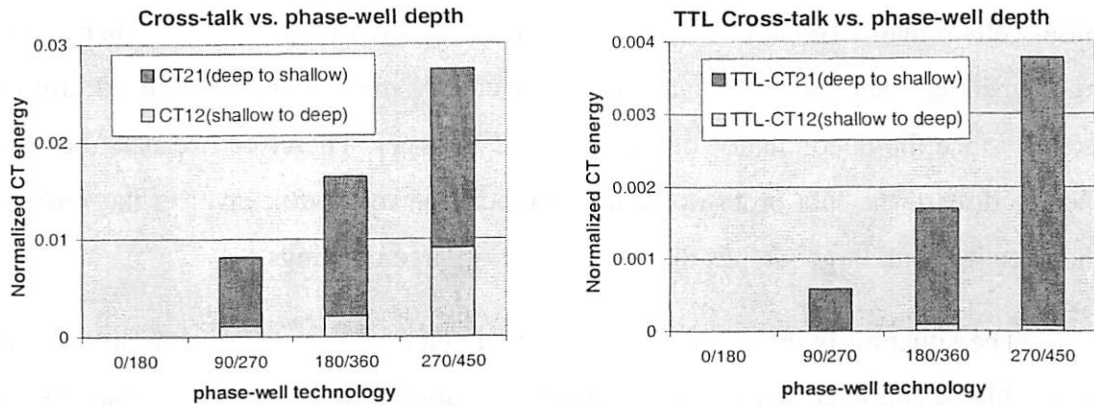

Figure 5-10. Cross-talk energy dependence on phase-well depth

Next, it is important to determine the dependence of cross-talk on pitch (period), since the present model points out that cross-talk should be insignificant when the lateral separation of adjacent phase-wells is relatively large, in which case the simpler zero-order decomposition method will suffice for the simulation of mask layouts. Figure 5-11 depicts the total and through-the-lens normalized cross-talk energy for a $180^{o}/360^{o}$ alt. PSM with a fixed line of CD=100nm (1X) and variable pitch. Three values of pitch are shown, namely 200nm, 250nm and 400nm, which correspond to 1:1 dense line/space, 1:1.5 semi-dense line/space and 1:3 sparse line/space patterns. The key result is that indeed the TTL cross-talk drops quickly with increasing pitch. This is however an artifact of the normalization. The larger pitches are a result of larger openings (spaces). On one hand the abso-

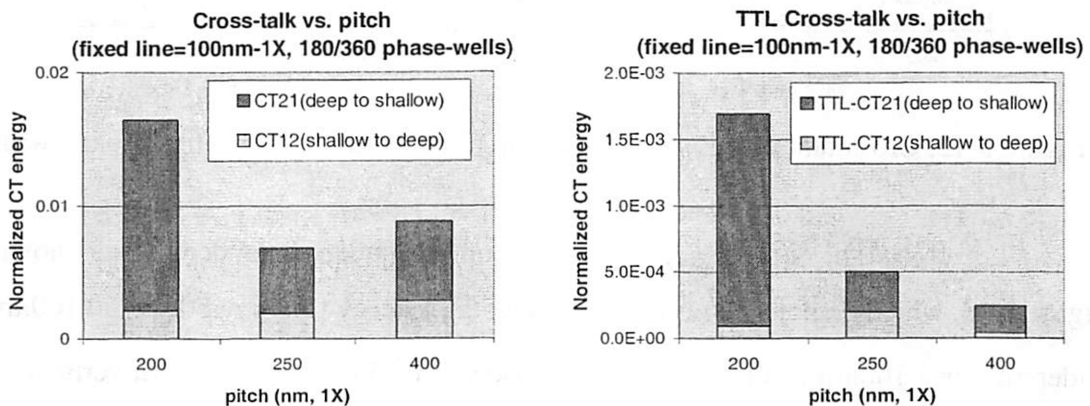

Figure 5-11. Cross-talk energy dependence on pitch (mask period) - fixed line-width

lute amount of cross-talk does not drop, since the relative position of edges of adjacent phase-wells remains constant - although the period increases, but on the other hand the larger openings increase the total transmitted energy making the normalized cross-talk smaller, since the denominator of Equation 5-2 is larger. Therefore one must be careful when to discard the first-order domain decomposition method in favor of the zero-order when dealing with large pitches that are a result of large openings.

The situation is different when the larger pitch is a result of increasing the line-width while keeping the space-widths (openings) constant. In that case the relative separation of edges of adjacent phase-wells increases, the unfavorable light paths that cause cross-talk according to the model of Figure 5-3 are less and as a result the absolute amount of cross-talk energy quickly drops. This is evident by the bar charts of Figure 5-12 that show the total and through-the-lens normalized cross-talk energy for a 180°/360° alt. PSM with fixed space-widths of CD=100nm (1X) and variable pitch. Again, three values of pitch are shown, namely 200nm, 250nm and 400nm, which correspond to 1:1 dense line/space, 1.5:1 semi-dense line/space and 3:1 sparse line/space patterns.

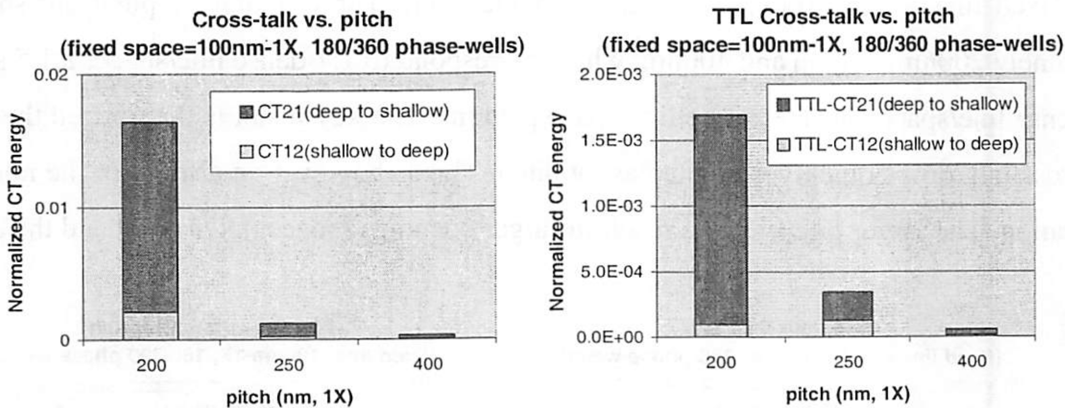

Figure 5-12. Cross-talk energy dependence on pitch (mask period) - fixed space-width

The cross-talk dependence on the amount of undercut (underetch) is shown in Figure 5-13, which depicts the normalized cross-talk energy for 0nm, 50nm and 100nm of undercut, for a 100nm (1X) 1:1 dense line/space, 180°/360° alt. PSM with vertical side-walls. Again, in order to explain the drop of cross-coupled energy with increasing undercut, the model of Figure 5-3 can be recalled, according to which the increased undercut pulls

the faces of the phase-wells behind the opening in the absorber layer and consequently cancels some of the light-paths that contribute to cross-talk.

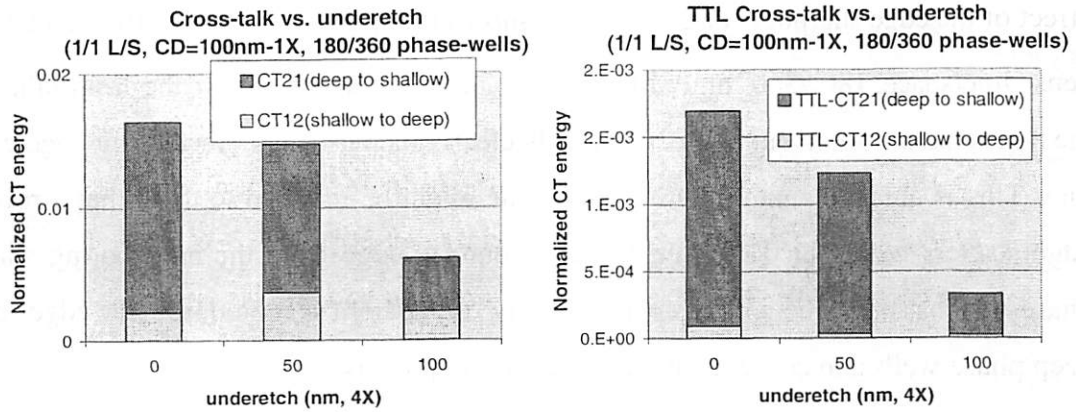

Figure 5-13. Cross-talk energy dependence on undercut

Figure 5-14 depicts the cross-talk dependence on the sidewall angle of the faces of phase-wells. The 100nm (1X) 1:1 dense line/space, $180^{\circ}/360^{\circ}$ alt. PSM example is chosen again to demonstrate the effect. The three bars on each chart correspond to 90° vertical sidewalls, ~80° sidewalls (labeled "tilted") and ~70° sidewalls (labeled "more tilted"). The behavior is now somewhat erratic, with the cross-talk energy appearing unchanged for slopes up to ~80° and then spiking up for larger sidewall angles. Since the integrity of the sidewalls in the alt. PSM fabrication process is typically good and very close to 90°, cross-talk changes are insignificant for such small sidewall slopes.

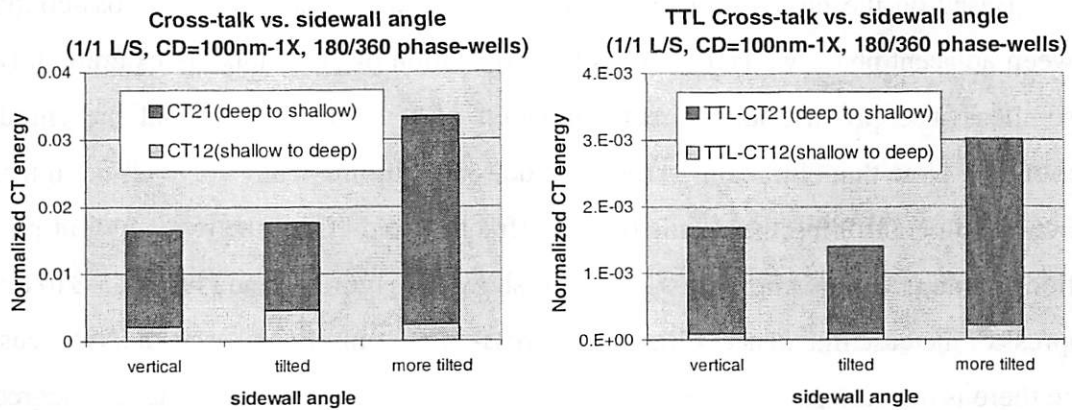

Figure 5-14. Cross-talk energy dependence phase-well profile (sidewall angle)

Finally, owing to the etching process in fabricating an alt. PSM sometimes the edges at the bottom of the phase-wells are not perfectly sharp, but they are rounded. The effect of the edge sharpness on cross-talk is shown in Figure 5-15, for the 100nm (1X), 1:1 dense line/space, $180^{o}/360^{o}$ alt PSM. The bar labeled "rounded" shows the cross-talk when the edges have a 50nm curvature. Cross-talk clearly increases with increasing edge curvature. This is almost counterintuitive, since one might be inclined to think that a rounded edge scatters less light. However, the also rounded edge from the neighboring shallow phase-well has now a better "acceptance ability" of the light scattered from the edges of the deep phase-wells and consequently more cross-coupling occurs.

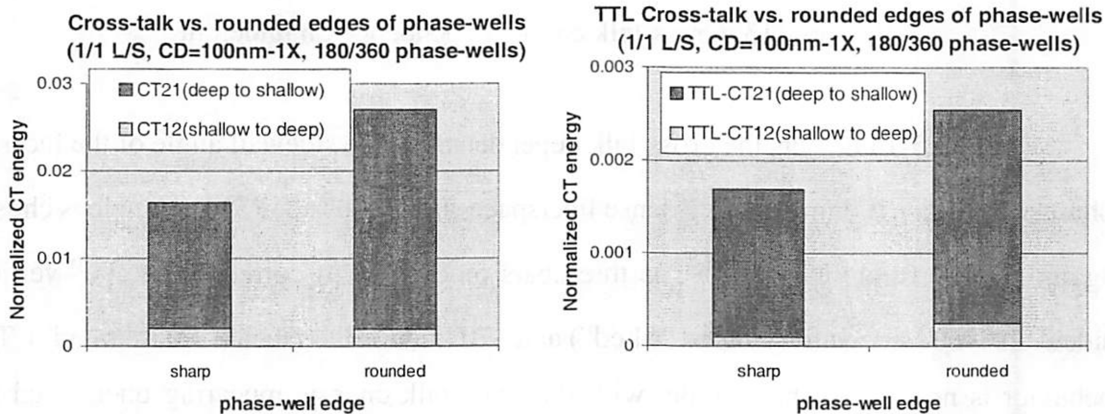

Figure 5-15. Cross-talk energy dependence phase-well profile (rounded edges)

5.6. Ideas for cross-talk elimination

Based on the physical understanding developed for the origin of cross-coupling between adjacent phase-wells, two ideas for elimination of cross-talk are examined. Both these ideas also provide an indirect validation of the cross-talk model presented in Section 5.4. Note that eliminating cross-talk does not automatically solve all the intrinsic difficulties in controlling the details of the diffracted fields from the two adjacent phase-shifted openings. For example, cross-talk was shown in Figure 5-6 and Figure 5-8 to either suppress or increase imbalance. Eliminating cross-talk definitely makes the analysis easier, since there is one less parameter to worry about, but at the same time a potential degree of freedom for engineering the diffracted fields is lost.

Covering the faces (sidewalls) of phase-wells with the absorbing layer blocks both the direct light paths of Figure 5-3(c) and the reflected light paths (reflected from the back side of the absorbing layer) of Figure 5-3(d) and should consequently completely eliminate cross-talk. This is demonstrated in Figure 5-16 that depicts the amplitude of the cross-talk terms for a 100nm (1X), 1:1 dense line/space, 180°/360°, vertical faces alt. PSM before and after covering the faces with a 50nm Cr-layer. After covering the sidewalls cross-talk drops to insignificant levels of less than 2%. This idea was implemented by Levenson *et al.* [50] as a means of controlling the imbalance and improving the performance of alt. PSMs for a wide range of pitches (periods).

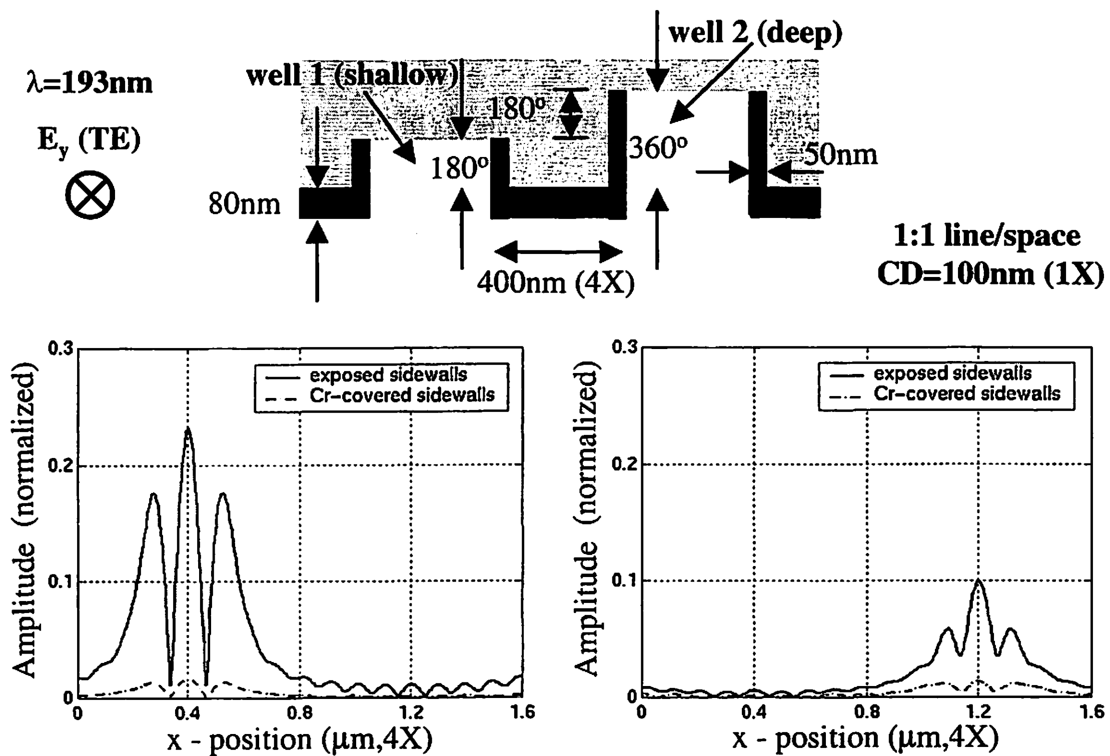

Figure 5-16. Cross-talk elimination through the use of "blinders"

The sidewalls are covered with a 50nm thick layer of Cr and the cross-coupling is eliminated.

One of the advantages of simulation is that it can evaluate situations where experiments are too difficult to control. To this end, instead of fully covering the faces of both phase-wells, the shallow phase-well was left intact (no absorbing layer deposited on its faces) and the deep phase-well was covered half-way with absorbing layer as shown in the

schematic diagram of Figure 5-17. According to the physical understanding and model of cross-coupling developed in Section 5.3, the scattered light from the edges at the bottom of the shallow well cannot go through the opening of the deep phase-well and consequently this component of cross-talk is eliminated as shown in Figure 5-17(b). On the other hand, the scattered light from the edges at the bottom of the deep phase-well can still go through the opening of the shallow phase-well unobstructed and therefore this component of cross-talk remains almost unchanged as shown in Figure 5-17(a). Note that the small increase of this cross-talk term is attributed to the extra scattered light caused by the discontinuity of the half-covered sidewalls of the deep phase-well with a 50nm thick layer of Cr. This simulation successfully demonstrates the validity of the physical model in place for cross-talk. Had the primary source of cross-talk been the whole face (sidewall) of phase-wells and not the edges at the bottom, the amount of cross-talk from the deep to the shallow phase-well

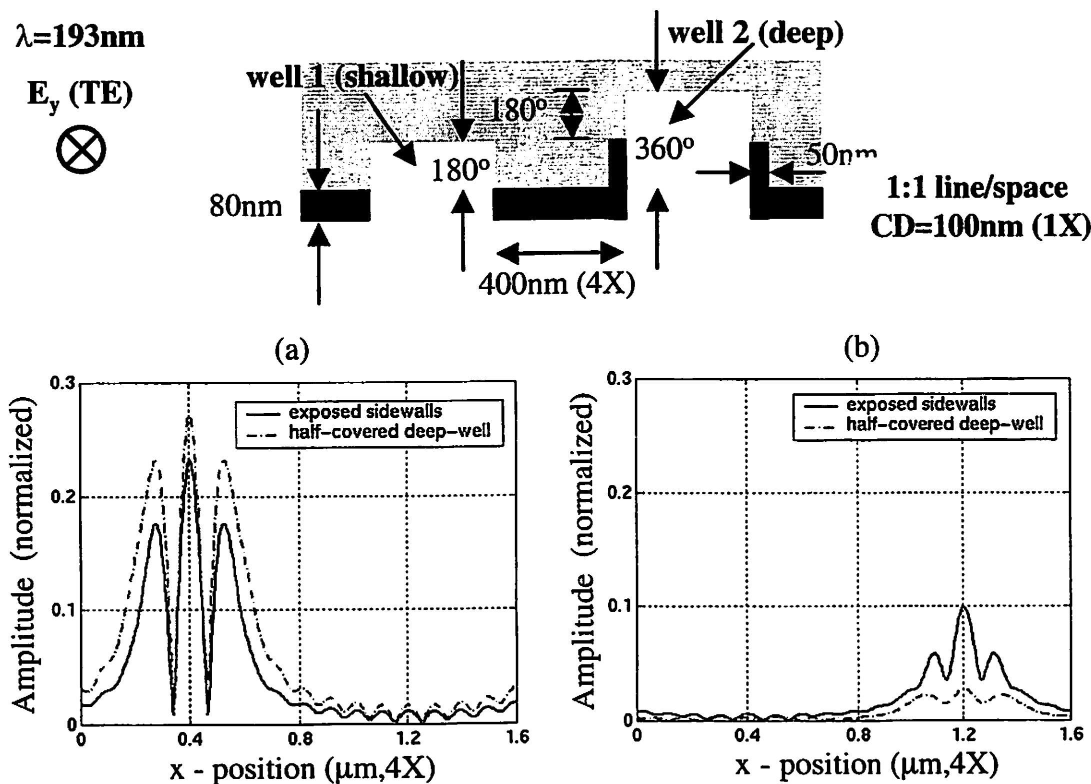

Figure 5-17. Validation of cross-talk model

The faces of the deep phase-wells are half-covered with 50nm of Cr-layer. This reduces dramatically the cross-talk from the shallow to the deep phase-well, whereas the cross-talk from the deep to the shallow remains almost unchanged.

would have been almost halved, when half of each face is covered, and would have not remain almost unchanged as this simulation demonstrated.

The second idea for cross-talk elimination is based on blocking the reflected light paths (reflected from the back side of the absorbing layer) of Figure 5-3(d). In order to do that, a 50nm thick layer of MoO_3 (with a refractive index of n=1.6+j0.69 at λ=193nm) was deposited before the 80nm thick absorbing Cr-layer that acts as an anti-reflective coating (ARC). This anti-reflective behavior is shown in Figure 5-18, where the addition of the 50nm MoO_3 layer is seen to significantly reduce the amplitude of the standing wave being established behind the 80nm thick Cr-layer to levels that equalize it with the standing wave amplitude for a glass/air interface. The amplitude of the cross-talk terms for a 100nm (1X), 1:1 dense line/space, 180°/360°, vertical faces alt. PSM without and with the 50nm MoO_3 ARC is shown in Figure 5-19. The cross-talk levels with the ARC have been suppressed by almost 50%. This is indicating that both the direct light paths of Figure 5-3(c) and the reflected light paths (reflected from the back side of the absorbing layer) of Figure 5-3(d) contribute approximately equally to the cross-coupling effect in alt. PSMs.

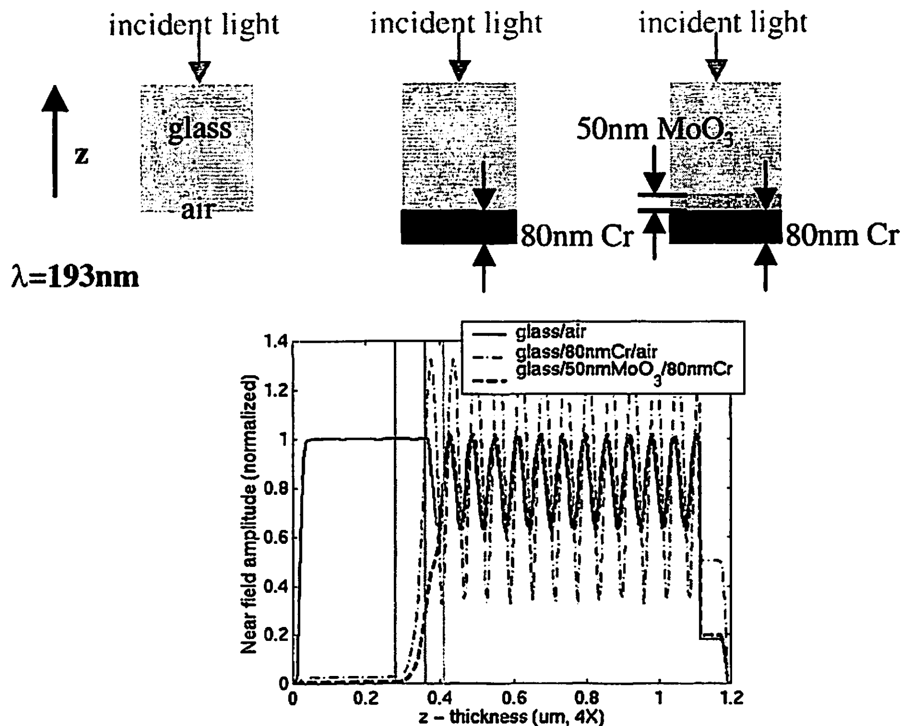

Figure 5-18. A 50nm thick layer of MoO_3 acts as anti-reflective coating

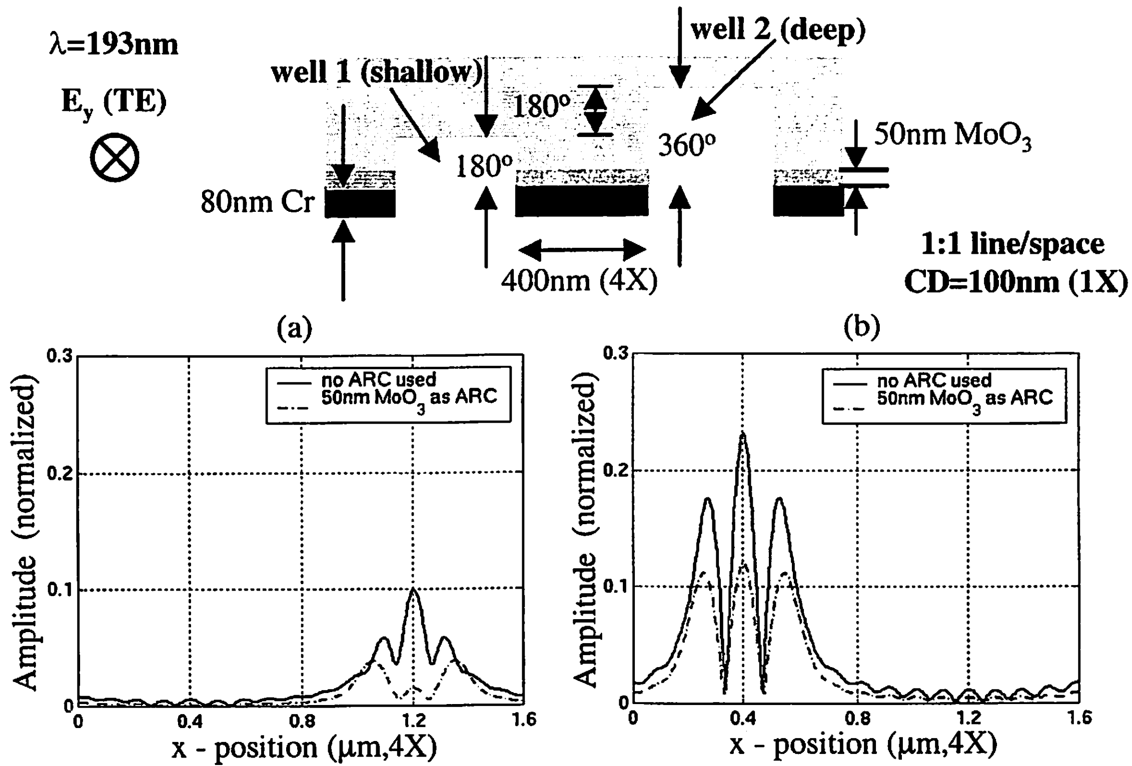

Figure 5-19. Cross-talk elimination through the use of ARC

The cross-talk levels reduce by ~50% when a 50nm MoO_3 layer is used as ARC

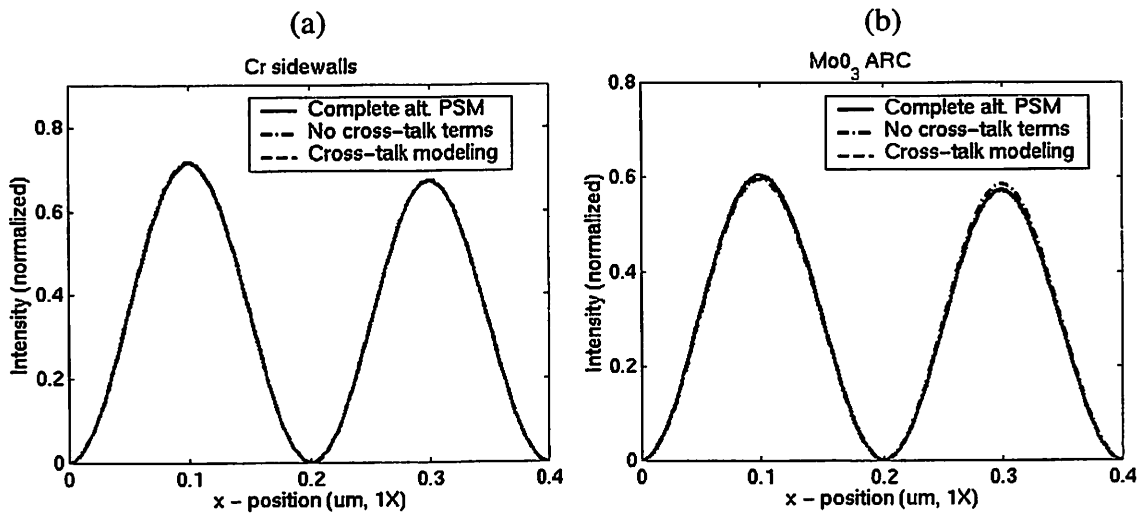

Figure 5-20. Aerial images for the alt. PSMs of Figure 5-16 and Figure 5-19

System parameters: NA=0.7, σ=0.3, R=4, best focus. Normalized image intensity for Cr-covered sidewalls (a) and use of 50nm MoO_3 ARC (b). The three simulation approaches are compared: Complete alt. PSM simulation (r-mask, no decomposition), 0th-order (no cross-talk terms) and 1st-order domain decomposition (including cross-talk).

The plots of Figure 5-20 depict the intensity of the aerial image for the alt. PSM geometries with the Cr-covered sidewalls and the 50nm MoO_3 ARC. Inclusion of the cross-talk terms in the calculation is shown to be redundant, since the reduced level of cross-coupling in both cases makes the images obtained from the simulation of the exact geometry (r-mask) and from both the zero- (no cross-talk modeling) and first-order (with cross-talk modeling) domain decomposition method identical.

5.7. 3D simulations where cross-talk is significant

In the examples presented at the end of Chapter 4, cross-talk was not included in the decomposition methods used (qr-DDM and mk-mask). Through the cross-talk modeling of this Chapter, it is now obvious why cross-talk was not significant in those examples. In the first, a $0^o/180^o$ alt. PSM with 1:1 dense line/space patterns and 50nm of undercut does not exhibit any significant amount of cross-talk between the 0° and 180° phase-wells according to Figure 5-9 and Figure 5-10. The same is true for the second example, in which a $90^o/270^o$ alt. PSM with 1:1.5 semi-dense contacts and 50nm of undercut doesn't have high levels of cross-talk as evidenced in Figure 5-10 and Figure 5-12. Consequently the qr-DDM and subsequent mk-mask methods were used and yielded accurate image results.

Two more examples of 2D mask layouts are presented next. The purpose of the first example is to demonstrate the successful inclusion of cross-talk terms in 2D layouts, when it is erroneous to ignore it, whereas the purpose of the second is to validate once again the physical understanding in place for cross-talk, by showing that cross-talk because of the corners at the bottoms of the phase-wells is insignificant and can be safely ignored.

Figure 5-21 shows a $180^o/360^o$, CD=120nm(1X), 1:1 dense layout for contacts with no undercut. The rigorous solution of the scattered field at the observation plane for the complete alt. PSM under TE (E_y) illumination at λ=193nm is shown in Figure 5-22(a). The amplitude of the error incurred using the DDM of Figure 5-21(b) is shown in Figure 5-22(b). Clearly, the relatively large error of the decomposition method is because cross-talk was neglected. Cross-talk effects can be included using only 2D simulations, as was done in Section 5.4. Note that this involves multiple cross-talk terms, both with TE and TM

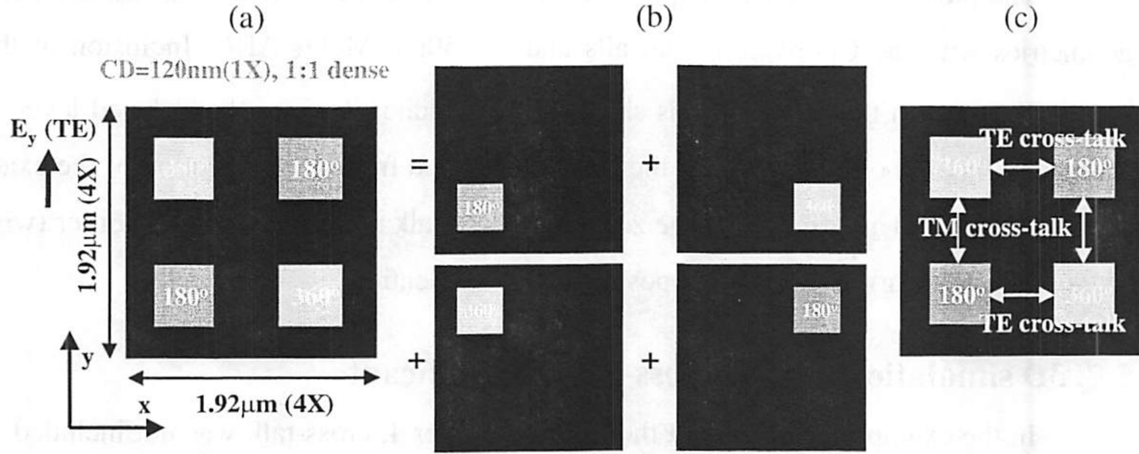

Figure 5-21. Dense contacts: Mask layout and DDM with cross-talk modeling

(a) 1:1 dense contact hole mask layout with CD=120nm (1X), (b) layout decomposition *via* the DDM into the four constituent single-opening masks and (c) schematic diagram of the various cross-talk terms that need to be included for an accurate image simulation.

light, as shown in Figure 5-21(c): The southwest 180° hole exhibits TE cross-talk effects with the southeast 360° hole (and its mirror 360° hole in the x-axis because of periodic boundary conditions). The same 180° hole also exhibits TM cross-talk effects with the northwest 360° hole (and its mirror 360° hole in the y-axis because of periodic boundary conditions). Similar cross-talk effects are observed between the northeast 180° hole and the

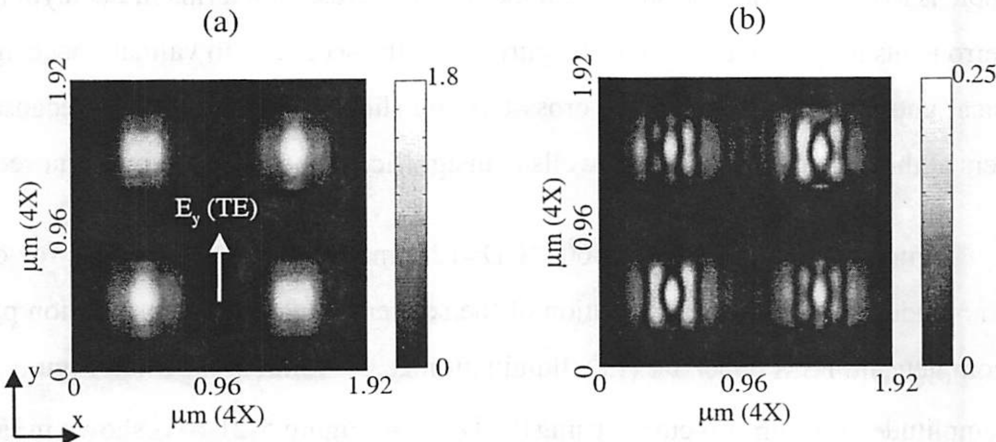

Figure 5-22. Dense contacts: Near field comparison

(a) Amplitude of the scattered field (E_y) of the mask layout shown in Figure 5-21(a) calculated with a rigorous 3D simulation and (b) amplitude of the error of the scattered field of the DDM shown in Figure 5-21(b) compared to the rigorous solution in (a).

southeast and northwest 360^0 holes. No cross-coupling occurs between diagonal holes. The final aerial images for a system with σ=0.3, NA=0.7 and R=4 are shown in Figure 5-23. In Figure 5-23(a) the image obtained using the fully rigorous r-mask is shown along with the 20% intensity contours for the three different approaches (r-mask, DDM without and with cross-talk modeling). From the comparison of the three distinct images along the cut-line and within the zoom boxes shown in Figure 5-23(b) and (c) it is obvious that including cross-talk effects restores the accuracy of the DDM. The normalized mean square error within the image field drops by more than a factor of 10, from 23.6E-4 to 1.5e-4.

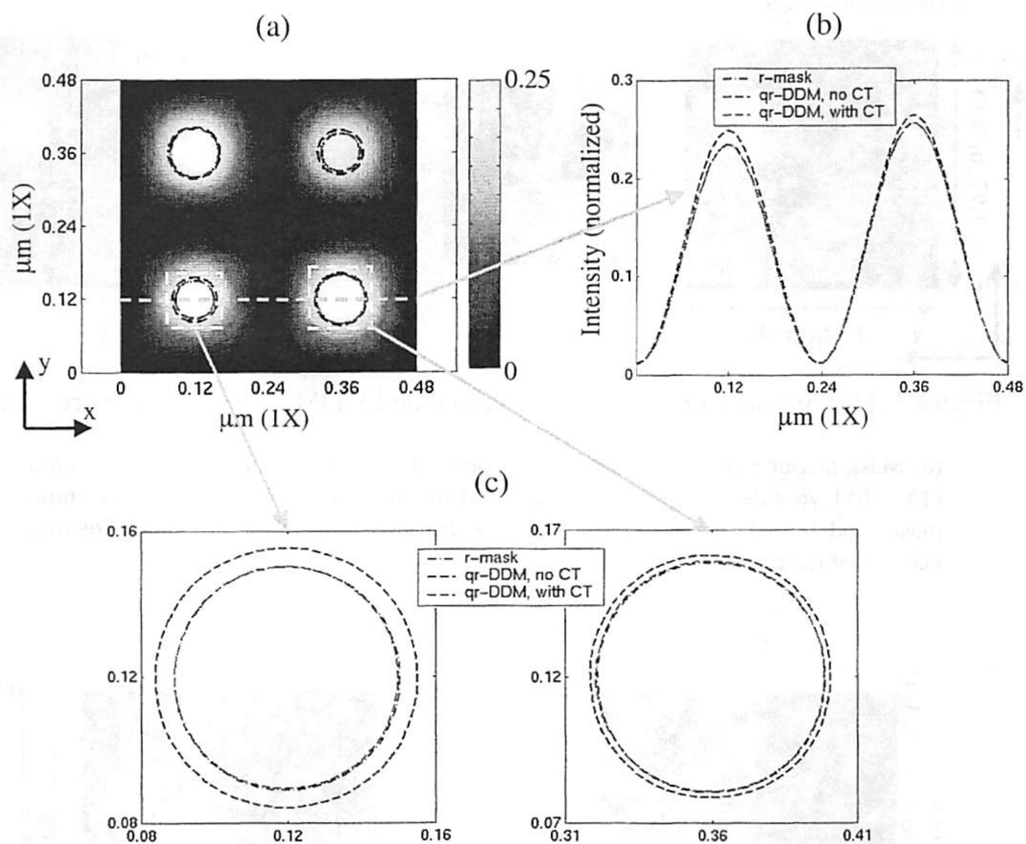

Figure 5-23. Dense contacts: Aerial image comparison

The image of the mask layout shown in Figure 5-21(a) (λ=193nm, σ=0.3, NA=0.7, R=4) calculated with the rigorous scattered field solution of Figure 5-22(a) is shown in (a). Three iso-intensity contours at the 20% level are also shown, one corresponding to the r-mask, one to the qr-DDM without cross-talk modeling and the other to the qr-DDM with cross-talk modeling. The three images are compared along the indicated cut-line in (b) and within the zoom boxes in (c).

In the second example, a $180^{0}/360^{0}$ alt. PSM layout bearing a pair of square holes with CD=120nm (1X) that are diagonally positioned is shown in Figure 5-24(a). The rigorous solution of the scattered field at the observation plane for the complete alt. PSM under TE (E_y) illumination at λ=193nm is shown in Figure 5-25(a). The amplitude of the error if the DDM of Figure 5-24(b) is used is shown in Figure 5-25(b). Observe that the level of the error is one order of magnitude smaller than in the previous example. This indicates that cross-talk effects are insignificant. Although the two holes in the layout are in

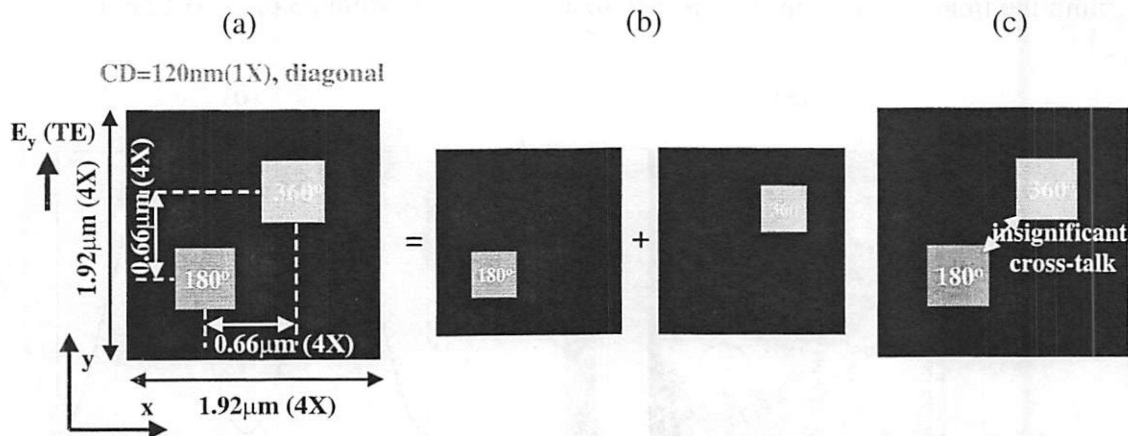

Figure 5-24. Diagonal contacts: Mask layout and DDM - insignificant cross-talk

(a) Mask layout with a diagonally positioned pair of contact holes with CD=120nm (1X), (b) layout decomposition *via* the DDM into the two constituent single-opening masks and (c) schematic diagram showing that cross-talk in the diagonal direction because of the corners is insignificant.

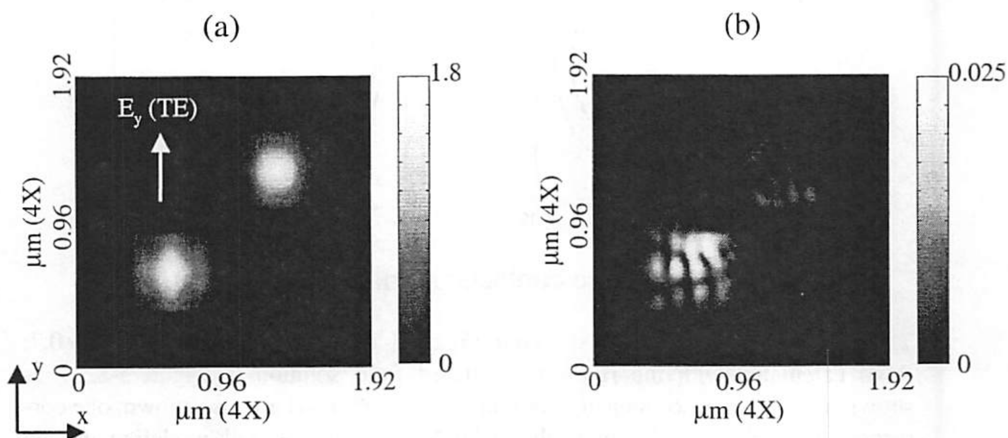

Figure 5-25. Diagonal contacts: Near field comparison

(a) Amplitude of the scattered field (E_y) of the mask layout shown in Figure 5-24(a) calculated with a rigorous 3D simulation and (b) amplitude of the error of the scattered field of the DDM shown in Figure 5-24(b) compared to the rigorous solution in (a).

close proximity, their diagonal displacement puts the sources of cross-talk (edges at bottom of phase-wells) in such relative locations, that it is impossible for scattered energy to be cross-coupled into neighboring openings. Had the corners been a significant contributor to cross-talk effects, the error shown in Figure 5-25(b) would have been comparable to the error levels of Figure 5-22(b). The aerial images for a system with σ=0.3, NA=0.7 and R=4 are shown in Figure 5-26. In Figure 5-26(a) the image obtained using the fully rigorous r-mask is shown along with the 10% intensity contours for the two approaches (fully rigorous r-mask and DDM without cross-talk modeling). Comparing the images along the diagonal cut-line and within the zoom boxes shown in Figure 5-26(b) and (c) further reinforces

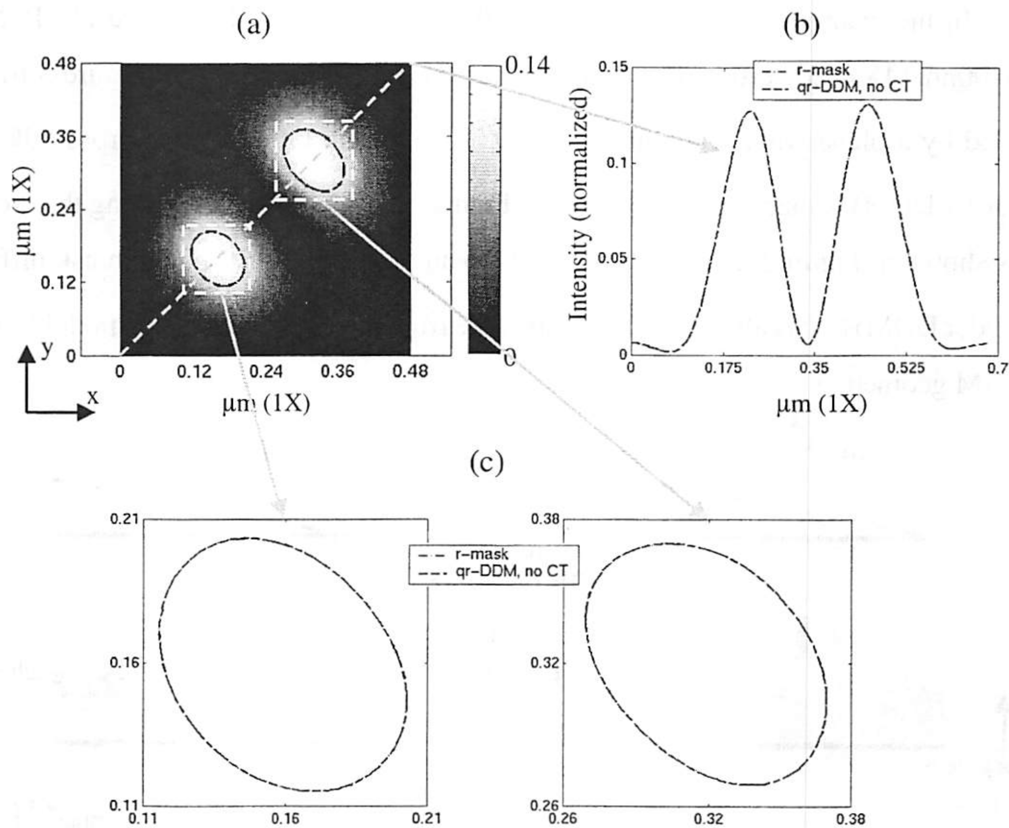

Figure 5-26. Diagonal contacts: Aerial image comparison

The image of the mask layout shown in Figure 5-24(a) (λ=193nm, σ=0.3, NA=0.7, R=4) calculated with the rigorous scattered field solution of Figure 5-25(a) is shown in (a). Two iso-intensity contours at the 10% level are also shown, one corresponding to the r-mask and the other to the qr-DDM without cross-talk modeling. The two images are compared along the indicated cut-line in (b) and within the zoom boxes in (c). Cross-talk effects are negligible, regardless of the fact that the contacts are in close proximity along the diagonal direction.

the idea that corner cross-talk effects are negligible. The two images are hardly distinguishable since the normalized mean square error of the DDM without cross-talk modeling is 6.2E-7!

5.8. Off-axis illumination

Here, it is of great importance to check to validity of the cross-talk models for off-axis illumination that would be required for the application of the decomposition methods in imaging formulations such as Abbe's or a modified Hopkins' method with varying diffraction orders *vs.* angle of incidence.

In the examples of Figure 5-27 a 180°/360°, 1:1 dense line/space alt. PSM with CD=400nm (4X) and vertical or tilted sidewalls (same geometries as in Figure 5-6) is illuminated by a plane wave traveling at ~10.9° off-normal. Omitting the cross-talk effects (0th-order DDM) is inaccurate, as shown in Figure 5-27(a) and (b). Including the cross-talk terms shown in Figure 5-27(c) and (d) leads to an accurate result for the mask diffraction (1st-order DDM) that is almost indistinguishable from the rigorous r-mask model (complete alt. PSM geometry).

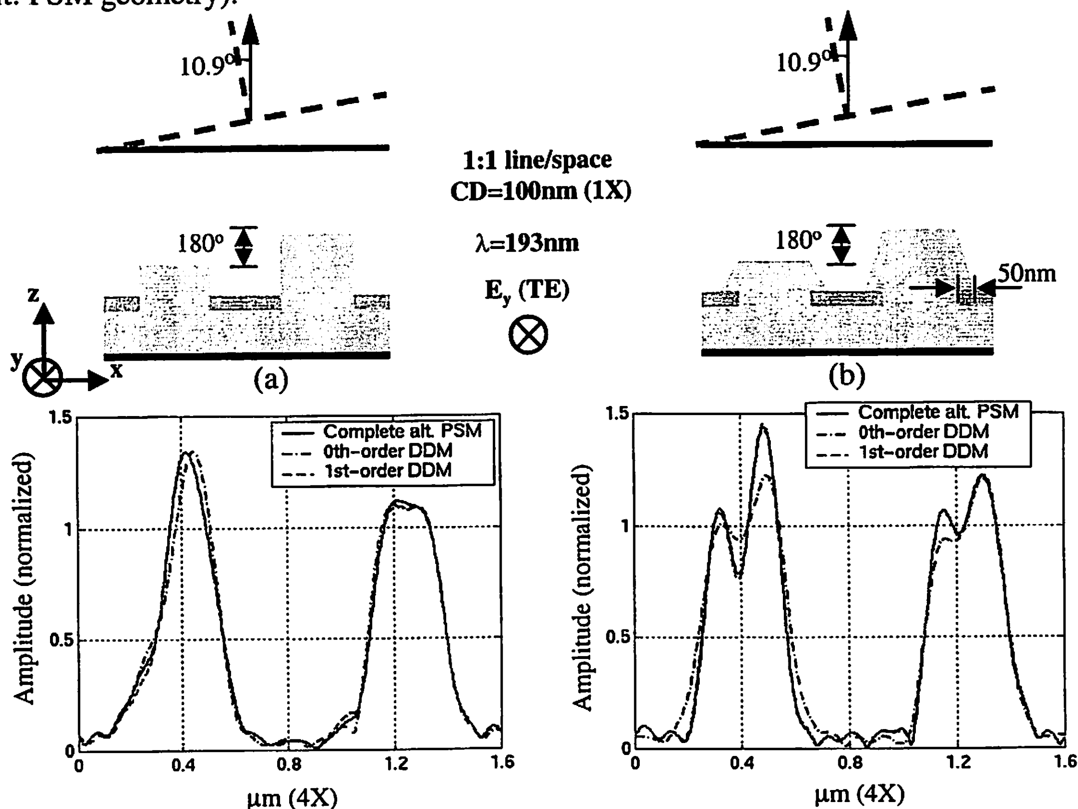

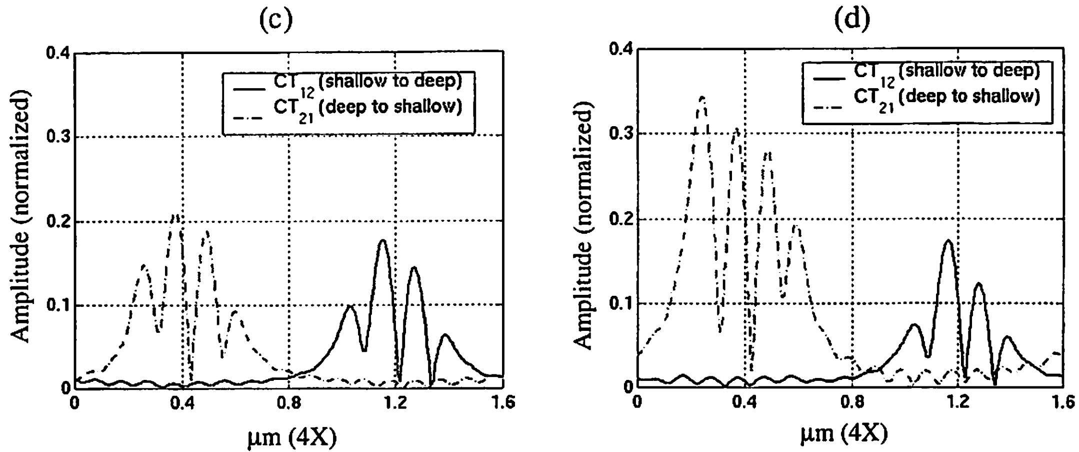

Figure.5-27. Examples of 1st-order DDM with off-axis illumination

The examples of Figure 5-6 are revisited to demonstrate the validity of the cross-talk model in off-axis illumination. The illuminating plane wave strikes the mask at 10.9^o off the normal (z-axis). A comparison of the three simulation approaches is shown: Complete alt. PSM simulation (no decomposition, r-mask), 0th-order and 1st-order DDM for vertical (a) and sloped (b) sidewall profile. The normalized amplitude of CT_{12} and CT_{21} is also shown for vertical (c) and sloped (d) sidewall profiles.

5.9. Conclusions

In this Chapter a novel methodology to model cross-talk between phase-wells in alt. PSMs was presented. Through the calculation of the scattered field from an isolated 90° air/glass discontinuity a new model for cross-talk was proposed. According to this model, the edges (not the faces or the corners) at the bottom of the phase-wells are the primary sources of cross-talk. The validity of the model was established directly through the successful first-order decomposition of alt. PSM in both 2D and 3D simulations that yield accurate results when compared with the simulation of the exact geometry. Also, indirect evidence of the validity was seen in the simulation of the half-covered sidewalls of the phase-wells and the MoO_3 ARC of Section 5.6. Cross-talk can potentially be a source of image imbalance but can also be used to “correct” imbalance. Recipes that reduce cross-talk and the way they achieve this task were also presented. Both these ideas are manufacturable (specifically the Cr-covered sidewalls has been demonstrated by Levenson *et al.* [50]). It was cautioned however that the elimination of cross-talk although gets rid of a hard-to-control phenomenon does not necessarily lead to superior images and cross-talk is definitely not the sole contributor to image imbalance. Although light power owing to

cross-talk is only a small portion of the total signal power (~1% or less), the abrupt phase changes in a PSM can amplify the effects of cross-talk through the constructive or destructive interference of cross-talk with the near diffracted field. The cross-talk model can also handle the important case of off-axis illumination.

6 The Edge Domain Decomposition Method

A powerful extension of the domain decomposition methods developed in Chapter 4 for the rapid and accurate simulation of light scattering from advanced photomasks is demonstrated here.

Researchers have in the past investigated the decomposition of mask layouts into individual openings, and even into edges, for ideal thin masks under coherent illumination [65], but such techniques have never been applied to the rigorous solution for the scattered field. Domain decomposition techniques, where a large electromagnetic problem is broken up in smaller pieces and the final solution is arrived at by synthesizing (field-stitching) the elemental solutions, have been recently proposed for the study of one-dimensional binary (phase only) diffractive optical elements [49], [72]. Another research group working on the same problem demonstrated how to create and use a perturbation model for binary edge-transitions based on the product of the ideal, sharp transition and the continuous field variations in the vicinity of the edge [48]. Independently, a similar technique to field-stitching has been invented and presented in Chapter 4 and Chapter 5 for the simulation of two-dimensional layouts of advanced photomasks (alternating PSM, masks with OPC) that properly models interactions from neighboring apertures (cross-talk) and furthermore takes advantage of the spectral properties of the diffracted fields to come up with a compact model for the edge-transitions [2].

In this Chapter, a domain decomposition method based on edges is described, where the pre-calculated electromagnetic field from the diffraction of isolated edges is recycled in the synthesis of the near diffracted field from arbitrary two-dimensional diffracting geometries. Although at first glance it might be tempting to discard edge-decom-

position techniques as inaccurate for masks with large vertical topography and features with small lateral dimensions, it will be shown that for a large set of practical situations they are accurate. A key difference in this method from the one in [48] is that the sum of the complex fields is taken instead of the product. The reason for that lies in the linearity of the Kirchhoff-Fresnel diffraction integral [15] and it is exactly because of this linearity that the decomposition method is possible.

The Chapter is organized as follows: First, a new method for the mask domain decomposition is introduced and applied in simple 1D layouts. The limits of this method are systematically examined and presented next. Then, the method is expanded in 2D layouts and its algorithmic implementation for arbitrary layouts is considered. Simple 2D layouts that establish the validity and accuracy of the approach and large, arbitrary layouts that demonstrate its versatility are covered next. Finally, an important direction for further enhancing the efficiency of the method that is based on spectral matching is discussed.

6.1. The edge-DDM applied in 1D layouts

A natural extension of the DDM shown in Figure 4-3(b) that is also based on the linearity of the Kirchhoff-Fresnel diffraction integral is shown in Figure 6-1. The 1D mask layout is first decomposed into single opening masks as in Figure 4-3(b) and subsequently each opening is decomposed into two edges and a uniform illumination field as in Figure 6-1. Such a decomposition can be proven to be exact for infinitely thin and perfectly conducting screens through the use of the electromagnetic form of Babinet's principle [16], but it should break down if applied to photomasks with "thick" vertical structures (compared to λ) and not perfectly absorbing screen materials. Also, because of the reduced ability of light to penetrate through small (compared to λ) openings it is expected to break down for small mask features. This decomposition method will be hereafter referred to as the *edge domain decomposition method* or *edge-DDM*. The application of the edge-DDM to a single isolated space and an isolated line are shown next, followed by a systematic evaluation of the limits of applicability of the method.

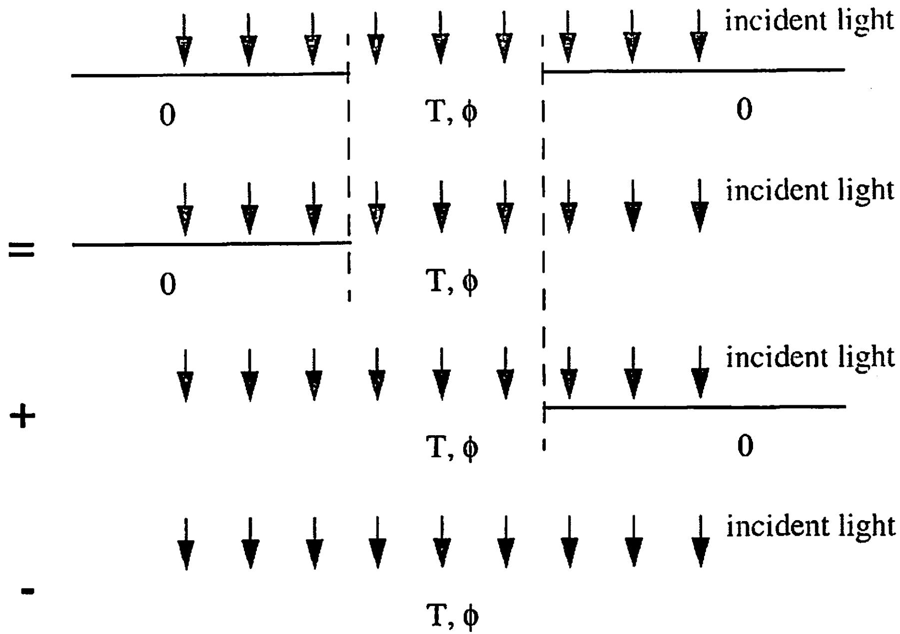

Figure 6-1. Decomposition of an opening into two edges

An opening with transmission T and phase ϕ in an infinitely thin, opaque screen can be decomposed by way of the linearity of the Kirchhoff-Fresnel diffraction integral into two edges. The uniform plane wave illumination is subtracted to restore the light level everywhere.

6.1.1. Decomposition of a space into two edges

Consider the isolated mask space (opening) shown in Figure 6-2(a). The amplitude of the complex E_y-field under E_y (TE) illumination is shown in (c) and the scattered field across the observation plane is shown in (e). According to Figure 6-1, the field across the observation plane can be alternatively obtained by using the scattered field from an edge that has the same vertical profile as the space, as shown in Figure 6-2(b) and (d). The resulting field from this edge-DDM is overlaid on the plot of Figure 6-2(e) along with the field from the edge-scattering. The normalized mean square error[1] (NMSE) between the r-mask and the edge-DDM is 0.19%. In Figure 6-2(f) the spectra of the r-mask and edge-DDM are compared and it is seen that they differ by 0.13% in a NMSE sense if the whole spectrum of propagating waves is considered and by merely 0.007% within the collection ability of

1. The normalized mean square error is defined by: $NMSE = \int |E_r - E_s|^2 dS / \int |E_r|^2 dS$, where E_r is the "true" field resulting from a rigorous simulation of the complete mask geometry and E_s is the synthesized field *via* the edge-DDM.

a projection system with NA=0.8 and R=4. Since only the portion of the spectrum that is collected by the projection system contributes to the image formation, the exceptional accuracy of the edge-DDM is this regime is more than adequate for accurate image simulations.

6.1.2. Decomposition of a line into two edges

Similar steps can be followed for the isolated line shown in Figure 6-3(a) illuminated with E_x (TM) polarized light. Note that it is not typical to have a line as shown here, where in both sides the glass has been etched. Normally only one side of the line is phase-shifted, but this example simply aims to introduce the principle of the edge-DDM. A line

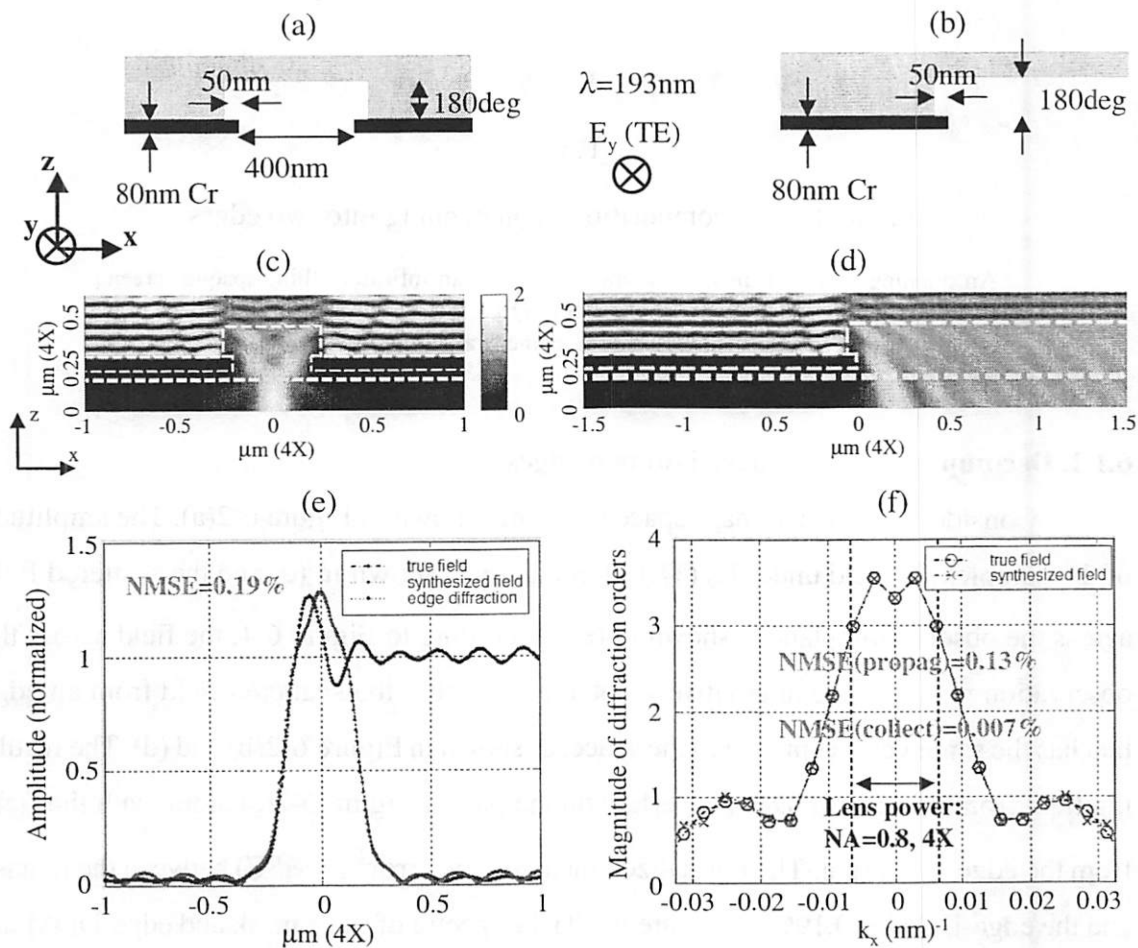

Figure 6-2. Edge-DDM applied on an isolated space

Geometry of mask with isolated space (a) and edge (b). Note that the vertical profile of the edge is the same as that of the isolated space. Amplitude of complex field from rigorous TEMPEST simulation for space (c) and edge (d). The true scattered field (r-mask) across the observation plane in (c) is compared with the edge-DDM (synthesized field) in (e) and their spectra are compared in (f). The normalized mean square errors (NMSE) are indicated on the plots.

with one side phase-shifted and the other left intact can still be decomposed *via* the edge-DDM using the diffraction fields from the two different edges. The amplitude of the complex E_x field everywhere in the domain of Figure 6-3(a) is shown in (c) and for the edge of Figure 6-3(b) in (d) respectively. The true (r-mask) scattered field is compared with the synthesized field with edge-DDM in (e) and the spectra are compared in (f). The error (NMSE) is seen to be small in both the near field and spectra plots and specifically the error of the through-the-lens (TTL) spectrum is just 1.5E-5.

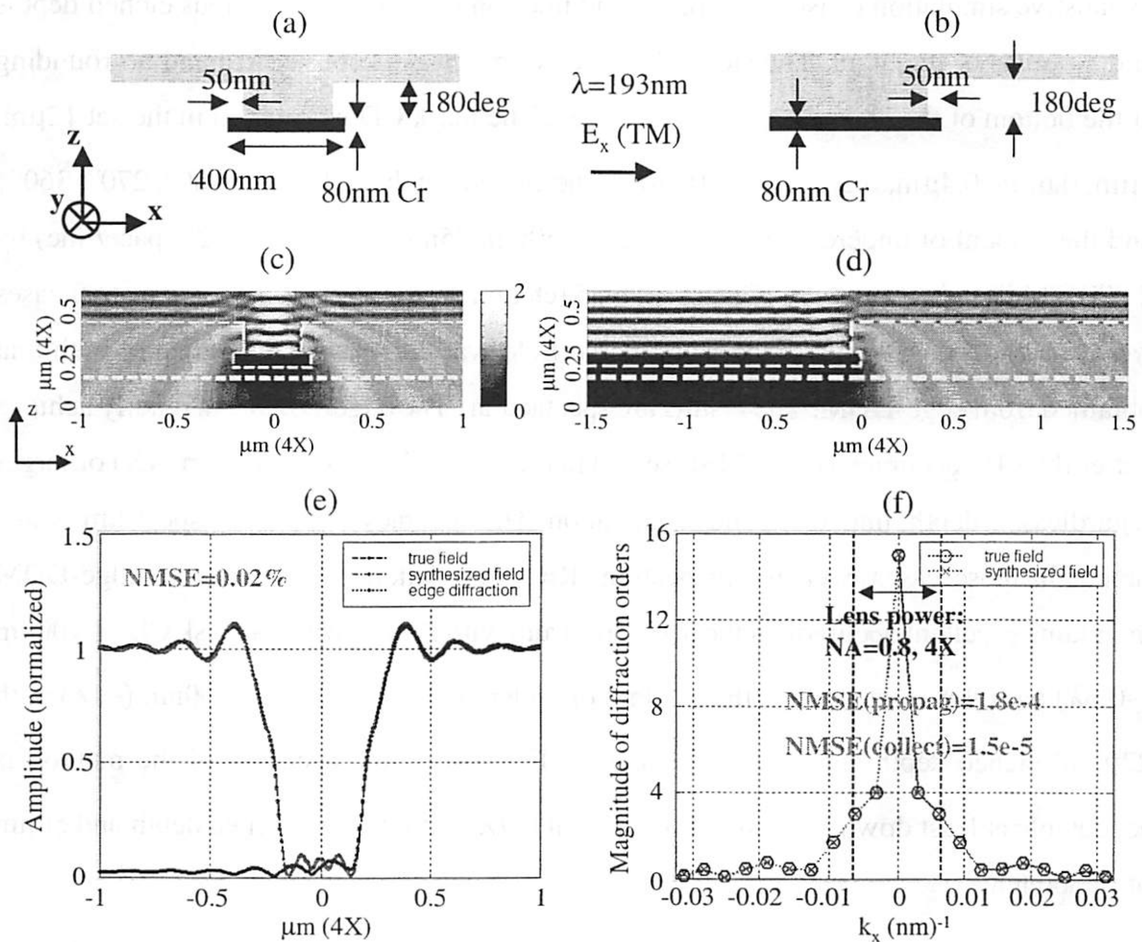

Figure 6-3. Edge-DDM applied on an isolated line

Geometry of mask with isolated line (a) and edge (b). Note that the vertical profile of the edge is the same as that of the isolated line. Amplitude of complex field from rigorous TEMPEST simulation for line (c) and edge (d). The true scattered field (r-mask) across the observation plane in (c) is compared with the edge-DDM (synthesized field) in (e) and their spectra are compared in (f). The normalized mean square errors (NMSE) are indicated on the plots.

6.1.3. Limits of the edge-DDM

In the examples of Figure 6-2 and Figure 6-3 the edge-DDM is seen to be accurate compared with the simulation of the exact mask structure. Although the vertical mask topography ($180^o \approx 170nm \approx 1\lambda$) is comparable to the wavelength, the fact that the lateral dimensions of the space and the line are relatively large compared with the wavelength ($CD = 400nm > 2 \times 193nm = 2 \times \lambda$) renders the edge-DDM accurate. One expects that as the lateral sizes become smaller and the vertical mask topography even larger the edge-DDM will eventually break down. The limits of the edge-DDM were investigated through exhaustive simulation of isolated spaces and lines on the mask with various etched depths and amounts of undercut. The sidewall angles were always kept vertical and no rounding at the bottom of the etched wells was included. The mask CD was varied in the set {2μm, 1μm, 0.6μm, 0.4μm, 0.2μm(~1λ), 0.1μm}, the etched depth in {0^o, 90°, 180°, 270°, 360°} and the amount of underetch in {0nm, 25nm, 50nm, 75nm, 100nm}. All 2 (space/line) by 2 (TE/TM illumination) by 6 (CD sizes) by 5 (etched depths) by 5 (underetch) = 600 cases were run and the rigorous (r-mask) scattered field was automatically compared with that obtained from edge-DDM. The results are spectacular! The edge-DDM can readily achieve better than 1% accuracy (in a NMSE sense) in the near field for CD=400nm (4X) or larger regardless of depth, underetch and polarization. The accuracy in the TTL-spectrum is sufficient in those cases even for inspection (R=1) simulations. For lines, the edge-DDM maintains excellent accuracy in the TTL-spectrum with R=4 down to a mask CD of 100nm (~0.5λ) with 90° of etched depth and 0nm of undercut, or mask CD of 200nm (~1λ) with 270° of etched depth and 25nm of undercut. For spaces, the accuracy of the method is acceptable at least down to mask CD of 200nm (~1λ) with 270° of etched depth and 50nm of underetch.

Current state-of-the-art photomasks and processes utilize sub-resolution assist features that are never less than one wavelength in size on the mask. This clearly implies that the edge-DDM has the potential to accurately simulate the most advanced photomask technologies (OPC, alt. PSM, OPC on alt. PSM). Again, as with the DDM of Chapter 4, the true power of the method lies on its application in 2D mask layouts. However, one key differ-

ence with the DDM of Chapter 4 is the following: Only one rigorous 2D simulation of an edge suffices for the scattered field reconstruction of *any arbitrary size on the mask!* The DDM of Chapter 4 requires a separate simulation of every different mask size. Next, the application of the edge-DDM in 2D layouts is developed.

6.2. The edge-DDM applied in 2D layouts

The application of the edge-DDM in 2D layouts is straightforward. A mask layout comprises of a large number of edges positioned at different locations and having different orientations. No matter how complicated the mask technology, there are usually only a small number of different types of edges present in the layout. For example, a single exposure $0^o/90^o/270^o$ alt. PSM has five types of edges: i) Cr-layer/0° edge, ii) Cr-layer/90° edge, iii) Cr-layer/270° edge, iv) $0^o/90^o$ edge and $0^o/270^o$ edge. Depending on the orientation of each edge in the layout it "sees" and responds to the incident field differently. If the illuminating field is a TE (E_y) normally incident plane wave and the edge is oriented along the y-axis it "sees" TE illumination, but if it is oriented along the x-axis it "sees" TM illumination. This is illustrated in Figure 6-4. The response of each edge to its respective illumination is taken into account rigorously from a pre-stored 2D edge-diffraction simulation. However, corner effects are effectively ignored, since the finite extent of each edge is not rigorously taken into account. Instead, the scattered field at the end points of every edge is abruptly terminated (truncated) in a perfect square-wave fashion to the field value of the k-mask model. As seen in Section 4.3.4, corner effects in typical imaging situations are mapped at the extremities of the spectra and do not contribute to the image formation. Owing to this observation, the edge-DDM applied in 2D layouts is successful in accurately capturing the true electromagnetic behavior of edges in a rapid manner, while the insignificant corner effects are safely ignored.

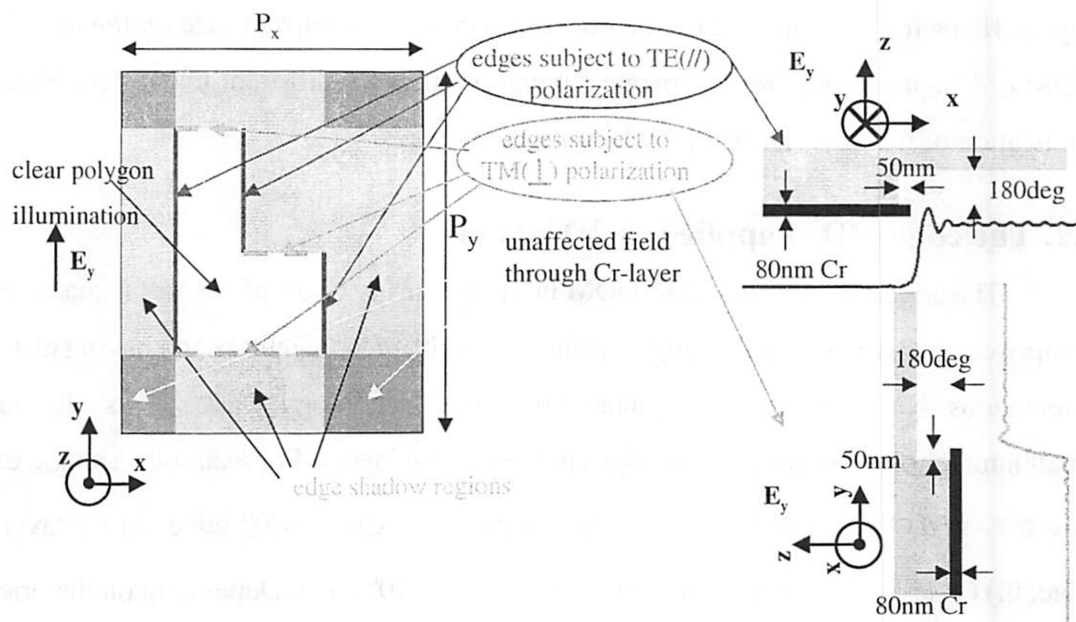

Figure 6-4. Edge-DDM applied on an arbitrary Manhattan-type polygon

Depending on the orientation of each edge in the layout it "sees" and responds to the incident field differently. Here the illuminating field is a TE (E_y) normally incident plane wave and the edges that are oriented along the y-axis "see" TE illumination (parallel to the edge), whereas the edges that are oriented along the x-axis "see" TM illumination (perpendicular to the edge). A separate 2D edge simulation is required to capture the different response of the edge to different field polarizations.

Slightly different embodiments of the edge-DDM applied in 2D layouts can be devised. One that is powerful and general in its application is described next. Then, scattering results from various edge profiles that would be encountered in alt. PSMs are presented for completeness. Next, application of the edge-DDM in simple 2D mask layouts is presented and the results of the method are compared with fully rigorous r-mask models in order to establish the validity of this approach. Finally, a large portion of a real layout from a single exposure $0^o/90^o/270^o$ alt. PSM that is too big for 3D rigorous simulation is simulated *via* the edge-DDM and the aerial image is compared with the simple k-mask model.

6.2.1. Algorithmic implementation of the edge-DDM

First, every distinct edge that is present on the layout is pre-simulated with all possible illumination directions (field polarizations) that are required, based on the orientations of the edge encountered within the layout. For simplicity only Manhattan-type layouts are

considered, where the edges are oriented along either the x- or the y-axis and require electromagnetic simulation under both parallel and perpendicular to the edge polarizations. The extension to non-Manhattan layouts although much more computationally laborious is straightforward. Subsequently, each distinct mask layer is broken up into a set of mutually disjoint (non-overlapping) rectangles. For example, a plain binary mask consists of two layers, namely the absorption layer (typically Cr-based) and the clear (uncovered) layer, whereas a more advanced $0^o/90^o/270^o$ three-phase alt. PSM consists of four layers, namely the absorption layer and the 0° clear, 90° clear and 270° clear layers. Next, looping through all rectangles of each layer, the type of each one of the four edges of the rectangle is determined based on what its neighboring layer is. Trivial edges (when the neighboring rectangle is of the same type) are discarded. It is also possible that only part of a single edge from a rectangle is neighboring with one layer and the rest is neighboring with a different layer (or different layers). In that case the edge is broken up in multiple edges, in a way that tracks the neighboring layer. What is left at the end of this process is a set of all non-trivial edges that are present in the layout (location, size and orientation) and their type, *i.e.* which are the two mask layers on each side of the edge. Given the mask layout, the k-mask (Kirchhoff-mask) model is readily available. Finally, the respective (complex) difference of the true edge-scattering from the ideal and sharp k-mask model is added to all non-trivial edges accordingly. This revised mask model that results from the edge-DDM includes accurate information about the electromagnetic scattering from the edges and it is a *quasi-rigorous mask model* (qr-mask) in the same sense that the term was used in Section 4.3, where only 2D mask simulations were used to approximate a 3D electromagnetic problem.

The above algorithm was implemented in the MATLAB environment. The part that deals with the polygon and edge extraction can probably be judged as rudimentary and most likely cannot compete in speed with more sophisticated implementations in production caliber CAD software, but it suffices for the purposes of this work, that is, to demonstrate the proof of concept of the edge-DDM and the feasibility of including accurate edge-scattering information in rapid aerial image simulations.

6.2.2. Dependence of edge-scattering on profile and polarization

Examining the departure of the scattered field from an edge from its ideal, sharp edge-transition and how it depends on the profile of the edge and the incident field polarization can provide intuition of the physical mechanisms involved.

Figure 6-5 shows the amplitude of the (near) scattered field from an edge with various profiles. The ideal, sharp edge-transition is also shown on every graph for comparison. In Figure 6-5(a) and (b) the edge-scattering for different etched depths (0°, 180° and 360°) and vertical sidewalls with no undercut is shown for TE (E_y) and TM (E_x) illumination respectively. The effect of undercut is depicted in Figure 6-5(c) and (d), where the edge-scattering for different amounts of undercut (0nm, 25nm, 50nm and 75nm) and vertical sidewalls with 180° etched depth is shown for TE and TM illumination respectively. It is interesting to note that increasing the etched depth is "making the edge response slower", meaning that the near scattered field from the edge requires more distance to reach its "on" value from its "off" value, although this effect is more pronounced for the first increment from 0° to 180° rather than from 180° to 360°. Similarly, increasing the amount of undercut appears to "make the edge response faster" and furthermore this behavior appears to be linear, since for every increment of the undercut the edge-transition gains a constant distance in its "off-on" behavior.

It is instructive to isolate the difference of the true edge-scattering from the ideal, sharp edge-transition. This is done in Figure 6-6, which depicts the amplitude of this (complex) difference for all respective plots of Figure 6-5. Observe that, indeed, by increasing the etched depth the difference has a larger spatial extent, whereas increasing the amount of undercut confines the spatial extent of the difference. This is crucial, because it is exactly the spatial extent of the difference that affects its spectral distribution. If the difference is well confined, its spectral distribution is spread out to higher spatial frequencies and the lower frequency content is small. In such a case the complex difference can be neglected and the approximation of the ideal, sharp transition is adequate.

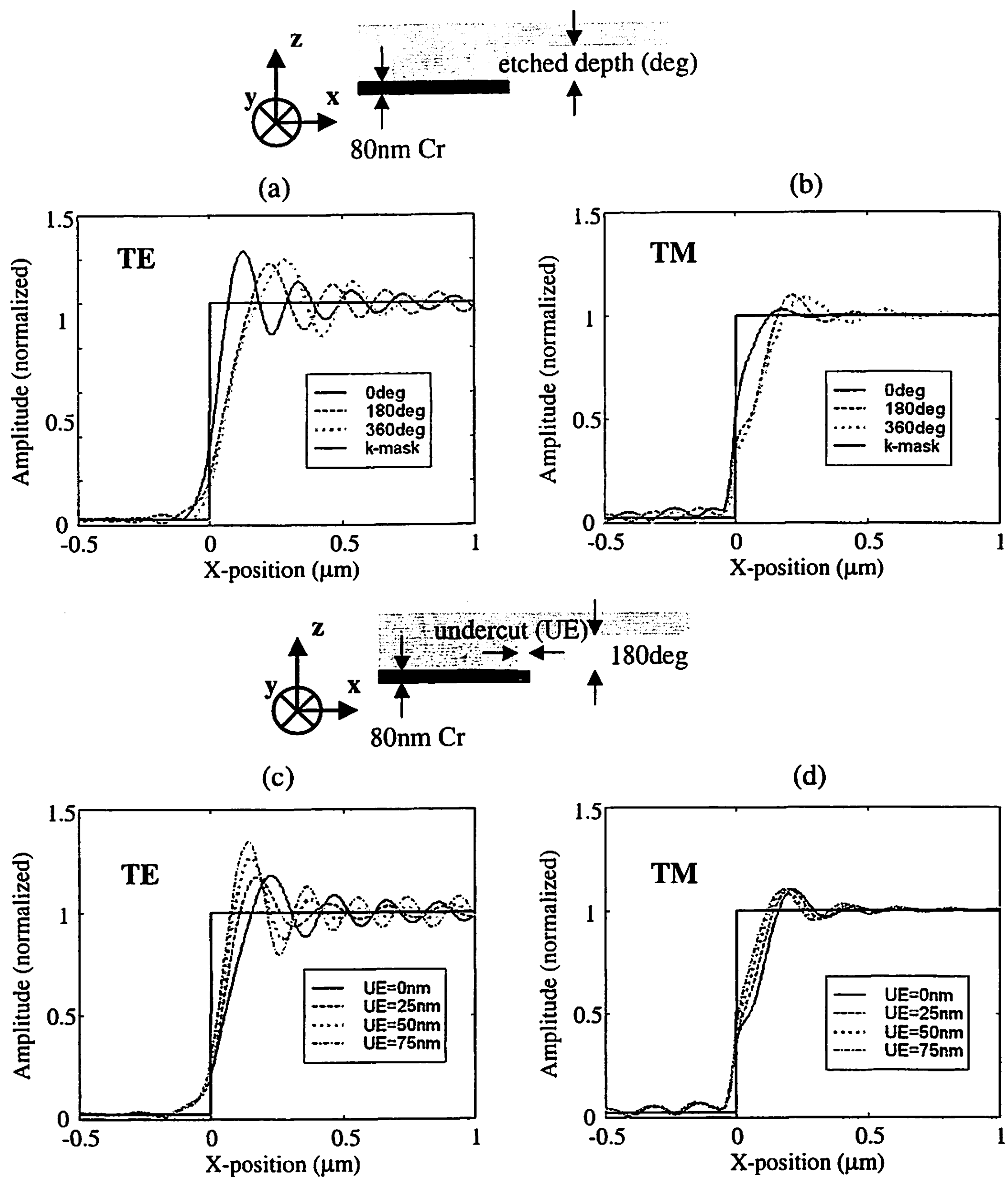

Figure 6-5. Dependence of edge-scattering on profile and polarization

Normalized amplitude of the near field across the observation plane for an edge with 0°, 180° and 360° of etched depth under TE (a) and TM (b) polarizations. Normalized amplitude of the near field for an edge with 180° of etched depth and 0nm, 25nm 50nm and 75nm of undercut under TE (c) and TM (d) polarizations. The ideal sharp edge-transition is shown in all cases for comparison. Observe that the "edge response" becomes slower for increasing etched depths and faster for increasing undercuts.

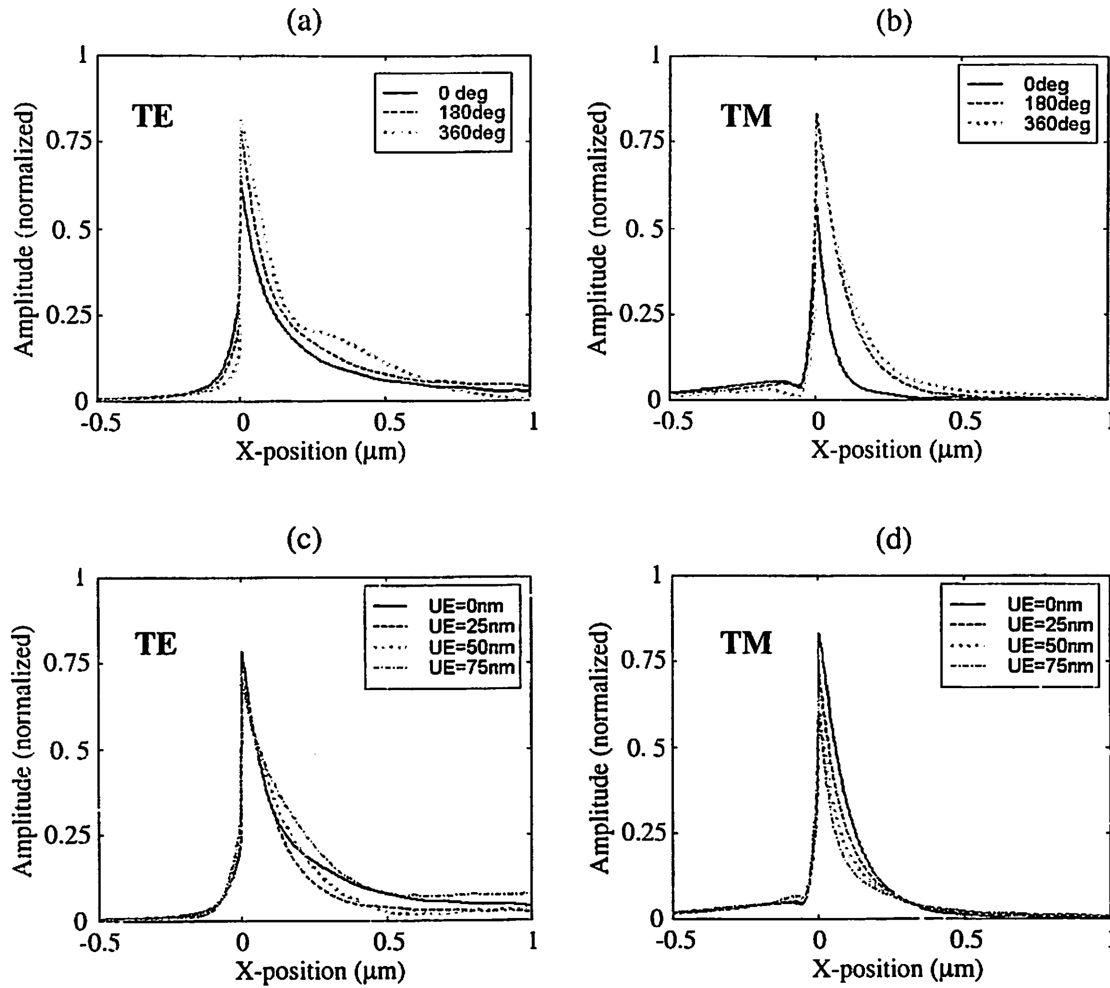

Figure 6-6. Complex difference of true edge-scattering from ideal, sharp transition

The amplitude of the complex difference of the true electromagnetic field scattered from an edge from the ideal, sharp transition (step-function) is shown in (a)-(d) for all edge profiles and illumination polarizations of Figure 6-5 respectively. (a) and (c) are for TE polarization and (b) and (d) are for TM polarization. The spatial extent of the difference grows with increasing etched depths, as seen in (a) and (b), and shrinks with increasing undercuts, as seen in (d) for TM polarization. The behavior in (c) appears somewhat erratic, but if the phase is also taken into account, it is shown in Figure 6-7 that this is also the case for TE polarization.

However, when the difference has a larger spatial extent, then its lower frequency content becomes significant and it cannot be neglected. This is shown in Figure 6-7, which depicts the magnitude of the spectra of all respective difference distributions of Figure 6-6. Observe that the TTL spectrum of the difference attains larger values when the etched depth increases and smaller values when the amount of undercut increases, as expected from

Figure 6-5 and Figure 6-6. Remember that the normalization used in spectra plots is that a constant (DC) value of 1 (clear field) would produce a Dirac δ-function at zero frequency with amplitude of 19.4 ($\sqrt{\eta} = \sqrt{\sqrt{\mu_0/\varepsilon_0}} \approx 19.4\Omega$).

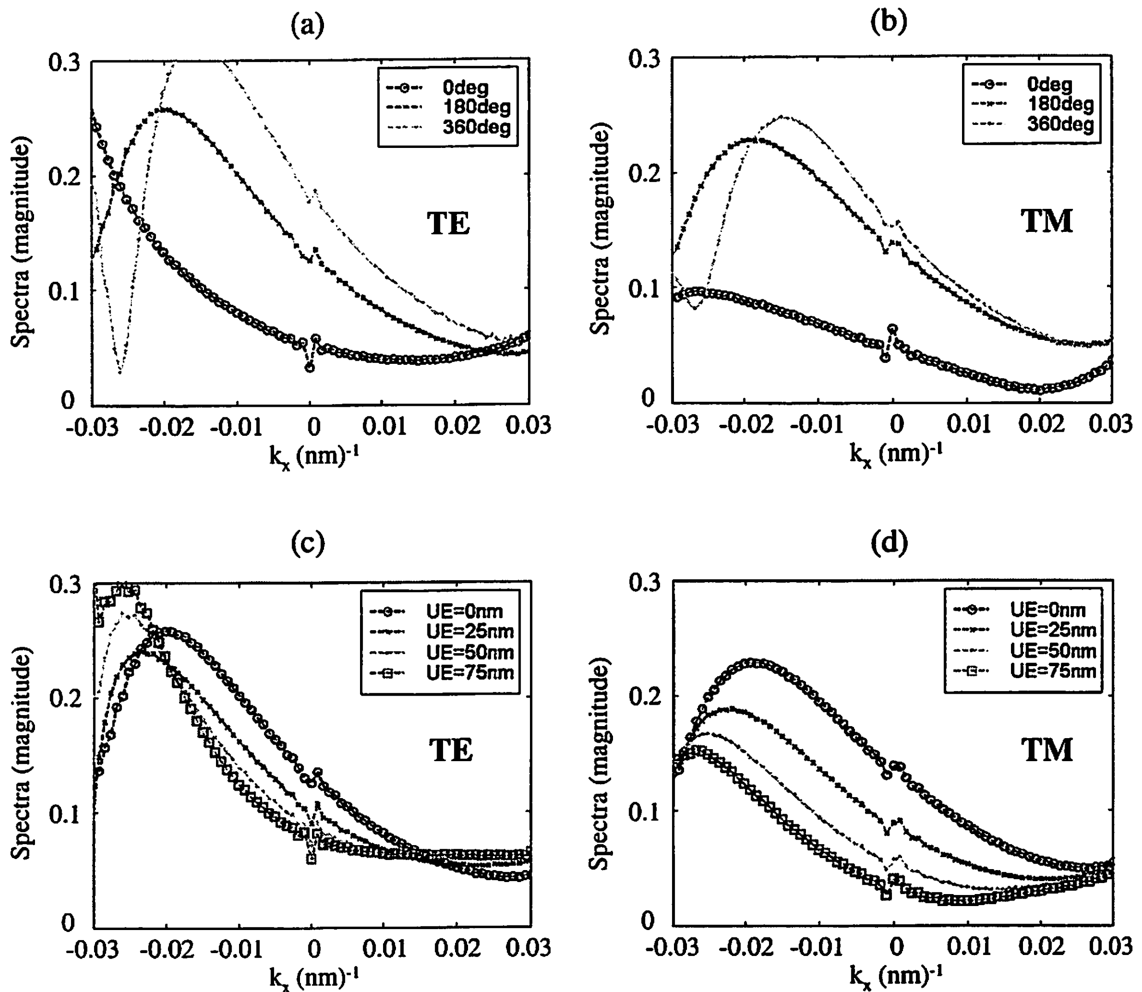

Figure 6-7. Spectrum of complex difference

The spectra of the complex differences shown in Figure 6-6 are depicted here respectively. (a) and (c) are for TE polarization and (b) and (d) are for TM polarization. Observe that the through-the-lens (TTL) parts of these spectra, which for typical lithographic imaging situations (R=4, NA~0.7-0.8) extent up to ~ +/- 0.008 (nm)$^{-1}$ are smaller for smaller etched depths and larger undercuts, regardless of polarization, as expected from the observations on the plots of Figure 6-5 and Figure 6-6.

6.2.3. Application of edge-DDM in simple 2D layouts

The application of the edge-DDM on an isolated square hole and an isolated square island (post) and comparison of the results with fully rigorous 3D mask simulations (r-masks) are presented here. The edge profile has a glass etched depth of 180° and an undercut of 50nm. The dimensions of both the hole and the island are 400nm x 400nm (4X), corresponding to approximately 2 x 2 wavelengths, for λ=193nm.

Figure 6-8(a) and (b) depict the amplitude of the scattered field across the observation plane below the hole obtained *via* the edge-DDM and *via* fully rigorous 3D simulation, respectively. The amplitude of their difference (error of the edge-DDM) is shown in Figure 6-8(c). Locally the amplitude of the error is seen to reach a discouraging level of

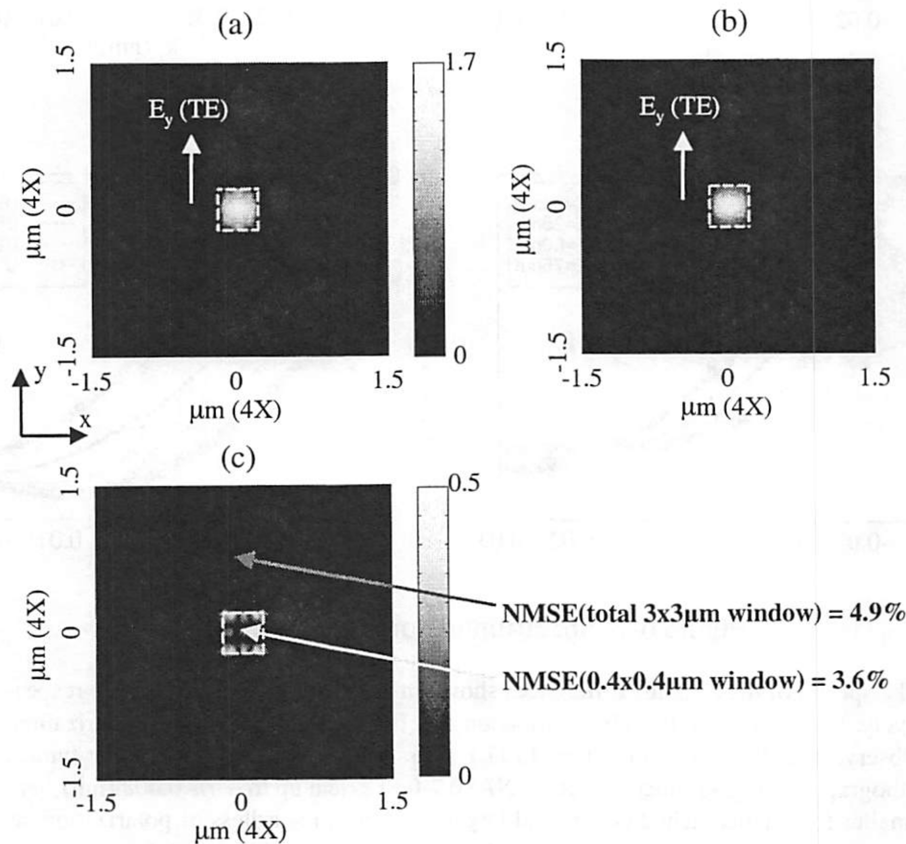

Figure 6-8. Edge-DDM applied on an isolated square hole (scattered field)

(a) Synthesized with the edge-DDM and (b) rigorously calculated scattered field (amplitude), across the observation plane below a 400nm x 400nm isolated hole. A 180° etch and 50nm undercut has been applied. The amplitude of the error (difference of r-mask from edge-DDM) is shown in (c). Locally the amplitude of the error reaches the 50% level, but the normalized mean square error does not exceed 5%.

almost 50% of the clear field value. The normalized mean square error is however more contained and is only about 4.9% if calculated within a 3μm by 3μm area or 3.6% if calculated within the 0.4μm by 0.4μm open area of the hole, as shown in Figure 6-8. From the work presented so far, it should be obvious that neither of these error levels is immediately relevant in the simulation of the image formation. What is rather more relevant is the error incurred on the diffraction orders that are collected by the imaging optics. If the spatial frequencies of the error depicted in Figure 6-8(c) are sufficiently high, this error will be discarded by the projection lens. This concept is shown in Figure 6-9, where the spectra (magnitude) of the scattered fields from edge-DDM and from rigorous 3D simulation are shown in (a) and (b) respectively. The marginal circles indicating the propagating plane waves (with $|\vec{k}| \leq 2\pi/\lambda$) and the collected by the imaging system plane waves (with

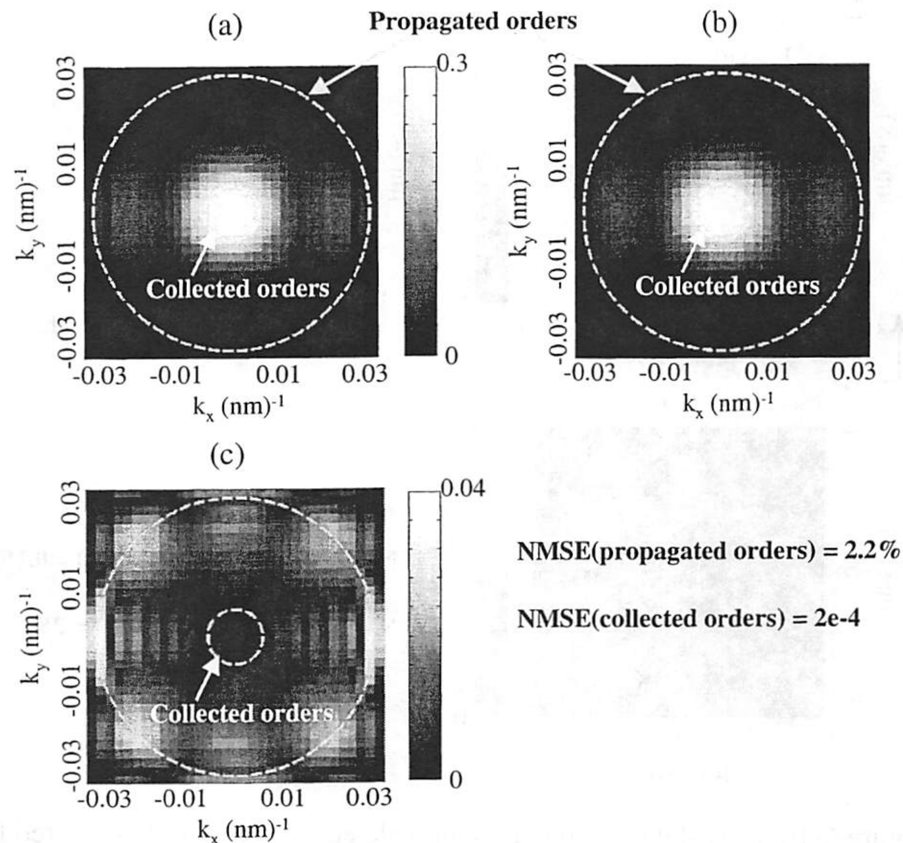

Figure 6-9. Edge-DDM applied on an isolated square hole (spectrum)

Magnitude of the plane wave spectra of the near field plots in Figure 6-8. Spectrum of the synthesized (edge-DDM) field in (a) and of the rigorous field (from 3D simulation) in (b). The spectrum of the error is depicted in (c). The error level within the collected orders circle is seen to be an insignificant 0.02%.

$|\vec{k}| \leq 2\pi NA(1+\sigma)/\lambda R$), for NA=0.75, R=4 and σ=0.3, are indicated on these plots. The magnitude of the error in the spectrum of the field obtained from edge-DDM is shown in Figure 6-9(c). Observe that most of the error is concentrated in the higher spatial frequencies for $|k_x|$ approaching 0.03 and only small levels of error exist in the collected orders. The normalized mean square errors of all propagated and collected orders are 2.2% and 2E-4 respectively.

Similarly, the amplitude of the scattered fields across the observation plane below the isolated island obtained with the edge-DDM and with fully rigorous 3D simulation and the amplitude of the error are shown in Figure 6-10. Again, a locally significant error

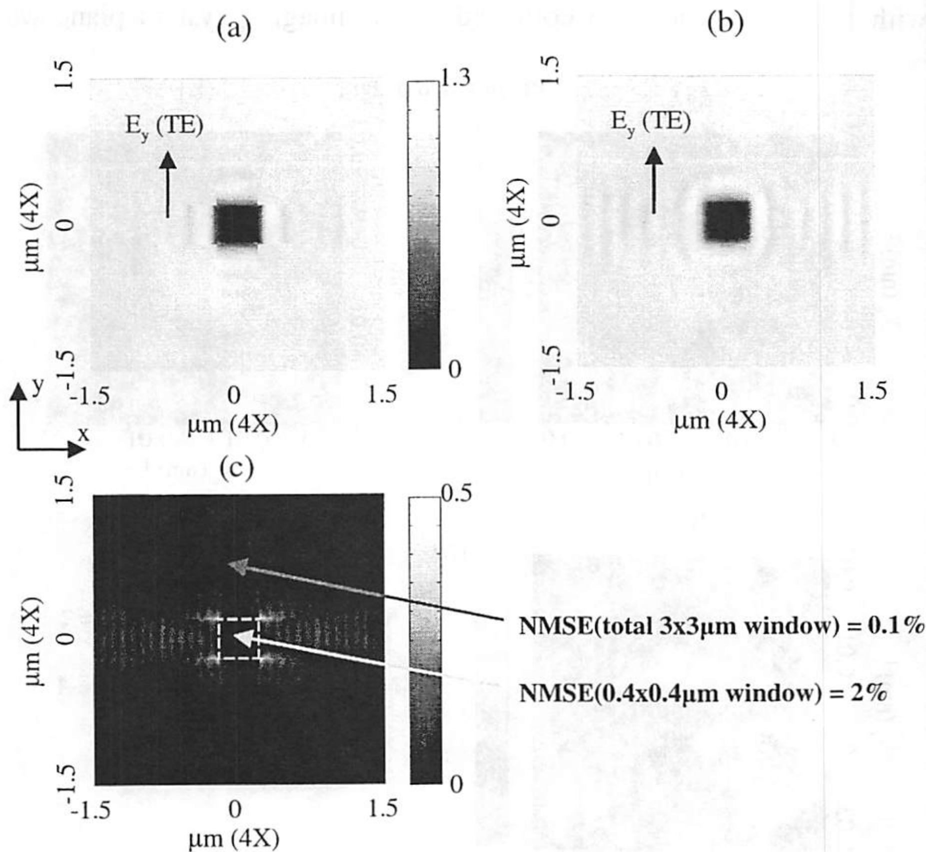

Figure 6-10. Edge-DDM applied on an isolated square island (scattered field)

(a) Synthesized with the edge-DDM and (b) rigorously calculated scattered field (amplitude), across the observation plane below a 400nm x 400nm isolated island (post). A 180° etch and 50nm undercut has been applied. The amplitude of the error (difference of r-mask from edge-DDM) is shown in (c). Locally the amplitude of the error reaches the 50% level, but the normalized mean square error does not exceed 2%.

amplitude near the corners is evident. However, the energy of this error is concentrated mostly at the higher spatial frequencies, for $|k_x|$ approaching 0.03 and the error in the collected orders is seen to be small, only 0.16% in a NMSE sense. Note that the large DC component of the isolated island mask layout was subtracted in order to make meaningful comparisons of the edge-DDM with fully rigorous simulations. Otherwise this large DC component would artificially show an even better accuracy, since the error level in comparison with a much stronger signal (containing the DC term) would be smaller.

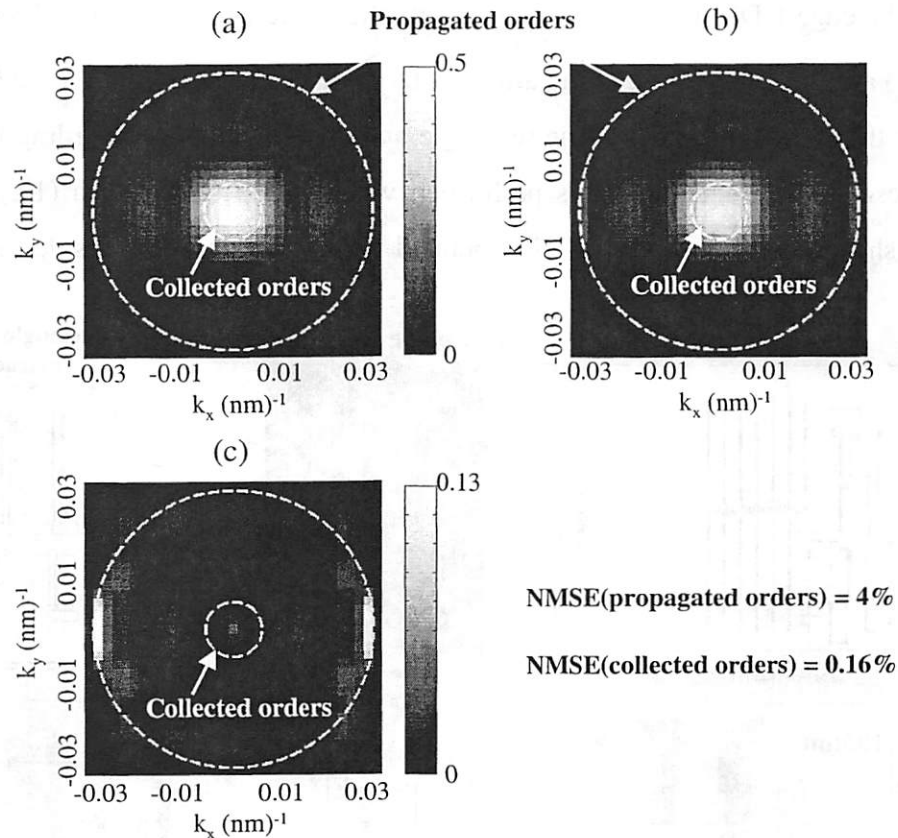

Figure 6-11. Edge-DDM applied on an isolated square island (spectrum)

Magnitude of the plane wave spectra of the near field plots in Figure 6-10. Spectrum of the synthesized (edge-DDM) field in (a) and of the rigorous field (from 3D simulation) in (b). The spectrum of the error is depicted in (c). The error level within the collected orders circle is only 0.16%.

It is worth mentioning that each fully rigorous mask simulation of the patterns of Figure 6-8 and Figure 6-10 that was performed with TEMPEST used approximately 1.8Gbytes of memory and required almost 2 days on a 550Mhz CPU. On the other hand, once all of the required 2D edge simulation results are available the scattered field can be

obtained with the edge-DDM in less than 1sec! The simulation of the isolated edge-diffractions is an off-line procedure. It only needs to be performed once and the edge-diffraction results are recycled as many times as are necessary for the reconstruction of the scattered fields of arbitrary layouts. In the above examples, it took approximately 5min for each rigorous, isolated-edge 2D simulation.

6.2.4. Example of edge-DDM on a large, arbitrary layout of a 0°/90°/270° alt. PSM

The edge-DDM is used here to generate the scattered field from a three level (0°/ 90°/270°) alt. PSM. A portion of the arbitrary target layout is shown in Figure 6-12 before and after the phase assignment. The rectangle and edge extraction according to the algorithm presented in Section 6.2.1 is performed within the 3μm by 4μm (1X) coherence window shown and the scattered field obtained with the edge-DDM inside the 12μm by

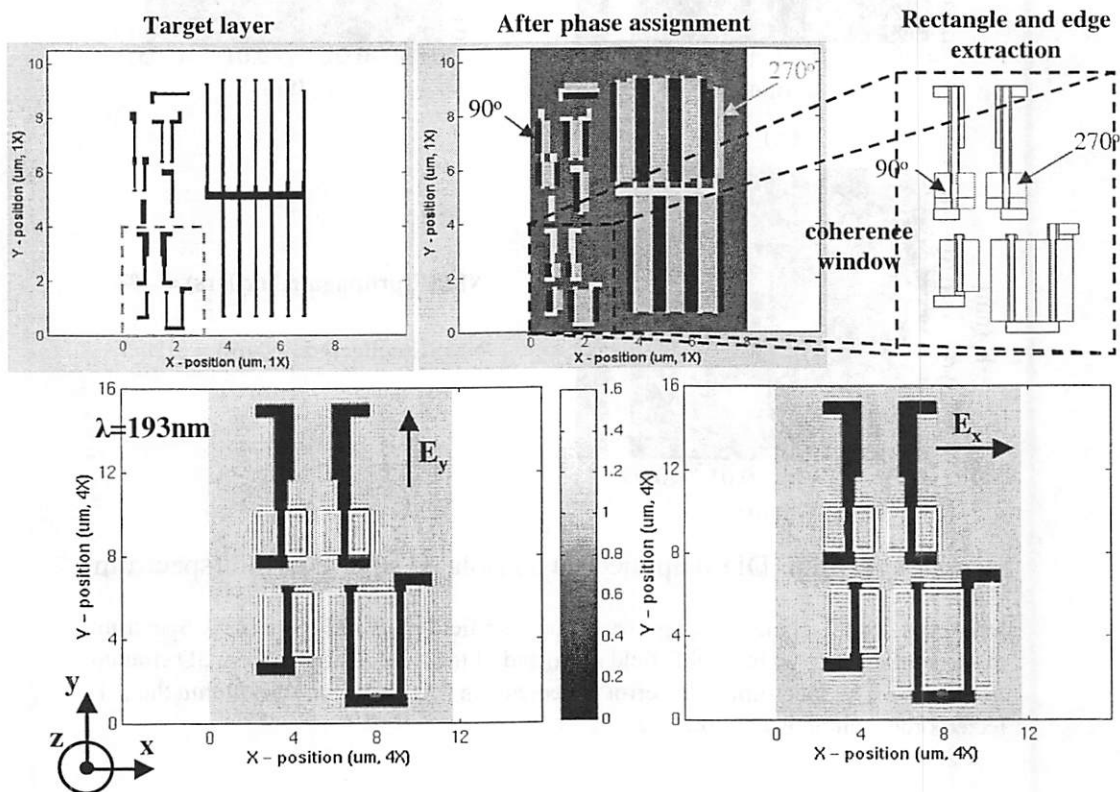

Figure 6-12. Example: Edge-DDM on a large 2D mask layout (algorithm and near fields)

The target mask layer and the mask after assignment of an arbitrary layout are shown. A three phase-level alt. PSM is assumed (0°/90°/270°). The rectangle and edge extraction within the 3μm by 4μm (1X) coherence window for the various polygons is also shown. Finally, the scattered near field within the coherence window for both TE and TM (λ=193nm) illumination is depicted.

16μm (4X) coherence window is also shown in Figure 6-12 for TE and TM illuminations at λ=193nm. Note that a fully rigorous 3D mask simulation of a 12μm by 16μm (4X) layout would require close to 40Gbytes of memory and would only be feasible on a multi-CPU architecture. The scattered field is obtained with the edge-DDM implementation in less than 1min. This time includes the polygon and edge extraction and the field synthesis from pre-calculated edge-diffractions. Therefore, the results of the edge-DDM cannot be immediately compared with a fully rigorous solution, but the accuracy of the edge-DDM within the imaging system's collection ability can reveal the inaccuracies of the ideal k-mask, where all transitions are assumed perfectly sharp. This is done in Figure 6-13, where the images (at the 30% intensity level) obtained with the k-mask and the edge-DDM for two different undercuts (0nm and 50nm) are compared. The system parameters are

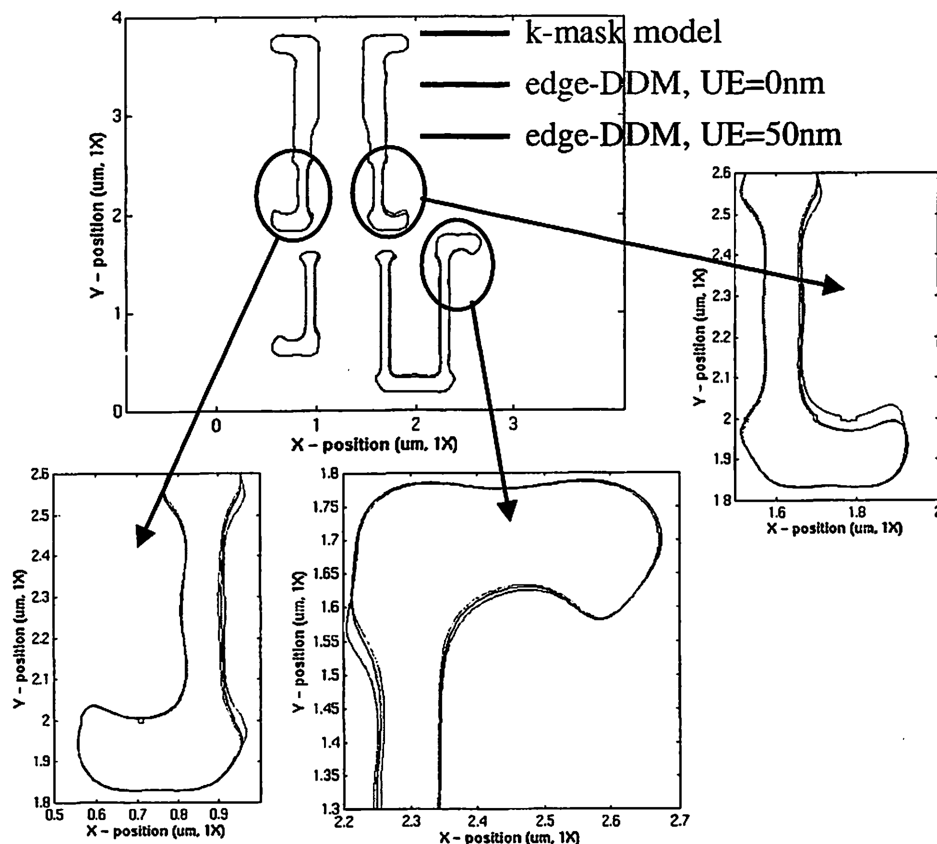

Figure 6-13. Example: Edge-DDM on a large 2D mask layout (images)

Image (30% intensity contours) of the layout within the 3μm by 4μm (1X) coherence window of Figure 6-12. The ideal k-mask (Kirchhoff-mask) model is compared with the edge-DDM for an undercut of 0nm and 50nm. The edge-DDM is capable of revealing the inaccuracies of the k-mask model and of accurately taking into account the edge-scattering of different edge profiles.

λ=193nm, NA=0.7, σ=0.3 and R=4. The inaccuracies of the k-mask model are revealed at various locations in the image as seen in Figure 6-13. The effect on the image of changing the undercut from 0nm to 50nm can be quickly and accurately evaluated. Observe the subtle differences evident in the intensity contours of the 0nm and 50nm masks of Figure 6-13.

6.3. Further speeding-up the edge-DDM

Although the edge-DDM presented earlier achieves excellent accuracy and tremendous speed-ups as compared to a fully rigorous mask simulation, there is still one more parameter to exploit in order to further speed-up the method. As was shown in Chapter 4, where the matched Kirchhoff mask model (mk-mask) was developed, there is no need to carry all the details of the true field scattering as far as the imaging process is concerned (with larger than 1 reduction factors), since the higher spatial frequencies are not used. If a lumped parameter model can be devised that closely matches the TTL spectrum of the scattered field then the task of an accurate field representation is accomplished. In Chapter 4 a rect-function, a raised cosine function and a Gaussian function were seen to successfully mimic the TTL spectra of scattered fields from various size and profile openings. A similar principle can be applied here with the purpose of matching the TTL spectra of edge-diffracted fields. Assuming a restriction to piecewise constant models, the scattered field from an isolated edge under TE or TM illumination can be approximated using the multi-step functions shown in Figure 6-14. Although not shown in Figure 6-14, the amplitude, phase and size of all steps are optimized to achieve the best spectral matching of the collected (TTL) orders with the orders resulting from the continuous edge-diffracted field. Note that the key factor for a good spectral match is to capture the finite extent of the "off-on" edge-transition. A piecewise constant function is probably not the best choice to achieve this task, but on the other hand a piecewise constant function offers a good lumped parameter approach and it lends itself nicely as an extension of the unmatched Kirchhoff approach, where all edge-transitions are assumed perfectly sharp.

If the matched bandwidth edge-DDM is applied on the 400nm by 400nm (4X) isolated hole of Figure 6-8 the scattered field across the observation plane can be represented in the compact way shown in Figure 6-15(a). Recall that the edges parallel to the y-axis

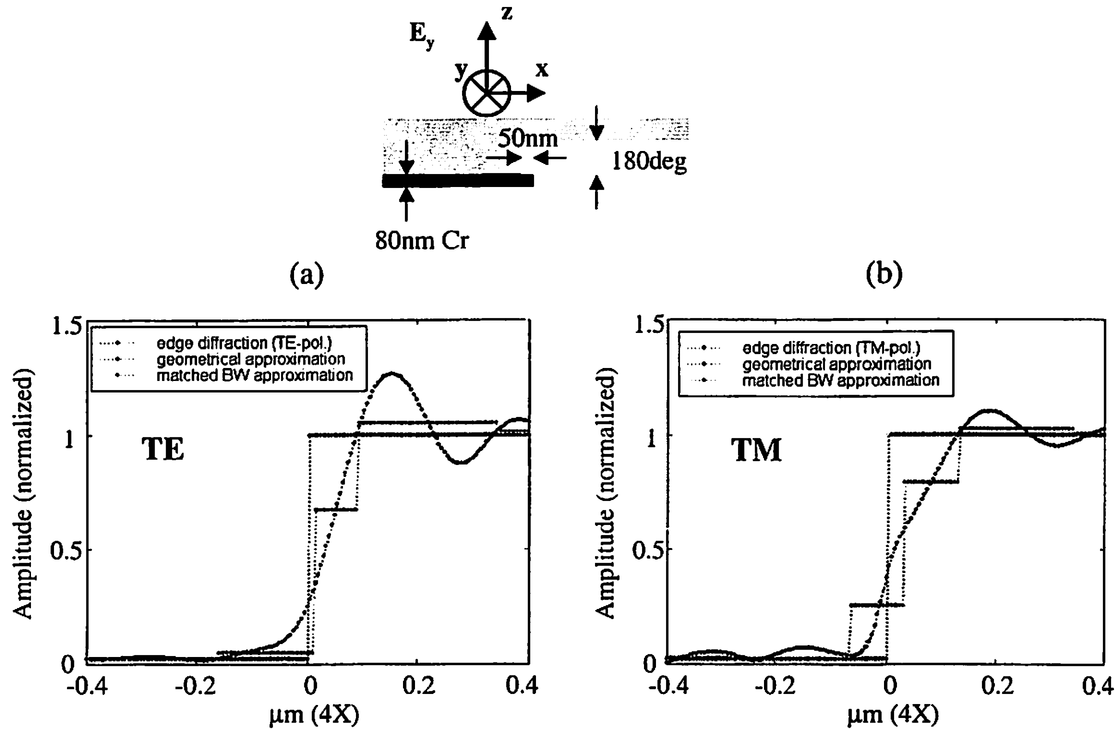

Figure 6-14. Matched bandwidth approximation to edge-diffraction

Instead of approximating the true edge-diffraction by a single step function (geometrical or Kirchhoff approximation) a multi-step piecewise constant function is employed. The amplitudes, phases and sizes of all steps are optimized to achieve the best spectral matching of the collected orders with the orders resulting from the continuous edge-diffracted field. The matched bandwidth approximations to the field diffracted by a 180° edge with 50nm undercut under TE and TM illuminations are shown in (a) and (b) respectively.

"see" TE polarization and the edges parallel to the x-axis TM polarization. The multi-step matched BW approximations to the edge-diffraction shown in Figure 6-14 for TE and TM illuminations intermingle in the x- and y-directions to produce the multi-color mask of Figure 6-15(a), where each color represents a different amplitude and phase region of the mask. The spectrum of the error of this approach is depicted in Figure 6-15(b). Note that compared to the error shown in Figure 6-9(c) this error has increased by almost four-fold. Nevertheless, the error in the TTL spectrum still remains at low enough levels for accurate imaging simulations. A better approximating function, other than the piecewise constant step function, that is more capable of capturing the true edge-diffraction profile (such as linear or higher order polynomial) should result in better spectral matching and consequently more accurate imaging simulations.

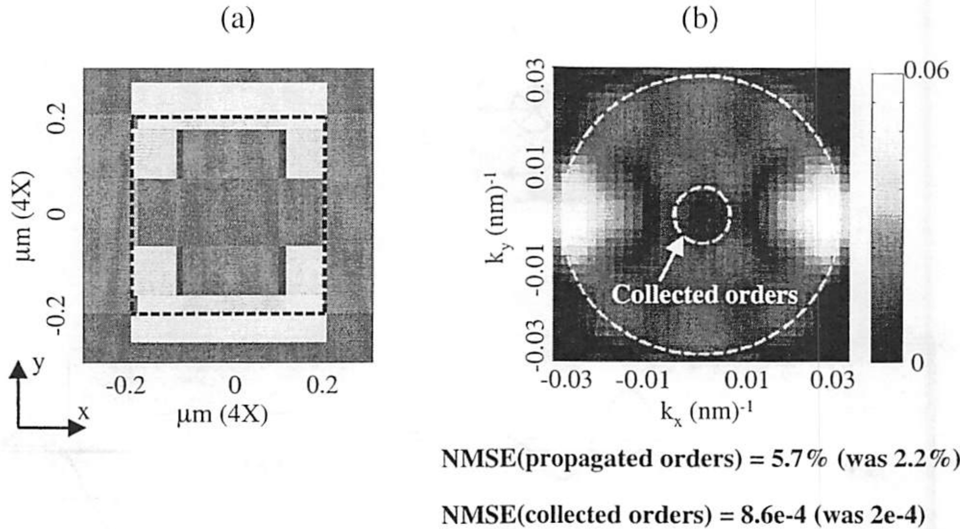

Figure 6-15. The matched BW edge-DDM applied to the hole of Figure 6-8

(a) Representation of the scattered field below a 400nm by 400nm hole (etched depth 180°, undercut=50nm) using the matched bandwidth edge-DDM, as shown in Figure 6-14. Each color represents a different amplitude and phase region of the mask. The spectrum of the error of the representation shown in (a) compared to the true solution of Figure 6-8(b) is depicted in (b). The error level within the collected orders circle is seen to increase from 0.02% to 0.086%.

6.4. Conclusions

This Chapter has dealt with the development of the edge-DDM (edge domain decomposition method). This method is an extension of the domain decomposition methods proposed and developed in Chapter 4 that introduces tremendous versatility, since only a small number of isolated edge-diffraction simulations is shown to contain all the necessary information for the synthesis of the scattered field from arbitrary 2D mask layouts and subsequent accurate imaging simulations. The limits of this method are reached when the mask features are smaller than a wavelength in size and the vertical mask topography is large. Through a systematic process it was determined that features as small as at least 200nm bearing 270° of phase-wells can be accurately decomposed *via* the edge-DDM, at λ=193nm. The method was tested for simple 2D layouts, where rigorous mask simulations are possible. Excellent accuracy accompanied by speed-up factors of 172,800 (1sec *vs.* 2days) were demonstrated. The accuracy of the method was attributed to the fact that on one hand the edge-diffraction phenomena are modeled rigorously through 2D edge-diffrac-

tion simulations and that on the other hand the errors incurred during the synthesis (primarily near the corners) are mapped at the extremities of the spectrum of propagating plane waves and do not contribute to the image formation. It was emphasized that all necessary rigorous 2D simulations of the diffraction from isolated edge profiles is performed off-line and recycled for the diffraction calculation of arbitrary layouts. If needed, the accuracy of the edge profile diffraction simulations can be pushed to extreme limits, since it is performed only once. This can aid for example in the correct simulation of unusual edge profiles whose geometrical details would require excessive discretization of the domain. It was also shown that the exact details of the edge-diffraction are not necessary for accurate imaging simulations (with larger than 1 reduction factors) and a piecewise constant, multi-step edge-transition model that matches the TTL spectrum was introduced. The range of validity of the edge-DDM is expected to be appropriate for rapid and accurate evaluation of aerial images whenever speed is critical, as for example in full-chip OPC software and die-to-database comparisons in the inspection of alt. PSMs.

7 Characterization of Phase Defects in Phase Shift Masks

PHASE-SHIFTING MASKS (PSMS) have shown promise in increasing the resolution and depth of focus in photolithography. Alternating phase-shifting masks (alt. PSMs) are one of the two most widely accepted types of PSM (the other being attenuated). Their fabrication process involves at least one quartz etching step, during which the patterned binary (Chromium on quartz) mask attains the required 180° phase difference between alternating sides of the Chromium-covered quartz. During the quartz etching process phase defects can occur, which are generally arbitrarily shaped three dimensional posts of quartz or voids in the clear area.

The strange electromagnetic behavior of light passing through phase-edges examined in Chapter 5, where it tends to emanate from the high refractive index material and deplete the low refractive index material ([105], [109]) can aid in understanding the impact of phase defects, since at a first glance they can be viewed as a number of phase-edges in close proximity. Recent simulation and experimental studies have related the deterioration of the feature linewidth with the size of phase defects and have also given an example of the fundamental difference between the two types of phase defects, namely quartz posts and voids in the quartz [23], [93], [30], [33], [4].

The main two themes of this Chapter are the following: First, imaging simulations that utilize the fully rigorous r-mask model are used to assess the tendency of non-planar phase defects to print in optical lithography with alternating phase-shifting masks. A schematic diagram of a defective alt. PSM is shown in Figure 7-1, where both types of defects are depicted. The steady state electromagnetic field throughout the volume of the mask structure is calculated with TEMPEST under the excitation of a harmonic, linearly polar-

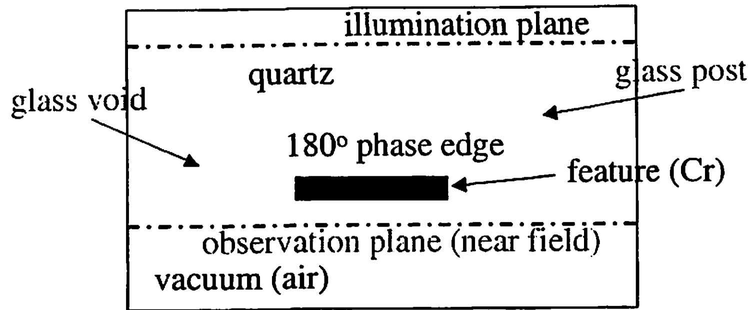

Figure 7-1. Schematic diagram of a defective alt. PSM

Both types of phase defects are shown (voids and posts). The 180° phase edge is located at the center behind the Chromium feature (50% underetch). Incident light originates from the illumination plane and the full vector electromagnetic solution is calculated with TEMPEST everywhere in the domain.

ized and normally incident plane wave, with illumination wavelength λ=248nm, originating from the illumination plane. The diffraction orders at the observation plane are then extracted as described previously and form the input to the imaging program (SPLAT) in order to calculate the aerial image. The imaging system assumed in this first part is aberration free and has NA=0.68, σ=0.3 and a reduction factor R=4. Initially, isolated phase defects are considered and their ability to transmit the electromagnetic field while shifting its phase is determined as a function of their lateral size. Then, the aerial image linewidth variation of isolated and dense features with CD_{mask}=150nm (1X) is determined in the presence of various phase defects.

In the second part of the Chapter, a domain decomposition strategy appropriate for handling wavelength sized phase defects is developed.

7.1. Phase and brightness of isolated phase defects

Light that travels the same distance h in two different lossless materials with refractive indices n_1, n_2 will have a phase difference in the electric field given by: $\mathrm{l} = \frac{2\pi}{\lambda} \cdot h \cdot (n_1 - n_2$, where λ is the illumination wavelength. The sign of this phase difference is chosen to accommodate a time retarded field emanating from the high refractive index material, where the velocity of propagation is smaller. Therefore, at λ=248nm where the refractive index of quartz is n_g=1.508 a phase defect (line/post or scratch/void) with

height h=240nm should transmit the electric field without changing its amplitude but with a phase difference of approximately -180° or +180° with respect to its surrounding. In this most frequently assumed ideal geometrical model for phase defects the phase shift depends only on the height of the defects and not on their lateral size. In the following, the ideal 1/180° model for phase defects is shown to be incorrect in most cases and the actual transmission and phase characteristics are seen to depend strongly on the lateral dimensions of the defects as well.

Figure 7-2(a) depicts the normalized amplitude of the near electric field in the vicinity of an isolated quartz line defect of height h=240nm and width w=200nm, when it is illuminated with a normally incident, linearly polarized plane wave with λ=248nm. Figure 7-2(b) and (c) show the amplitude and phase of the complex electric field across the observation plane. The observation plane is located 100nm below the quartz line. It is evident that

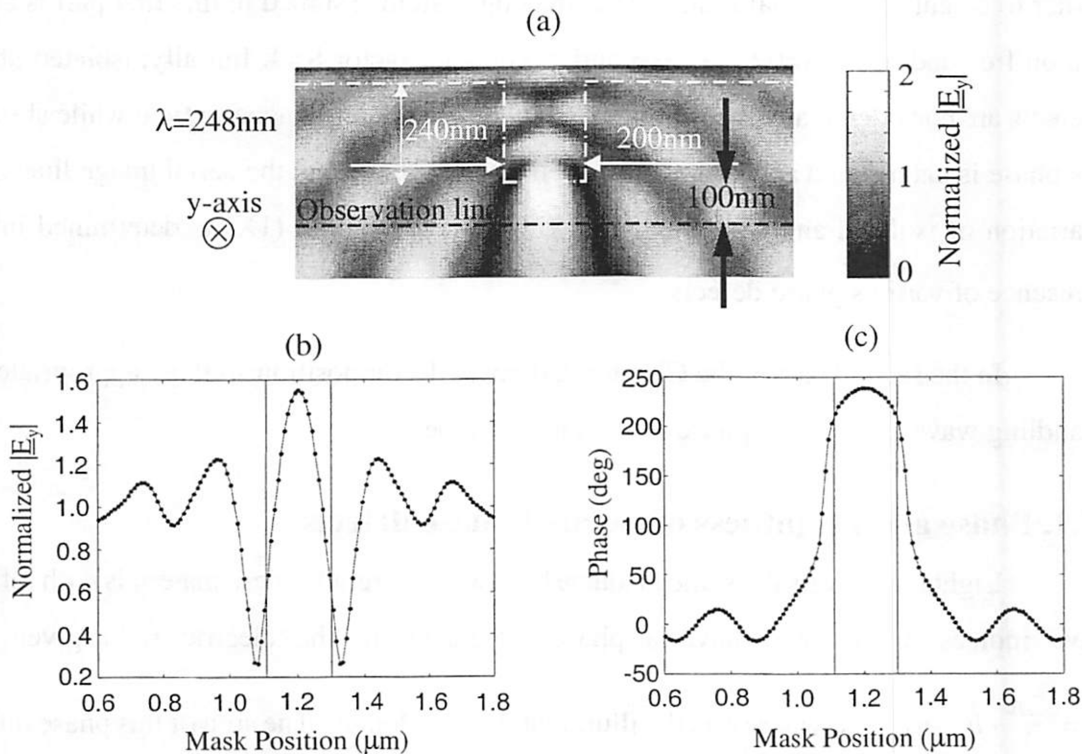

Figure 7-2. Isolated line defect

(a) Normalized amplitude of the near electric field in the vicinity of an isolated quartz line defect of height h=240nm and width w=200nm, when it is illuminated with a normally incident, linearly polarized plane wave with λ=248nm. (b) and (c) Amplitude and phase of the complex electric field across the observation line respectively.

the average amplitude across the geometrical shadow of the defect, which is denoted by the two vertical lines, is larger than one, immediately drops sharply, and further has shorter peaks and valleys. Also, the average phase at the geometrical shadow of this defect is 230°, or a change of only -130° in the interval (-180°,180°). Figure 7-3(a) depicts the normalized amplitude of the near electric field throughout the cross-section of an isolated quartz scratch defect of depth h=240nm and width w=200nm. Figure 7-3(b) and (c) show the amplitude and phase of the complex electric field across the observation plane, respectively. The average light intensity below the defect is much less than the unit intensity of the surrounding clear area and the average phase only goes down to 60° instead of 0° as expected by geometric optics. There is an even more pronounced deviation from the ideal 1/180° model in 3D as shown in Figure 7-4 for an isolated quartz post and void of equal height (or depth) h=240nm, having a 200nmx200nm square lateral cross-section. The aver-

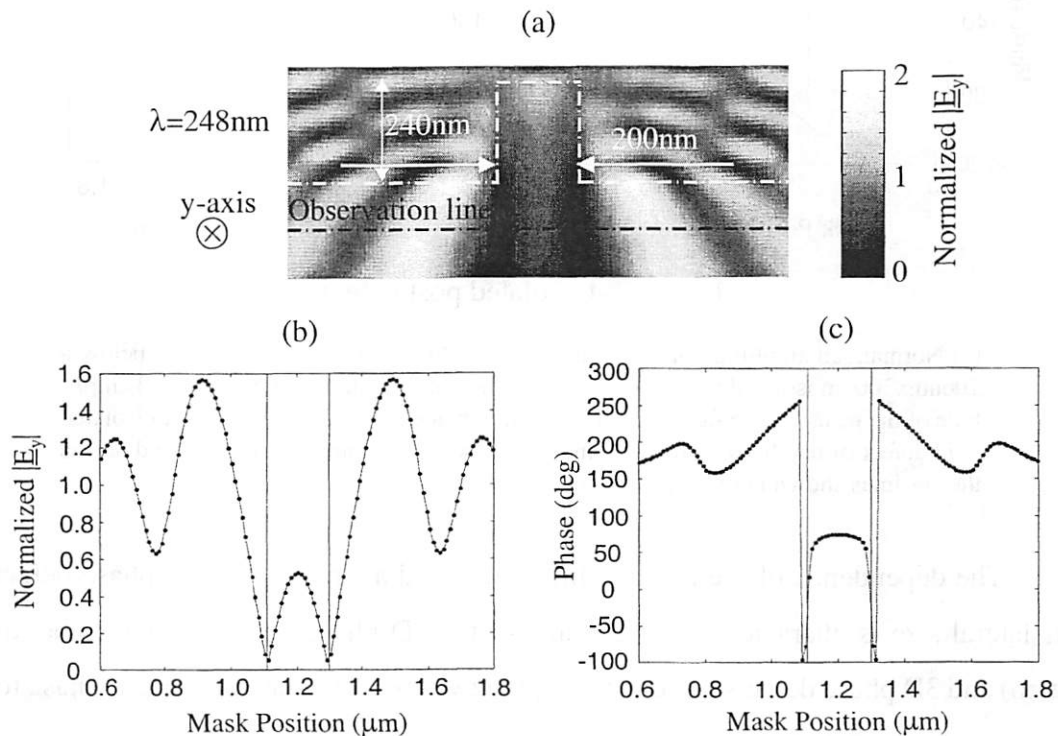

Figure 7-3. Isolated space defect

(a) Normalized amplitude of the near electric field in the vicinity of an isolated quartz scratch defect of depth h=240nm and width w=200nm, when it is illuminated with a normally incident, linearly polarized plane wave with λ=248nm. (b) and (c) Amplitude and phase of the complex electric field across the observation line respectively.

age brightness (squared amplitude) and phase for the post are 2.1 and -90°, whereas for the void they are 0.1 and 145° respectively.

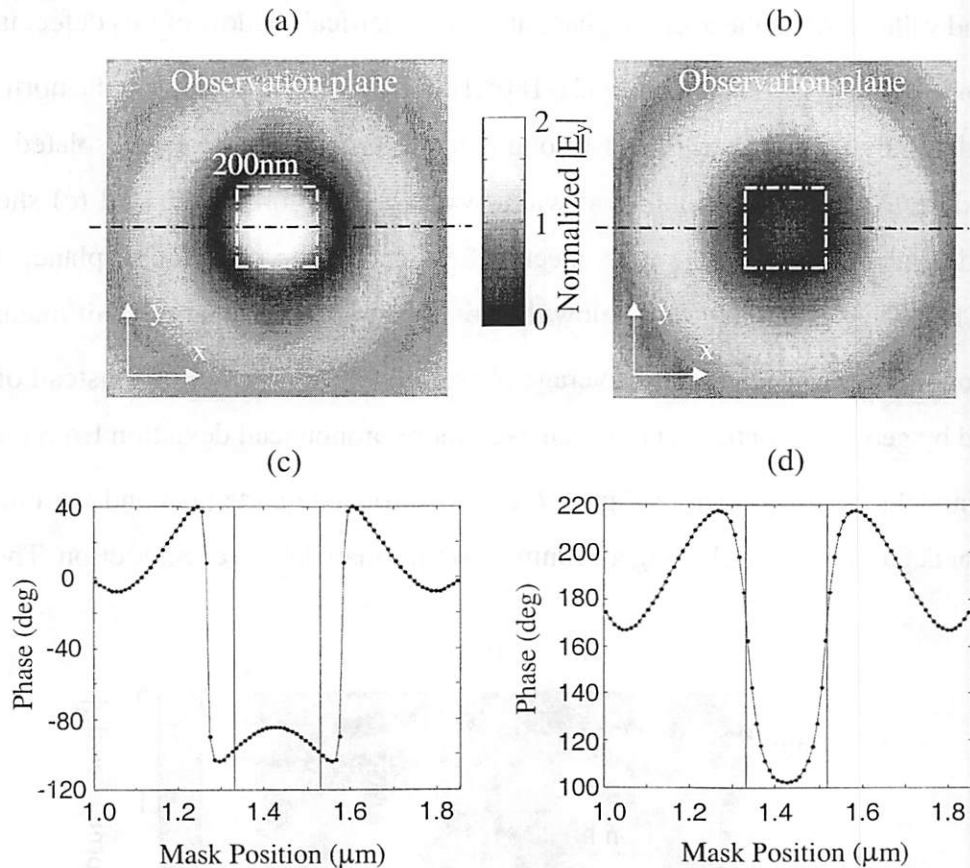

Figure 7-4. Isolated post defect

(a) Normalized amplitude of the near electric field at the observation plane below a 200nmx200nm isolated quartz post defect of height h=240nm. (b) Normalized amplitude of the near electric field at the observation plane below a 200nmx200nm isolated void defect of depth h=240nm. (c) and (d) Phase of the complex electric field across the cut-lines shown in (a) and (b) respectively.

The dependence of the average brightness and average phase of phase defects on their lateral size is characterized in Figure 7-5 for 2D phase defects (quartz line, quartz scratch) and 3D phase defects (quartz post, quartz void). Note that the average phase for 3D defects deviates faster from the background phase (0° for posts, lines and 180° for voids, scratches) than does the phase for 2D defects. Even for large 2D defects the phase is significantly different than the background phase. Figure 7-5(c) shows that the average brightness of protruding phase defects (posts, lines) is larger than 1 and posts (3D) appear much brighter than lines (2D). The average brightness of scratches and voids is seen in Figure 7-

5(d) to be less than 1 and it attains a minimum at a defect size of approximately one free-space wavelength. The fact that voids appear darker than posts (or equivalently scratches are darker than quartz lines) can be understood by viewing the phase defect as four phase edges in close proximity, where light depletes the air-filled regions and concentrates in the quartz-filled regions.

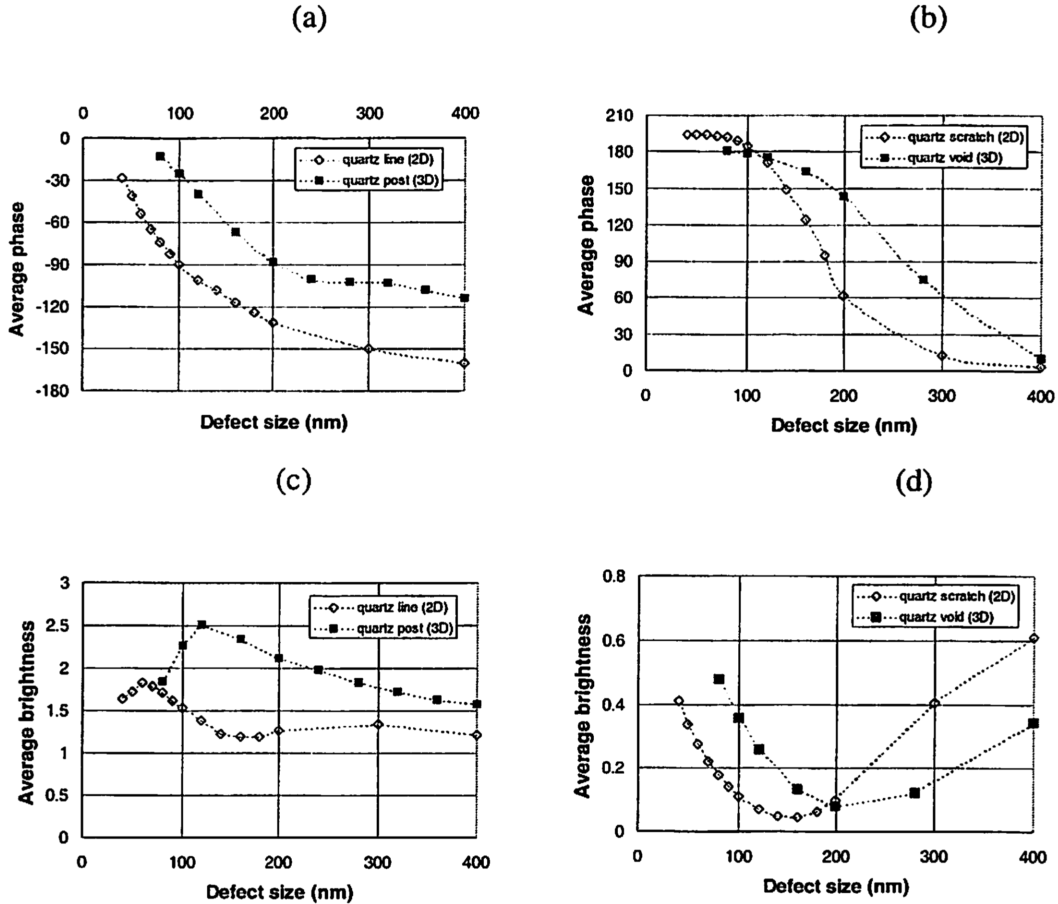

Figure 7-5. The effect of defect size

(a) and (b) Average phase and (c) and (d) average brightness (squared amplitude) of the complex electric near field underneath a phase defect versus its size for lines/posts and scratches/voids. The height (depth) is held constant in all cases at h=240nm.

The minimum intensity of the aerial image for isolated posts and voids is plotted in Figure 7-6 with respect to defect size for phase defects with square lateral shape. Posts larger than 150nmx150nm cause a dip in intensity almost twice as large as the dip caused by voids of equal size. The ideal 1/180° model for phase defects, which does not distin-

guish between posts and voids, predicts an intensity dip that is between that of a post and a void. The minimum intensity of the aerial image for isolated square Chromium defects is also plotted in Figure 7-6 versus their size for comparison. The fact that voids smaller than 150nmx150nm approach this curve indicates that they are acting almost like opaque defects of equal size.

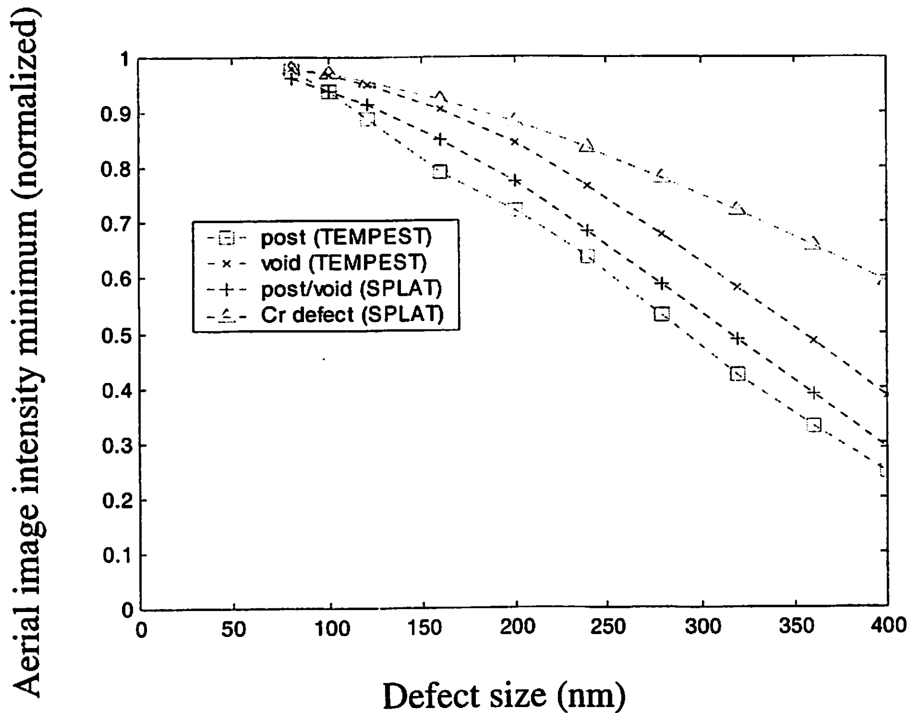

Figure 7-6. Minimum intensity of the aerial image for isolated posts and voids with respect to defect size for phase defects with square lateral shape and h=240nm. The minimum intensity caused by Chromium (opaque) defects is also shown for comparison.

7.2. Simulation results for defective alt. PSMs

The aerial image degradation of the critical dimension (CD) of 150nm (1X) isolated lines and dense line/space patterns was evaluated in the presence of 3D phase defects. Quartz posts and voids of various shapes, sizes and heights were placed at various distances from the features, while varying the amount of underetch and polarization direction of the illumination. The CD_{aerial} was evaluated at the 30% level of the normalized intensity and a comparison was made in each case between the worse CD_{aerial} of the defective mask and that of the defect-free reference mask.

Figure 7-7(a) depicts the fractional change of CD_{acrial} $((CD_{defective}-CD_{reference})/CD_{reference})$ versus defect size. The triangles are the 1/180° geometrical model and serve as a point of reference. A 50nmx50nm (1X) post or void is predicted to produce a 10% linewidth variation. Void defects are less than 50% as harmful to the aerial image than posts of equal size. For example, a 50nmx50nm (1X) void results in a 5% aerial image linewidth variation in a dense line/space pattern, whereas a post of the same size results in a potentially catastrophic 13%! The ideal 1/180° model for phase defects (triangles) overestimates the linewidth variation caused by a void defect by as much as 100% and underestimates the linewidth variation caused by a post defect by as much as 40%. These results are in excellent agreement with the recently presented experimental evidence by Chen *et al.* [23]. Fully buried defects cause minimal linewidth variations and should not be a problem, but when they become so large that one of their phase edges exceeds the Chromium edge of the feature they can result in significant (>10%) linewidth variations. Additional simulations also suggested that the above observations hold regardless of the polarization direction of the incident radiation and the exact shape of the defect. In particular, various small shape perturbations were tested and they resulted in almost equal linewidth variations, which renders the simplification of parallelepipedly shaped defects valid. This result was independently verified by Pistor [67].

The fraction of underetch (with respect to the full feature size) was found to have no impact on the linewidth variation of a defective mask, unless no underetch is applied, in which case the interaction of the phase edge and the defect result in an abrupt increase in the linewidth variation. This is shown in Figure 7-7(b), where for a 70nmx70nm defect the fractional change of CD_{aerial} jumps from 30% for 50% underetch to 100% (bridging of the lines) for no underetch.

The effect of the defect height on the printability of defects is explored in Figure 7-7(c). The fractional change of CD_{aerial} is plotted versus the deviation of the defect phase from 180° (a defect shorter than h=240nm corresponds to a height-phase smaller than 180°, therefore the shorter it is the larger its deviation from 180°). The fractional change of CD_{aerial} declines slowly when the phase deviation increases, or equivalently when the

defect becomes shorter. Similar observations can be found in the recently presented experiments in [23]. There is an immediate impact of this observation in the repair process, in that the partial removal of the phase defect is not as effective as predicted by the 1/180° model.

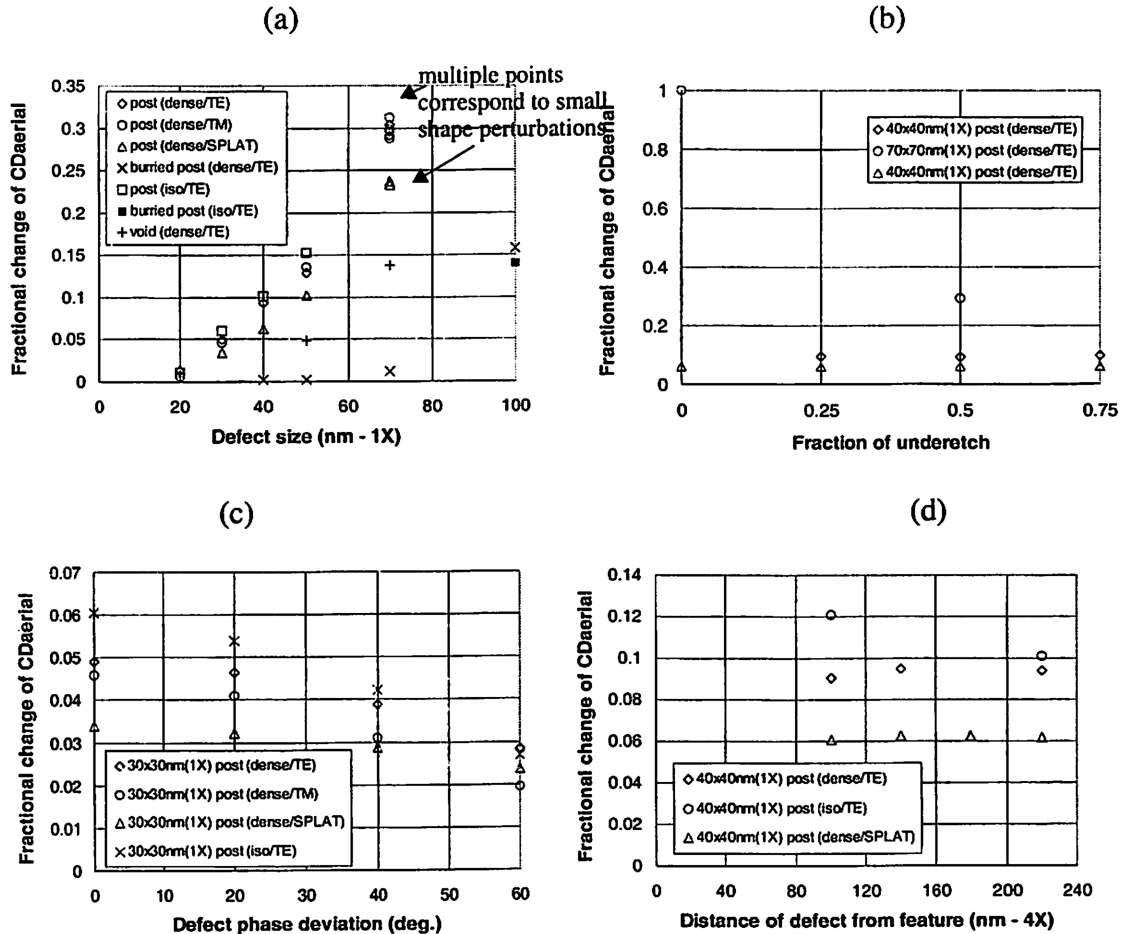

Figure 7-7. Defect printability dependence

(a) Fractional change of CD_{aerial} at the 30% intensity level with respect to defect size for 150nm (1X) isolated lines and dense line/space patterns. The impact of posts, voids and buried posts under different polarizations (TE or TM) is depicted. The effect of ideal 1/180° phase defects (denoted by the triangles) is also shown for comparison. Defect non-planarity and sidewall angle changes produced only small additional CD variations as indicated by the clusters of points so labeled. (b)-(d) Fractional change of CD_{aerial} versus the amount of underetch, phase deviation (defect height) and proximity to the feature respectively.

The fractional change of CD_{aerial} is plotted with respect to the location of the defect in Figure 7-7(d). For the dense line/space pattern the location of the defect is irrelevant for the linewidth change, whereas for an isolated line placing the defect closer to the line

appears to result in a larger linewidth error. This was verified experimentally by Tejnil *et al.* in [93].

7.3. Efficient phase defect modeling *via* DDM

The bright future for alt. PSMs as a major resolution enhancement technique (RET) has been plagued primarily by the difficulty to reliably inspect them, flag locations that phase defects are present and subsequently repair the defective locations. State-of-the-art inspection systems utilize a focused laser beam that can be either *at-wavelength* (up to λ=248nm), meaning that the wavelength of the inspection beam is the same as the wavelength that the alt. PSM was designed for[1], or emit light of a larger wavelength. This beam scans the entire mask and the reflected or transmitted scattered fields from the particular mask location under inspection are imaged with a very high resolution imaging system that typically has a reduction factor of R=1 and NA close to 1. But here is the caveat: After the signal from the inspection tool for a particular mask location is available it needs to be compared to something in order to determine whether or not a phase-defect (or other defect) is present within that location. Such a comparison is in general very difficult, because not only does it need to be accurate in order to reliably flag defective locations, but it also needs to be rapid enough for the entire reticle to be inspected in a reasonable amount of time.

The most promising direction that has been adopted by researchers working on the problem has been what is known as a *die-to-database* comparison. By that, it is meant that the local signal is compared to the signal that the same mask location would produce if it were defect-free. The problem now shifts to building the database of signals from defect-free masks. Note that all possible mask geometries that will be encountered in every inspected reticle need to exist in the database. One way to building the database would be to produce a (set of) test reticle(s) that includes every single geometry situation that is anticipated to exist in all designed layouts to come. This (set of) test reticle(s) is then metic-

1. Recall that the depths of the phase-wells in an alt. PSM depend on the wavelength and on the refractive index of the glass substrate, which is in turn a strong function of wavelength. Therefore, although the design leads to the required 180° path length difference between alternating apertures "at-wavelength", for different wavelengths this is not the case.

ulously inspected with a reliable tool (maybe an atomic force microscope - AFM) to guarantee that it is defect-free and finally all signals from the different locations are collected and placed in the vault (database). Clearly, the immensity of this task has to do not only with the *a priori* precise anticipation of what layout situations to take provision for, not only with manufacturing the test reticle(s), characterizing it and building the database, but also with the sheer volume of data that such a database would contain. Moreover, a precise diagnosis of the type, size and location of a phase defect requires an even larger database of benchmark signals, where every possible combination of defect type, size and location in every possible layout configuration needs to exist in the database. Performing such a task in a way similar to the one outlined is impractical.

Simulation can again come to the rescue, at least in principle. If a simulation tool that can rapidly and accurately predict the expected signal resulting from a defect-free or defective location on the mask is available, then the task of building the database is simplified tremendously. Moreover, if such a tool is really fast (and accurate of course) then a database is not even needed! The required benchmark signal from the defect-free layout is generated *in-situ*, while the inspection system gathers measurements. The problem with this solution is that to date there exists no simulation tool that possesses both the rapidity and accuracy properties. The family of simulation tools that rigorously solve Maxwell's equations around the reticle (such as TEMPEST) and subsequently use a vectorial formulation for the image formation to calculate the expected optical signal from the inspection system are impractical because of large memory and time requirements. On the other hand the accuracy of speedier simulation programs that circumvent the solution of Maxwell's equations around the mask is unacceptable.

Yet another important consideration of an inspection system for alt. PSMs should be the following: Phase-defects that are not critically affecting the image that a projection printing tool will produce on the wafer surface should be discarded, *i.e.* not flagged and not repaired. But this is also a difficult task, since the only bullet-proof way of achieving this would be to expose wafers with the suspect defect present and examine if the printed resist images have intolerable artifacts. Clearly, such a process now involves the close cooperation of the inspection system with the projection printing tool. However, an accurate and

properly calibrated simulation tool can alternatively assess the tendency of the defect to print or cause other image artifacts. Consequently, the costly step of exposing wafers can be avoided and a decision of repairing or not the defect rests fully upon the simulation result. Again, to date, results from no simulation tool, that is fast enough in calculating expected images with phase defects present, can be trusted to base repair decisions on.

The domain decomposition methods developed in Chapters 4 - 6 are appropriate for solving the problem of the rapid and accurate evaluation of the benchmark signal from non-defective masks for the inspection system. In this Section, a domain decomposition method is presented that addresses the problem of the defect printability assessment, after a defect is previously found. The generation of benchmark signals from defective mask locations can also be based on the domain decomposition technique, although more work will be needed to adapt it and test it for the high-NA inspection optics with R=1. As will soon be obvious, the speed and efficiency of the method are inherited by virtue of the domain decomposition methods presented in Chapters 4 - 6, although for simplicity in the present discussion the qr-DDM and edge-DDM of Chapters 4 and 6 are not explicitly employed in the following. In the simulation examples of this Section the illumination wavelength is 193nm and the phase-wells are designed accordingly, so as to provide the required phase shifts for that wavelength.

Consider the example depicted in Figure 7-8. In (a) the near scattered field below a small layout of a $0^o/180^o$ alt. PSM is shown when a square 120nm x 120nm (4X), 180° post phase defect is present at various locations within the layout. Note that although neither the layout nor the phase defect geometry change, a different simulation altogether is needed because of the different relative positions of the defect within the layout. Each one of the nine 3D simulations in the matrix shown in (a) take approximately 10hrs on a 450MHz CPU and utilize 300Mb of memory. Subsequently, the aerial images for all nine situations are calculated for an imaging system with R=4, NA=0.75 and σ=0.3. Then, the fractional change of CD_{aerial} at the middle and at the end of the line because of the defect is found for all nine defect locations and is shown in Figure 7-8(b). From the plot in Figure 7-8(b) it can be deduced that when the defect is located in the middle of the phase-

wells or is mostly "tucked" underneath the absorbing layer (columns 3 and 1 of Figure 7-8(a) respectively) the CD_{aerial} is not critically affected, but locations such as those in column 2 of Figure 7-8(a) cause larger CD_{aerial} variations. In the former cases the defects could probably be discarded whereas in the latter repair seems necessary. Clearly, the luxury of the 10hr-long simulations is only available as a proof of concept and such an approach is not viable for full-chip characterizations.

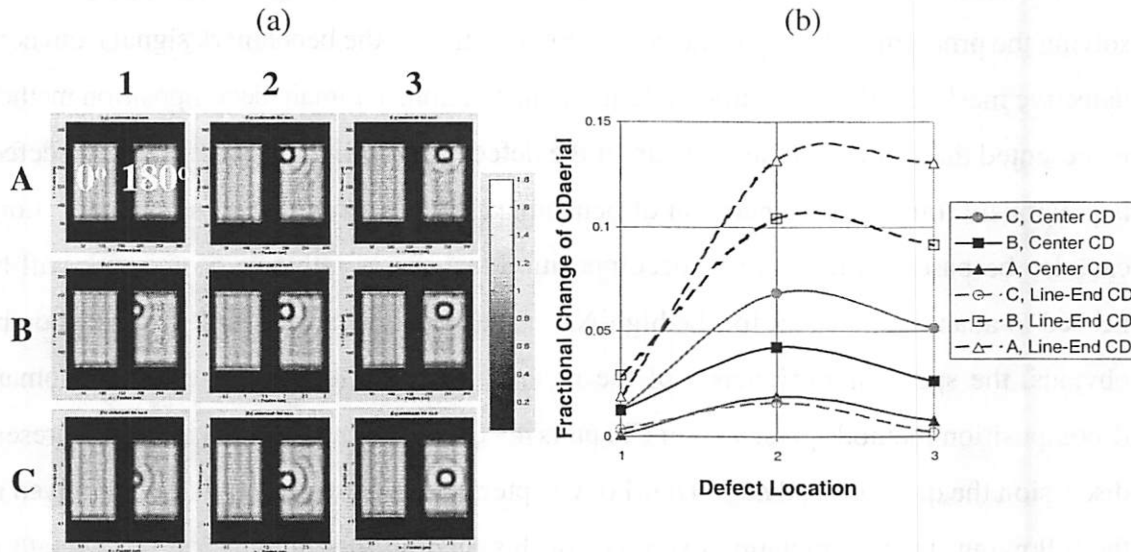

Figure 7-8. Defect printability assessment (the laborious way)

A square 120nm x 120nm phase defect (post) with 180° height causes different CD variations depending on its relative location with respect to the center line. In general, larger CD variation is evidenced when the defect is close to the line (column 2 in (a)). However, when the defect is partially covered by the Cr-layer of the line, smaller CD changes are observed. This is quantified in (b). The imaging system parameters are: λ=193nm, NA=0.75, R=4, σ=0.3. Note that each simulation in (a) requires ~10hrs on a 450MHz CPU.

Now, consider the paradigm shown in Figure 7-9. A domain decomposition method is again invoked, where instead of a one-step simulation of the defective layout two separate rigorous simulations are performed, one with just the defect-free layout and one with just the defect in clear surroundings. The scattered field below the defect is then shifted accordingly, such that the defect is effectively placed at the location it appears in the defective mask, and the uniform background light is subtracted, so as to retrieve the (complex) signal of the local perturbation that the defect causes. This perturbation is added to the defect-free layout signal for an approximation to the signal from the rigorous simulation of

the defective mask. The non-defective mask simulation can be performed rapidly using the decomposition methods of Chapters 4 - 6.

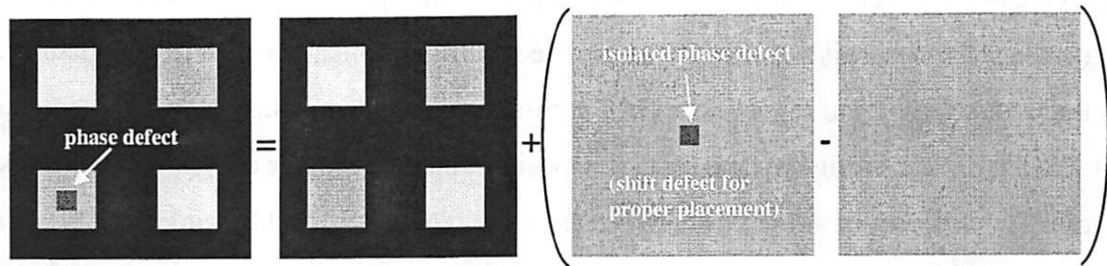

Figure 7-9. Domain decomposition method when a defect is present

A strategy can now be devised, where a database of the near electromagnetic field scattered from isolated phase-defects in clear surroundings is created for all possible potential defects that are critical. The volume of such a database can be reduced based on the earlier observations that defects with similar footprints (lateral dimensions) and small shape perturbations are equivalent from an electromagnetic point-of-view.

The suggested decomposition method will be introduced through the following example: Suppose a 150nm (1X), 1:1.5 semi-dense, 90°/270° alt. PSM contact mask. The layout and the scattered field across the observation plane under normal incidence E_y (TE) polarization are shown in Figure 7-10.

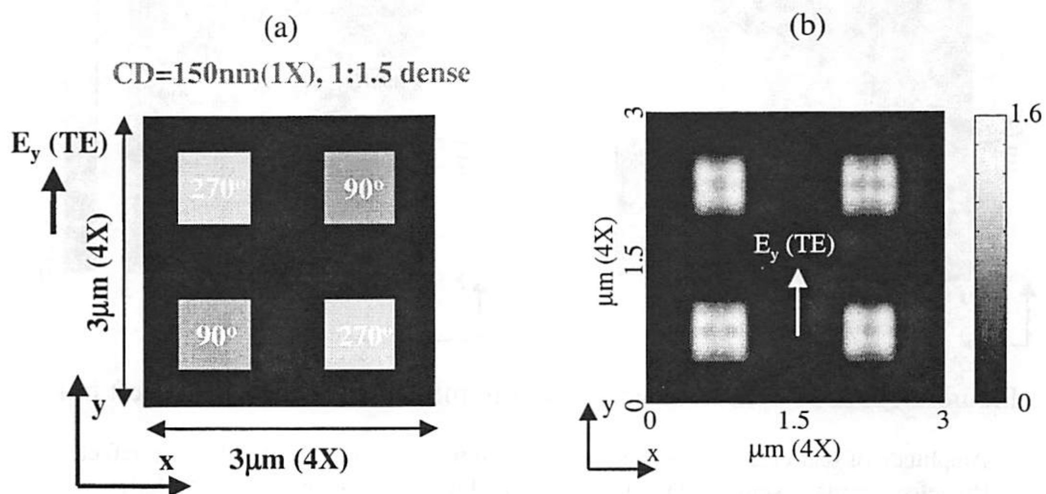

Figure 7-10. Example: 150nm (1X), 1:1.5 semi-dense, 90°/270° alt. PSM contact mask

(a) Layout and (b) amplitude of scattered field below the mask at the observation plane.

Now, suppose that a 200nm by 200nm (4X) 90° post defect is present in the center of the bottom left hole. According to the paradigm of Figure 7-9, the mask scattering simulation can be broken up into two constituent parts. This approach is shown in Figure 7-11. In (a) the phase defect is simulated in an isolated configuration at the location that it appears in the layout. In (b) and (c) the near field across the observation plane below the defective alt. PSM is shown, using the domain decomposition method and the complete mask respectively. The differences are not discernible from the plots of (b) and (c) and one has to look at the amplitude of the error in (d). Again, not only is the error level of the decomposition

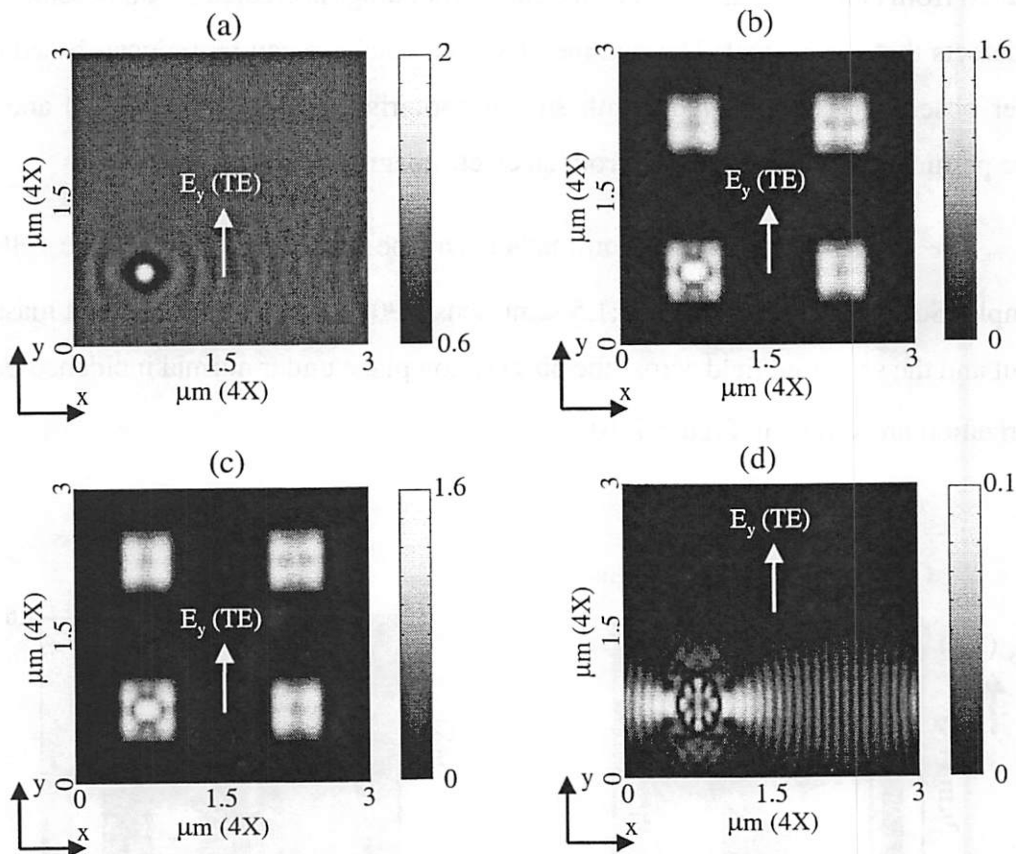

Figure 7-11. A 90° phase defect present in the center of the bottom-left hole

Amplitude of scattered field across the observation plane for (a) isolated phase defect, (b) defective mask simulated with the DDM and (c) rigorous (one-step) simulation of defective mask. The amplitude of the error of the DDM compared to the rigorous simulation is shown in (d). The normalized mean square error calculated at the bottom left (defective) quadrant is only 0.7%.

low, but the frequency content is very high, so that it will be filtered out by the imaging system.

Next, suppose that the same 90° post defect is present in the center of the bottom right hole. The important observation here is that *no new simulation is necessary for the decomposition method*! The scattering of the isolated phase defect can be recycled from the database, *i.e.* from Figure 7-11(a). However, the scattered field is now properly shifted in the lateral x-direction and also (a key step) it is propagated in the z-direction according to the discussion in Appendix A. This results in the plot of Figure 7-12(a), where a larger dif-

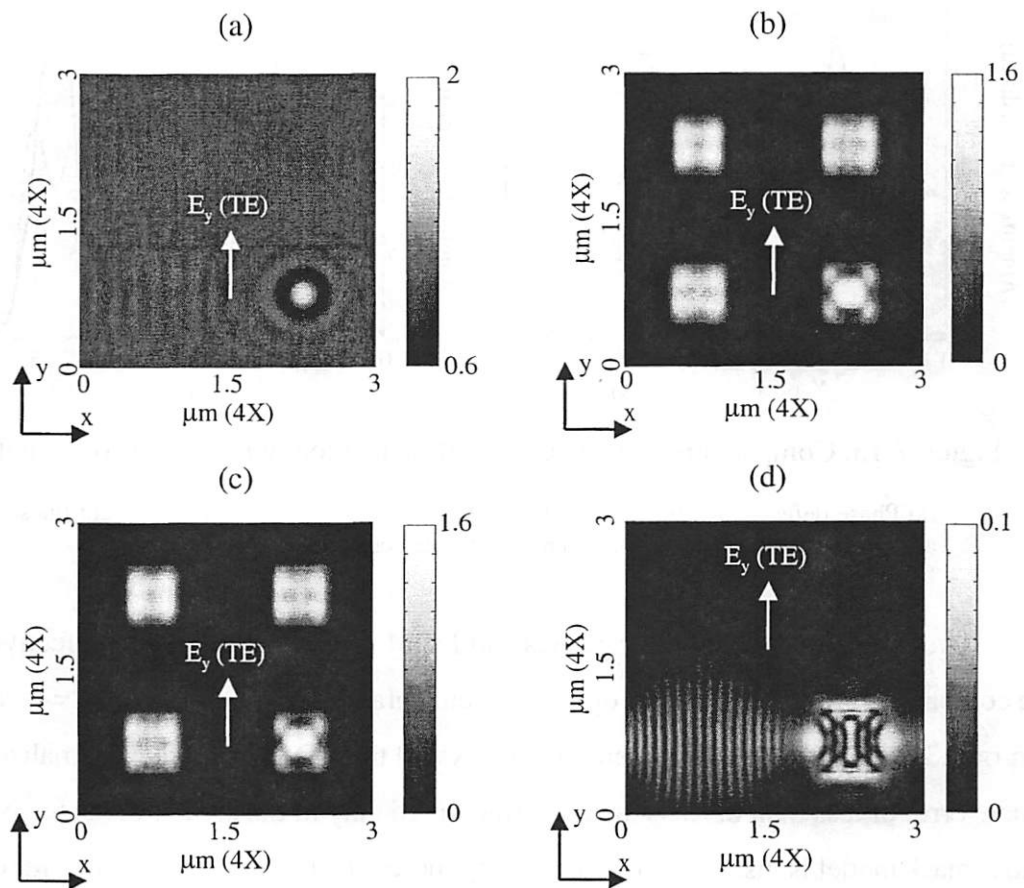

Figure 7-12. A 90° phase defect present in the center of the bottom-right hole

Amplitude of scattered field across the observation plane for (a) isolated phase defect, (b) defective mask simulated with the DDM and (c) rigorous (one-step) simulation of defective mask. Note that the scattered field in (a) does not result from a new simulation. It comes from the field plot calculated in Figure 7-11(a) that is properly shifted in x and propagated in z to account for the different location of the defect. The amplitude of the error of the DDM compared to the rigorous simulation is shown in (d). The normalized mean square error calculated at the bottom right (defective) quadrant is only 0.5%.

fraction spreading is evident. In (b) and (c) the near field across the observation plane below the defective alt. PSM is shown, using the domain decomposition method and the complete mask respectively. The amplitude of the error is shown in (d) and similar observations apply in Figure 7-11(d).

The near fields across cut-lines passing through the center of the bottom two holes are shown for the two defective masks in Figure 7-13, comparing the rigorous (r-mask) and the decomposition methods (DDM). The non-defective case is also plotted for comparison.

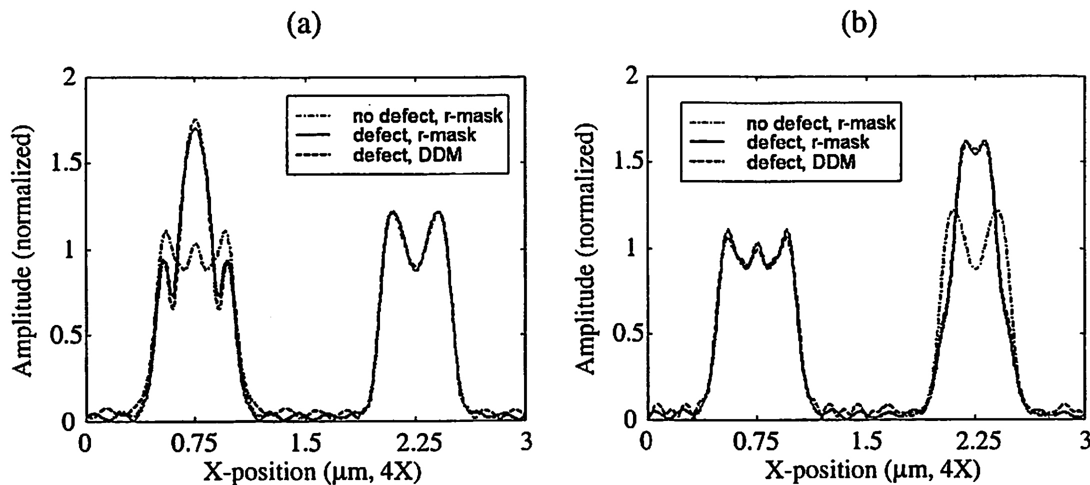

Figure 7-13. Comparison of the decomposition method with the rigorous solution

(a) Phase defect in the 90° hole and (b) phase defect in the 270° hole. The cut-lines are across x, passing through the center of the defective holes.

Next, the images of both rigorous and DDM approaches, for both defective masks are compared in Figure 7-14. The optical system parameters are λ=193nm, R=4, NA=0.75 and σ=0.3. The agreement between the r-mask and the DDM is good, a normalized mean square error of less than 0.3% is incurred (measured only in the area of the defective hole). The k-mask model is insufficient for capturing these effects and is only shown for comparison.

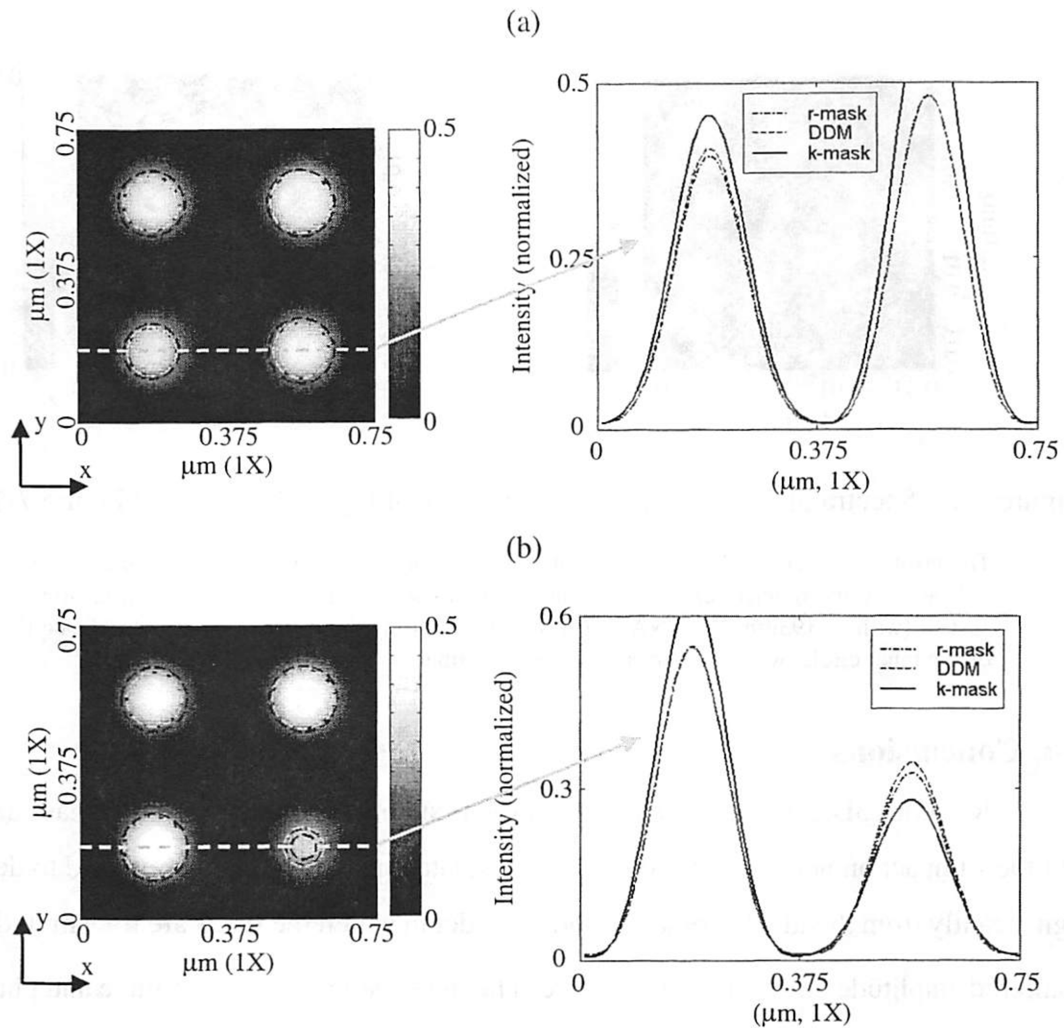

Figure 7-14. Aerial images of defective masks of Figure 7-11 and Figure 7-12

(a) Phase defect in the 90° hole (bottom-left) and (b) phase defect in the 270° hole (bottom-right). Imaging system parameters λ=193nm, R=4, NA=0.75, σ=0.3.

The reason of the excellent agreement in the predictions of the aerial image can be traced back to the plots of Figure 7-11(d) and Figure 7-12(d). The high spatial frequency variation of the error means that it is mapped at the extremities of the spectrum of propagating plane waves and is not collected by the optical system. The normalized spectra (magnitude) of the near field errors are shown in Figure 7-15. Observe that the implied accuracy from these plots should be enough even for R=1 and NA~0.8-0.9, which would be sufficient for inspection simulations.

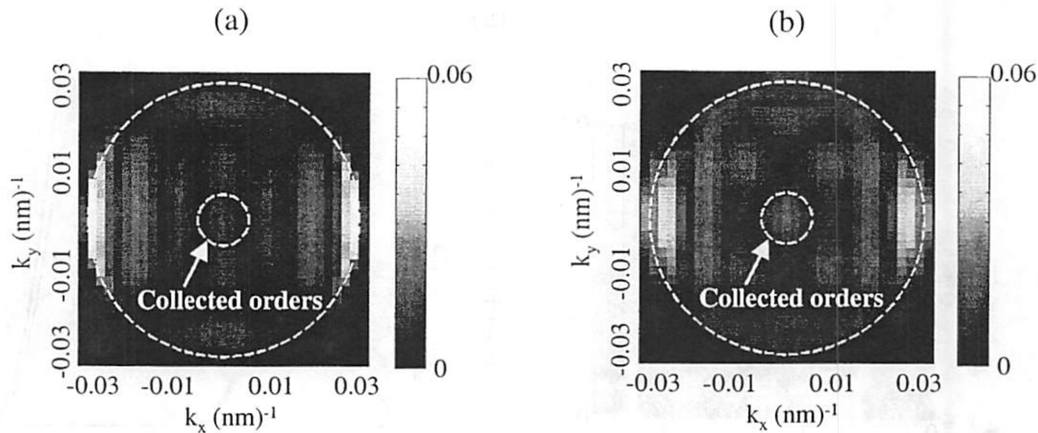

Figure 7-15. Spectra plots (magnitude) of the errors of Figure 7-11(d) and Figure 7-12(d)

The error is concentrated at the extremities of the spectrum of propagating plane waves indicated by the outer circle and does not exceed 6%. However, the projection printing system (with λ=193nm, R=4, NA=0.75, σ=0.3) uses only the diffraction orders indicated by the inner circle, where the error levels are minimal.

7.4. Conclusions

Rigorous 3D electromagnetic simulation is suitable for understanding phase defects and their impact on aerial images of features. Isolated phase defects were found to deviate significantly from the ideal geometric-optics model in which the fields are transmitted with unaltered amplitude and 180° shift in phase. The dependence of the amplitude and phase of the transmitted field on the lateral size of defects for both isolated quartz posts and voids was found. Small voids behave more like opaque defects of equal size, whereas posts can result in a twice as large intensity drop as voids. This results in posts being more than twice as harmful to the aerial image than voids of equal size, when phase defects are located close to features. In particular, a 50nmx50nm (1X) void results in an acceptable 5% linewidth change whereas a post of the same size causes an unacceptable 13% variation. Fully buried defects result in minor linewidth variations. Light polarization conditions, the amount of underetch and the defect height are 2nd order important in defect printability. The linewidth variations of the aerial images were also insensitive to the exact defect shape, which validates the use of parallelepipeds as a sufficient shape to address defect printability issues. The interesting part of this research work is that most of these results were first observed

through simulations and recently experimental evidence is becoming available that validates the above observations.

In the second part of the Chapter a suitable extension of the domain decomposition framework for the simulation of alternating phase shift mask with phase defects was developed. The value of this approach is believed to be significant in the problem of rapid assessment of defect printability once a defect has been found, or in the die-to-database comparisons of inspection systems when deciding about the existence or not of a phase-defect.

8 Conclusions

As integrated circuit technology marches towards a minimum feature resolution of less than 100nm and k_1 factors well below 0.5, the already important role of process simulation and modeling of the various physical phenomena that take place is expected to grow. In particular, many of the proposed resolution enhancement techniques (RET), such as optical proximity correction (OPC), phase shifting masks (PSM), concurrent illumination/mask optimization, *etc.*, that are expected to prolong the life of optical photolithography, rely heavily on modeling and computer simulations. On one hand, rigorous methods are based on the solution of Maxwell's equations for the electromagnetic field in three-dimensional structures and possess excellent accuracy but their computational requirements (memory and speed limitations) render them inappropriate for large scale problems. On the other hand, the simplifying assumptions made for the mask scattering in scalar or vector diffraction theory formulations are inaccurate for a number of problems of practical interest. A central part of this work has been an attempt to bridge the gap between rigorous simulation methods and simpler methods based on diffraction theory for the photomask imaging process.

In this final Chapter, a summary of the most important results of this research is given first, and directions for future research and further development of the presented simulation methods are discussed next.

8.1. Summary of important results

The most important contribution of this work is doubtlessly the domain decomposition methods (DDMs) developed and used in Chapters 4 through 6 and partly in Chapter 7. Two central ideas were sequentially exploited for the development of DDMs: First, orig-

inating from the linearity of the Kirchhoff-Fresnel diffraction integral, a division of a multiple-opening diffracting screen (photomask with a number of features carved on it) was performed and the problem was broken up in elemental, single-opening pieces. Each one of these pieces was treated separately and it was shown that the near scattered field below such a single-opening mask, that would normally require solving Maxwell's equations on a three-dimensional domain, can be accurately approximated by combining the results of the scattered field from two two-dimensional structures. The errors incurred near corners and the fact that light polarizations other than the excited one were neglected were shown to be insignificant. The reason for that was traced to the energy concentration of both corner effects and perpendicular polarizations into the higher spatial frequencies of the diffraction spectra. The role of the imaging system (with NA<1 and R~4 or 5) as a filter for the higher spatial frequencies is such that these errors are filtered-out and they do not confound the simulation of image formation. The second idea had to do with the use of simple functions (like the rect-function, raised-cosine, or Gaussian) that substitute the true, rigorously calculated, diffraction field profiles below the elemental two-dimensional geometries in a way that they perfectly match (to within some level of accuracy that was shown to be better than 99%) their through-the-lens spectra. A good spectral match within the part of the spectrum that is actually used by the projection system for the image formation is all that is required for these models to work. And so they do.

Being able to handle arbitrary two-dimensional layouts is key for the practical aspect of domain decomposition methods. To this extent a methodology was developed in Chapter 4 that involved breaking up arbitrary (Manhattan-type) polygons into the set of maximally overlapping rectangles and it was explained why this break-up method is superior from an electromagnetic point-of-view to the one where the polygon is divided into a set of mutually disjoint rectangles.

Cross-talk effects between neighboring apertures in alternating phase shift masks were the theme of Chapter 5. A successful model for their prediction was build based upon a single simulation for the electromagnetic field scattered from a 90° corner at a glass/air interface, from which it became clear that the edges at the bottom of the phase-wells are

the primary sources of cross-talk. Two paths, of almost equal strength, that cause cross-talk were identified and the amount of cross-talk was quantified for various mask geometries, edge profiles and field polarizations. Recipes for cross-talk elimination were also suggested. Proper modeling of cross-talk effects was shown to be an integral part of domain decomposition methods. In particular, examples of two-dimensional mask layouts where cross-talk cannot be neglected were presented.

In Chapter 6 the edge domain decomposition method was developed. The main ideas were similar to those in Chapter 4, but here the decomposition was based on edges, *i.e.* the electromagnetic field diffraction profiles from isolated edges. This edge-decomposition allowed for tremendous versatility, since only a small number of two-dimensional simulations of edges is enough for the reconstruction of accurate approximations of the near field below two-dimensional arbitrary mask layouts. A 12μm by 16μm layout of a three level alternating PSM that is out of reach for fully rigorous methods was simulated in under 1min. Matching the spectra of the fields from edge-diffractions with simple piecewise constant models was also possible here and further accelerated the calculations. Although in essence the method is not different than the domain decomposition method of Chapter 4, its algorithmic implementation for arbitrary 2D layouts is easier and it requires far less rigorous simulations to build the library of required edges, as opposed to building a library for every possible feature size required by the decomposition method in Chapter 4.

Useful design strategies for optical proximity correction can be found in Chapter 3. A critical comparison between rigorous simulation methods and scalar methods based on the Kirchhoff approximation for the mask was carried out and it was found that the ~10% bias in the results for binary Cr-on-glass (COG) masks obtained from the two different methods can be adequately explained by the use of a perturbation model that incorporates the electromagnetic behavior of light penetrating through small (wavelength-sized) holes.

Differences in the two types of defects (posts and voids) encountered in alternating phase shift masks were exposed in Chapter 7. The surprising behavior of light passing through phase-defects, where the change in phase depends strongly of the footprint (lateral size) of the defect for small defects was characterized. This behavior was further used to

explain the changes in critical dimension (CD) that phase defects cause depending on their geometry and proximity to layout features. Recent experimental results are in excellent agreement with those observations. Also, in Chapter 7 a methodology based on domain decomposition was proposed for the rapid simulation of defective masks. This methodology is expected to have a significant impact in die-to-database comparisons in mask inspection systems and in the rapid evaluation of defect printability.

8.2. Future research

Speed-up factors in excess of 200, without compromising the accuracy, were possible with the domain decomposition methods of Chapter 4. However, it was stressed that a possible algorithmic implementation could involve the pre-calculation of all different feature sizes that will be encountered on a layout and creation of a database with their diffraction characteristics (parameters of the compact mk-mask model). Such an approach is expected to lead to a much larger acceleration. The speed-up factor of 172,800 (1sec. instead of 2days) achieved in the simulation of a simple (isolated hole and isolated island) 3μm by 3μm layout in the case of the edge-DDM should be possible for the DDM in Chapter 4 also. However, the automation of this task requires considerable effort. Algorithms for the rapid synthesis of the diffraction characteristics of arbitrary, complex layouts will be needed, especially in order to decide when cross-talk effects are important and automatically include them.

Cross-talk effects were not treated in the case of the edge-DDM of Chapter 6. It should be obvious that although this method has an easier algorithmic implementation compared to the decomposition methods of Chapter 4, including cross-talk effects raises the complications to a similar level as in the methods of Chapters 4 and 5. It was also found in Chapter 6 that the accuracy of the edge-DDM drops sharply for sub-wavelength sized features. Clearly, in that regime a new cross-talk effect emerges, that between the closely packed edges. It would be worth to explore if including this cross-talk effect is possible, and if so, determine whether the revised edge-DDM is more or less efficient in large scale computations than simulating every feature size separately without decomposing it in edges, as in the methods of Chapters 4 and 5.

There is nothing that is restrictive in the use of the domain decomposition methods for normal incidence illumination. This fact was validated with off-axis illumination examples, where the methods still perform excellent. However, a considerable effort is required in order for the method to become available for off-axis partially coherent illumination, when the Hopkins' approximation of constant diffraction orders with respect to the angle of incidence breaks down. Such an extension of Hopkins' approximation will be needed for example, if the DDM is used in the simulation of images from inspection systems (R=1, NA~1).

A Angular spectrum decomposition of electromagnetic waves

IF the complex field distribution of a monochromatic disturbance is Fourier-analyzed across any plane, the various spatial Fourier components can be identified as plane waves traveling in different directions away from that plane. The field amplitude at any other point or across any other parallel plane can be calculated by adding the contributions of these plane waves, taking into account the phase shifts they have undergone during propagation. The following discussion is very helpful in understanding the physical meaning of the spectrum (Fourier transform) of the scattered complex electromagnetic field across the observation plane below photomasks, and also how the choice of the location of the observation plane affects the spectrum, as seen throughout this work.

A.1. The angular spectrum and its physical interpretation

Suppose the presence of an electromagnetic wave traveling with a component of propagation in the positive z-direction and observed on a transverse (x,y) plane. Let U(x,y,0) be the complex field across the z=0 plane. U can represent either one of the three cartesian components of the electric or magnetic field. An expression is sought that relates the field U(x,y,z) appearing across a plane z>0, parallel to z=0 plane, with the field U(x,y,0) across the z=0 plane.

Across the z=0 plane, the function U has a two-dimensional Fourier transform given by:

Equation A-1.
$$A(k_x, k_y;0) = \iint_{-\infty}^{\infty} U(x, y, 0)\exp[-j(k_x x + k_y y)]dxdy$$

where $k_x=2\pi f_x$ and $k_y=2\pi f_y$. U(x,y,0) can also be written as an inverse Fourier transform of its spectrum $A(k_x,k_y;0)$:

Equation A-2. $$U(x, y, 0) = \int\int_{-\infty}^{\infty} A(k_x, k_y;0)\exp[j(k_x x + k_y y)]dk_x dk_y$$

To give physical meaning to the functions in the integrand of the above integral, consider the form of a simple plane wave propagating with wave vector $\vec{k}$, where $\vec{k}$ has magnitude $2\pi/\lambda$ and has direction cosines (α,β,γ), as illustrated in Figure A-1. Such a plane wave has a complex representation of the form:

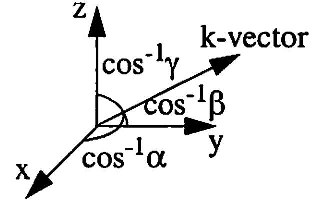

Figure A-1. Wave vector $\vec{k}$ and direction cosines (α,β,γ)

Equation A-3. $$w(x, y, z;t) = \exp[j(\vec{k}\cdot\vec{r} - \omega t)]$$

where $\vec{r} = x\hat{x} + y\hat{y} + z\hat{z}$ is a position vector, ω is the angular frequency of the monochromatic wave and the wavevector $\vec{k}$ is:

Equation A-4. $$\vec{k} = k_x\hat{x} + k_y\hat{y} + k_z\hat{z} = \frac{2\pi}{\lambda}(\alpha\hat{x} + \beta\hat{y} + \gamma\hat{z})$$

Dropping the time dependence, the complex phasor amplitude of the plane wave across a constant z-plane is:

Equation A-5. $$P(x, y, z) = \exp(j\vec{k}\cdot\vec{r}) = \exp\left[j\frac{2\pi}{\lambda}(\alpha x + \beta y)\right]\cdot\exp\left(j\frac{2\pi}{\lambda}\gamma z\right)$$

Note that the direction cosines are not independent but they are related through:

Equation A-6. $$\gamma = \sqrt{1 - \alpha^2 - \beta^2}$$

Therefore across the plane z=0, a complex-exponential function $\exp[j(k_x x + k_y y)]$ may be viewed as a unit-amplitude plane wave propagating with direction cosines:

Equation A-7. $$\alpha = \frac{\lambda k_x}{2\pi} \quad \beta = \frac{\lambda k_y}{2\pi} \quad \gamma = \sqrt{1 - \left(\frac{\lambda k_x}{2\pi}\right)^2 - \left(\frac{\lambda k_y}{2\pi}\right)^2}$$

In the Fourier decomposition of U, the complex amplitude of the plane-wave component with spatial frequencies (k_x,k_y) is simply $A(k_x,k_y;0)dk_x dk_y$, evaluated at ($k_x=2\pi\alpha/\lambda$, $k_y=2\pi\beta/\lambda$). For this reason, the function $A(k_x,k_y;0)$ (spectrum of U(x,y,0)) expressed explicitly as function of α, β is called the *angular spectrum* of the disturbance U(x,y,0):

Equation A-8. $$A\left(\frac{\alpha}{\lambda}, \frac{\beta}{\lambda};0\right) = \int\int_{-\infty}^{\infty} U(x, y, 0)\exp\left[-j2\pi\left(\frac{\alpha}{\lambda}x + \frac{\beta}{\lambda}y\right)\right]dxdy$$

A.2. Propagation of the spectrum

Let $A(k_x,k_y;z)$ be the spectrum of the disturbance U(x,y,z) across a plane parallel to the (x,y) plane but at a distance z from it:

Equation A-9. $$A(k_x, k_y;z) = \int\int_{-\infty}^{\infty} U(x, y, z)\exp[-j(k_x x + k_y y)]dxdy$$

If the relation between $A(k_x,k_y;0)$ and $A(k_x,k_y;z)$ can be found, then the effects of wave propagation on the spectrum of the disturbance will be evident. Expressing U(x,y,z) as the inverse Fourier-transform of its spectrum $A(k_x,k_y;z)$:

Equation A-10. $$U(x, y, z) = \int\int_{-\infty}^{\infty} A(k_x, k_y;z)\exp[j(k_x x + k_y y)]dk_x dk_y$$

and considering the fact that U must satisfy the Helmholtz equation at all source-free points:

Equation A-11. $$\nabla^2 U + k^2 U = 0 \quad \text{(Helmholtz eq.)}$$
it follows that A must satisfy the following differential equation:

Equation A-12. $$\frac{d^2}{dz^2}A(k_x, k_y;z) + (k_0^2 - k_x^2 - k_y^2)A(k_x, k_y;z) = 0$$

where $k_0=2\pi/\lambda$ is the magnitude of the wavevector in the ambient. An elementary solution of Equation A-12 can be written as:

Equation A-13. $$A(k_x, k_y;z) = A(k_x, k_y;0)\exp(j\sqrt{k_0^2 - k_x^2 - k_y^2} \cdot z)$$

Based on this result, when $k_x^2 + k_y^2 < k_0^2 = \left(\frac{2\pi}{\lambda}\right)^2$ or equivalently when the direction cosines (α,β) satisfy $\alpha^2 + \beta^2 < 1$, as all true direction cosines must, the effect of propagation over distance z is simply a change of the relative phases of the various components of the angular spectrum. Since each plane-wave component propagates at a different angle, each travels a different distance between two parallel planes, and relative phase delays are therefore introduced.

However, when $k_x^2 + k_y^2 > k_0^2$ or equivalently when the direction cosines (α,β) satisfy $\alpha^2 + \beta^2 > 1$, a different interpretation is required. α and β can no longer be viewed as direction cosines. The square root in Equation A-13 is imaginary, and that equation can be rewritten as:

Equation A-14. $$A(k_x, k_y;z) = A(k_x, k_y;0)\exp(-\mu z)$$

where $\mu = \sqrt{k_x^2 + k_y^2 - k_0^2}$. Since m is a positive real number, these wave components are rapidly attenuated by the propagation phenomenon. Such components are called evanescent waves and they carry no energy away from the transverse plane.

A.3. Choosing the location of the observation plane

Throughout this work whenever the scattered field below a photomask is rigorously calculated (with TEMPEST) the choice of the observation plane has seemed somewhat arbitrary. Although the observation plane has been typically chosen at a distance $d \cong \lambda/4$ (for example at d=50nm for λ=193nm in Chapters 4-6) it has been suppressed how the choice of the exact location of the observation plane affects the subsequent results. The following example demonstrates how the spectrum (diffraction orders for periodic masks) of

the scattered field changes as the observation plane is moved at different distances from the mask, according to the theory presented in Section A.1 and Section A.2.

An isolated 400nm (4X) mask opening with 180° phase shift and 50nm of isotropic underetch is shown in Figure A-2(a). The amplitude of the complex electromagnetic field being established when a plane wave of λ=193nm is normally incident on the mask is also

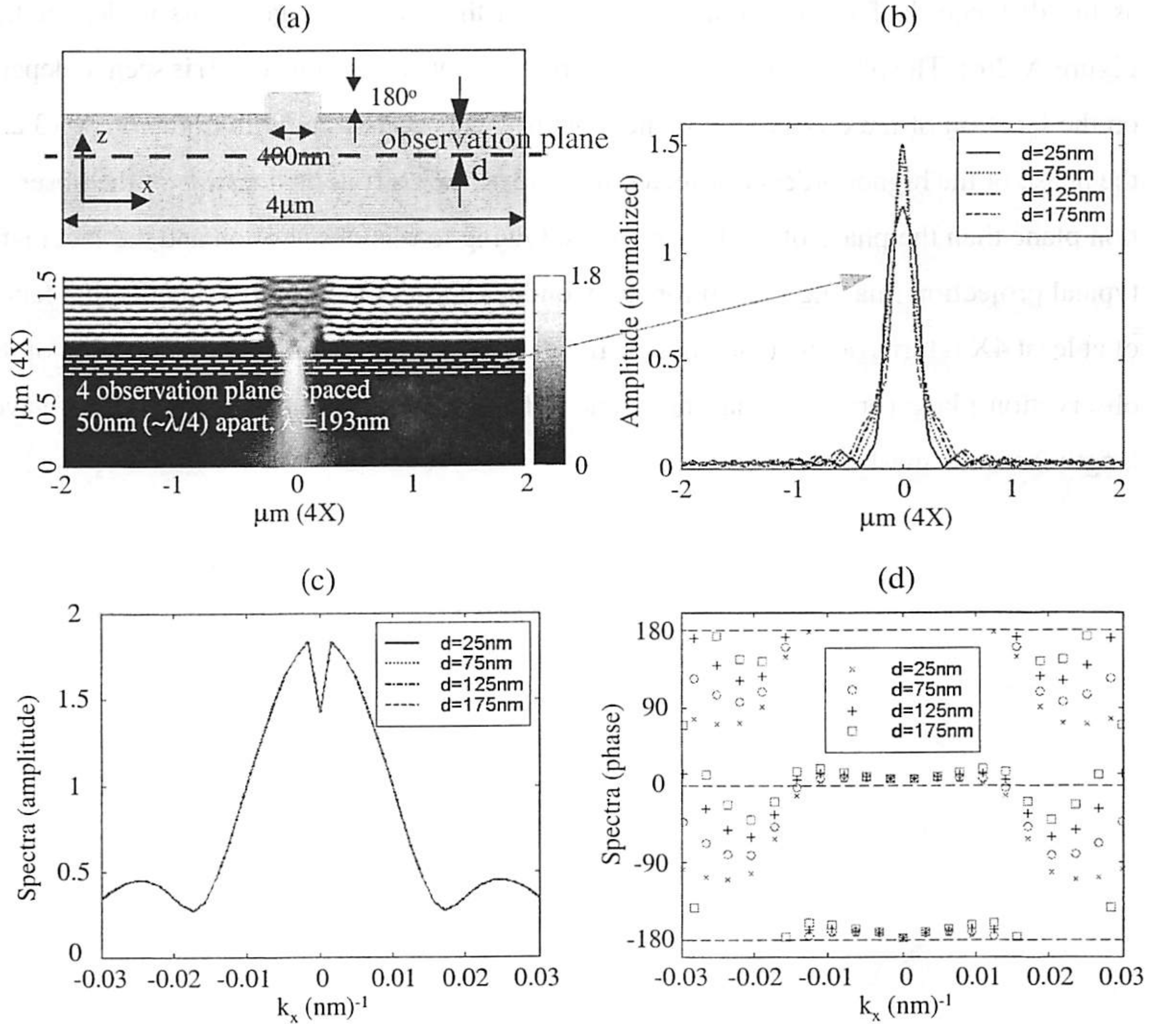

Figure A-2. Location of observation plane and diffraction spectrum

An isolated 400nm (4X) mask opening with 180° phase shift and 50nm of isotropic underetch is shown in (a) with the amplitude of the field everywhere in the simulation domain under a normally incident plane wave excitation at λ=193nm. Although the profile of the scattered near field depends strongly on the exact choice of the location d of the observation plane, as shown in (b), the amplitude of the spectrum does not depend on d, as shown in (c). However, the phase of the higher diffraction orders is seen to vary rapidly with d, whereas the phase of the lower diffraction orders is quite insensitive to d. These results are in exact agreement with Equation A-13.

shown in Figure A-2(a) everywhere in the simulation domain. Four observation planes separated by 50nm (~$\lambda/4$) are also indicated, where the one nearest to the mask is located 25nm below the Cr-based absorption layer. There are visible changes in the amplitude of the scattered field at the different observation planes, as shown in Figure A-2(b). This however is not significant as one might expect from the previous treatment on the propagation of the spectrum. Consistent with Equation A-13, the amplitude of the spectrum does not change as the distance d of the observation plane from the mask changes. This is depicted in Figure A-2(c). The phase of the diffraction orders shown in Figure A-2(d) is seen to depend on the location of the observation plane. Again, this is consistent with Equation A-13 and the phase of the higher orders is affected more from the shift in the location of the observation plane than the phase of the lower orders. Owing to this observation and the fact that a typical projection imaging system for semiconductor manufacturing has a reduction factor of at least 4X it turns out that the image will be quite insensitive on the exact location of the observation plane (provided that this plane is kept nearer than approximately one wavelength from the mask).

Bibliography

[1] E. Abbe, "Beitrage zur Theorie des Mikroskops und der Mikroskopischen wahrnehmung", *Archiv. Microskopische Anat.*, vol. 9, pp. 413-468, 1873.

[2] K. Adam, A. R. Neureuther, "Simplified Models for Edge Transitions in Rigorous Mask Modeling", *Proceedings of the SPIE,* vol. 4346, pp. 331-344, 2001.

[3] K. Adam, A. R. Neureuther, "Analysis of OPC Features in Binary Masks at 193 nm", *Proceedings of the SPIE,* vol. 4000, pp. 711-722, 2000.

[4] K. Adam, S. Hotta, A. R. Neureuther, "Characterization of Phase Defects in Phase Shift Masks", *J. Vac. Sci. Technol. B,* vol. 18(6), pp. 3227-3231, Nov. 2000.

[5] K. Adam, R. Socha, M. Dusa, A. R. Neureuther, "Effect of Reticle CD Uniformity on Wafer CD Uniformity in the Presence of Scattering Bar Optical Proximity Correction", *Proceedings of the SPIE,* vol. 3546, pp. 642-650, 1998.

[6] K. Adam, A. R. Neureuther, R. Socha, T. Pistor, "Analysis of Sub-wavelength Sized OPC Features", *Microelectronic Engineering*, vol. 41-42, pp. 137-140, March 1998.

[7] C. A. Balanis, *Advanced Engineering Electrodynamics*, Wiley, pp.196-206, 1989.

[8] *ibid.*, Chapter 14.

[9] *ibid.*, Chapter 12.

[10] D. Bernard, J. Li, J.C. Rey, K. Rouz, V. Axelrad, "Efficient Computational Techniques for Aerial Imaging Simulation", *Proceedings of the SPIE,* vol. 2726, pp. 273-287, 1996.

[11] M. Born, E. Wolf, *Principles of Optics,* 7th (expanded) edition, Cambridge University Press, 1999.

[12] *ibid.*, pp. 598-599.

[13] *ibid.*, pp. 619-626.

[14] *ibid.*, pp. 572-577.

[15] *ibid.*, pp. 417-423.

[16] *ibid.*, pp. 636-637.

[17] J. F. Chen, T. Laidig, K. E. Wampler, R. Caldwell, K. H. Nakagawa, A. Liebchen, "A Practical Technology Path to Sub-0.10 Micron Process Generations Via Enhanced Optical Lithography", *Proceedings of the SPIE*, vol. 3873, pp. 995-1016, 1999.

[18] J. F. Chen, T. Laidig, K. E. Wampler, R. Caldwell, A. Naderi, D. Van De Brooke, "An OPC Technology Roadmap to 0.14 μm Design Rules", *Proceedings of the SPIE*, vol. 3236, pp. 382-396, 1998.

[19] J. F. Chen, T. Laidig, K. E. Wampler, R. Caldwell, "Optical Proximity Correction for Intermediate-Pitch Features Using Sub-Resolution Scattering Bars", *J. Vac. Sci. Technol. B*, vol.15(6), pp. 2426-2433, Nov/Dec 1997.

[20] J. F. Chen, T. Laidig, K. E. Wampler, R. Caldwell, "Practical Method for Full-Chip Optical Proximity Correction", *Proceedings of the SPIE*, vol. 3051, pp. 790-803, 1997.

[21] J. F. Chen, J. A. Matthews, "Masks for Improved Lithographic Patterning for Off-Axis Illumination Lithography", US Patent 5,447,810, Sep. 5, 1995.

[22] J. F. Chen, J. A. Matthews, "Mask for Photolithography", US Patent 5,242,770, Sep. 7, 1993.

[23] J. X. Chen, J. Riddick, C. Tabery, C. Spence, *et al.*, "ArF(193nm) Alternating PSM Quartz Defect Repair and Printability for 100nm Node", *Proceedings of the SPIE*, vol. 4562, to be published.

[24] N. Cobb, A. Zakhor, "Experimental Results on Optical Proximity Correction with Variable Threshold Resist Model", *Proceedings of the SPIE*, vol. 3051, pp. 458-468, 1997.

[25] N. Cobb, A. Zakhor, E. Miloslavsky, "Mathematical and CAD Framework for Proximity Correction", *Proceedings of the SPIE*, vol. 2726, pp. 208-222, 1996.

[26] N. Cobb, A. Zakhor, "Fast, Low-Complexity Mask Design", *Proceedings of the SPIE*, vol. 2440, pp. 313-327, 1995.

[27] N. Cobb, A. Zakhor, "Large Area Phase-Shift Mask Design", *Proceedings of the SPIE*, vol. 2197, pp. 348-360, 1994.

[28] D. C. Cole, E. Barouch, U. Hollerbach, S. A. Orszag, "Extending Scalar Aerial Image Calculations to Higher Numerical Apertures", *J. Vac. Sci. Technol. B,* vol. 10(6), pp. 3037-3041, Nov/Dec 1992.

[29] Eastman Kodak Company, "Techniques of Microphotography: Precision Photography at Extreme Reductions", *Kodak Publication*, no. P-52, Rochester, New York, 1976.

[30] A. Erdmann, C. Friedrich, "Rigorous Diffraction Analysis for Future Mask Technology", *Proceedings of the SPIE*, vol. 4000, pp. 684-694, 2000.

[31] D. G. Flagello, T. Milster, A. E. Rosenbluth, "Theory of High-NA Imaging in Homogeneous Thin Films", *J. Opt. Soc. Am. A,* vol. 13(1), pp. 53-64, January 1996.

[32] P. D. Flanner III, *Two-Dimensional Optical Imaging for Photolithography Simulation,* M.S. Thesis, University of California, Berkeley, 1986.

[33] C. M. Friedrich, L. Mader, A. Erdmann, *et al.*, "Optimising Edge Topography of Alternating Phase-Shift Masks Using Rigorous Mask Modeling", *Proceedings of the SPIE*, vol. 4000, pp. 1323-1335, 2000.

[34] J. Gamelin, "Simulation of Topography Scattering for Optical Lithography with the Connection Machine", M.S. Thesis, University of California, Berkeley, 1989.

[35] J. Gamelin, R. Guerrieri, A. R. Neureuther, "Exploration of Scattering from Topography with Massively Parallel Computers", *J. Vac. Sci. Technol. B*, vol.7(6), pp. 1984-1990, Nov./Dec. 1989.

[36] J. W. Goodman, *Introduction to Fourier Optics,* 2nd edition, McGraw-Hill, 1996.

[37] *ibid.*, pp. 33-34.

[38] *ibid.*, pp. 55-58.

[39] *ibid.*, pp. 159-160.

[40] J. W. Goodman, *Statistical Optics,* John Wiley & Sons, 1985.

[41] *ibid.*, pp. 109-111.

[42] J. Gortych, A. E. Rosenbluth, "Method and System for Optimizing Illumination in an Optical Photolithography Projection Imaging System", US Patent 5,680,588, Oct. 21, 1997.

[43] Y. Granik, "MEEF as a Matrix", *Proceedings of the SPIE,* vol. 4562, to be published.

[44] R. Guerrieri, K. Tadros, J. Gamelin, A. R. Neureuther, "Massively Parallel Algorithms for Scattering in Optical Lithography", *IEEE Trans. CAD*, vol. 10(9), pp. 1091-1100, Sep. 1991.

[45] W. Henke, D. Mewes, M. Weiss, G. Czech, and R. Schiessl-Hoyler, "Simulation of Defects in 3-Dimensional Resist Profiles in Optical Lithography", *Microelectronic Engineering*, vol. 13, pp. 497-501, 1991.

[46] S. Hotta, T. V. Pistor, K. Adam, A. R. Neureuther, "Effects of Shifter Edge Topography on Through Focus Performance", *Proceedings of the SPIE*, vol. 4186, pp. 827-837, 2001.

[47] J. D. Jackson, *Classical Electrodynamics*, 2nd edition, Wiley, pp. 638-641, 1975.

[48] V. Kettunen, M. Kuittinen, J. Turunen, "Effects of Abrupt Surface-Profile Transitions in Nonparaxial Diffractive Optics", *J. Opt. Soc. Am. A*, vol. 18(6), pp. 1257-1260, Jun. 2001.

[49] B. Layet, M. R. Taghizadeh, "Electromagnetic Analysis of Fan-out Gratings and Diffractive Cylindrical Lens Arrays by Field Stitching", *J. Opt. Soc. Am. A*, vol. 14(7), Jul. 1997.

[50] M. D. Levenson, J. S. Petersen, D. G. Gerold, C. A. Mack, "Phase Phirst! An improved strong-PSM paradigm", *Proceedings of the SPIE*, vol. 4186, pp. 395-404, 2001.

[51] M.D. Levenson, N.S. Viswanathan, R.A. Simpson, "Improving Resolution in Photolithography with a Phase-Shifting Mask", *IEEE Trans. Electron Devices*, vol. ED-29(12), pp. 1828-1836, December 1982.

[52] J. Li, D. Bernard, J.C. Rey, V.V. Boksha, "Model Based Optical Proximity Correction Including Effects of Photoresist Processes", *Proceedings of the SPIE*, vol. 3051, pp. 643-651, 1997.

[53] B.J. Lin, "Partially Coherent Imaging in Two Dimensions and the Theoretical Limits of Projection Printing in Microfabrication", *IEEE Trans. Electron Devices*, vol. ED-27(5), pp. 931-938, May 1980.

[54] Y. Liu, A. Zakhor, A. Neureuther, "Method for Making Masks", US Patent 5,326,659, Jul. 5, 1994.

[55] Y. Liu, A. Pfau, A. Zakhor, "Systematic Design of Phase-Shifting Masks with Extended Depth of Focus and/or Shifted Focus Plane", *IEEE Trans. on Semicond. Manuf.*, vol. 6(1), pp. 1-21, Feb. 1993.

[56] Y. Liu, A. Zakhor, "Computer Aided Phase Shift Mask Design with Reduced Complexity", *Proceedings of the SPIE*, vol. 1927, pp. 477-493, 1993.

[57] Y. Liu, A. Zakhor, "Binary and Phase Shifting Mask Design for Optical Lithography", *IEEE Trans. on Semicond. Manuf.*, vol.5(2), pp. 138-152, May 1992.

[58] G.E. Moore, "Lithography and the Future of Moore's Law", *Proceedings of the SPIE,* vol. 2440, pp. 2-17, 1995.

[59] A. R. Neureuther, P. Flanner III, S. Shen, "Coherence of Defect Interactions with Features in Optical Imaging", *J. Vac. Sci. Technol. B,* vol. 5(1), pp. 308-312, Jan/Feb 1987.

[60] W. G. Oldham, S. N. Nandgaonkar, A. R. Neureuther, and M. M. O'Toole, "A General Simulator for VLSI Lithography and Etching Processes: Part I - Application to Projection Lithography", *IEEE Trans. Electron Devices,* vol. ED-26, no. 4, pp. 717-722, Apr. 1979.

[61] M. M. O'Toole, *Simulation of Optically Formed Image Profiles in Positive Photoresist*, Ph.D. Dissertation, University of California, Berkeley, 1979.

[62] O.W. Otto, J.G. Garofalo, K.K. Low, C. Yuan, R.C. Henderson, C. Pierrat, R.L. Kostelak, S. Vaidya, P.K. Vasudev, "Automated Optical Proximity Correction - A Rules-Based Approach", *Proceedings of the SPIE,* vol. 2197, pp. 278-293, 1994.

[63] Y. C. Pati, A. A. Ghazanfarian, R. F. Pease, "Exploiting Structure in Fast Aerial Image Computation for Integrated Circuit Patterns", *IEEE Trans. Semiconductor Manufacturing,* vol. 10(1), pp. 62-74, February 1997.

[64] Y. C. Pati, T. Kailath, "Phase-shifting Masks for Microlithography: Automated Design and Mask Requirements", *J. Opt. Soc. Am. A,* vol. 11(9), pp. 2438-2452, September 1994.

[65] C. Pierrat, "Investigation of Proximity Effects in Alternating Aperture Phase Shifting Masks", *Proceedings of the SPIE,* vol. 4186, pp. 325-335, 2001.

[66] C. Pierrat, A. Wong, S. Vaidya, "Phase-Shifting Mask Topography Effects on Lithographic Image Quality", *IEDM Tech. Digest*, pp. 53-56, 1992.

[67] T. Pistor, "Rigorous 3D Simulation of Phase Defects in Alternating Phase-Shifting Masks", *Proceedings of the SPIE,* vol. 4186, to be published.

[68] T. Pistor, *Electromagnetic Simulation and Modeling with Applications in Lithography,* Ph.D. Dissertation, University of California, Berkeley, 2001.

[69] *ibid.*, Chapter 4.

[70] T. V. Pistor, A. R. Neureuther, R. J. Socha, "Modeling Oblique Incidence Effects in Photomasks", *Proceedings of the SPIE,* vol. 4000, pp. 228-237, 2000.

[71] T. Pistor, *Expanding the Simulation Capability of TEMPEST*, M.S. Thesis, University of California, Berkeley, 1997.

[72] D. Prather, S. Shi, J. S. Bergey, "Field Stitching Algorithm for the Analysis of Electrically Large Diffractive Optical Elements", *Optics Letters*, vol. 24(5), pp. 273-275, Mar. 1999.

[73] Lord Rayleigh, "On the Dynamic Theory of Gratings", *Proc. Royal Soc. London A*, vol. 79, pp. 399-416, 1907.

[74] M. L. Rieger, J. P. Stirniman, "Customizing Proximity Correction for Process-Specific Objectives", *Proceedings of the SPIE,* vol. 2726, pp. 651-659, 1996.

[75] M. L. Rieger, J. P. Stirniman, "Using Behavior Modeling for Proximity Correction", *Proceedings of the SPIE,* vol. 2197, pp. 371-376, 1994.

[76] A. E. Rosenbluth, S. Bukofsky, M. Hibbs, K. Lai, A. Molless, R. N. Singh, A. Wong, "Optimum Mask and Source Patterns to Print a Given Shape", *Proceedings of the SPIE,* vol. 4346, pp. 486-502, 2001.

[77] B. E. A. Saleh, S. I. Sayegh, "Reduction of Errors of Microphotographic Reproductions by Optimal Corrections of Original Masks", Optical Engineering, vol. 20(5), pp. 781-784, 1981.

[78] F. Schellenberg, O. Toublan, N. Cobb, E. Sahouria, G. Hughes, S. MacDonald, C. West, "OPC Beyond 0.18μm: OPC on PSM Gates", *Proceedings of the SPIE,* vol. 4000, pp. 1062-1069, 2000.

[79] J.R. Sheats, B.W. Smith, *Microlithography - Science and Technology*, Marcel-Dekker, chap. 3, 1998.

[80] *ibid.*, chap. 4.

[81] R. J. Socha, M. V. Dusa, L. Capodieci, J. Finders, J. F. Chen, D. G. Flagello, K. D. Cummings, "Forbidden Pitches for 130-nm Lithography and Below", *Proceedings of the SPIE,* vol. 4000, pp. 1140-1155, 2000.

[82] R. J. Socha, *Propagation Effects of Partially Coherent Light in Optical Lithography and Inspection,* Ph.D. Dissertation, University of California, Berkeley, 1997.

[83] *ibid.*, pp. 31-34.

[84] *ibid.*, pp. 121-122 and 126-129.

[85] *ibid.*, Chapters 3, 6 and 7.

[86] A. Starikov, "Use of a Single Size Square Serif for Variable Print Bias Compensation", *Proceedings of the SPIE,* vol. 1088, pp. 34-46, 1989.

[87] J.P. Stirniman, M.L. Rieger, "Spatial Filter Models to describe IC Lithographic Behavior", *Proceedings of the SPIE,* vol. 3051, pp. 469-478, 1997.

[88] J.P. Stirniman, M.L. Rieger, "Fast Proximity Correction with Zone Sampling", *Proceedings of the SPIE,* vol. 2197, pp. 294-301, 1994.

[89] J. A. Stratton, *Electromagnetic Theory,* Section 8.14, McGraw-Hill, 1941.

[90] K. Tadros, A. R. Neureuther, R. Guerrieri, "Understanding Metrology of Polysilicon Gates through Reflectance Measurements and Simulation", *Proceedings of the SPIE,* vol. 1464, pp. 177-186, 1991.

[91] K. Tadros, A. R. Neureuther, J. Gamelin, R. Guerrieri, "Investigation of Reflective Notching with Massively Parallel Simulation", *Proceedings of the SPIE,* vol. 1264, pp. 322-332, 1990.

[92] A. Taflove, S. C. Hagness, *Computational Electrodynamics - The finite-difference time-domain method,* 2nd ed., Artech House, 2000.

[93] E. Tejnil, A. R. Stivers, R. S. Schenker, L. S. Zurbrick, "Evaluation of Printability and Inspection of Phase Defects on Hidden-Shifter Alternating Phase-Shift Masks", *Proceedings of the SPIE,* vol. 4066, pp. 376-387, 2000.

[94] K. Toh, *Two-Dimensional Images with Effects of Lens Aberrations in Optical Lithography,* M.S. Thesis, University of California, Berkeley, 1988.

[95] O. Toublan, E. Sahouria, N. Cobb, "Phase and Transmission Errors Aware OPC Solution for PSM: Feasibility Demonstration", *Bacus News,* vol. 17(2), February 2001.

[96] O. Toublan, E. Sahouria, N. Cobb, T. Do, T. Donnelly, Y. Granik, F. Schellenberg, P. Schiavone, "Phase Aware Proximity Correction for Advanced Masks", *Proceedings of the SPIE,* vol. 4000, pp. 160-170, 2000.

[97] R. M. von Bunau, Y. C. Pati, Y. Wang, R. F. W. Pease, "Optimal Coherent Decompositions for Radially Symmetric Optical Systems", *J. Vac. Sci. Technol. B,* vol. 15(6), pp. 2412-2416, Nov/Dec 1997.

[98] Y. Wang, Y.C. Pati, H. Watanabe, T. Kailath, "Automated Design of Halftoned Double-Exposure Phase-Shifting Masks", *Proceedings of the SPIE,* vol. 2440, pp. 290-301, 1995.

[99] Y. Wang, Y.C. Pati, J. Liang, T. Kailath, "Systematic Design of Phase-Shifting Masks", *Proceedings of the SPIE,* vol. 2197, pp. 377-387, 1994.

[100] G. Wojcik, J. Mould Jr., R. Ferguson, R. Martino, K. K. Low, "Some Image Modeling Issues for I-line, 5X Phase Shifting Masks", *Proceedings of the SPIE,* vol. 2197, pp. 455-465, 1994.

[101] G. L. Wojcik, D. K. Vaughan, J. Mould, F. Leon, Q. Qian, M. A. Lutz, "Laser Alignment Modeling Using Rigorous Numerical Simulations", *Proceedings of the SPIE,* vol. 1463, pp. 292-303, 1991.

[102] G. L. Wojcik, D. K. Vaughan, L. K. Galbraith, "Calculation of Light Scatter from Structures on Silicon Surfaces", *Proceedings of the SPIE,* vol. 774, pp. 21-31, 1987.

[103] A. Wong, *Resolution Enhancement Techniques in Optical Lithography,* vol. TT47, SPIE Press, Chapter 1, 2001.

[104] *ibid.*, figure 2.4.

[105] A. Wong, *Rigorous Three-Dimensional Time-Domain Finite Difference Electromagnetic Simulation*, Ph.D. Dissertation, University of California, Berkeley, 1994.

[106] *ibid.*, Chapter 7.

[107] *ibid.*, Chapters 6 and 7.

[108] *ibid.*, pp. 67-72.

[109] A. Wong, A.R. Neureuther, "Mask Topography Effects in Projection Printing of Phase Shift Masks", *IEEE Trans. on Electron Devices*, vol. 41, pp. 895-902, 1994.

[110] A. Wong, T. Doi, D. Dunn, A. R. Neureuther, "Experimental and Simulation Studies of Alignment Marks", *Proceedings of the SPIE*, vol. 1463, pp. 315-323, 1991.

[111] K. S. Yee, "Numerical Solution of Initial Boundary Value Problems Involving Maxwell's Equations in Isotropic Media", *IEEE Trans. Ant. Propag.*, vol. 14, pp. 302-307, 1966.

[112] S. C. M. Yeung, *Validity of the Classical Theory of Spontaneous Emission and the Fast Multipole Method for Electromagnetic Scattering*, Ph.D. Dissertation, University of California, Berkeley, Table 1.1, 1995.

[113] M. S. Yeung, D. Lee, R. Lee, A. R. Neureuther, "Extension of the Hopkins Theory of Partially Coherent Imaging to Include Thin-Film Interference Effects", *Proceedings of the SPIE,* vol. 1927, pp. 452-463, 1993.

[114] M. S. Yeung, "Modeling High Numerical Aperture Optical Lithography", *Proceedings of the SPIE,* vol. 922, pp. 149-167, 1988.

[115] C. Yuan, "Calculation of One-Dimensional Aerial Images Using the Vector Theory", *IEEE Trans. Electron Devices,* vol. 40(9), pp. 1604-1613, September 1993.

[116] http://www.sigma-c.de/products.html

[117] http://www.kla-tencor.com/products/litho_sim/products_prolith7.html

[118] http://www.millennium.berkeley.edu